University of Cincinnati

Date: 6/15/2020

I, Alex R Walker, hereby submit this original work as part of the requirements for the degree of Doctor of Philosophy in Aerospace Engineering.

It is entitled:

Genetic Fuzzy Attitude State Trajectory Optimization for a 3U CubeSat

Student's name: **Alex R Walker**

This work and its defense approved by:

Committee chair: Kelly Cohen, Ph.D.

Committee member: Manish Kumar, Ph.D.

Committee member: Ou Ma, Ph.D.

Committee member: Phil Putman, Ph.D.

Committee member: Anoop Sathyan, PhD

36764

Genetic Fuzzy Attitude State Trajectory Optimization for a 3U CubeSat

A dissertation submitted to the
Graduate School
of the University of Cincinnati
in partial fulfillment of the
requirements for the degree of

Doctor of Philosophy
Aerospace Engineering & Engineering Mechanics
College of Engineering and Applied Science

Alex R. Walker

M.S. University of Cincinnati (2013)

June 2020

Committee Chair: Kelly Cohen, Ph.D.

Abstract

A novel approach to parameterize and solve for optimal satellite attitude state trajectories is presented. The optimal trajectories are parameterized using fuzzy inference systems (FISs), and the FISs are optimized using a genetic algorithm. Eight different constrained optimization problems are solved. The objective of each optimization problem is either battery charge maximization, link margin (equivalent to antenna gain) maximization, or experiment temperature minimization. All optimization problems consider reaction wheel angular velocity and reaction wheel angular acceleration constraints, and five of the optimization problems consider either battery charge constraints, antenna gain constraints, or both battery charge and antenna gain constraints. Reaction wheel constraints are satisfied using an attitude state filter at the output of the FISs and an optimal magnetic torque / reaction wheel desaturation algorithm, the design of both of which is presented herein. Optimal attitude state trajectory, or attitude profile, FISs are compared with a nominal attitude profile. It is shown that, while the nominal attitude profile offers good performance with respect to both battery charge and link margin, the optimal attitude profile FISs are able to outperform the nominal profile with respect to all objectives, and a minimum temperature attitude profile FIS is able to achieve average experiment temperatures 30–40 K lower than the nominal attitude profile. The attitude state trajectory optimization solutions presented in this work are motivated by the needs and constraints of the CryoCube-1 mission. Because this work is integral to the functionality of the CryoCube-1 satellite system, the effort taken to successfully build, test, deliver, launch, and deploy this CubeSat is detailed. The intent of providing this systems view is to provide the context necessary to understand exactly how the attitude state trajectory optimization results were used within the satellite system.

Acknowledgements

This work would not have been possible without the support I received from my family, friends, and co-workers. Thank you to my “work family,” including Cody Kornowski, Jason Epperson, Steve Faetanini, Scott Baaske, Marty Roth, Vince Jones, Jon Sasson, Matt Holdren, Terry Hui, Alex Yeckley, and Marty Offineer, for providing the support I needed to finish this dissertation and help build this satellite in the process. Thank you to the CryoCube team at NASA KSC, including Nick Pack, Tony Carta, and Mike Harris. Thank you to George Satornino and Dan Lowe for funding my education and providing a great place to work. And thank you to Tony Skaff for providing your words of advice and the flexibility in my schedule. I would especially like to thank Dr. Phil Putman for starting the CryoCube project, for allowing me the opportunity to play as big a role as I did in this project, and for serving on my dissertation committee.

Thank you to my family. Thank you Andy, Melessa, Quincy, and Lucy for allowing me to live with you for a semester while I had to take classes. Thank you, Aaron, for talking through some of the problems in this work with me and for pushing me to get out of the house once in a while. Thank you, mom, for supporting me when I needed it, for providing me space when I needed it, and for helping verify functionality of the FIS code. Thank you, dad, for driving me to my first day of classes for this PhD (4 hours each way) and for supporting me in numerous other little ways throughout this journey.

Thank you to the members of my committee: Phil (again), Ou, Manish, Anoop, and Kelly. I would especially like to thank my advisor, Dr. Kelly Cohen, for believing in my abilities and for pushing me to get this degree. Thank you for introducing me to the world of fuzzy logic and genetic algorithms. Thank you for all of the advice you’ve given me through the years. And thank you for helping to open up many new opportunities for me. I look forward to what the future holds.

Contents

List of Figures

List of Tables

1 Introduction

1.1 Background and Motivation

The work in this dissertation is motivated by CryoCube-1, a satellite developed by NASA Kennedy Space Center (KSC) and Sierra Lobo, Inc. (SLI), and its mission to demonstrate passive cooling technology for use on small satellites. CryoCube-1, pictured in Fig. 1-1 and Fig. 1-2, is a 3U CubeSat, a class of small satellites, or satellites with mass less than 500 kg, whose sizes are defined by a common unit of measure, U, where one U is a cube with side length 10 cm. The goal of CryoCube-1 is to demonstrate technology developed by SLI to passively cool elements of a CubeSat to cryogenic or near-cryogenic temperatures. For CryoCube-1, passive cooling is accomplished by use of a deployable sunshield which shades parts of the spacecraft from direct view of thermal radiation sources, such as the sun and earth. Careful selection of geometry and materials in the shield and other parts of the spacecraft help insulate the cryogenically cooled portions of the spacecraft from the warmer, near-room-temperature portions of the spacecraft, preventing the cryogenic portions of the spacecraft from warming up.

Passive cryogenic cooling technology has several practical applications on satellites of all sizes. One area in which CryoCube-1's passive cooling technology may be applied is cryogenic fluid management (CFM), particularly in maintaining cryogenic propellants, such as liquid oxygen (LOX), liquid methane, and liquid hydrogen, in a liquid state for long durations, on the order of months or years, while in space. Cryogenic chemical propulsion systems generally offer higher specific impulse (I_{SP}), higher thrust, and/or lower toxicity than the alternative space propulsion systems[1]. For example, non-cryogenic hypergolic systems (e.g. N_2O_4 and monomethylhydrazine) generally have high I_{SP} and high thrust but also high toxicity; monopropellant systems (e.g. cold gas, hydrazine) have low I_{SP}, high thrust, and varying toxicity; and electric propulsion systems (e.g. hall effect and ion thrusters) have very high I_{SP} (orders of magnitude higher than chemical propulsion) but very low thrust (orders of magnitude lower than chemical propulsion) and low toxicity[1]. These general characteristics make cryogenic chemical propulsion systems particularly well-suited for maneuvers requiring large changes in velocity to occur on the order of several minutes to several hours (e.g. launch, landing, time-sensitive orbit maneuvers, etc.). However, modern space propulsion systems that use cryogenic propellants carry only marginally more propellant than they need to perform a given maneuver, typically just launch and early orbit operations, and allow excess liquid propellants to boil off into gases which are then vented to space[2]. This strategy has led to a pattern of thinking that the farther a spacecraft must go, the larger

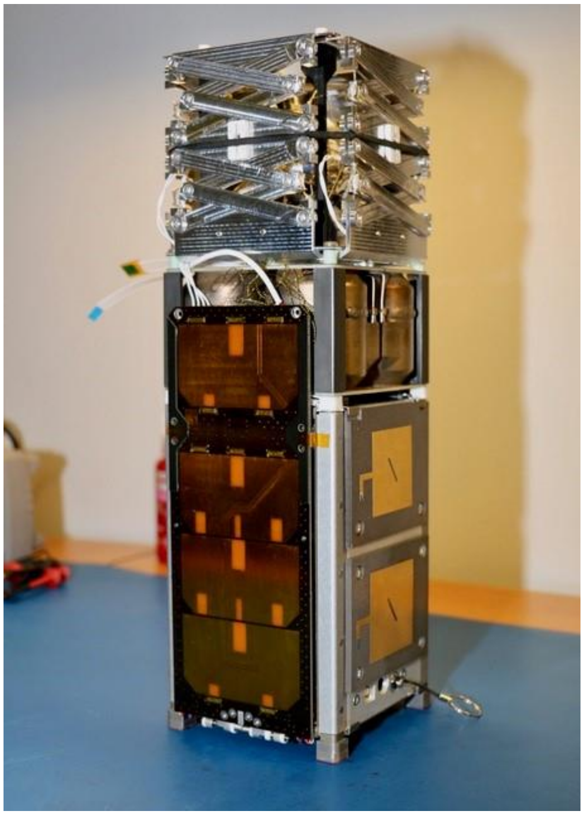

Fig. 1-1—CryoCube-1 in stowed configuration.

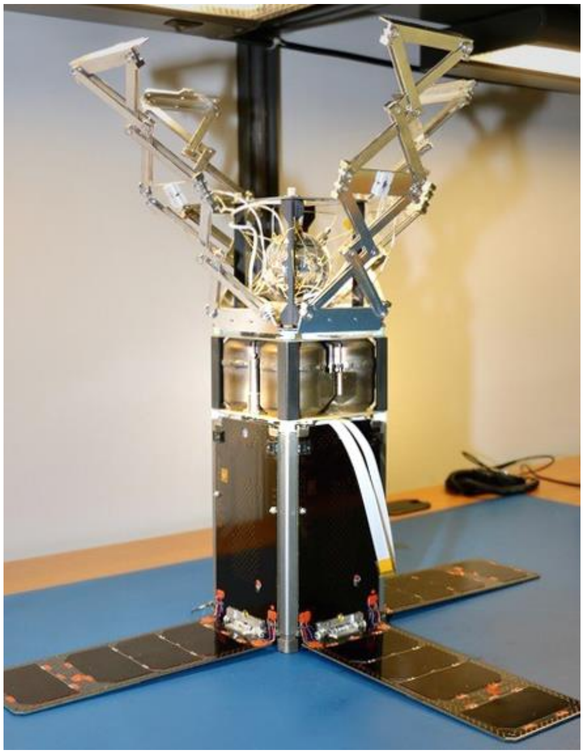

Fig. 1-2—CryoCube-1 in semi-deployed configuration.

the launch vehicle needs to be, because, of course, the farther the spacecraft must go, the larger the Delta V required to get there; the larger the Delta V, the more propellant; the more propellant, the heavier the vehicle at takeoff; and the heavier the vehicle at takeoff, the more propellant and larger the engines. Famously, the Saturn V rocket which launched the first people to the moon, was about 98.5% propellant and propulsion systems, by mass, at launch[3]. While it is true that a single space vehicle must be larger the farther it has to go, there is another strategy for space propulsion which has not been widely implemented: in-space fueling of space vehicles. With in-space fueling, a launch vehicle could carry a spacecraft whose propellant tanks are empty at launch to a propellant depot, or in-space storage vessel capable of transferring propellant to and from other spacecraft (like a gas station), where the spacecraft's propellant tanks would be filled. The mass savings at time of launch would mean less fuel and therefore a smaller launch vehicle could be used to get the spacecraft to space. Recent space transportation architecture studies have shown that using just two or three propellant depots, strategically deployed in different orbits, would enable manned missions to the moon and Mars with currently available expendable launch vehicles[3,4]. Depots also enable missions to service geostationary satellites, providing cost "savings, in terms of dollars per pound… by a factor of two or greater"[2]. In its Technology Taxonomy, NASA has identified the need to "enhance… conservation of fluids to reduce commodity costs and losses (from boil off…)" and specifically cites "zero boil-off storage" as an example technology which could help meet this need[5]. Long-duration, low boil-off storage of cryogenic propellants has not been demonstrated in the space environment, and is a significant gap in developing the technology required to implement propellant depots[2].

Fig. 1-3—CryoCube-1's gas pressure system is designed to liquefy gaseous Xenon at cryogenic temperatures.

The cryogenically-cooled portion of CryoCube-1 contains a Xenon gas pressure system, shown in Fig. 1-3, which is intended to demonstrate long-duration storage of a cryogenic liquid on-orbit. However, unlike a propellant depot, CryoCube-1's pressure system is a sealed volume with a constant amount of Xenon gas, so the satellite cannot transfer propellant to other spacecraft and cannot use the propellant to generate propulsion[*]. As the Xenon gas in CryoCube-1's pressure system cools to cryogenic temperatures, it condenses into a liquid. Like all cryogens, liquid Xenon is hundreds of times denser than gaseous Xenon at the same temperature, so as the Xenon condenses into a liquid, the pressure of the pressure system decreases rapidly. This rapid pressure decrease is measured by a pressure transducer installed in CryoCube-1's experiment tank. Temperature sensors on the exterior of the experiment tank are also used to estimate the state of the Xenon fluid within the tank.

Another area in which passive cryogenic cooling technology may be applied is space-based telescopes. Space-based telescopes are used to image many different portions of the electromagnetic spectrum, depending on the application, either for space or earth observation for science or defense applications. The sensing elements, or focal plane arrays, of infrared (IR) and

---

[*] Xenon is a common propellant in electric propulsion systems.

gamma ray optical systems in such telescopes often require cryogenic cooling to function at useful levels of sensitivity[6]. Passive cooling techniques are preferable to active coolers, such as Stirling, thermoacoustic, or Brayton cryocoolers, because active coolers tend to induce vibrations in the optics systems, causing jitter, which must be compensated for to maintain required image quality. Long-duration passive cryogenic cooling of space-based telescopes has been successfully demonstrated both in the Spitzer telescope, which maintained a superfluid helium dewar, and the Wide-Field Infrared Survey Explorer (WISE) telescope, which maintained a solid hydrogen dewar[2]. Using its superfluid helium dewar and supporting thermal management system, the Spitzer telescope was able to maintain temperatures as low as 1.5 K for over five and a half years[2]. Though CryoCube-1 contains no optical systems, its sunshield technology could be adapted to shade a thermal radiator used to directly cool a focal plane array or to shade a thermal radiator attached to the heat rejection element of an active cryocooler which is used to cool a focal plane array.

As mentioned above, CryoCube-1 is a 3U CubeSat (10 cm × 10 cm × 30 cm) with an experimental sunshield and fluid storage pressure system comprising approximately half the spacecraft volume (the top half of the CubeSat as shown in Fig. 1-1 and Fig. 1-2) and an electronics bus comprising the other half. The experimental fluid storage system consists of a spherical experiment tank, four cylindrical storage tanks, a fill port, and a manifold which is used as a central connection point for the tanks and fill port; the manifold connects to all tanks and the fill port via 1/32" tubing. The interior volume of the tubes, tanks, manifold, and fill port cannot be isolated from one another and thus allow the Xenon gas to flow freely among the tanks at all times during the mission. The fill port contains a check valve, similar to the Schrader valves in bike and car tires, which prevents the Xenon gas from leaking out when the system is pressurized. The experiment tank is a single part made from additively manufactured Inconel and the storage tanks are each two parts, each made from additively manufactured Inconel, welded together. During operation, Xenon gas in the experiment tank cools to cryogenic temperatures and condenses while the gas in the storage tanks cools but does not condense, remaining warm relative to the experiment tank. The deployable sunshield consists of a spring-loaded aluminum mechanism, two deployment circuits, and a single layer of aluminized Mylar. Each deployment circuit consists of two resistors, wired in parallel, which heat up when a current passes through them in order to burn through Spectra fishing line which holds the sunshield in its stowed state; one circuit is a primary and the other is a backup. In its deployed state, the aluminized Mylar of the sun shield stretches into an approximately pyramidal shape, pulled taught by the mechanism, and shrouds the top third of the satellite containing the experiment tank. The structure to which the sunshield and experimental pressure system mount is primarily composed of low-thermal-conductivity plastics, including G10 and/or FR4, but also contains four anodized aluminum rail sections adjacent to the storage tanks to meet requirements for deployment from rail-based CubeSat deployment systems, such as the NanoRacks CubeSat Deployer (NRCSD)[7]. The experiment tank does not directly touch the structure in order to limit thermal conduction from warmer parts of the spacecraft to the cryogenically cooled tank. Instead, low-thermal-conductivity, high-strength strings are used to suspend the experiment tank from the structure in such a way that resonant modes of the string suspension system are not excited by vibrations from launch. Throughout the experiment and gas storage sections of the spacecraft, surface coatings and other materials are chosen and applied with the goal of attaining as low of an experiment temperature as possible. The experiment section and gas storage sections are instrumented with temperature sensors to validate in-flight thermal performance against computer models, and the pressure system is instrumented with a pressure transducer to determine the state (liquid or gas) of the Xenon fluid.

The electronics stack, pictured in Fig. 1-4, fits within an aluminum chassis separate from the gas storage and experiment sections of CryoCube-1. Three deployable solar panels (resting on the table in Fig. 1-2), one non-deployable solar panel (on the downward facing face in Fig. 1-1 and Fig. 1-2), and transmit and receive antennas (visible on the right side of the electronics section in Fig. 1-1) attach to the outside of the electronics section chassis. Each solar panel has a magnetorquer embedded in it, and each magnetorquer is capable of producing a magnetic moment normal to the face of its solar panel. In its fully assembled state, the chassis, solar panels, and antennas obscure the internal electronics from view. The internal electronics include: an electrical power conditioning and distribution board or electrical power subsystem (EPS) which manages electrical power from the solar panels to recharge the spacecraft's batteries, converts electrical energy stored in the batteries to voltage levels usable by the spacecraft's circuits, and manages electrical power distribution to all spacecraft circuits; a rechargeable lithium ion battery; a command and data handling (C&DH) board which processes ground commands, processes experiment data, and executes attitude determination and control algorithms; a set of three orthogonal reaction wheels which manage spacecraft angular momentum, an experiment interface board for collecting and routing raw experiment data and radio communication signals; a radio for sending and receiving data with the ground station; and two 9-degree-of-freedom IMUs mounted on a plate above the radio.

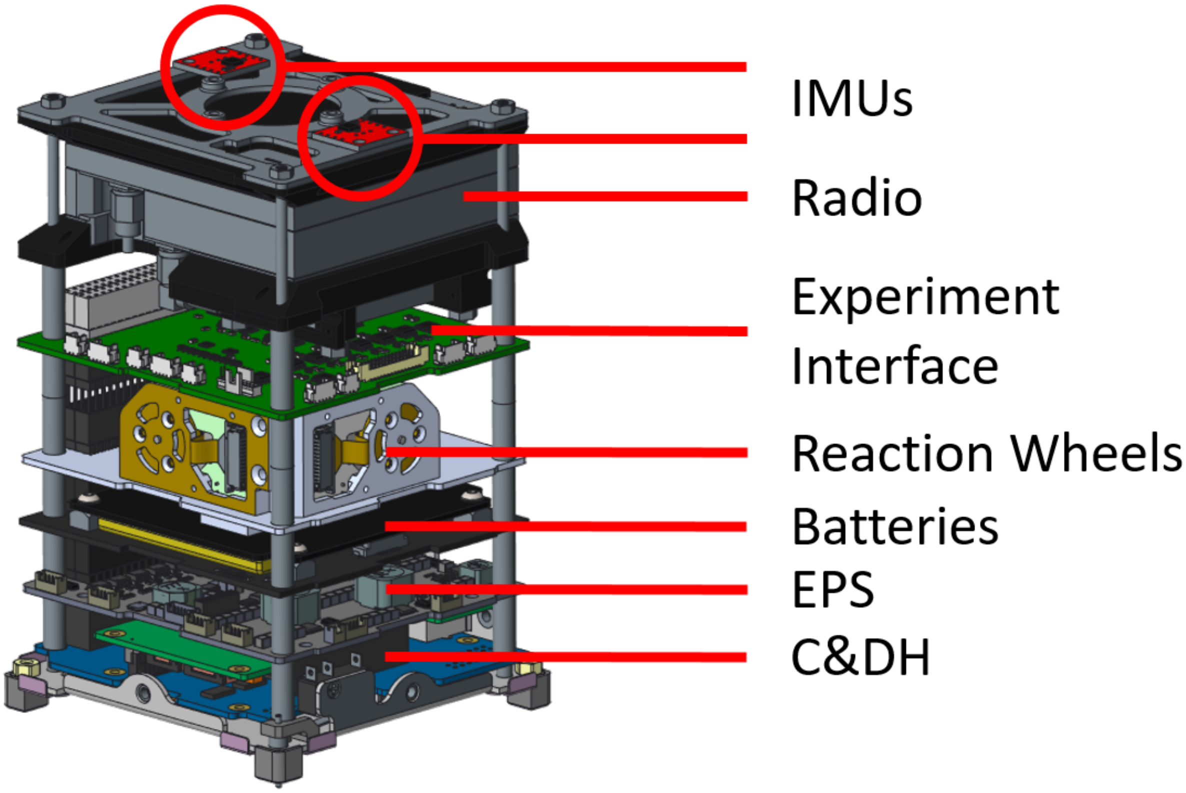

Fig. 1-4—CryoCube-1 electronics stack.

Though CryoCube-1's experiment tank temperature is not actively controlled by a cryocooler, active attitude control is required to ensure the open end of the sun shield points to deep space, passively cooling the experiment. In addition to experiment temperature, CryoCube-1's attitude determination and control subsystem (ADCS) also influences battery charge and communication link strength, which are both critical to mission success. Without sufficient battery charge, the spacecraft will be unable to control its attitude or transmit experiment data, and without sufficient communication link margin, the spacecraft will be unable to transmit experiment data to the ground. Fig. 1-5 shows how the hardware and software components of CryoCube-1's ADCS work together to directly control its attitude and influence its experiment temperature, battery state of charge, and communication link strength. The C&DH contains CryoCube-1's only microprocessor which runs code that collects, stores, and disseminates experiment data and vehicle health data;

executes ground commands; and performs all attitude determination and control tasks. The ADCS code may receive commands directly from the ground to update the two-line element set (TLE), which defines the on-board orbit model, or to switch desired attitude modes. The TLE and current time are used to estimate orbit position and velocity as well as coordinate transformations required to determine spacecraft attitude. Spacecraft position, velocity, and coordinate transformations are used to determine the desired attitude. The current attitude state estimate is recursively calculated using an extended Kalman filter (EKF) with three-axis gyroscope and three-axis magnetic field measurements taken from the two IMUs. Desired attitude and estimated attitude are used to calculate an attitude state error. The state error is input into a selectable control law, either full-state constant gain or fuzzy, which outputs magnetic moment and reaction wheel acceleration commands. The reaction wheels accelerate, storing excess spacecraft angular momentum, and magnetorquers generate a magnetic moment, exchanging spacecraft and reaction wheel angular momentum with the earth. The spacecraft attitude changes in response to actuator output and environmental disturbance torques acting on the spacecraft. As spacecraft attitude changes, sun shield orientation changes, affecting experiment temperature. Additionally, spacecraft attitude also affects solar panel orientation, which affects solar power generation, and antenna orientation, which affects ground communication link strength. Radio use, reaction wheel use, and magnetorquer use drain battery charge while solar power generation replenishes battery charge.

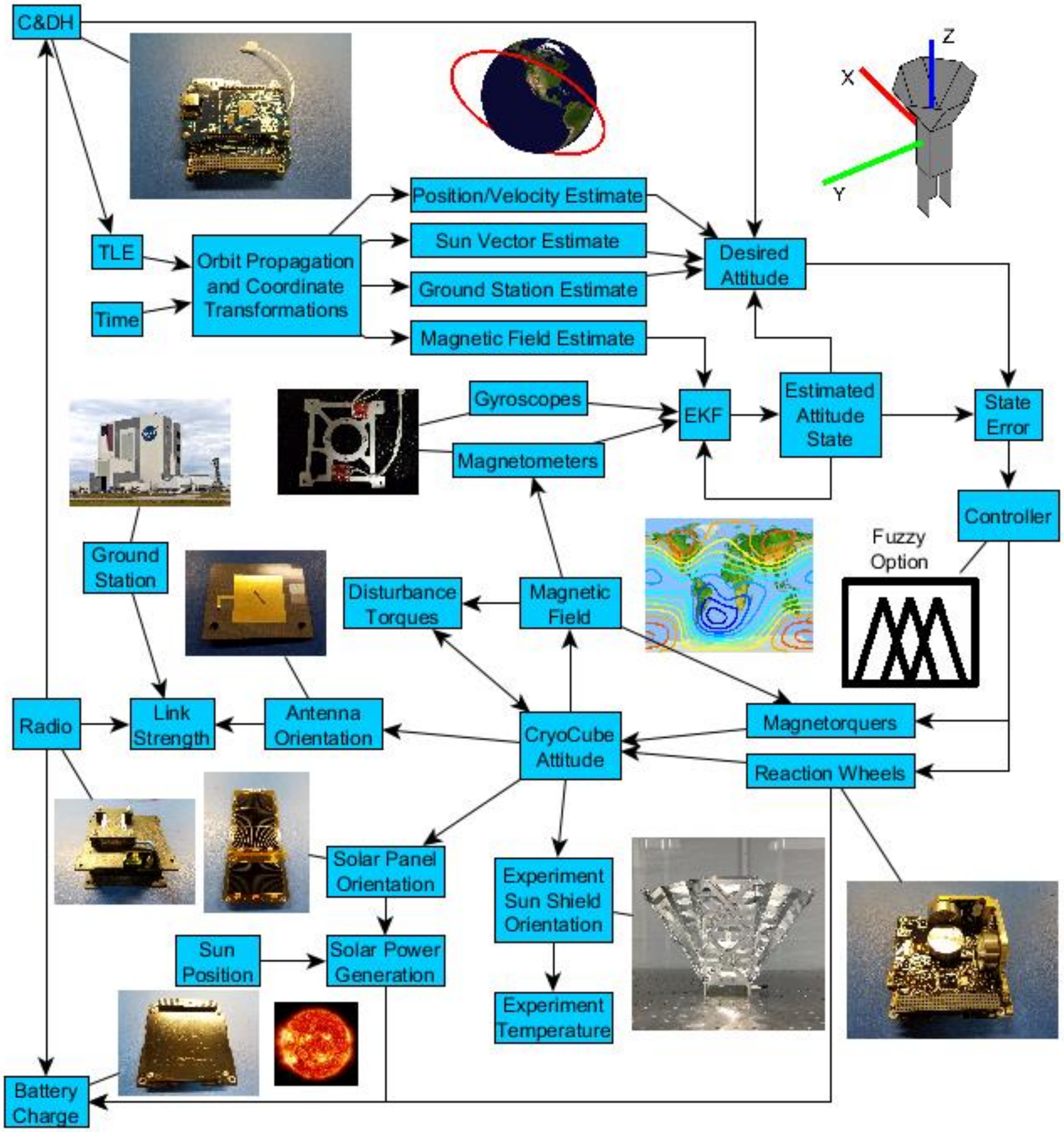

Fig. 1-5—CryoCube-1 functional block diagram.

The highly-coupled dependence of satellite power, communication link strength, and experiment temperature on spacecraft orientation makes selection of the best attitude(s) an important task for the CryoCube-1 mission. Prior to the work presented in this dissertation, several attitude concepts had been investigated, including: (1) nadir-pointing while in eclipse with slews to sun-pointing solar arrays while in sunlight, (2) constant sun-pointing solar arrays, and (3) off-nadir pointing. However, it was unclear which attitude was best for accomplishing the mission goal of passively cooling the experiment to cryogenic temperatures. Additionally, it was unclear if the attitude or attitude state trajectory that reaches the lowest experiment temperature is achievable given CryoCube-1's attitude control hardware, communication hardware, power storage hardware, and power generation hardware constraints. Hardware selection was primarily driven by volume constraints of the 3U spacecraft with roughly half of the satellite volume dedicated to the cryogenic fluid management experiment. Notably, CryoCube-1's reaction wheels are undersized for a wide range of potential attitude profiles (state trajectories) as the atmospheric drag torque on the sun shield is relatively large, and CryoCube-1's reaction wheels were selected primarily for their low profile in the electronics stack. In order to answer these questions and find the best attitude profile(s) to accomplish the CryoCube-1 mission goals, a series of feasibility search and optimization problems were set up and solved. These feasibility search and optimization problems and their solutions are presented in this dissertation.

CryoCube-1, as with many satellites, is a somewhat complicated system with many interdependent components that are designed to fit together and operate in very specific ways all in a relatively small package. The systems engineering effort to design, prototype, assemble, test, and deliver CryoCube-1 took eight years and was fraught with challenges, some of which many CubeSat project teams experience, including: volume constraints of the 3U CubeSat form factor, ambitious initial technology demonstration goals, shifting deployer interface and operational requirements, varied funding and prioritization of the project, and use of a small and relatively inexperienced design team. The volume constraints made it particularly challenging to develop a system that could meet the ambitious technology demonstration goals initially set by the

CryoCube-1 project team. These initial goals included using Oxygen instead of Xenon as the working fluid, operating the pressure system at 2000 psia, demonstrating reduced-gravity liquid-vapor interface (wet/dry) sensor technology, and taking images and video of the condensation process. The additional hardware required to accomplish these goals did not leave much room for other hardware, such as reaction wheels, which were found to be necessary to reliably point the open end of the sunshield. The design team quickly discovered that many components one may consider small actually take up a considerable fraction of the volume within the CubeSat and can become very difficult to deal with from a packaging perspective. Attempting to find solutions to these difficult technical challenges cost the team years of schedule and funding. CryoCube-1 was initially funded under a Phase 1 NASA SBIR, but was unable to receive follow-on funding due to growth in the number of SLI employees above the SBIR standard for small business size. The project was sustained under SLI internal funding for the remainder of its lifecycle, though a Space Act Agreement with NASA Kennedy Space Center (KSC) allowed work on the communication subsystem to be completed by the government.

During the initial design phase of the CryoCube-1 project, the design team developed CryoCube-1 from its initial concept through several major design iterations. System models, including solid models, thermal models, power budget, link budget, and attitude determination and control models were developed and maintained to document the system design. A Preliminary Design Review (PDR) was held in 2014, and over the next few years, a series of subsystem-level Critical Design Reviews (CDRs) were held for many of the subsystems (circuit boards) purchased as commercial off-the-shelf (COTS) components, though the CDRs served more as formal reviews of engineering specifications prior to submitting purchase requests (PRs). These PRs resulted in requests for bid in full and open competitions for each subsystem, a standard practice for purchasing items over a given dollar value threshold. After nearly six years of relatively slow progress, in early 2018, the first of two periods of highly-focused, concerted effort to finish CryoCube-1 and deliver it for launch began. During this time, the design team adopted more of a spiral approach to its engineering processes, assembling prototypes, assembling proto-flight hardware, and rapidly developing and testing software. By May of 2018, the proto-flight system had been assembled for the first time and some of the major hurdles of software development had been overcome. Continuing the spiral approach to iterate system design, in early 2019 the sunshield design was completed, prototyped, and tested; all flight software was developed and tested; the communication system underwent radio frequency (RF) testing; the battery underwent qualification testing; and the EPS and battery subsystems both were replaced due to last-minute hardware failures. While finishing the design and assembly, the CryoCube-1 team worked with NanoRacks, a company which provides services to put CubeSats into orbit, to get CryoCube-1 manifested on a flight to the International Space Station (ISS). Prior to the ISS program accepting delivery of the satellite, the team was required to provide NanoRacks with various documentation which NanoRacks presented to the ISS Safety Review Board on behalf of the CryoCube-1 team. Once the documentation was accepted by the ISS program and functional testing was complete to the satisfaction of SLI and NASA KSC team members, CryoCube-1 was delivered to the ISS program. Chapter 7 provides a detailed discussion of the systems engineering approach to management, assembly, and testing of CryoCube-1 as well as a discussion of launch and early operations and the key lessons the CryoCube-1 team learned in developing its first CubeSat.

1.2 Scope and Uniqueness of Dissertation

This dissertation considers the design of optimal attitude state trajectories for the CryoCube-1 mission and provides an in-depth systems engineering perspective of the satellite system and its development to contextualize the optimal state trajectory work. Additional functionality of the attitude determination and control system, including design of the attitude determination algorithms and design of the attitude controllers is not presented. A conventional Extended Kalman Filter (EKF) approach is taken to estimate CryoCube-1's attitude. Three different attitude controllers are implemented on CryoCube-1: a B-dot controller for detumble, a conventional infinite-horizon linear quadratic regulator (LQR) for full state feedback control, and a fuzzy controller as an alternative method for full state feedback control. EKFs, LQRs, and B-dot controllers are all well-documented in literature, and the author has previously presented methods for using fuzzy logic for full state attitude feedback control[8].

Novel methods for determining and parameterizing optimal attitude state trajectories are presented herein. The optimal state trajectories are parameterized using fuzzy inference systems (FISs) which are optimized using genetic algorithms. Furthermore, parameterization of the optimal attitude in this work leaves all three rotational degrees of freedom unconstrained. Full unconstrained three-degree-of-freedom attitude profile optimization for spacecraft is not widely presented in literature. Because many satellites have imagers/cameras for taking pictures or directional antennas for communicating with high data rates, most of the attitude profile optimization problems of interest either seek to point a single axis of a spacecraft in a known direction and find the best rotation angle about this fixed axis or seek to determine the best direction to point a single axis of a spacecraft, choosing to use two attitude parameters to represent this pointing direction, because rotation about the pointing axis does not matter.

2 Literature Review

Active attitude control is an important aspect of almost every satellite mission and is, therefore, very well-documented in literature. Whether it be to point an instrument at an astronomically interesting object many light-years away, point an antenna to an Earth-based ground station, or point a thermal radiator to deep space, nearly every spacecraft needs to point some part of itself at a specific target during some part of its mission. Sometimes this pointing may be accomplished completely passively, taking advantage of the local predictable disturbance environment to stabilize the satellite in a desired orientation. However, it is often the case that some active means of control is required to accomplish the task of pointing the spacecraft.

Ultimately, the attitude profile, the attitude control system modes of operation, and the attitude control system hardware, if any, are determined from mission requirements and both subsystem-level and system-level spacecraft design iteration[9]. Dependencies among the attitude control subsystem and the electrical power subsystem, thermal control subsystem, communications subsystem, and spacecraft structure all drive design of the attitude control subsystem[9]. In Cryo-Cube-1, for instance, the attitude control subsystem must point the open end of the sun shield to deep space for thermal control, point the antennas toward ground stations for communication, and point solar arrays toward the sun for power generation, but the attitude control actuators are constrained in size by the volume of the 3U cubesat structure and are constrained in their ability to actuate by the available power stored in the batteries of the electrical power subsystem. Nevertheless, the actuators must be powerful enough to reject disturbances, specifically torques exerted on the spacecraft, in order to maintain the desired attitude, as these disturbances generally move the spacecraft away from its desired attitude.

Disturbance torques result from a variety of forces acting on the spacecraft along directions that do not pass through the spacecraft's center of mass[9]. The magnitude and source of these disturbance torques is highly dependent on the spacecraft's orbit. Aerodynamic torques, for instance, result from the interaction of an atmosphere with the spacecraft; these torques are largest in low Earth orbit or in orbits close to other planetary bodies with atmospheres[9,10]. Similarly, solar pressure torques result from the interaction of sunlight with the spacecraft[9,10]. Sunlight photons, like all photons, have nonzero momentum, and when they strike spacecraft surfaces, these photons are absorbed or reflected, exchanging their momentum with the spacecraft resulting in a net solar pressure force and torque[9]. As the flux of solar photons decreases with the square of the distance to the sun, the solar pressure torque is greatest near the sun[9]. Gravity gradient torques result from the small difference in the strength of gravity over the relatively small distances on the order of the size of the spacecraft[11]. The gravity force on an amount of spacecraft mass closer to the planet is greater than the gravity force on an equal amount of spacecraft mass farther from the planet, decreasing with the cube of the distance from the center of the planet; this difference in gravitational force produces a torque which tends to align the spacecraft axis of minimum mass moment of inertia with the gravity force vector[10,11]. Magnetic forces result from the interaction of spacecraft-generated magnetic fields with local magnetic fields, such as Earth's magnetic field for spacecraft in Earth orbit, and are therefore strongest close to objects with relatively strong magnetic fields[9,10]. Other forces a spacecraft may encounter likely result from the interaction of the spacecraft with micrometeoroids, dust, and ionizing radiation, such as alpha and beta particles emitted from the sun and higher-energy galactic cosmic radiation emitted from other stars;

however, for spacecraft in near earth orbits, these forces are much less predictable and relatively small magnitude compared with aerodynamic, solar pressure, gravity gradient, and magnetic field disturbance torques[10].

2.1 Design and Optimization of Spacecraft Attitude

One of the main tasks of designing the attitude control system is to select attitude control modes of operation[9]. In each mode, a particular attitude profile, type of pointing, or method of control is selected or designed to accomplish some task integral to achieving the mission objective. For instance, a spacecraft designed to make astronomical observations of multiple stars may have a mode to perform inertial pointing, a mode to perform a slew maneuver between inertial points of interest, and a mode to point its antennas toward ground stations for data up/downlink. These operational modes are designed independently, and mode transition criteria are developed so that the attitude determination and control system may operate as a deterministic finite state machine, wherein the attitude determination and control program deterministically transitions from one state to another based on transition criteria. As presented in literature on the topic, the attitude design or selection process for a single operational mode, and more generally all design processes, tend to be defined by two mutually exclusive characteristics: (1) whether the design process is single-discipline or multidisciplinary and (2) whether the design decision-making process is guided by heuristics or rigorous mathematical optimization. Single-discipline attitude design approaches only consider the spacecraft attitude from a geometrical point of view, ignoring coupling of the attitude with other disciplines, such as communications or thermal, whereas multidisciplinary approaches to attitude design consider how other disciplines or subsystems may be affected by attitude design and/or how the design of other subsystems affects attitude design. Heuristic decision-making tends to be used when the performance of feasible solutions throughout the design space is relatively indistinguishable, a generally applicable solution is known to work for a given design problem, or the optimal solution is very difficult to find, whereas optimal decision-making is used when the best, or even an improved solution is sought.

A single-discipline optimization approach was taken to attitude design in Ref. 12, wherein it was desired to observe a geostationary satellite from a space-based platform. There, the observation satellite was constrained to take measurements in an inertial or nearly inertial orientation[12]. However, it was desired to maximize the observation time, so Powell's method, a gradient-free optimization approach, was used to find the optimal inertial attitude for observation[12]. The observation satellite would nominally be oriented in a local level frame until a given switch time, at which point it would maintain switch time attitude as observed from an inertial frame or from a frame that changes with the procession of the observation satellite's orbit plane[12].

A multidisciplinary heuristic approach was used to design the attitudes attained during the Astro-1 and Astro-2 missions. In these missions, the Space Shuttle, a mature vehicle design at the time, was used as a host for several astronomical observation instruments[13,14]. A suite of attitude profile design tools were developed for the Astro-1 program to select inertially-pointing attitudes the Space Shuttle could attain that would meet mission requirements, including: (1) pointing two different imagers at different objects, often at the same time, (2) keeping imager lines of sight pointed away from the sun, quantified by a sun exclusion angle, (3) maintaining acceptable communication with TDRS Ku-band satellites, and (4) providing acceptable heating of Space Shuttle window Viton seals, which could fail if allowed to get too cold for too long[13]. The tool suite was used in a design workflow consisting of first pointing the orbiter –Z-axis (i.e. shuttle payload compartment and instrument boresight direction) toward the object(s) of interest, then adjusting this orientation so that the orbiter +X-axis (i.e. nose of the shuttle, where the windows are) would be as close to sun-pointing or Earth-pointing as possible without losing sight of the science target(s); often, the science targets were opposed to the sun, so the orbiter +X-axis would be roughly perpendicular to the sun vector prior to the secondary adjustment[13]. Though 250 attitudes were planned prior to the mission, a large number of anomalies, including failed data acquisition starts and control hardware out of limits errors, caused on-the-fly attitude redesign, made easier by the tool suite and workflow developed pre-mission[13]. Of the 220 attitudes actually executed for the Astro-1 mission, 120 were designed 12 hours prior to execution, and 78 more were designed with an even faster turnaround time[13]. The Astro-2 mission had a slightly different set of requirements, including a requirement to keep the boresight of one of its instruments (the Hopkins Ultraviolet Telescope, or HUT) at least 20 degrees from the velocity vector and excluding the window seal heating requirement of Astro-1, so the attitude design workflow was modified slightly[14]. First, the orbiter –Z-axis was pointed toward the object(s) of interest, and then the orbiter was rotated about its Z-axis until the Ku-band antenna pointed between two TDRS satellites, ideally, yet heuristically, maximizing data rate[14]. Applying lessons learned from the Astro-1 mission, only instrument activation and calibration were planned prior to launch of Astro-2, and all 367 science attitudes executed during the mission were generated in shifts 12 hours prior to data collection, a method dubbed the “blank timeline concept,” which allowed scientists to submit desired observations “without regard to an existing timeline”[14].

Similar to the Astro-1 and Astro-2 missions, a multidisciplinary heuristic approach was taken in selection of the attitude profile for the operational mode of the COLD-SAT spacecraft, a cryogenic fluid management mission proposed in the early 1990’s which never flew but would have demonstrated technology necessary to develop propellant depots, or gas stations in space, similar to the technology demonstration CryoCube-1 is designed to perform[15]. It was noted that "[a]ttitude selection [had] a critical impact on the thermal performance" of the COLD-SAT experiments as solar, earth albedo, and earth infrared radiation fluxes all tend to heat the spacecraft[15]. However, it was also noted that "[r]esults of this study [were] spacecraft and tank design dependent and may not be applicable to other, similar spacecraft configurations[15]." Designers evaluated three different attitude configurations for the primary mission, immediately eliminating a configuration in which one side of the spacecraft would face earth at all times because it would require articulating solar arrays which would have made the science experiments' requirement for low acceleration environment (10^{-6} g) difficult or impossible to achieve[15]. Both remaining candidate attitudes were sun-pointing, attitude A with the spacecraft's long axis in the orbit plane and attitude B with the spacecraft's long axis perpendicular to the orbit plane[15]. Toward one end of the spacecraft's long axis, the solar panels would have been attached, and toward the other end, the experiment would have been packaged[15]. In both configurations, the plane containing the solar arrays was fixed and inclined at an angle with respect to the orbit plane to maximize power generation[15]. The spacecraft also had to rotate 180 degrees about the earth-nadir vector whenever the sun vector crossed the orbit plane to maximize power generation[15]. Attitude A provided greater shading of the experiment from solar radiation flux and was therefore able to achieve lower temperatures than attitude B, though attitude B had the advantage of experiencing no orbital perturbations due to planned experimental thrusting[15]. As radiation flux and experiment temperature was the primary factor driving attitude design, attitude A was ultimately selected for the COLD-SAT mission[15].

When a multidisciplinary optimization approach is taken for a given design, it is usually referred to as multidisciplinary design optimization (MDO). In recent years, MDO has experienced increased use for design and optimization of complicated systems, especially those in the aerospace industry[16,17]. The typical MDO approach seeks to design whole systems, using design variables that span multiple disciplines, and is therefore used when many aspects of design can still be changed, such as in the early stages of design. When used at the system level, MDO is an effective tool that can be used to optimize the performance of a complicated system, exploring portions of the trade space that may be unexplored in either single-discipline or heuristic approaches[16]. Satellite MDO often uses mass minimization as the objective of optimization as mass is generally viewed as a proxy for launch cost[17,18]. However, Ref. 16 sought to maximize total data that could be downloaded from the University of Michigan's CADRE CubeSat. MDO problems can be extremely complex, with tens of thousands of design variables and millions of state variables[16]. Disciplines included in spacecraft optimization often comprise a subset of: orbit dynamics, attitude dynamics, power generation/storage/distribution, thermal performance, communication, and structures[16,17,18]. As noted in Ref. 16, "attitude profile over time can be designed" as part of MDO problems, as well. MDO can be accomplished using several different architectures, including the multidisciplinary feasibility (MDF) architecture and the simultaneous analysis and design (SAND) architecture, the choice of which can significantly impact the design solution[16]. Additionally, the choice of optimization algorithms can significantly impact the solution time of MDO problems. Gradient-based algorithms have been demonstrated to be effective for solving very large MDO problems, even when those problems have discontinuities and significant nonlinearities[16]. Discontinuities, for example, are often dealt with by using surrogate models which approximate the shapes of discontinuous functions but are themselves continuous[18]. Non-gradient algorithms, such as genetic algorithms, have been used extensively for design optimization in the past, but are often slow to find optimal solutions for large problems, because such algorithms tend to require more sampling of the design space[16]. However, neither gradient-based optimization nor genetic algorithms are guaranteed to find globally optimal solutions; often local optima are found[16].

Though design of CryoCube-1's attitude profile is multidisciplinary, in that it relies on direct analysis of attitude, thermal, communications, and electrical power subsystem models, it would not be considered MDO, because the only design variables considered are those within the attitude control subsystem. In addition, CryoCube-1's attitude profile design was highly constrained because, at the time this design was done, the attitude control system hardware had already been selected on the basis of being COTS hardware with flight heritage that was able to fit within the small available volume.

2.2 Attitude Control Hardware

In the typical attitude determination and control system design workflow, once an attitude profile is selected for each spacecraft mode of operation, the disturbance torque environment can be analyzed and actuators can be selected based on their ability to reject those disturbance torques. Generally, the purpose of attitude actuators is to manage momentum of the spacecraft, which may be accomplished one of two ways: storing momentum onboard or dumping momentum overboard[9]. Actuators used to store momentum onboard include reaction wheels, momentum wheels, and control moment gyros (CMGs). Reaction wheels start with zero angular velocity and are accelerated in response to external torques. Momentum wheels start with nonzero angular velocity, which provides gyroscopic stiffness that resists motion due to external torques, and are accelerated or decelerated as necessary to maintain attitude or a spacecraft spin rate. Control moment gyros are wheels spun at constant high speed and rotated perpendicular to their spin axis to generate very large control torques. Actuators used to dump momentum overboard commonly include thrusters and magnetorquers but may also include aerodynamic or solar pressure control surfaces[10]. Thrusters expel propellant at high velocity from the spacecraft, exerting an external force on the spacecraft, and if the line of action of this thrust force is offset from the spacecraft center of mass, the thrusters affect spacecraft angular momentum. Due to their relatively large volume and mass, thrusters are not widely used on nanosatellites, but are commonly used on larger spacecraft. Magnetorquers, also commonly referred to as magnetic torquers, are electromagnets that generate magnetic fields, commonly approximated as magnetic dipoles, which exert forces on other magnetized objects, such as the Earth. Therefore, magnetorquers allow a spacecraft in low earth orbit to exchange its angular momentum with that of the Earth; however, it is only possible for a spacecraft to generate a control torque perpendicular to the local magnetic field vector using magnetorquers, so other means of control are often required.

Typically, both momentum storage and momentum dumping devices are used in satellite attitude control systems[9]. Momentum storage devices are used to achieve high accuracy pointing, and momentum dumping devices are used to unload momentum storage devices so they do not saturate, which occurs when wheel motors reach their maximum speed and can no longer accelerate[9]. Momentum storage devices are typically sized to store the sum of the maximum worst-case momentum imparted by periodic disturbance torques over the course of a quarter to half an orbit and the worst-case momentum imparted by non-periodic, or secular, disturbance torques over a given time period determined by mission-level requirements[9]. In addition, momentum storage devices must be able to reject (i.e. exert a torque much larger than) worst-case disturbance torques and be capable of meeting any slew requirements, while momentum dumping devices must be able to unload the momentum from storage devices over the life of the mission and may be required to exert relatively small torques if used for fine pointing[9].

There are a number of competitors in the market offering CubeSat attitude control components and prepackaged systems in addition to some literature which has been published detailing the design of complete attitude control systems for CubeSats. Ref. 19, for example, details the design, analysis, and testing of a U/8-sized (5 cm x 5 cm x 5 cm) attitude control system with three orthogonal magnetorquer coils, three orthogonal reaction wheels, three magnetometers for measuring the magnetic field, and redundant electronics to avoid faults due to single event upsets. Many of the commercially available attitude control systems for CubeSats are relatively expensive, given the typical cost constraints of small satellite projects, so Ref. 20 presented a university-developed cost-effective design for a CubeSat attitude determination and control system. The system consisted of three orthogonal reaction wheels, three orthogonal magnetorquer coils, sun sensors, and an inertial measurement unit (IMU) as well as the supporting electronics and control algorithms[20]. Component-level testing was conducted with future plans to conduct system-level hardware-in-the-loop testing to validate system performance[20]. Similar commercial CubeSat attitude determination and control systems which contain reaction wheels and magnetorquers are sold by many different companies, including Blue Canyon Technologies, AAC Clyde Space, and Adcole Maryland Aerospace. Commercially available thrusters suitable for CubeSat attitude control are also available from a number of different companies, including: Busek, Moog, and CU Aerospace.

2.3 Attitude Control Algorithm Design

Once the attitude determination and control system hardware has been selected, the methods and algorithms used to control spacecraft attitude may be selected and designed. Generally, the attitude control system utilizes proportional-integral-derivative (PID) error state feedback to stabilize the spacecraft in a desired orientation, but proportional-derivative (PD) control may also be used, if acceptable performance is attainable[9]. State feedback may be linear, in which case control torque is a linear combination of PID errors, or it may be nonlinear, in which case control torque is a nonlinear function of PID errors. In addition to or instead of active control, some spacecraft may take advantage of passive stabilization, such as gravity gradient stabilization or passive magnetic stabilization[9]. A wide variety of techniques exist for designing state feedback attitude controllers and demonstrating these controllers meet stability criteria imposed by mission requirements.

One of the oldest and most widely used methods to design an attitude state feedback controller is to use a linearized model of the attitude dynamics along with classical frequency-domain controls techniques to select linear feedback gains that meet stability and accuracy requirements[9]. Other more modern methods of state-space pole placement may also be used with linearized dynamic models to select linear feedback gains. Even if more modern approaches are taken, results are often analyzed using frequency-domain techniques to gain a better insight into controller performance[9]. For instance, in Ref. 21, an H_∞ technique was used to design a pitch controller and a yaw, or azimuth, controller using linearized dynamics of attitude, gravity gradient boom vibration, gravity gradient torque, and reaction wheel torque to achieve better than one degree pointing accuracy and attenuate disturbances associated with boom vibrations. After an initial design, it was found that bandwidth of the controller was too large, causing the control torque to be unattainable, so reduced response time was accepted for more attainable levels of torque[21]. Using similar techniques, Ref. 22 developed an H_2 and H_∞ controller for a system using the angular momentum of fluid in a heat pipe for attitude control, Ref. 23 developed an H_2/H_∞ controller for a satellite without a priori knowledge of the type of actuator, and Ref. 24 developed a robust nonlinear H_∞ controller for an underactuated satellite with only two functioning reaction wheels.

While H_2 and H_∞ methods frame controller design as an output error signal magnitude minimization task, another common technique for choosing linear feedback gains, linear quadratic regulation (LQR), frames controller design as a task to minimize a quadratic function of state error and control effort. A number of researchers have used LQR techniques for attitude controller design, some of which integrate nonlinear techniques for improved performance. For instance, Ref. 25 developed an LQR in conjunction with a Kalman filter, forming an LQR/LQG estimator/controller for a microsatellite with control moment gyros. Ref. 26 developed a suboptimal LQR attitude and translational controller that computed feedback gains at each time step based on equations of motion linearized about the state at that time step and tested this algorithm on a translating air bearing testbed, achieving full six degree-of-freedom motion. Ref. 27 developed a periodically time-varying LQR, using numerical results to show that the periodic LQR outperformed a constant gain LQR, and although no specific actuators were modeled in the controller's mathematical formulation, a distributed network of ion thrusters was mentioned as a potential set of actuators for this mission.

In addition to linear techniques, there are several nonlinear techniques that may be used to design spacecraft attitude controllers. Many nonlinear methods utilize Lyapunov's second method to verify stability of the control law. For instance, Ref. 28 developed a minimum control effort, switched (bang-off-bang type) controller based on a benchmark linear PD controller, using a bilinear Lyapunov function to prove stability of both the benchmark and switched controller, and demonstrated via simulation that the switched controller was faster to settle when total integrated control effort of the two controllers was equal. Similarly, Ref. 29 developed a controller with quaternion feedback and integrator backstepping, using Lyapunov's method to prove this controller is universally asymptotically stable. Lyapunov's method is also used in the design of sliding mode controllers to select sliding surfaces, reduced-dimension regions of the state space on or along which the state trajectory converges to equilibrium, and control laws that may guarantee asymptotic, exponential, or even faster convergence of the state trajectories to equilibrium along those surfaces. For example, Ref. 30 developed a three-stage sliding mode controller which was shown to converge in finite time, and Ref. 31 developed sliding mode controllers with a novel class of linear sliding manifolds and two Lyapunov functions for controller design and stability analysis.

Time-optimal control is a nonlinear technique which, in general, does not use Lyapunov's method for design or stability analysis. In fact, time-optimal controllers are likely the only controllers in the literature that do not use state feedback at all; minimum-time maneuvers only require knowledge of the initial state, the final desired state, and a good model of the system. These controllers are sensitive to modeling and initial state estimation errors, because small errors integrate and propagate through the actual system dynamics with time. Like many nonlinear dynamic optimization problems, time-optimal control trajectories are computationally difficult to calculate. For this reason, approximate methods, such as the collocation techniques presented in Ref. 32, have been used to solve for minimum-time control and state trajectories.

2.4 Genetic Fuzzy Systems

Genetic fuzzy systems are a class of intelligent systems which utilize genetic algorithms to train or optimize fuzzy inference systems to perform given decision-making and control tasks. Fuzzy inference systems act as universal approximators, capable of approximating any function to any arbitrary degree of accuracy, and are therefore flexible enough to be applied to a variety of different tasks. Unlike other intelligent systems, such as neural networks or support vector machines, fuzzy inference systems are structured using natural language that is capable of being interpreted by humans, providing a built-in means to understand exactly why a fuzzy system performs a given task the way it does. This natural language rule structure also allows fuzzy inference system designers to hand-tune these systems using expert knowledge or intuition. Optimization via a genetic algorithm acts as a form of reinforcement learning for the fuzzy system and is relatively straightforward to implement because, unlike many optimization algorithms, genetic algorithms require no derivative information to determine optima[33].

Recently, genetic fuzzy systems have experienced increasing interest for use in aerospace applications. Such systems have been successfully applied to critical decision-making and control tasks for unmanned combat aerial vehicles (UCAVs)[34,35], separation assurance and collision avoidance of heterogeneous networks of unmanned aircraft systems (UAS)[36,37], position estimation of UAS[38], attitude control of small satellites[8,39], and collaborative control of distributed space robotic systems[40]. Genetic fuzzy systems demonstrate robustness to noisy environments and imperfect system models, making them ideal for use in complex systems[33]. Recent research has also sought to apply formal methods techniques to verification and validation of fuzzy systems in order to prove a given fuzzy system is guaranteed to always exhibit a given set of desired behaviors and never exhibit a given set of undesired behaviors[41]. Such proof of assured autonomy may be highly desirable or even required to implement an intelligent algorithm, such as a genetic fuzzy system, in a broader system, especially if the intelligent algorithm affects safety-critical aspects of the broader system, because in general, intelligent systems may exhibit unpredictable or nondeterministic behaviors that may be detrimental to the performance of the broader system.

One of the most notable applications of genetic fuzzy systems has been to the strategic decision-making and control of UCAVs. Ref. 34 introduced a novel genetic fuzzy system architecture, the genetic fuzzy tree (GFT), and applied it to UCAVs, which "must traverse through a battle space and counter enemy threats, utilize imperfect systems, cope with uncertainty, and successfully destroy critical targets."[34] A GFT is a fuzzy system organized into a series of multiple cascading fuzzy inference systems, or a directed graph of fuzzy inference systems, thereby reducing the overall complexity from that of a monolithic fuzzy inference system with an extremely large rule base to that of a handful of small fuzzy inference systems with manageable rule bases[34]. This GFT architecture effectively broke the UCAV control process into a series of smaller decisions, including which role to assume, whether to behave bravely or cowardly, which weapon to choose, and when to utilize the weapon[34]. The GFTs were trained in a low-fidelity simulation environment using six different training missions, introduced sequentially with increasing difficulty[34]. The optimal GFT was then tested in the same low-fidelity simulation environment using twelve different "live" mission profiles[34]. It was found that the controller was "consistently capable of completing missions not trained for" and "resilient to uncertainties and randomness."[34] It was also noted that the GFT approach is very scalable and applicable to a wide range of problem domains[34]. Continued work on the UCAV GFT yielded ALPHA, "a GFT that serves as an AI for flights of UCAVS in air-to-air combat missions."[35] Colonel (retired) Gene Lee, a United States Air Force Fighter Weapon School Adversary Tactics (Aggressor) instructor who has flown in thousands of air-to-air intercepts, has described it as "the most aggressive, responsive, dynamic and credible AI [he's] seen-to-date."[35] ALPHA was trained in the extremely high-fidelity AFSIM simulation environment and is intended to act as a hostile force against which pilots may train[35]. The fuzzy inference system utilized by ALPHA is also very quick to be evaluated as it is capable of running on the order of hundreds of microseconds on a 3.2 GHz core of a CPU, thus demonstrating how efficient genetic fuzzy systems can be at optimally executing complex tasks[35].

Similar to the UCAV application, fuzzy systems have been employed in separation assurance and collision avoidance algorithms for heterogeneous groups of small unmanned aerial systems (sUAS)[36,37]. Ref. 36 used a crisp logic algorithm with two simple hand-tuned fuzzy inference systems at two distinct computational steps to provide corrective courses of action for both fixed-wing and vertical take-off and landing (VTOL) sUAS. The system ultimately outputs turning commands to a given sUAS such that it passes in front of or behind a given intruder sUAS without knowledge of the intent or corrective action the intruder sUAS is taking[36]. The separation assurance system was shown to be 84.77% successful at mitigating loss of separation (LOS)[36]. The collision avoidance system was shown to be 99.97% successful in resolving collision conflicts without the LOS algorithm running and 99.51% successful in resolving collision conflicts with the LOS algorithm running[36]. Though genetic algorithms were not used to optimize the fuzzy inference systems, it was mentioned that they could be employed along with a cascading fuzzy inference system structure to achieve improved performance[36]. In follow-on work, a formal methods approach, specifically the use of satisfiability modulo theories (SMT) solvers and model checkers, was taken to generate a collision avoidance system which was 100% effective when separation assurance was enabled[37]. This approach required a very simple fuzzy inference system structure that could easily be input into the formal methods solvers employed[37].

In addition to aircraft control, genetic fuzzy systems have been employed in spacecraft attitude control. Ref. 8 developed a fuzzy gain scheduler for a proportional-derivative attitude state feedback control law for a CubeSat with only magnetic actuation. The gain scheduler was optimized to perform a 60 degree slew maneuver for a single set of initial conditions with an objective to settle to less than ten degree pointing error in minimum time[8]. A Monte Carlo analysis was run to evaluate the performance of the controller for a large set of initial conditions, and it was found that the average settling time was on the order of 1.5 orbits, or more than double that of the settling time for the optimized set of initial conditions, but consistent with expected settling times of these underactuated systems[8]. An infinite horizon linear quadratic regulator (LQR) was also manually optimized for the design set of initial conditions and compared to the fuzzy controller[8]. The fuzzy controller was found to outperform the LQR for the design set of initial conditions in terms of settling time and average angular error, but the fuzzy system only outperformed the LQR for the Monte Carlo analysis in terms of settling time[8].The work in Ref. 8 was performed as part of an initial iteration of the CryoCube-1 system design. However, through further design iteration, sun shield geometry and conceptual approach to power generation and thermal management underwent significant changes, and better estimates of mass moment of inertia and aerodynamic disturbance torque were developed. With these changes, it became infeasible to use only magnetic control to maintain spacecraft attitude and accomplish the goals of the mission and so reaction wheels were added to the attitude control system. In similar work reported in the literature, an adaptive fuzzy controller was developed and compared to a classical PID controller for a spacecraft attitude control system with momentum wheels[39]. It was found that the fuzzy controller was significantly more energy efficient at performing maneuvers and that, in general, the fuzzy system achieved greater accuracy than the PID controller, and it was mentioned that genetic algorithms could be used to improve performance of the fuzzy inference system[39].

Genetic fuzzy systems have also been utilized in various other estimation and control problems, including control tasks in the space robotics domain, control of an inverted pendulum, and estimation of sUAS position. Ref. 40 considered the use of five homogenous robots at fixed locations whose common objective was to move an object to a target, a simplified model of a collaborative task robots may be expected to perform in space. The object is attached to elastic strings on which the robots may pull with varying force, including with no force at all, and the robots are not able to communicate with one another but are aware of the position of the object and the position of the target in a global coordinate frame[40]. After training via the genetic algorithm, this preliminary work resulted in a FIS controller for the robots that was able to bring the object to the target region 85% of the time[40]. Similarly, Ref. 33 developed a fuzzy logic controller for a double inverted pendulum using a genetic algorithm to optimize the controller in the presence of sensor noise. It was found that tuning with five percent sensor noise resulted in a controller which was more robust to the effects of noise than the baseline controller tuned without noise[33]. In Ref. 38, a FIS was developed to perform sensor fusion of sUAS position data obtained from various instrument types, including GPS, onboard estimators, and radar. Estimates from a number of each type of sensor were first combined in a Maximum a Posteriori (MAP) estimator[38]. Then a fuzzy inference system was used to generate weights, which all sum to unity, and which are multiplied by the MAP estimates and added together to produce a weighted average estimate of position[38]. It was found that the fuzzy fusion estimates were more accurate than any individual MAP estimate and that using all the available sensor types to produce the position estimate resulted in the best performance[38]. Furthermore, although genetic algorithms were not used in this work, it was noted that they could be used to improve the results of the fuzzy fusion estimator[38].

As genetic fuzzy systems are increasingly used in aerospace applications, methods for verification and validation of such systems are increasingly being investigated. Aerospace systems that seek to employ intelligent algorithms, such as genetic fuzzy systems, include safety critical and mission critical systems whose guaranteed performance is imperative for safe and successful operation of these systems. Often, intelligent systems are employed for their robustness and adaptability, which allow them to handle novel situations without needing specific training or programming. However, robustness and adaptability are qualities that imply nondeterministic behavior, which can be extremely undesirable in safety or mission critical systems which need to guarantee that they will function as intended in all circumstances. Historically, intelligent systems designers have employed statistical or Monte Carlo analysis techniques to verify performance over a range of use cases. The systems are trained using a (usually) relatively large training data set and are verified to function using another separate verification data set. This procedure is adequate to verify functionality for many intelligent systems applications if performed thoroughly enough to yield valid statistical results. However, it rarely if ever checks all possible system states to determine whether or not the system will always behave as intended. For a more mathematically rigorous approach which can guarantee a system will behave as intended in every possible state, a set of techniques known as formal methods is used. For instance, Ref. 37 and Ref. 41 used formal methods known as Satisfiability Modulo Theories (SMT) to design and prove fuzzy controllers always behave as desired. In Ref. 37, SMT solvers and model checkers were used to design separation assurance and collision avoidance systems for sUAS, which were shown to be 100% effective at preventing collisions when operating together. SMT solvers verify that system behaviors which can be reduced to first-order logic always hold true and that there are not possible truth assignments that violate the behavior[37]. SMT "model checkers are tools that exhaustively check the states of a system," either a discrete or continuous model, "to search for combinations of variable assignments that violate behavioral specifications."[37] In Ref. 41, an SMT solver was used to test a fuzzy logic controller and a classical PD controller to verify they provided negative feedback and to verify Lyapunov stability of the systems with controllers. Expert knowledge and genetic algorithms were used to tune the fuzzy controller[41]. Both controllers were shown to always generate negative feedback, but Lyapunov stability was unable to be proven for either of the controllers using the formal methods techniques[41]. It was noted that this could have been a result of the choice of Lyapunov function, and it was suggested that an optimization technique could be used to satisfy the Lyapunov constraint with the given Lyapunov function[41]. While formal methods can be used to guarantee a given set of system behaviors, fuzzy systems which employ these techniques in their design, verification, and validation are significantly constrained in the methods of inference, composition, and defuzzification that can be used due to the need to express these processes within a set of logic statements; the more complex these operations become (e.g. using large rule bases, min-max instead of product composition, etc.), the more difficult it is to apply formal methods.

2.5 Testing Attitude Control Systems

Most of the attitude controllers presented in Section 2.3 were verified to work using simulation, though some were able to be tested on ground-based testbeds, and some were even deployed on operational satellites. Ideally, satellite attitude control systems all would be verified to operate adequately by way of testing in environments representative of their operational environments. However, attitude control system requirements frequently are verified only by analysis or by testing with equipment that significantly restricts or completely inhibits rotational degrees of freedom about one or more axes[42]. For small satellites, there are two primary methods for testing attitude control systems reported in the literature: (1) using an air bearing table and (2) suspending the satellite from a string.

Of the two methods commonly used to test small satellite attitude control systems, air bearings offer the greatest range of motion, frequently 360 degree range of motion in yaw and anywhere from a few degrees to twenty degrees or more in pitch and roll. However, air bearing testbeds can be difficult to set up to mimic the mass properties of the satellite and the low-torque environment on orbit. Typically, the largest disturbance torque present in air bearing testbeds that is not present in on-orbit environments is the pendulum stability torque, which results from an offset of the testbed center of mass with the testbed center of rotation, causing the testbed to rotate so that the center of mass is below the center of rotation; this pendulum stability torque should not be confused with gravity gradient torque, which is usually orders of magnitude less than the pendulum stability torque and is roughly the same order of magnitude on the surface of earth as it is in low earth orbit. In order to make an air bearing testbed in which the pendulum stability torque is insignificant compared with the torques experienced on orbit, the testbed center of mass must be very close to its center of rotation, but it is often very difficult to machine or assemble components within the tolerances necessary to position the center of mass close enough to the center of rotation[43]. Furthermore, if the center of mass of the spacecraft changes during the mission, as is the case in spacecraft that spin parts of their bodies (i.e. spinners) or have deployables, constructing an air bearing testbed that adequately mimics the spacecraft environment is very difficult, if not impossible[43]. To overcome the difficulties of balancing an air bearing table, Ref. 44 and Ref. 45 developed automatic balancing systems to dynamically position the center of mass, though it was noted that precise (i.e. potentially expensive) linear actuators and/or encoders were needed in order for the systems to work well. Other sources of error in using an air bearing testbed are usually more easily overcome. For instance, in air bearing testing of the BioSentinel CubeSat, it was noted that the torque produced by air flowing from the bearing resulted in a torque less than that of the pendulum stability torque[42]. Additionally, the inertia of the BioSentinel air bearing table initially did not closely match that of the actual spacecraft, so more mass was added to the testbed to make inertias match[42]. The inertia mismatch between the MicroMAS CubeSat and its air bearing testbed was more difficult to correct for, because the inertia of the testbed was three times that of the spacecraft[43]. Though the inertia of air bearing testbeds is often larger than the inertia of smaller spacecraft, especially CubeSats, Ref. 44 and Ref. 45 present results on the design and buildup of air bearing testbeds specifically designed to accommodate CubeSats.

In contrast with air bearing testbeds, string suspension testbeds are much simpler. String suspension only allows one rotational degree of freedom to be tested at a time, so spacecraft dynamics with significant off-axis coupling cannot be simulated well. Additionally, the string used to suspend the satellite tends to act as a torsional spring, which exerts an additional disturbance torque on the spacecraft. Attitude determination and control subsystem testing of the MicroMAS CubeSat was performed using a string suspension testbed following an unsuccessful attempt to use an air bearing setup. The attitude controller performance of MicroMAS' four operational modes was evaluated by comparing data collected from the string suspension testbed with single degree of freedom linear models of the rotational dynamics and string effects of the testbed[43]. Testing of an operational mode was considered successful if it was found that the controller performance matched the expected behavior of the simplified models[43]. For instance, detumble mode testing was considered successful because rotation damped faster with the mode engaged than without, and slew mode testing was considered successful because the satellite rotated from a stationary position to a commanded angle about the string axis and stayed there until its reaction wheels saturated due to the relatively large, constant restoring force generated by the string[43].

In addition to hardware allowing rotational freedom, attitude determination and control testbeds also normally contain hardware to simulate important environmental conditions, such as Earth's magnetic field or the position of the sun and stars. The magnetic field is one of the easier aspects of the environment to simulate, so many attitude determination and control testbeds, especially those for smallsats and CubeSats, incorporate Helmholtz cages or similar devices to generate nearly constant magnetic fields over the length scales of the satellites[42,43]. Some attitude determination and control testbeds also incorporate solar emulators, or electrically powered lights that mimic the light intensity of the sun, to verify functionality of sun sensors and the attitude determination algorithms that use them. Solar emulators on attitude control testbeds are typically placed very close to sun sensors so that the light flux, expressed in watts per square meter, is representative of the solar flux experienced by spacecraft on orbit. For instance, in Ref. 42, the solar emulator was placed two inches from the sun sensor so that the correct flux was achieved. Similar to sun emulators, some attitude determination and control testbeds also employ star field emulators, typically computer monitors with astronomically accurate maps of the star-filled sky that update based on testbed-simulated spacecraft attitude[43]. Though it may be possible to emulate environment variables in addition to the magnetic field, solar flux incident on sun sensors, and star field visible from star trackers, emulation of an environment variable is only required if that variable is integral to the function of the attitude determination and control subsystem, and it is rare to see simulation of other environment variables reported in the literature.

3 Problem Statement

An attitude profile is sought for the CryoCube-1 mission. Previous work developing an all magnetic control subsystem for the CryoCube-1 mission showed promising results[8]. However, as the CubeSat design and mission concept matured, it was found that all magnetic control would not be a feasible means by which to meet all demands placed on the attitude control subsystem. Specifically, better estimates of the spacecraft inertia tensor and center of aerodynamic pressure altered the dynamics enough that a solely magnetically controlled CryoCube-1 was found not to be stabilizable about attitudes which would satisfy communications requirements and thermal performance desires. Therefore, a set of 3-axis reaction wheels was added to the attitude control subsystem to provide a means of momentum storage. However, the reaction wheels were selected primarily for their low profile, which allows a larger volume for the experimental payload, and for their ability to reject instantaneous disturbance torques, not for their total momentum storage capacity. As demonstrated in section 3.1.4 below, CryoCube-1's reaction wheels will quickly saturate if tasked with rejecting the worst-case instantaneous torque the CubeSat would be expected to experience if it were in an unfavorable orientation for an extended period of time.

In the sections below, the dynamic equations of motion required to describe the attitude profile optimization problem are developed along with mathematical models relating spacecraft attitude to electrical power generation, communication link strength, and experiment steady-state temperature. Next, the mathematical representation of the optimization problems is presented. Informally, the primary attitude profile optimization objective is to minimize experiment temperature subject to attitude dynamics and constraints of the control subsystem, electrical power subsystem, and communication subsystem.

3.1 Mathematical Models

3.1.1 Rigid Body Attitude Dynamics and Kinematics

CryoCube-1 is a 3U CubeSat, which is a small structure of relatively stiff or rigid construction. On orbit, CryoCube-1 experiences three degrees of freedom in translation and three degrees of freedom in rotation. Because the satellite is small and rigidly constructed with no large or flexible appendages, the modes associated with translational and rotational degrees of freedom are much lower frequency than structural vibration modes, so structural modes do not contribute significantly to the spacecraft dynamics. Therefore, CryoCube-1 is modeled as a rigid body subject to full six degree of freedom rotational and translational dynamics. To derive the rotational dynamics, consider the angular momentum of a rigid body satellite with reaction wheels:

$$h = I_b \omega_b + I_w \omega_w \tag{3-1}$$

Using the equivalent of Newton's second law for rotational motion, the rate of change of angular momentum is equal to the sum of external torques applied to the spacecraft. Expressed in spacecraft body-fixed coordinates, this is:

$$\dot{h} = \omega_b \times (I_b \omega_b + I_w \omega_w) + I_b \dot{\omega}_b + I_w \dot{\omega}_w = \tau = \tau_{dist} + \tau_{cntrl} \tag{3-2}$$

Rearranging to a form suitable for use by an ordinary differential equation solver yields:

$$\dot{\omega}_b = -I_b^{-1}\big(\omega_b \times (I_b \omega_b)\big) - I_b^{-1}\big(I_w \dot{\omega}_w + \omega_b \times (I_w \omega_w)\big) + I_b^{-1}\tau_{dist} + I_b^{-1}\tau_{cntrl} \tag{3-3}$$

Inspecting the right-hand side of this equation, it is noted that the first term is the quadratic off-axis coupling term of typical rigid-body motion, the second term is the contribution of the reaction wheels to the otherwise simple rigid body dynamics, the third term is the contribution of external disturbance torques, and the fourth term is the contribution of external (i.e. momentum dumping) control torques. Also note that the second term within the parenthesis of the reaction wheel contribution term is considered as a small internally generated disturbance which is not directly controlled by the reaction wheels, whereas the first term of the reaction wheel contribution term is directly controlled with the demanded reaction wheel acceleration. In general, the external disturbance torques, whose mathematical models are developed in section 3.1.3.1, are functions of spacecraft attitude, position, and velocity. The only external control torque considered is the magnetic control torque, whose mathematical model is developed in section 3.1.3.2.

The spacecraft attitude is represented using a four parameter quantity known as a unit quaternion. Quaternion attitude representation was chosen because, unlike three-parameter representations, such as Euler angles, quaternions offer a continuous representation of the attitude space using a set of differential equations that are quadratic with respect to quaternion parameters and spacecraft angular velocities; many other attitude representations use transcendental functions in their differential equations. One of the only drawbacks to quaternion attitude representation, however, is that it does not use the theoretical minimum number of parameters, three, so each attitude corresponds to exactly two sets of quaternion parameters[46]. However, there is no known attitude representation that does utilize three parameters without singularities or discontinuities, and unit quaternions are the "preferred parameterization for spacecraft attitude control systems" [46].

The quaternion attitude representation is governed by the following ordinary differential equation:

$$\dot{q} = \begin{bmatrix} \dot{q}_0 \\ \dot{q}_1 \end{bmatrix} = \begin{bmatrix} -\omega^T q_1 \\ q_0 \omega + q_1 \times \omega \end{bmatrix} \tag{3-4}$$

Note that this equation is presented in a general form, without subscripts identifying particular coordinate systems, demonstrating the quaternion's use in describing the orientation and motion of any one coordinate system with respect to any other known coordinate system. As far as a quaternion represents a coordinate transformation from one coordinate system to a second coordinate system, the angular velocity in Eq. 3-4 is that of the second coordinate system with respect to the first coordinate system expressed in the coordinates of the second coordinate system. In practice, the spacecraft body-fixed coordinate system, shown in Fig. 3-1, is expressed as an attitude quaternion with respect to a desired attitude coordinate system, the ideal attitude attained by the spacecraft, and it is this desired-to-spacecraft-body-fixed quaternion which is used along with spacecraft-body-fixed angular velocity error in CryoCube-1's full state attitude control algorithms.

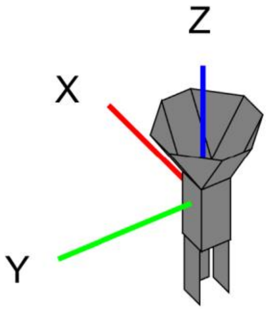

Fig. 3-1—CryoCube-1 body-fixed coordinate system.

In most missions, the desired attitude coordinate system is either an inertial coordinate system or an earth-oriented coordinate system. An inertial attitude a spacecraft may need to attain, or equivalently, a desired inertial attitude coordinate system with which a spacecraft may need to align its body axes can be expressed as a constant coordinate transformation from a reference inertial coordinate system, such as the Earth-centered inertial (ECI) coordinate system defined using the Earth's mean equator at mean equinox at the J2000 epoch. The J2000 ECI coordinate system x-axis is aligned with the mean equinox, ♈, z-axis is aligned with the earth's rotational axis, and y-axis completes the right-handed coordinate system 90 degrees east of the x-axis on the mean equator. A common earth-oriented coordinate system with which a spacecraft may need to align its body axes is the local vertical local horizontal (LVLH) coordinate system, shown in Fig. 3-2. The LVLH y-axis is perpendicular to the orbit plane pointing opposite the direction of the orbit angular momentum vector, z-axis points nadir, and x-axis completes the right-handed coordinate system in the orbit plane in the direction of, but not necessarily aligned with the spacecraft velocity vector. The LVLH coordinate system is easily defined using spacecraft orbital parameters, which are typically either given in terms of right ascension, inclination, argument of periapsis, true anomaly, eccentricity, and orbit period (e.g. in a two-line element set) or given in terms of a position vector and a velocity vector. Orbital parameters are often referenced to the J2000 ECI coordinate system, so coordinate transformations between J2000 ECI and LVLH can be directly computed.

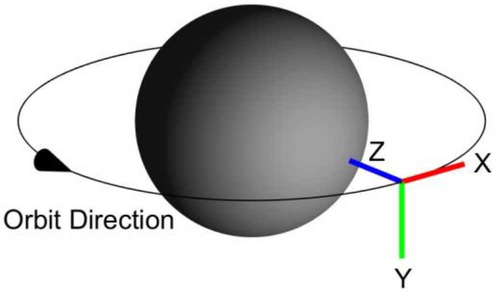

Fig. 3-2—Local Vertical Local Horizontal (LVLH) coordinate system.

Though many missions use inertial or earth-oriented attitudes, it may not be necessary to constrain all axes of a spacecraft to a particular orientation at a particular time, or it may be necessary to use other specially tailored attitude profiles to point one or more axes of the spacecraft at objects other than inertially fixed points or the earth. For instance, it may not matter where the two non-nadir-pointing axes of a nadir-pointing spacecraft point at a particular time, so only one axis of the desired or reference earth-oriented coordinate system needs to be used for attitude control. On the other hand, a spacecraft like CryoCube-1, which needs to point the open end of its sun shield away from the sun and earth while also pointing its antennas toward the ground, may do best to follow some attitude trajectory which is close to earth-oriented but requires some periodic rotation of the spacecraft about one of its axes to simultaneously avoid unfavorable sun angles, desaturate its reaction wheels, and keep its antennas pointed toward the ground. In this case, it is possible to construct a potentially time-varying coordinate system based on another reference coordinate system, such as the J2000 ECI or earth-oriented coordinates. One of the more straightforward methods to define a coordinate system based on a reference coordinate system is to use a constant coordinate transformation from the reference, as was discussed for inertial pointing not aligned with J2000 ECI. Another method is to choose a constant angular velocity vector for the new coordinate system with respect to the reference coordinate system and solve for the time-varying orientation using Eq. 3-4, for example. These two methods could also be used multiple times sequentially to achieve more complicated motion. Additionally, a coordinate transformation from a reference coordinate system could be defined as a function of one or more parameters of interest (e.g. the sun vector, location of the nearest ground station, reaction wheel speeds, etc.). In section 4.5, the optimal attitude profile for CryoCube-1 is treated as a generic function to be optimized.

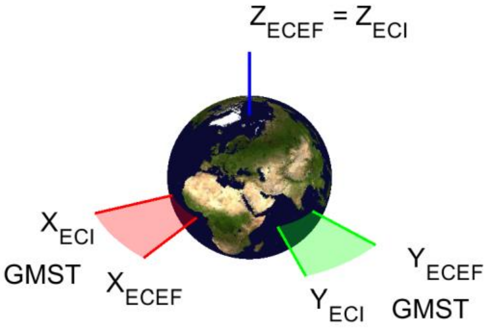

Fig. 3-3—Earth-Centered Earth-Fixed coordinate system with respect to Earth-Centered Inertial coordinate system.

In addition to spacecraft body-fixed, J2000 ECI, earth-oriented, and desired attitude coordinate systems, a good attitude control simulation requires the Earth-Centered Earth-Fixed (ECEF) coordinate system, shown in Fig. 3-3. Several important quantities, including magnetic field models and ground station locations are defined in ECEF frames. The ECEF coordinate system origin is at the center of the earth, x-axis is from the origin through the intersection of the Greenwich Meridian, z-axis is from the origin through the Celestial North Pole (earth rotation axis), and y-axis completes the right-handed coordinate system at 90 degrees east longitude, 0 degrees north latitude. Like the LVLH coordinate system, there is a straightforward method to calculate the coordinate transformations between the ECEF coordinate system and the J2000 ECI coordinate system. As shown in Fig. 3-3, the Greenwich Mean Sidereal Time (GMST) is the angle between the x-axis of the ECEF coordinate system and the x-axis of the J2000 ECI coordinate system, and the coordinate transformation is a simple rotation about the coordinate systems' shared z-axis.

3.1.2 Translational Dynamics

CryoCube-1 has been deployed in low earth orbit where it is subject to aerodynamic, gravitational, solar pressure, and magnetic forces. All of these forces are dependent on the position and velocity of the spacecraft. Therefore, in order to model the attitude dynamics of CryoCube-1, a model of orbit dynamics, or position and velocity, is required. The general perturbation method SGP4[†] was chosen to model the position and velocity of CryoCube-1, because this method was designed specifically to be used with TLEs to accurately propagate satellite orbits[47]. The SGP4 method takes into consideration perturbations from the gravitational pull of the earth, moon, and sun as well as atmospheric drag forces. However, because TLEs are only generated for satellites

---

[†] https://celestrak.com/publications/AIAA/2006-6753/

actually in orbit, and CryoCube-1 had not been delivered prior to completion of the majority of the attitude profile optimization work, a TLE from a CubeSat that had been deployed from the ISS in 2018 (RaInCube) was used as a close proxy of CryoCube-1's anticipated orbit, as it was known CryoCube-1 would most likely be deployed from the ISS.

3.1.3 Torque

3.1.3.1 Disturbance Torque

The most significant torques in low earth orbit, where CryoCube-1 is expected to operate, are the aerodynamic, gravity gradient, solar radiation pressure, and residual magnetic field torques. In the models presented below, the aerodynamic and solar pressure torques are calculated from the aerodynamic and solar pressure forces as well as the moment arm from the spacecraft center of mass to the respective centers of pressure whereas the gravity gradient and magnetic field torques are calculated directly from the spacecraft moment of inertia tensor and residual magnetic dipole, respectively. A simplified model of the spacecraft geometry, shown in Fig. 3-4, is used to calculate the atmospheric drag and solar radiation pressure torques. This model assumes the spacecraft geometry is equivalent to that of a convex polyhedron whose adjacent faces are orthogonal to one another. A convex geometry avoids the complexities of determining how faces of the spacecraft occlude other faces of the spacecraft and how particles reflected from one surface may then interact with another surface. Orthogonal faces with normal perpendicular to the spacecraft body-fixed axes further simplifies the model such that only three surface normals are required to determine the torque. A reference geometric coordinate system (X_g, Y_g, Z_g), shown in Figure 1, is used to identify the centers of the surfaces projected on the planes normal to each spacecraft body-fixed axis. The spacecraft center of mass is also shown for reference. The surface areas, centers of area, and reflectivity values are used to locate the centers of aerodynamic pressure and solar pressure, and the known center of mass location is used to find the aerodynamic and solar pressure torque moment arms.

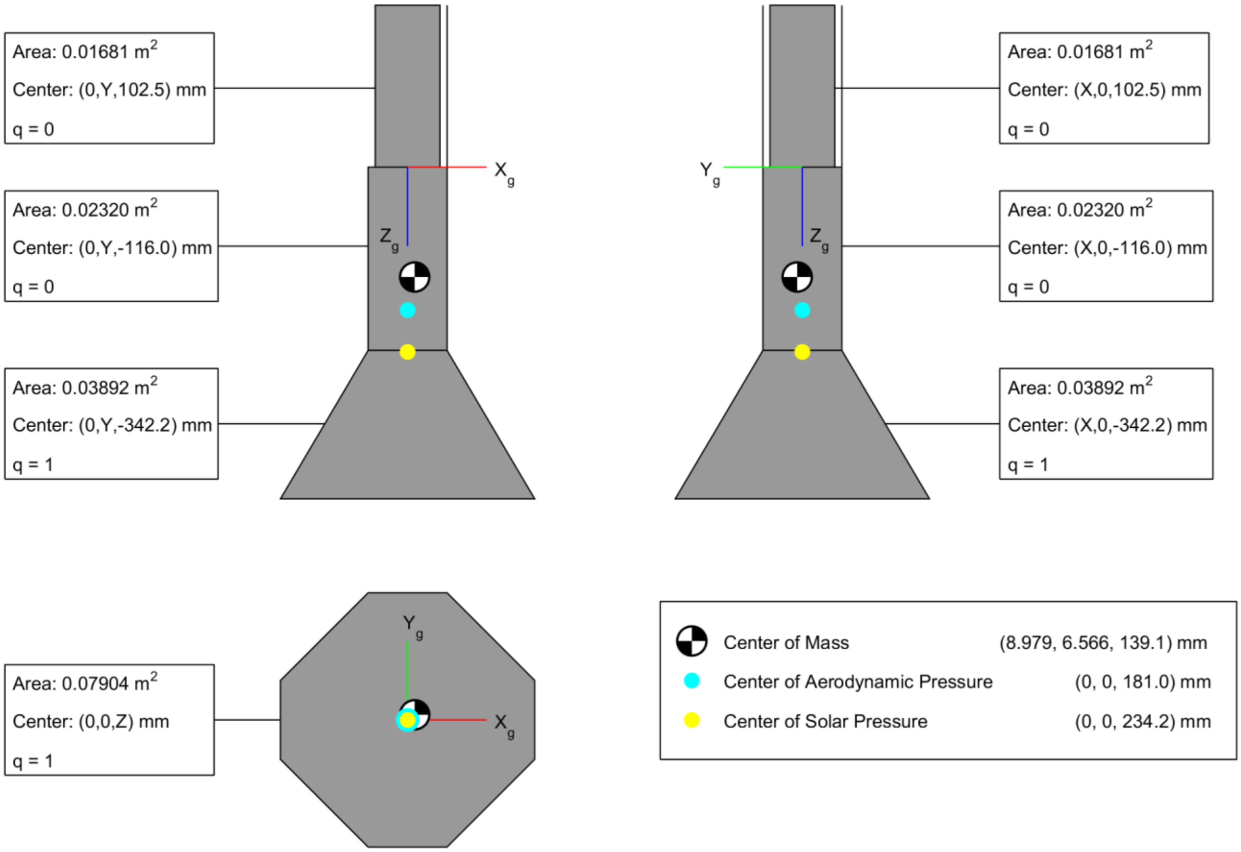

Fig. 3-4—CryoCube-1 centers of mass, aerodynamic pressure, and solar pressure.

Simulated aerodynamic drag is based on the one-dimensional, continuum, inviscid, incompressible drag model, Eq. 3-5.

$$F_d = \frac{1}{2}\rho\|V\|^2 AC_D \tag{3-5}$$

Density of the rarefied atmosphere is given by Table I-1 of Ref. 9, velocity of the spacecraft is calculated in the J2000 ECI coordinate system using SGP4 and transformed to the spacecraft body-fixed coordinate system using the coordinate transformations described in section 3.1.1, the drag coefficient is taken to be 2.25 as suggested by Ref. 9, and the area is that projected perpendicular to the velocity vector. Using this definition and the fact that drag force is in the opposite direction of spacecraft velocity, the three-dimensional drag force on the spacecraft is given by Eq. 3-6.

$$F_D = -\frac{1}{2}\rho C_D(\bar{A}^T V)V \tag{3-6}$$

Here, $\bar{A}^T = [A_x \quad A_y \quad A_z]$ is a vector of areas projected perpendicular to each axis of the spacecraft, and the term $\bar{A}^T V$ is the area of the spacecraft projected perpendicular to the velocity vector and scaled by the velocity magnitude. Note that the choice of modeling the spacecraft as a solid with orthogonal faces allows this simplification.

The location of aerodynamic center of pressure is calculated as the center of area of each side of the spacecraft perpendicular to the body fixed coordinate axes using Eq. 3-7, where $\tilde{A}_x = \{(A_{x,i}, \{y_i, z_i\}) \in \mathbb{R} \times \mathbb{R}^2 \mid i \in \mathbb{Z}^+\}$, $\tilde{A}_y = \{(A_{y,i}, \{x_i, z_i\}) \in \mathbb{R} \times \mathbb{R}^2 \mid i \in \mathbb{Z}^+\}$, and $\tilde{A}_z = \{(A_{z,i}, \{x_i, y_i\}) \in \mathbb{R} \times \mathbb{R}^2 \mid i \in \mathbb{Z}^+\}$ are the sets of areas and corresponding centers of area of each shape composing the spacecraft silhouette. The dimensions shown in Fig. 3-4 are used to calculate center of area. Note that the location of center of pressure along each axis may be calculated using two of the sets of areas and centers of areas and that, for the simplified CryoCube-1 geometry model, the resulting centers of pressure are equal, though, in general, the center of pressure of a spacecraft changes as a complicated function of spacecraft orientation and geometry, especially non-convex geometries.

$$c_{p,D} = \frac{1}{\sum_{i=1}^{n} A_i}\left[\sum_{i=1}^{n} A_{z,i}x_i \quad \sum_{i=1}^{n} A_{z,i}y_i \quad \sum_{i=1}^{n} A_{x,i}z_i\right]^T \tag{3-7}$$

The aerodynamic torque is calculated using Eq. 3-8, where the moment arm vector is the location of the center of aerodynamic pressure with respect to the spacecraft center of mass, and the location of the center of aerodynamic pressure is shown in Fig. 3-4.

$$\tau_D = \left(c_{p,D} - c_M\right) \times F_D \tag{3-8}$$

The worst-case aerodynamic torque magnitude as a function of spacecraft altitude is shown in Table 3-1. These values will be compared to the estimated magnitudes of the other torques, also shown in Table 3-1, in section 3.1.4 to determine which torques are most significant and require modeling.

Table 3-1—Comparison of worst-case disturbance torques as a function of altitude.

Altitude (km)	Aerodynamic Torque (N·m)	Gravity Gradient Torque (N·m)	Solar Pressure Torque (N·m)	Residual Mag. Torque (N·m)
350	$4.17\text{x}10^{-6}$	$8.44\text{x}10^{-8}$	$5.13\text{x}10^{-8}$	$2.66\text{x}10^{-8}$
375	$2.81\text{x}10^{-6}$	$8.35\text{x}10^{-8}$	$5.13\text{x}10^{-8}$	$2.63\text{x}10^{-8}$
400	$1.89\text{x}10^{-6}$	$8.26\text{x}10^{-8}$	$5.13\text{x}10^{-8}$	$2.60\text{x}10^{-8}$
450	$9.00\text{x}10^{-7}$	$8.08\text{x}10^{-8}$	$5.13\text{x}10^{-8}$	$2.54\text{x}10^{-8}$

Gravity gradient torque is modeled using Eq. 3-9, and the worst-case magnitude is estimated using Eq. 3-10, with 0.053 kg·m^2 as the maximum mass moment of inertia and 0.010 kg·m^2 as the minimum mass moment of inertia. The worst-case gravity gradient torque as a function of spacecraft altitude is shown in Table 3-1.

$$\tau_G = \frac{3\mu}{\|R\|^3}\left(\frac{R}{\|R\|}\right) \times \left(I\,\frac{R}{\|R\|}\right) \tag{3-9}$$

$$\tau_{G,max} = \frac{3\mu}{2\|R\|^3}\left|I_{max} - I_{min}\right| \tag{3-10}$$

Solar radiation pressure force on a spacecraft surface is calculated using Eq. 3-11, a modified version of that presented in Ref. 9, where Φ is the solar flux (1366 W/m^2 at earth), c is the speed of light (3.0x10^8 m/s), A is the surface area over which the solar pressure acts projected on a plane normal to the solar vector ($\hat{n}_s$ – the unit vector from the spacecraft to the sun), and q is the fraction of light reflected by the surface; light that is not reflected is assumed to be absorbed. The projected area perpendicular to each body axis is divided into discrete areas (A_t), and the reflectivities (q) and physical dimensions of those discrete areas, shown in Fig. 3-4, are used to calculate the solar pressure forces on each area. The largest force is generated when the sun vector and surface normal vector are in the same direction.

$$F_S = \frac{\Phi}{c} A(1 + q) \tag{3-11}$$

The total solar pressure force along each spacecraft axis is calculated using Eq. 3-12, which sums the forces on areas perpendicular to each axis. Similar to Eq. 3-6, the term in parenthesis in Eq. 3-12 is the area projected normal to the sun vector, with reflectivity scaling for portions of the surface that are more or less reflective than others. Note that, although not explicitly stated in Eq. 3-12, when the spacecraft enters eclipse, the solar pressure force vanishes.

$$F_S = -\frac{\Phi}{c}\left(\hat{n}_s{}^T \begin{bmatrix} \sum_{i=1}^{n_x} A_{x,i}\left(1 + q_{x,i}\right) \\ \sum_{i=1}^{n_y} A_{y,i}\left(1 + q_{y,i}\right) \\ \sum_{i=1}^{n_z} A_{z,i}\left(1 + q_{z,i}\right) \end{bmatrix} \right) \hat{n}_s \tag{3-12}$$

Similar to Eq. 3-7, Eq. 3-13 is used to calculate the center of solar pressure along each axis. The solar pressure torque is calculated using Eq. 3-14, where the moment arm vector is the location of the center of solar pressure with respect to the spacecraft center of mass, and the location of the center of solar pressure is shown in Fig. 3-4.

$$c_{p,S} = \frac{1}{\sum_{i=1}^{n} A_i(1+q_i)} \left[\sum_{i=1}^{n} A_{z,i}\left(1 + q_{z,i}\right)x_i \quad \sum_{i=1}^{n} A_{z,i}\left(1 + q_{z,i}\right)y_i \quad \sum_{i=1}^{n} A_{x,i}\left(1 + q_{x,i}\right)z_i \right]^T \tag{3-13}$$

$$\tau_S = \left(c_{p,S} - c_M\right) \times F_S \tag{3-14}$$

The worst-case solar pressure torque magnitude as a function of spacecraft altitude is shown in Table 3-1.

Residual magnetic field torque is calculated using Eq. 3-15, where M is the residual magnetic dipole of the spacecraft and B is the local magnetic field vector. Because the residual magnetic field strength of the spacecraft is unknown, a dipole strength of 0.001 A·m^2 is estimated based on dipole strengths of electromechanical devices of similar size and power consumption. The worst-case residual magnetic field torque magnitude as a function of spacecraft altitude is shown in Table 3-1.

$$\tau_B = M \times B \tag{3-15}$$

The Earth's magnetic field is modeled using the International Geomagnetic Reference Field (IGRF) model with 13th order IGRF-12 coefficients with secular variation terms included[48]. The IGRF model expresses Earth's magnetic field as a scalar potential function, Eq. 3-16, whose negative gradient at a given location is the local magnetic field vector at that location.

$$V(r,\theta,\phi,t) = a\sum_{n=1}^{N}\sum_{m=0}^{n}\left(\frac{a}{r}\right)^{n+1}\left[g_n^m(t)\cos(m\phi) + h_n^m(t)\sin(m\phi)\right]P_n^m(\cos(\theta)) \tag{3-16}$$

Here, V is the scalar potential function, g_n^m and h_n^m are the IGRF-12 Gaussian coefficients with secular variations, r is the geocentric distance to the point of interest, θ is the coelevation of the point of interest, ϕ is the East longitude of the point of interest, N is the order of the model, t is time, a is earth's radius, and P_n^m are Schmidt normalized Legendre functions. Appendix H of Ref. 11 provides algorithms for calculating the magnetic field using this model, including those for calculating P_n^m and its derivative with respect to coelevation.

3.1.3.2 Control Torque

CryoCube-1 has two types of attitude control actuators: reaction wheels and magnetorquers. The reaction wheel control torque has been introduced in section 3.1.1, where it was derived by applying the law of conservation of momentum to the equation for total spacecraft momentum. Explicitly including reaction wheel momentum as a term in the equation of total vehicle momentum was done to capture the small uncontrolled coupling between the spacecraft body's angular velocity and the reaction wheels' momentum. CryoCube-1's reaction wheels are Clyde

Space's Standalone Three Axis Reaction Wheel assembly, shown in Fig. 3-5, with operation specifications presented in Table 3-2.

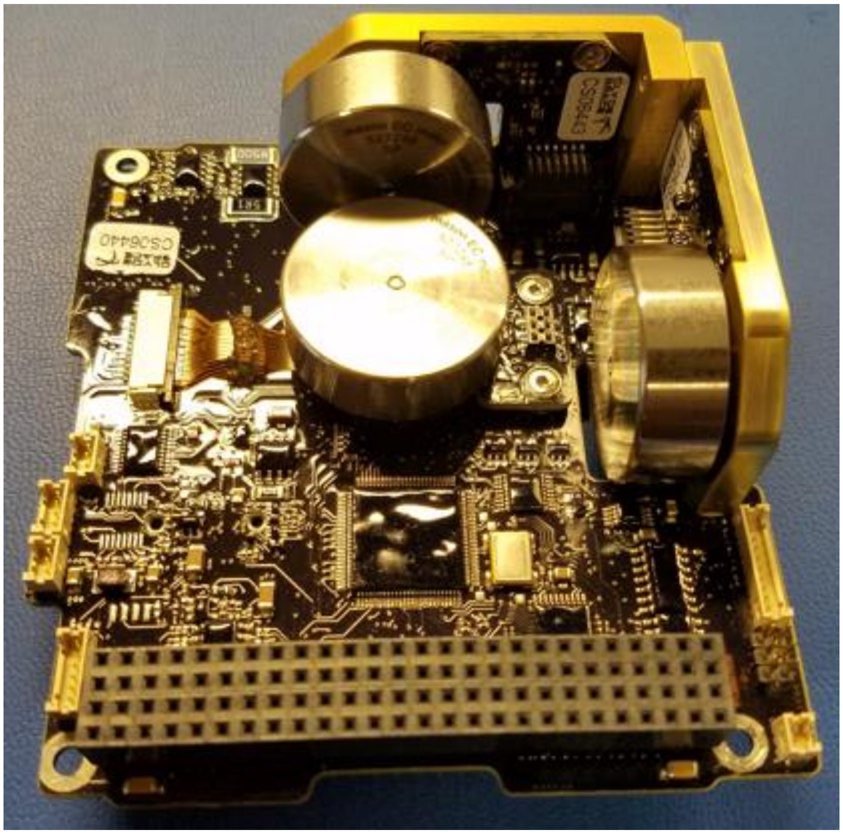

Fig. 3-5—CryoCube's 3-axis reaction wheel assembly from Clyde Space.

Table 3-2—CryoCube's 3-axis reaction wheel assembly's performance specifications.

Performance Parameter	Value	Unit
Maximum Commandable Torque (each axis)	1.57×10^{-2}	mN·m
Maximum Momentum (each axis)	3.534	mN·m·s
Maximum Wheel Acceleration	±33.33	RPM/s
Maximum Wheel Speed	7500	RPM

The magnetic control torque is the only component of τ_{cntrl} in Eq. 3-3 and is modeled identically to the residual magnetic field disturbance torque in Eq. 3-15, except that the magnetic moment, M, of the magnetorquers is a controllable vector. CryoCube-1's magnetorquers are integrated into its solar panels, Clyde Space's double-sided 2U deployable panel on the +X face, Clyde Space's single-sided 2U deployable panels on the +Y and –Y faces, and Clyde Space's 1U non-deployable top/bottom panel on the –Z face, shown in Fig. 3-6 and Fig. 3-7. Taking into account the redundant magnetorquers in the Y-direction, the operation specifications of the magnetorquers are presented in Table 3-3.

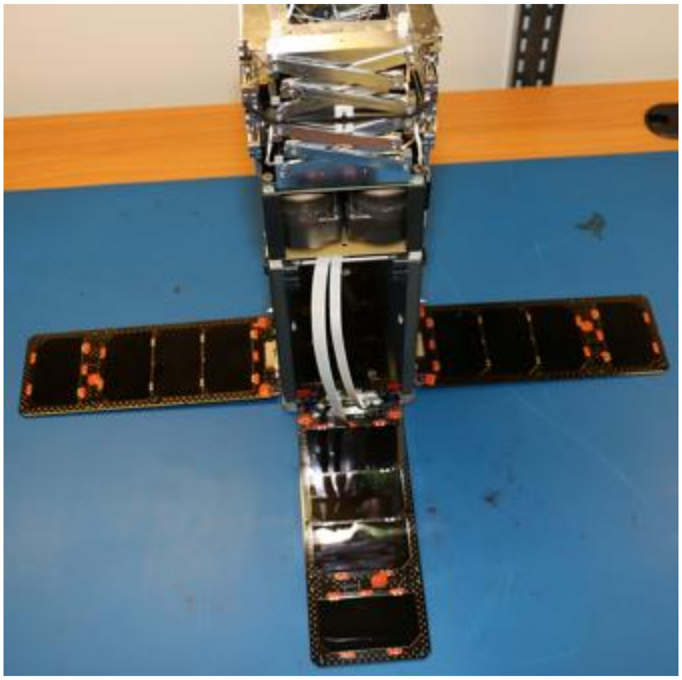

Fig. 3-6—Clyde Space's 2U single-sided and double-sided deployable solar panels installed on CryoCube chassis.

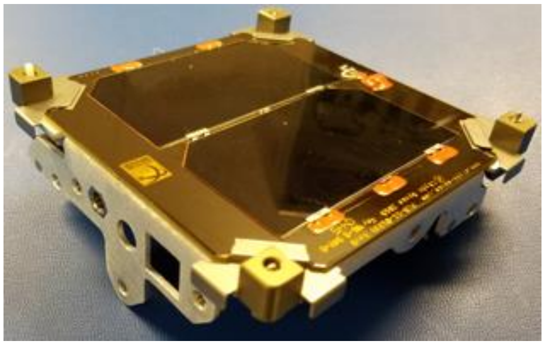

Fig. 3-7—Clyde Space's 1U non-deployable solar panel installed on CryoCube base plate.

Table 3-3—Magnetorquer (built into solar panels) maximum magnetic dipole strength in each axis of CryoCube.

Axis	Magnetic Dipole Strength ($A\cdot m^2$)
X	0.094
Y	0.188
Z	0.080

3.1.4 Control Authority

Examining the maximum commandable reaction wheel torque in Table 3-2 and the worst-case disturbance torques in Table 3-1, it is clear that the reaction wheels are capable of rejecting the largest magnitude disturbance torque; the maximum commandable torque is about an order of magnitude larger than the worst-case disturbance torque magnitude. However, the reaction wheels cannot reject these torques for an indefinite period, and will eventually saturate. To determine the worst-case (shortest) time until reaction wheels may saturate, the momentum capacity of a single reaction wheel is divided by the worst-case torques listed in Table 3-1. Table 3-4 shows the amount of time, in orbits, it would take the largest combinations of torques to saturate the reaction wheels, starting with just the largest torque and adding each subsequent largest torque not previously included. Clearly, the reaction wheels would saturate within one orbit if they had to absorb the momentum that would be transferred to the spacecraft by the worst-case torques. This indicates the reaction wheels are undersized for attitude profiles requiring more active control and suggests the spacecraft is better at handling more passively stable attitude profiles.

Table 3-4—Time (orbits) to saturate reaction wheels with worst-case disturbance torques.

Altitude (km)	Time (orbits) to Saturate Reaction Wheels for Given Torque Combinations			
	Aero	Aero + Gravity	Aero+ Gravity + Solar	All
350	0.1523	0.1505	0.1475	0.1466
375	0.2263	0.2222	0.2159	0.2140
400	0.3368	0.3278	0.3144	0.3105
450	0.7061	0.6680	0.6158	0.6010

To reduce complexity of the spacecraft model and allow for faster solution of optimal attitude profiles, it is desirable to minimize the calculation of disturbance torques. Table 3-1 clearly shows the aerodynamic torque is much larger than all other torques by about two orders of magnitude, indicating one or more disturbance torques may be much more significant than the others. To determine which torques are significant enough to model, two quantities are used to analyze the disturbance torques: (1) the difference in time to saturate reaction wheels when all torques are modeled versus when only a subset of the largest torques are modeled and (2) the amount of time it would take reaction wheels to saturate if only a subset of the smallest torques are modeled. The former quantity provides an estimate of the worst-case time it would take the model to be inaccurate if the reaction wheels were solely responsible for disturbance torque rejection, and the latter quantity provides an estimate of the worst-case time it would take the model to be inaccurate if the momentum from the largest torques were managed passively or by magnetic actuation. Table 3-5 shows the difference between the saturation time for all torques and saturation time for the largest combinations of torques, starting with the largest torque and adding each subsequent largest torque not previously modeled; the last column is not included because all entries are zero. Table 3-6 shows the time it would take the reaction wheels to saturate for the smallest combinations of torques, starting with the maximum number of smallest torques and subtracting each subsequent largest torque previously included; the last column is not included because all entries are infinity.

Table 3-5— Time (in orbits) to Saturate Reaction Wheels with All Disturbance torques Less Time to Saturate Reaction Wheels with Given Torque Combinations.

Altitude (km)	Modeled Disturbance Torques		
	Aero	Aero + Gravity	Aero+ Gravity + Solar
350	0.005703	0.003852	0.000904
375	0.012272	0.008212	0.001911
400	0.026297	0.017382	0.003993
450	0.105156	0.067068	0.014804

Table 3-6—Time (in orbits) to Saturate Reaction Wheels with Smallest Un-modeled Disturbance Torques

Altitude (km)	Modeled Disturbance Torques		
	Aero	Aero + Gravity	Aero+ Gravity + Solar
350	3.92	8.16	23.91
375	3.95	8.19	24.18
400	3.98	8.22	24.45
450	4.04	8.28	25.00

It has been shown that magnetic actuation is capable of controlling momentum of a spacecraft over longer periods, on the order of orbits[49], so it is desirable for the un-modeled torques to require multiple (more than five) orbits to saturate reaction wheels. Additionally, it is desirable that the additional time it would take the un-modeled torques to saturate reaction wheels is much less than one orbit period. Examination of Table 3-5 and Table 3-6 suggests that modeling only the aerodynamic torque and the gravity gradient torque satisfies both of these desires with about an order of magnitude margin. Therefore, only aerodynamic and gravity gradient torque are modeled in simulations in this work.

3.1.5 Electrical Power Generation, Use, and Storage

CryoCube-1, like most, if not all, CubeSats, is a solar-powered spacecraft using a COTS electrical power subsystem (EPS) module whose main functions are to condition electrical power generated by solar panels, distribute electrical power to the other subsystems, and store excess electrical power in batteries. CryoCube-1 uses Clyde Space's 3rd Generation EPS (shown in Fig. 3-8), four Clyde Space solar panels as described in section 3.1.3.2, and Clyde Space's Standalone 10 Wh battery. The EPS charges the battery at constant current until the maximum battery voltage is reached, at which point the EPS charges the battery at constant voltage with exponentially decreasing current until a cutoff current is reached, stopping the charge cycle. While charging the battery in constant current mode, the EPS uses a Maximum Power Point Tracking (MPPT) algorithm to operate the solar panels at their maximum electrical power output. The maximum power capable of being output by each solar panel is a function of the light flux incident on the panel, the total area of solar cells on the panel, the solar cell light-to-electrical power conversion efficiency (28.3% for the solar cells used), and the EPS electrical power conversion efficiency (90% for the Clyde Space EPS's battery charging circuit). Light flux incident on the panel is

Fig. 3-8—The Clyde Space 3rd Generation EPS is used to charge batteries and distribute electrical power to CryoCube-1's electrical subsystems.

calculated by multiplying the solar flux constant (1366 W/m^2) by the dot product of the solar panel outward-facing normal unit vector ($\hat{n}_p$) and the unit vector from panel surface to the sun ($\hat{n}_s$); this value is set to zero when the dot product is negative (the sun is behind the panel) and when the spacecraft is in eclipse. Each 2U panel has four solar cells and the 1U panel has two solar cells. All cells have an area of 0.002662 m^2. For modeling simplicity and conservatism, the non-deployable 1U panel and the -X face of the deployable double-sided 2U panel on the +X face of the satellite are not modeled; both are shaded by the three deployable panels in most orientations. Multiplying all constants together, the solar power generation model for each solar panel is given by Eq. 3-17.

$$P_{panel,i} = (3.707\ W)(\hat{n}_{p,i} \cdot \hat{n}_s) \tag{3-17}$$

Electrical power is consumed by all subsystems in the electronics stack. All of these subsystems have a nominal power draw which is nearly constant as they all utilize passive components which consume some amount of power whenever voltage is applied (i.e. whenever the EPS is on). The aggregate nominal power usage was measured during CryoCube-1's final checkout testing. Table 3-7 shows the breakdown of the power consumed on each of the EPS's voltage busses (reported by the EPS) along with the power conversion efficiency of each bus in converting from battery voltage to bus voltage (reported in the EPS user manual) and the actual power consumed from the battery taking into account the conversion efficiency. Totaling the values in the final column of Table 3-7, CryoCube-1's nominal power consumption ($P_{nominal}$) is 1.836 W.

Table 3-7—Nominal power consumption reported by CryoCube-1 EPS during final checkouts.

Bus Voltage	Reported Consumption	Bus Conversion Efficiency	Actual Consumption
Battery	0.15 W	99%	0.152 W
12 V	1.00 W	92%	1.087 W
5 V	0.40 W	93%	0.430 W
3.3 V	0.15 W	90%	0.167 W

Though most of the electrical subsystems have a constant rate of power consumption, the radio, reaction wheels, and magnetorquers have highly variable power consumption rates. The radio uses significantly more power when it transmits (P_{comm}). Based on data taken from the EPS during final checkouts, transmitting uses an additional 7.0 W or, taking into account the 92% power conversion efficiency of the 12 V bus, an additional 7.610 W from the battery. The radio only transmits after it receives a ground command to do so and is commanded to transmit for no longer than the duration of the pass over the ground station. Therefore, all simulations in this work add the power consumed by radio transmission only when the ground station is visible from the satellite's position. Like the radio, the reaction wheels draw an additional amount of power proportional to the velocity of each wheel. Based on information provided in the reaction wheel datasheet, this power draw is 7×10^{-5} W/RPM per wheel, accounting for power conversion efficiency. Similarly, the magnetorquers draw an additional amount of power proportional to the dipole moment strength of each magnetorquer. Based on information provided in the solar panel datasheet, the magnetorquers consume 5.638 $\mathrm{W/A\cdot m^2}$, accounting for power conversion efficiency. The sum of the additional power consumed by the reaction wheels and the additional power consumed by the magnetorquers is the total power required for active attitude control ($P_{control}$).

The battery state of charge is governed by Eq. 3-18, which expresses the rate of change of state of charge, $\dot{C}$, as a function of battery power input/output (P), battery open circuit voltage (V_{bat}), and battery total capacity (Q). Power input/output is effectively the sum of all power input to the battery (i.e. from solar panels) less the sum of all power consumed by all spacecraft subsystems, as shown in Eq. 3-19.

$$\dot{C} = \frac{P}{V_{bat}Q} \tag{3-18}$$

$$P = \sum_{i=1}^{3} P_{panel,i} - (P_{control} + P_{comm} + P_{nominal}) \tag{3-19}$$

Battery open circuit voltage is generally a function of the total amount of charge discharged from the battery, the rate at which the battery is discharged, and the temperature of the battery. However, the electrochemical processes that result in this behavior are complex, and accurately modeling such processes is beyond the scope of this dissertation. Therefore, a surrogate model, a least squares fit of battery voltage with respect to battery discharge data, is used. Battery voltage versus discharge data is provided by Clyde Space in their Battery User Manual for a number of different discharge rates. Battery discharge rates, or C ratings, are reported in terms of inverse time, hours^{-1}, required to discharge the total battery capacity. A C rating is for a discharge time of one hour, a 2C rating is for a discharge time of 30 minutes, and a C/2 rating is for a discharge time of two hours. In general, the faster the battery is discharged, the less total charge will be output from the battery; battery voltage falls off rapidly at the total discharge amount, and discharging to very low battery voltages will permanently ruin the battery. Clyde's Battery User Manual recommends a maximum C/2 charge/discharge rate, which has a minimum total discharge capacity of about 1200 mA·h, compared with the approximately 1400 mA·h capacity at C/15 and almost 2500 mA·h capacity at C/50. Because the C/2 discharge rate is the most conservative with respect to the total storable electrical power, the C/2 voltage versus discharge data from the Clyde Space

Battery User Manual is used for the surrogate model; therefore, Q in Eq. 3-18 is taken as 1200 mA·h. The surrogate, Eq. 3-20, models battery voltage as a ratio of polynomials in discharge: the numerator a third order polynomial and the denominator a first order polynomial. This model was chosen to capture the very rapid decrease in battery voltage near maximum discharge, hence the first order polynomial in the denominator, as well as the general cubic appearance of the data over the remainder of the domain. The least squares fit has an R^2 value of 0.986 with respect to data points taken from the plot in Clyde Space's Battery User Manual.

$$V_{bat} = \frac{-0.638(C_{max}-C)^3+1.676(C_{max}-C)^2-4.29(C_{max}-C)+4.11}{1-0.763(C_{max}-C)} \tag{3-20}$$

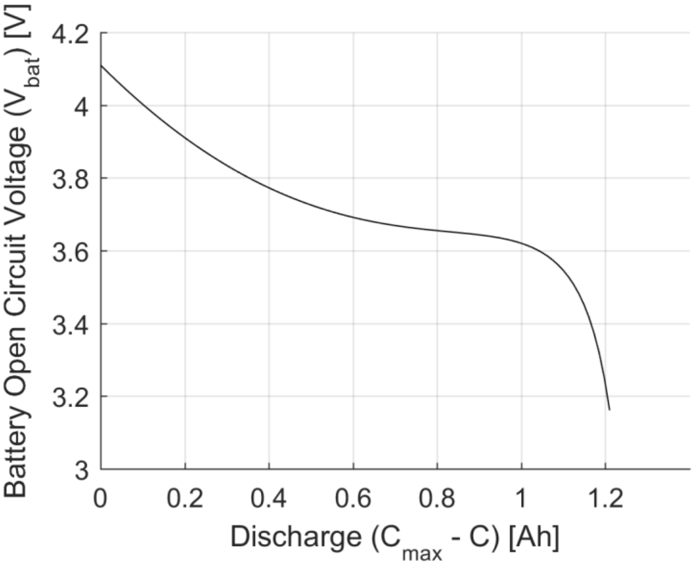

Fig. 3-9—CryoCube battery open-circuit voltage versus discharge (single cell).

3.1.6 Communication Link Strength

Communication link strength is analyzed from the baseline Friis link equation, Eq. 3-21, which expresses the power of the signal received, P_r, as a function of transmitter power (P_t), transmitter gain (G_t), receiver gain (G_r), distance between transmitter and receiver (d), and carrier signal wavelength (λ). The received signal power is divided by system noise power to calculate signal to noise ratio (SNR) in Eq. 3-22, where $k = 1.38 \times 10^{-23}\,\frac{\mathrm{W}}{\mathrm{K{\cdot}Hz}}$ is the Boltzmann Constant, T_S is the system temperature, and B is the noise bandwidth. Similarly, the received power is divided by temperature noise power and data rate, R, to calculate E_b/N_o, the ratio of energy per bit to noise power spectral density, in Eq. 3-23.

$$P_r = \frac{P_t G_t G_r}{(4\pi d/\lambda)^2} \tag{3-21}$$

$$SNR = \frac{P_t G_t G_r}{(4\pi d/\lambda)^2 k T_S B} \tag{3-22}$$

$$E_b/N_o = \frac{P_t G_t G_r}{(4\pi d/\lambda)^2 k T_S R} \tag{3-23}$$

The logarithmic forms of these equations are often used with quantities expressed in dB, because the terms on the right hand sides of these equations are often many orders of magnitude different from one another; non-unitless quantities (e.g. power) are expressed in decibels with additional units after (e.g. dB_W for units of watts or dB_m for units of milliwatts). Expressing groups of the right-hand-side terms in logarithmic form allows for simple addition and subtraction of gain and loss components and provides a means of quickly identifying the components responsible for the largest gains and losses. Additional terms may be added or subtracted from the equations to account for losses in cables, losses due to spacecraft body effects, and atmospheric losses. Table 3-8 lists all gain and loss terms calculated for data downlink for CryoCube-1, and Table 3-9 lists all gain and loss terms calculated for data uplink for CryoCube-1. Terms that are a function of position and attitude are indicated, though some position and attitude-dependent terms, such as ground station G/T and atmospheric losses are taken as constant; values of these terms are calculated at worst-case conditions, typically five degrees elevation.

The minimum SNR and/or E_b/N_o are typically specified based on a known desired maximum bit error rate, encoding/decoding scheme, and modulation/demodulation scheme, and, when using the logarithmic form of the link equations, the specified SNR or E_b/N_o are subtracted from the calculated SNR or E_b/N_o, respectively, to determine the link margin. Positive margin indicates the link will likely achieve the desired data rate. Zero margin indicates the link may just barely achieve the desired data rate. And negative margin indicates the desired data rate will not be achieved. A minimum margin may also be specified to account for uncertainties in the link analysis, helping to ensure the desired data rate is achievable. Table 3-10 lists the uplink and downlink bit rates and E_b/N_o ratios required to achieve the desired bit error rates (BERs).

Table 3-8—Downlink gains and losses used for link margin analysis.

Gain/Loss Source	Gain or Loss	Equation or Value
Transmit Power	Gain	1 W = 0 dB_W
Spacecraft Antenna Gain	Gain	Dependent on orientation (see Fig. 3-10)
Passive Spacecraft Components	Loss	1.60 dB
Polarization Loss	Loss	0.67 dB
Pointing Errors	Loss	0.50 dB
Atmospheric, Rain, Cloud	Loss	0.50 dB
Free Space Wave Propagation	Loss	$(4\pi d/\lambda)^2 = 39.49\ dB + 20\log_{10}(d)$
Ground Station G/T	Gain	3.49 $dB_{/K}$
Boltzmann's Constant	Loss	$k = -228.60$ $dB_{/Hz\cdot K}$
Implementation Loss	Loss	3.00 dB

Table 3-9—Uplink gains and losses used for link margin analysis.

Gain/Loss Source	Gain or Loss	Equation or Value
Ground Station EIRP (transmitter power and antenna gain)	Gain	34 dB_W
Free Space Wave Propagation	Loss	$(4\pi d/\lambda)^2 = 38.82\ dB + 20\log_{10}(d)$
Atmospheric, Rain, Cloud	Loss	0.50 dB
Spacecraft Antenna Gain	Gain	Dependent on orientation (see Fig. 3-10)
Pointing Errors	Loss	0.50 dB
Passive Spacecraft Components	Loss	2.1 dB
Polarization Loss	Loss	0.67 dB
Spacecraft Noise Temperature	Loss	734.61 K = 28.66 dB_K
Boltzmann's Constant	Loss	$k = -228.60$ $dB_{/Hz\cdot K}$
Implementation Loss	Loss	3.0 dB

Table 3-10—Signal strength and E_b/N_o needed to achieve desired bit rate with given encoding and modulation.

Bit Rate	**Signal Strength Needed for Bit Rate**	**Req'd E_b/N_o for BER = 10^{-5}**
Uplink 200 kbps	53.01 dB_bps	4.20 dB
Downlink 4 kbps	36.02 dB_bps	24.48 dB

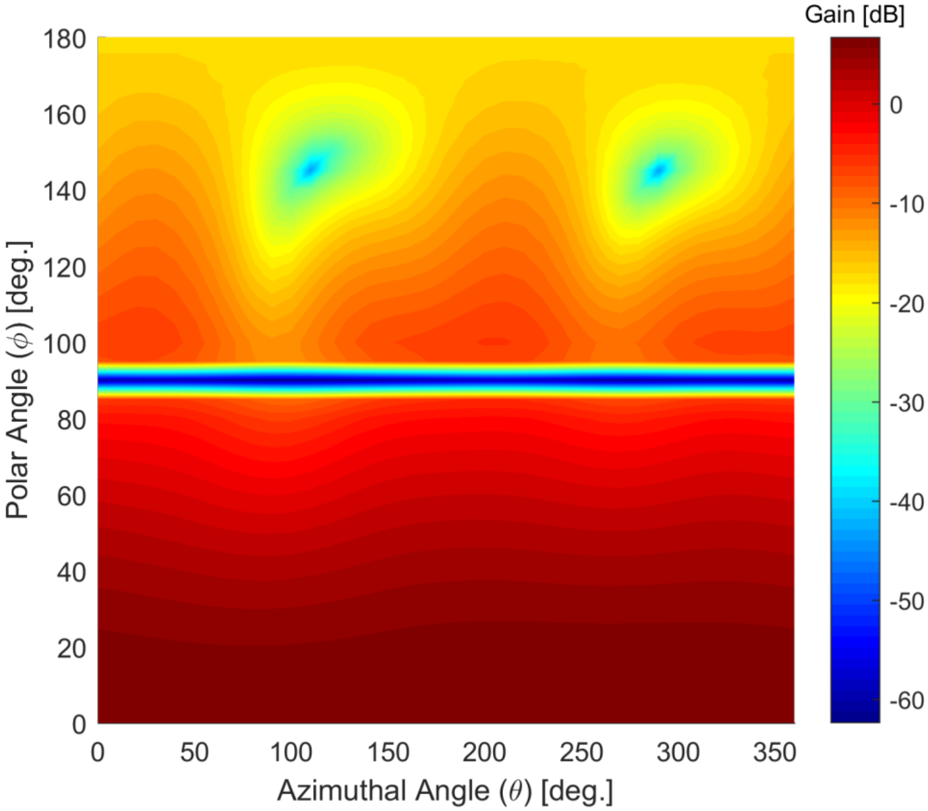

Fig. 3-10—CryoCube Rx and Tx antenna direction-dependent gain.

Adding gain terms and subtracting loss terms in Table 3-8 and Table 3-9, then subtracting both the signal strength required for the target bit rate and the required E_b/N_0 to achieve the desired bit error rate yields the simplified Eq. 3-24 for downlink margin (G_{down}) and Eq. 3-25 for uplink margin (G_{up}). Note that, in both equations, the only term which is affected by the spacecraft attitude is the antenna gain. Also, note that G_{up} is always smaller than G_{down} by exactly 1.23 dB; the antennas are mounted to the same side of the spacecraft and have identical gain patterns. For this reason, the concept of a generic communication link margin, the smaller of the two link margins, is used in this work to signify when both uplink and downlink have margin, and Eq. 3-25 is used to calculate communication link margin.

$$G_{down} = 129.08\, dB + G_{ant} - 20\log_{10}\left(\left\|\bar{d}\right\|\right) \tag{3-24}$$

$$G_{up} = G_{margin} = 127.85\, dB + G_{ant} - 20\log_{10}\left(\left\|\bar{d}\right\|\right) \tag{3-25}$$

It is clear that the communication link strength is dependent on the distance between the spacecraft and the ground station as well as whether or not there is a clear line of sight between the two. CryoCube-1 will communicate with a single ground station located at 28°35’6”N, 80°38’53”W. Using the WGS 84 reference ellipsoid, these geodetic coordinates are transformed to Cartesian coordinates in the ECEF coordinate system. The Cartesian coordinates of the ground station location on the reference ellipsoid surface, R_G, are then used with the known spacecraft location, R_s, to calculate the vector from the ground station to the spacecraft, $\bar{d}$, as shown in Eq. 3-26. The magnitude of $\bar{d}$ is the distance between the spacecraft and ground station used in the link equation.

$$\bar{d} = R_s - R_G \tag{3-26}$$

Furthermore, the dot product of $\bar{d}$ and R_G is used to determine whether or not the spacecraft is at least five degrees above the horizon, or equivalently, the vectors are separated by less than 85 degrees, because worst-case atmospheric losses are generally calculated for a five degree elevation. It is assumed that a link cannot be maintained when spacecraft elevation is below five degrees. Eq. 3-27 shows how the link loss due to Earth occultation of the ground station is calculated (Note: $\cos(85°) \approx 0.08716$).

$$G_E = \begin{cases} 0\, dB & \frac{\bar{d}\cdot R_G}{\|\bar{d}\|\|R_G\|} \geq 0.08716 \\ \infty\, dB & \frac{\bar{d}\cdot R_G}{\|\bar{d}\|\|R_G\|} < 0.08716 \end{cases} \tag{3-27}$$

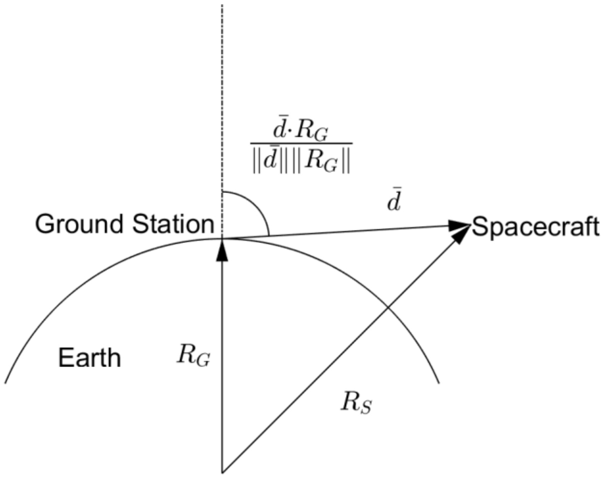

Fig. 3-11—Ground station elevation geometry.

3.1.7 Experiment Temperature

A finite element heat transfer model developed in COMSOL Multiphysics and shown in Fig. 3-12 is used to calculate the temperature of CryoCube-1's experiment tank. The geometrically simplified model accounts for the major sources of internally-generated heat from the electronics components, conduction within spacecraft components, conduction among the spacecraft components in contact, radiation among internal components, radiation from the sun and earth to the spacecraft, and radiation from the spacecraft to deep space. Both the sun and earth are modeled as point sources of radiation at infinite distance, the sun radiating 1,360 W/m^2 at 5,778 K and the earth radiating 250 W/m^2 at 300 K. Deep space is modeled as a background radiation sink at a uniform temperature of 4 K. Appropriate thermal conductivities, specific heats, densities, and emissivities are assigned to all spacecraft components and surfaces, and appropriate thermal contact resistances are assigned between surfaces in contact with one another per the guidance of Ref. 50.

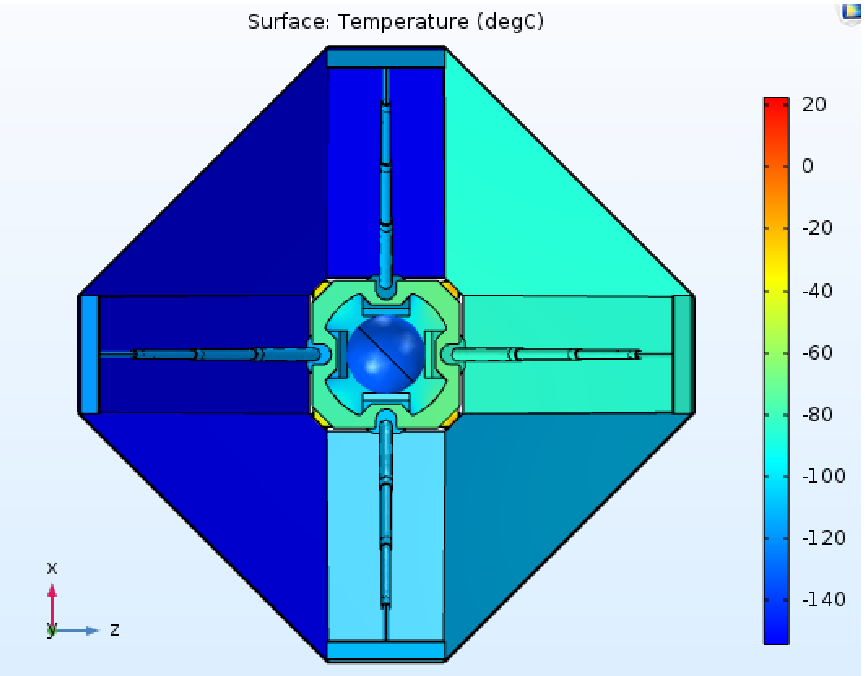

Fig. 3-12—COMSOL Multiphysics thermal model of CryoCube-1.

A time-dependent solution of the finite element model in COMSOL Multiphysics takes on the order of several minutes to solve, whereas a steady-state solution takes on the order of several seconds to solve. Because many evaluations of the thermal model are required to perform optimization, the steady-state temperature of the experiment tank is used as a proxy for the actual time-dependent experiment tank temperature when performing optimization. Steady-state solutions are solved for a number of sun vector and earth vector positions prior to performing the optimization, and spacecraft experiment tank temperatures are interpolated from these pre-computed solutions using the sun vector and earth vector positions encountered during optimization. The main shortfall of this approach is that, in general, spacecraft temperature at any given time is dependent on the initial temperature of the spacecraft as well as the complete time history of spacecraft position and attitude. Though it is possible that the dynamics of the thermal model could be driven by the attitude dynamics to a state significantly different from the steady state, this is assumed to be extremely unlikely.

When interpolating the temperature from the results of the steady-state thermal model, both the direction of the earth and the direction of the sun in the spacecraft body-fixed coordinate system are required. The direction of the earth with respect to the spacecraft is given by the earth nadir vector, simply the opposite direction of the spacecraft position vector expressed in spacecraft body-fixed coordinates. The direction of the sun with respect to the spacecraft is given by a solar ephemeris, Eq. 3-28 – Eq. 3-33, which expresses the direction of the sun in the J2000 ECI coordinate system, and the coordinate transformation from the J2000 ECI to the spacecraft body-fixed coordinate system[51].

$$Julan\ Day = 367 \times year - floor\left(\frac{7\times\left(year+floor\left(\frac{month+9}{12}\right)\right)}{4}\right) + floor\left(275 \times \frac{month}{9}\right) + day + 1{,}721{,}013.5 \tag{3-28}$$

$$d = Julian\ Day - 2{,}415{,}020 \tag{3-29}$$

$$L_m = 279.696678 + 0.9856473354d + (2.267 \times 10^{-13})d^2 \tag{3-30}$$

$$M = 358.475845 + 0.985600267d - (1.12 \times 10^{-3})d^2 - (7 \times 10^{-20})d^3 \tag{3-31}$$

$$L = L_m + 1.918\sin(M) + 0.02\sin(2M) \tag{3-32}$$

$$\hat{r}_{sun} = \begin{bmatrix} \cos(L) \\ \sin(L) \\ 0 \end{bmatrix} \tag{3-33}$$

3.2 Objective Function

The ultimate objective of the CryoCube-1 mission is to demonstrate the ability of the 3U CryoCube bus technology to provide passive cooling of its experiment payload to cryogenic temperatures while on orbit. However, the CryoCube bus is highly constrained in its ability to achieve this goal. The main constraints of the CryoCube bus have been identified as follows: its reaction wheels have relatively small total momentum capacity for its expected operating environment, its antennas are not omnidirectional and generally must point toward the ground to communicate, and its batteries have limited electrical power storage capacity. A carefully-designed or optimized attitude profile has the potential to compensate for these disadvantages. This section introduces a set of highly constrained multidisciplinary feasibility search and optimization problems that will be used to determine the attitude trajectories that provide CryoCube-1 as much of its intended operational capability as possible and to determine what, if any, of its intended operational capability is infeasible.

Feasibility of CryoCube-1's intended operational capability is assessed by solving a set of mathematical optimization problems. Each optimization problem is defined by a single objective and a set of inequality constraints. Three different objectives, listed in Table 3-11, are considered: maximum electrical power storage, maximum antenna gain, and minimum experiment payload temperature. Maximum antenna gain is used instead of communication link margin, because the constant and distance-dependent terms of Eq. 3-25, which the spacecraft orientation does not affect, tend to dominate the communication link margin numerical value, and maximization of antenna gain is equivalent to maximizing communication link margin. Five different inequality constraints, listed in Table 3-12, are considered. Reaction wheel speed and angular acceleration constraints are common for all optimization problems considered as these are physical limits of the system hardware, whereas electrical power storage and communication link margin (antenna gain) constraints are ideal operational constraints. Each optimization problem represents a feasibility assessment of a potential operational mode of the spacecraft. An optimization problem solution satisfying all constraints represents a feasible operational mode. The optimal attitude trajectory, or formally speaking, the argument of the optimal solution, is the attitude trajectory for the operational mode.

Table 3-11—Attitude trajectory optimization problem base objective definitions.

Unconstrained Objective	Unconstrained Objective Definition
Battery Charge	$\bar{C} = \frac{1}{T}\int_{t=0}^{T} C(t)dt$
Antenna Gain	$\bar{G}_{ant} = \frac{100}{T}\int_{t=0}^{T} 10^{0.1G_{ant}(t)}dt$
Temperature	$\bar{T}_{payload} = \frac{1}{T}\int_{t=0}^{T} T_{payload}(t)dt$

Table 3-12—Inequality constraints derived from operational constraints and mission objective.

Constraint	Criterion
Electrical Power Storage	$C \geq 0.2C_{max}$
Communication Link Margin	$G_{ant} \geq 5dB\ at\ least\ 50\%\ of\ total\ pass\ time$
Reaction Wheel Speed	$\|\omega_w\| \leq 6500\ RPM$
Reaction Wheel Acceleration	$\|\dot{\omega}_w\| \leq 33\ RPM/s$

Table 3-13 lists all modes of operation under consideration along with their corresponding optimization problems. In general, the operational modes are listed from higher priority to lower priority tasks required to perform the mission. The highest priority task is to generate electrical power, because without electrical power, the spacecraft will not be able to communicate with the ground, reorient itself to communicate with the ground, or perform the primary science mission. The next highest priority task is to communicate with the ground, because, without ground communication, it will be impossible to determine if the spacecraft successfully completes its science mission or if the spacecraft is even still operational, but the spacecraft can still generate electrical power if it does not have a link to the ground. The lowest priority task is to complete the science mission, because the spacecraft can still generate power and communicate to the ground even if it does not complete the science mission.

The methodology used to solve the optimization problems is discussed in further detail in section 4.5.

Table 3-13— Candidate spacecraft modes of operation and corresponding constrained attitude trajectory optimization problems.

Operational Mode	Optimization Problem
Emergency Power Generation	Maximize average stored electrical power, subject to reaction wheel constraints $\underset{q(t)}{\arg\max}(\bar{C})$ $subject\ to: \quad orbit, attitude\ dynamics$ $\lVert\omega_w\rVert \leq 6500\ RPM$ $\lVert\dot{\omega}_w\rVert \leq 33\ RPM/s$
Nominal Power Generation	Maximize average stored electrical power, subject to reaction wheel and link margin constraints $\underset{q(t)}{\arg\max}(\bar{C})$ $subject\ to: \quad orbit, attitude\ dynamics$ $\lVert\omega_w\rVert \leq 6500\ RPM$ $\lVert\dot{\omega}_w\rVert \leq 33\ RPM/s$ $G_{ant} \geq 5dB \quad at\ least\ 50\%\ of\ total\ pass\ time$
Power Positive Ground Station Tracking	Maximize average link margin, subject to reaction wheel and solar power generation constraints $\underset{q(t)}{\arg\max}(\bar{G})$ $subject\ to: \quad orbit, attitude\ dynamics$ $\lVert\omega_w\rVert \leq 6500\ RPM$ $\lVert\dot{\omega}_w\rVert \leq 33\ RPM/s$ $C \geq 0.2C_{max}$
Nominal Ground Station Tracking	Maximize average link margin, subject to reaction wheel constraints $\underset{q(t)}{\arg\max}(\bar{G})$ $subject\ to: \quad orbit, attitude\ dynamics$ $\lVert\omega_w\rVert \leq 6500\ RPM$ $\lVert\dot{\omega}_w\rVert \leq 33\ RPM/s$

Operational Mode	Optimization Problem
Power Positive Science	Minimize average payload temperature, subject to reaction wheel and electrical power storage constraints $\arg\min_{q(t)}(\bar{T})$ $subject\ to: \quad orbit, attitude\ dynamics$ $\|\omega_w\| \leq 6500\ RPM$ $\|\dot{\omega}_w\| \leq 33\ RPM/s$ $C \geq 0.2C_{max}$
Science with Ground Station Tracking	Minimize average payload temperature, subject to reaction wheel and link margin constraints $\arg\min_{q(t)}(\bar{T})$ $subject\ to: \quad orbit, attitude\ dynamics$ $\|\omega_w\| \leq 6500\ RPM$ $\|\dot{\omega}_w\| \leq 33\ RPM/s$ $G_{ant} \geq 5dB \quad at\ least\ 50\%\ of\ total\ pass\ time$
Science with Power Generation and Ground Station Tracking	Minimize average payload temperature, subject to reaction wheel, electrical power storage, and link margin constraints $\arg\min_{q(t)}(\bar{T})$ $subject\ to: \quad orbit, attitude\ dynamics$ $\|\omega_w\| \leq 6500\ RPM$ $\|\dot{\omega}_w\| \leq 33\ RPM/s$ $C \geq 0.2C_{max}$ $G_{ant} \geq 5dB \quad at\ least\ 50\%\ of\ total\ pass\ time$
Nominal Science	Minimize average payload temperature, subject to reaction wheel constraints $\arg\min_{q(t)}(\bar{T})$ $subject\ to: \quad orbit, attitude\ dynamics$ $\|\omega_w\| \leq 6500\ RPM$ $\|\dot{\omega}_w\| \leq 33\ RPM/s$

4 Methodology

The methods used to represent and optimize attitude state trajectories are presented in this section. Typical trajectory optimization problems are solved using the numerical techniques of optimal control theory in which the optimal control problem is discretized, or transcribed, into a nonlinear constrained parameter optimization problem, either directly or indirectly (i.e. from construction of necessary and sufficient conditions of optimality) via shooting, collocation, or pseudospectral methods, then solved using nonlinear programming techniques. In this work, fuzzy logic, in the form of fuzzy inference systems (FISs), is used to define or parameterize the attitude trajectories in terms of the time-dependent sun and ground station vectors, and genetic algorithms are used to search for optimal attitude trajectories by modifying parameters of the FISs.

4.1 Fuzzy Logic

Fuzzy logic is a multivalued logic system which can be used in what is termed a fuzzy inference system (FIS) to infer a set of outputs from a set of inputs with a set of logic-based rules that map inputs to outputs. Various methods, including the Mamdani and Sugeno methods exist for performing the mapping, but all methods have been shown to allow fuzzy inference systems to act as universal approximators, or systems that can approximate any function to any arbitrary degree of accuracy, though increasing accuracy of universal aproximators is generally associated with higher computational complexity[52]. All FISs in this work use Mamdani's method, as it is the most common fuzzy inference system method[52].

A FIS uses a set of if-then rules, the rule base, along with an inference process to transform inputs into outputs. Fig. 4-1 shows the Mamdani fuzzy inference process in graphical form. The inputs and outputs are termed linguistic variables, and a number of fuzzy sets are defined over the domain of each linguistic variable. Fuzzy sets are multivalued sets, meaning that an item can belong partially to a fuzzy set, unlike classical bivalent sets to which items either belong or do not belong. The fuzzy sets defined over the domain of a linguistic variable are termed membership functions, because they describe the degree of membership of a specific domain value to the fuzzy set; membership functions act as adjectives to the linguistic variables. Using an input membership function to evaluate the corresponding input linguistic variable's degree of membership to that membership function is termed fuzzification and is the first step in the evaluation of a FIS, labeled as 1 in Fig. 4-1. Following fuzzification is inference, which is itself a multistep process to convert fuzzified values to a composite output membership function via the if-then rules of the rule base. Each if-then rule contains statements of the form '*linguistic variable* is *membership function*', both before and after the *then*. In the antecedent (after the *if* and prior to the *then*), these statements evaluate the degree of membership of the linguistic variable to its specified membership function. Usually, multiple statements of this form are separated by logical operators, which define the first half of a composition operation, labeled as 2 in Fig. 4-1, converting these degrees of membership to a single value in the range [0 1]; for this work, the logical operators are ORs, and the operation is maximization. In the second half of composition, labeled as 3 in Fig. 4-1, this single value is combined with the output membership function specified for a given linguistic variable after the *then* statement to produce a modified output membership function defined over the range of the output linguistic variable; for this work, the minimum of the value of the membership function and the single value is taken as the modified output membership function value at each point in the output linguistic variable domain. The modified output membership functions for all rules are then combined over the range of the output linguistic variable using the same operation (minimization for this work) to form a composite output membership function, near label 4 in Fig. 4-1. Following this composition, the composite output membership function is defuzzified, usually by finding the centroid of the composite membership function, to produce a single output value for each output linguistic variable, as shown by the vertical red line near label 4 in Fig. 4-1.

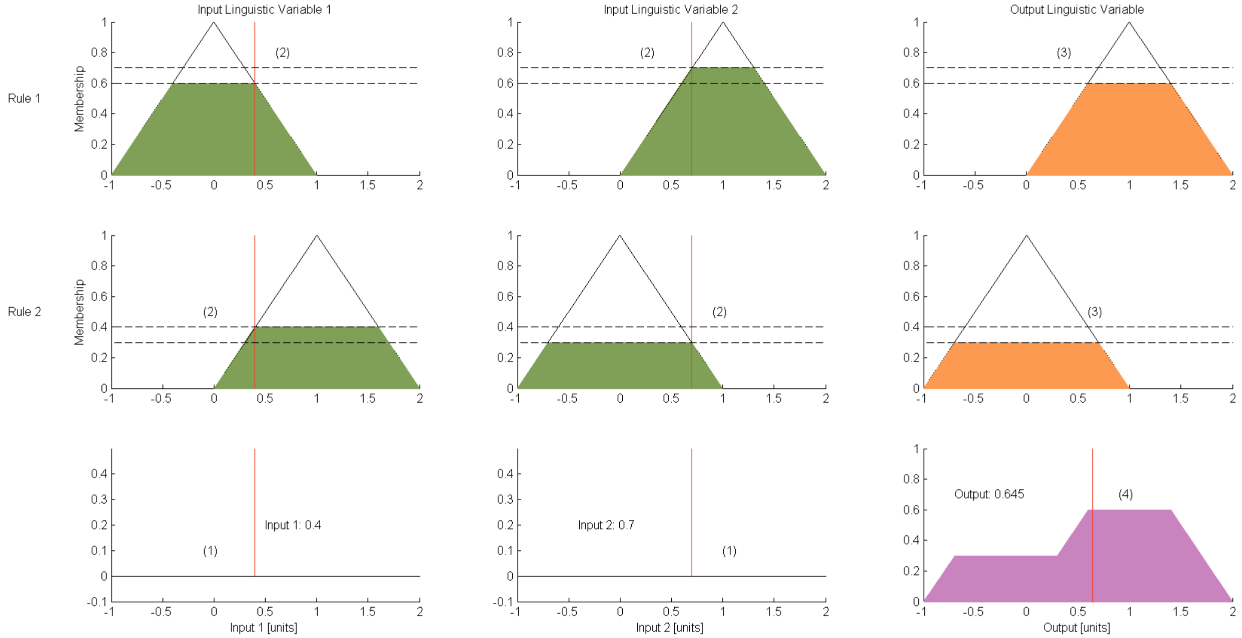

Fig. 4-1—Mamdani-type fuzzy inference process.

4.2 Attitude Trajectory FISs

Attitude trajectories for the candidate operational modes are defined using FISs. In general, an attitude trajectory is a time-dependent sequence of attitude states which may or may not be continuous. Discontinuous trajectories essentially define a series of waypoints which an attitude control algorithm could track, possibly by performing large angle slew maneuvers between trajectory waypoints. However, when tracking a discontinuous trajectory, the attitude states a spacecraft attains between waypoints may be decidedly non-optimal. Therefore, attitude trajectories that are continuous in time, but not necessarily continuously differentiable (i.e. by examination of Eq. 3-4, angular velocities may not be continuous) in time, are sought.

Furthermore, it is desirable that the attitude trajectories are capable of being expressed as a function of variables other than time so that the trajectories are valid for a variety of orbit geometries and do not have to be computed periodically for specific epochs. Upon examination of the objectives and constraints presented in section 3.2, some simple strategies emerge. For maximizing or constraining battery charge, a good strategy might be to point either the (+X, +Y) or (+X, -Y) corner of the spacecraft directly toward the sun to maximize total flux on the solar cells. For maximizing or constraining antenna gain, a good strategy might be to point the spacecraft's –X face unit normal directly at the ground station at all times. For minimizing experiment temperature, a good strategy might be to point the open end of the sunshield away from the sun and earth. Now, these strategies might seem obvious, but they help to illustrate which input variables may be important when constructing FISs. They tend to suggest that optimization problems with power generation and temperature objectives or constraints need sun vector information, optimization problems with antenna gain objectives or constraints need ground station vector information, and optimization problems with temperature objectives need earth nadir information. Careful selection of reference coordinate system can reduce the input required to the FISs. For instance, the reference coordinate system is chosen to be a local-level coordinate system in which nadir is always along the –X-axis, the orbit angular velocity vector is always along the +Z-axis, and the +Y-axis completes the right-handed coordinate system (in the same sense as, but not necessarily aligned with spacecraft orbit velocity). This choice eliminates the need to input earth nadir direction into the FIS as this would be represented by a constant set of values, leaving only sun vector and ground station vector as potential inputs needed for the FISs. These unit vectors are each represented using a minimum set of parameters: an azimuth (α) and a coelevation (ε).

The generic attitude trajectory FIS, Eq. 4-1, takes the azimuth and elevation of both the sun and ground station vector as inputs and outputs an axis-angle representation of attitude. The axis-angle attitude representation is used here because it is easily related to the attitude quaternion via Eq. 4-2, and it can be expressed compactly as a set of three angles, an azimuth of the axis (α_q), a coelevation (or polar angle) of the axis (ε_q), and the angle of rotation about the axis (θ_q).

$$\begin{aligned} \alpha_q &= F_\alpha(\alpha_s, \varepsilon_s, \alpha_g, \varepsilon_g) \\ \varepsilon_q &= F_\varepsilon(\alpha_s, \varepsilon_s, \alpha_g, \varepsilon_g) \\ \theta_q &= F_\theta(\alpha_s, \varepsilon_s, \alpha_g, \varepsilon_g) \end{aligned} \tag{4-1}$$

$$\begin{aligned} q &= \left[\cos\left(\frac{\theta_q}{2}\right) \quad v_q \sin\left(\frac{\theta_q}{2}\right)\right] \\ v_q &= \left[\sin(\varepsilon_q)\cos(\alpha_q) \quad \sin(\varepsilon_q)\sin(\alpha_q) \quad \cos(\varepsilon_q)\right]^T \end{aligned} \tag{4-2}$$

Using the chain rule to evaluate the time derivative of the attitude trajectory in Eq. 4-2, and noting that, in general, the FISs are designed to be of differentiability class C^0, it is clear that the attitude trajectory defined in this manner is also class C^0, so it satisfies the requirement of being continuous but not necessarily continuously differentiable. In order to be class C^0, it is sufficient for the FISs to have the following properties: for every point in the input range, the maximum value in the set of all degree of membership values output by all input membership functions used in the rule base is greater than zero, and no input membership function has a step change in membership value at any point in the input range. By definition, any point in the input domain which has no mapping to the output domain is undefined, so any point in a FIS's input domain that has zero input linguistic variable membership value for all input membership functions has an undefined output; in practice, a FIS outputs some predetermined value, such as the average of the output range, which can yield discontinuities at the points the mapping becomes undefined. If just a single point is undefined, the output value will transition abruptly, a discontinuity, from the centroid of one composite output membership function to the centroid of another composite output membership function, given the rule base does not map the adjacent input membership functions to identical output membership functions, though even in this instance, at the transition point, the FIS may output an inconsistent value based on the value it returns when the mapping is undefined. As for the other condition that could cause a FIS to have a discontinuous output, it is clear that a step change in input membership function value could result in a step change to the shape of the composite output membership function, which could further result in a step change to the composite output membership function centroid.

The properties sufficient to produce a C^0 FIS motivate the use of as few inputs as possible for each mode of operation, because the rule base must contain at least a set of membership functions that span the input range with no undefined points, and the rule base size is equal to the product of the number of membership functions in each input, so it grows exponentially as a function of the number of inputs. Table 4-1 shows the input state variables chosen for each operational mode under consideration along with the number of membership functions chosen to span each state variable and the total size of the rule base.

Table 4-1—Input state variables and number of input membership functions used for each trajectory FIS,

Operational Mode Under Consideration	State Variables used as Inputs to FIS	Number of Membership Functions	Total Rule Base Size
Emergency Power Generation	α_s	13	91
	ε_s	7	
Nominal Power Generation	α_s	7	784
	ε_s	4	
	α_g	7	
	ε_g	4	
Power Positive Ground Station Tracking	α_s	7	784
	ε_s	4	
	α_g	7	
	ε_g	4	

Operational Mode Under Consideration	State Variables used as Inputs to FIS	Number of Membership Functions	Total Rule Base Size
Nominal Ground Station Tracking	α_g	13	91
	ε_g	7	
Power Positive Science	α_s	13	91
	ε_s	7	
Science with Ground Station Tracking	α_s	7	784
	ε_s	4	
	α_g	7	
	ε_g	4	
Science with Power Generation and Ground Station Tracking	α_s	7	784
	ε_s	4	
	α_g	7	
	ε_g	4	
Nominal Science	α_s	13	91
	ε_s	7	

The membership functions of the attitude trajectory FISs are chosen to provide a relatively simple means of evaluation onboard the spacecraft and to provide a means of modifying the FIS during optimization. All input membership functions are triangular, parameterized by three distinct values. Azimuth input linguistic variables span the range [0 360] degrees and coelevation input linguistic variables span the range [0 180] degrees. Membership functions of these linguistic variables are constrained to provide a consistent treatment of the inputs at the apparent singularities of the spherical coordinate representation used. These singularities occur at the boundaries of the input ranges: 0 and 360 degrees azimuth and 0 and 180 degrees coelevation. Membership functions are placed at these locations such that their maximum membership value occurs on the boundary. (Note that this placement leaves only one degree of freedom for designing these boundary membership functions, whereas all three degrees of freedom are available to specify all other input membership functions.) Because an azimuth of 0 degrees is equal to an azimuth of 360 degrees, the rules including the 0 degree azimuth boundary membership function must match the rules including the 360 degree azimuth boundary membership function to prevent a discontinuity. Additionally, at coelevations of 0 degrees and 180 degrees, the direction of the vector parameterized in spherical coordinates is independent of the azimuth, so the rule base collapses to one rule, rather than one rule per azimuth membership function, at these locations. This collapse to a single rule at the poles does not affect the C^0 property of the FIS, because the FIS is still dependent on at least one input variable, not independent of all input variables, at these points. An example of input membership functions and a rule base consistent with this design is shown in Fig. 4-2 and Table 4-2.

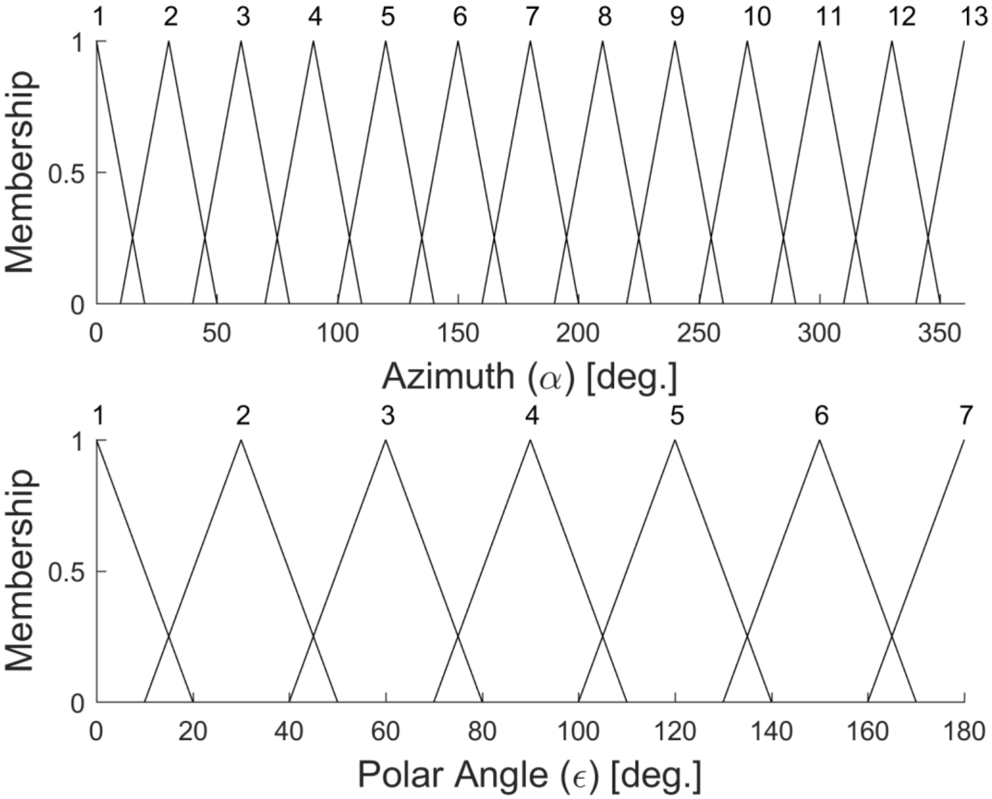

Fig. 4-2—Input membership functions for FIS consistent with constraints of optimal trajectory.

Table 4-2— Rule base for FIS consistent with constraints of optimal trajectory.

		Input Polar Angle (ε)						
		1	2	3	4	5	6	7
Input Azimuth (α)	1	α MF 1 ε MF 8 θ MF 15	α MF 6 ε MF 11 θ MF 10	α MF 11 ε MF 14 θ MF 5	α MF 16 ε MF 1 θ MF 16	α MF 5 ε MF 4 θ MF 11	α MF 10 ε MF 7 θ MF 6	α MF 15 ε MF 10 θ MF 1
	2	α MF 1 ε MF 8 θ MF 15	α MF 9 ε MF 16 θ MF 7	α MF 14 ε MF 3 θ MF 2	α MF 3 ε MF 6 θ MF 13	α MF 8 ε MF 9 θ MF 8	α MF 13 ε MF 12 θ MF 3	α MF 15 ε MF 10 θ MF 1
	3	α MF 1 ε MF 8 θ MF 15	α MF 12 ε MF 5 θ MF 4	α MF 1 ε MF 8 θ MF 15	α MF 6 ε MF 11 θ MF 10	α MF 11 ε MF 14 θ MF 5	α MF 16 ε MF 1 θ MF 16	α MF 15 ε MF 10 θ MF 1
	4	α MF 1 ε MF 8 θ MF 15	α MF 15 ε MF 10 θ MF 1	α MF 4 ε MF 13 θ MF 12	α MF 9 ε MF 16 θ MF 7	α MF 14 ε MF 3 θ MF 2	α MF 3 ε MF 6 θ MF 13	α MF 15 ε MF 10 θ MF 1
	5	α MF 1 ε MF 8 θ MF 15	α MF 2 ε MF 15 θ MF 14	α MF 7 ε MF 2 θ MF 9	α MF 12 ε MF 5 θ MF 4	α MF 1 ε MF 8 θ MF 15	α MF 6 ε MF 11 θ MF 10	α MF 15 ε MF 10 θ MF 1
	6	α MF 1 ε MF 8 θ MF 15	α MF 5 ε MF 4 θ MF 11	α MF 10 ε MF 7 θ MF 6	α MF 15 ε MF 10 θ MF 1	α MF 4 ε MF 13 θ MF 12	α MF 9 ε MF 16 θ MF 7	α MF 15 ε MF 10 θ MF 1
	7	α MF 1 ε MF 8 θ MF 15	α MF 8 ε MF 9 θ MF 8	α MF 13 ε MF 12 θ MF 3	α MF 2 ε MF 15 θ MF 14	α MF 7 ε MF 2 θ MF 9	α MF 12 ε MF 5 θ MF 4	α MF 15 ε MF 10 θ MF 1
	8	α MF 1 ε MF 8 θ MF 15	α MF 11 ε MF 14 θ MF 5	α MF 16 ε MF 1 θ MF 16	α MF 5 ε MF 4 θ MF 11	α MF 10 ε MF 7 θ MF 6	α MF 15 ε MF 10 θ MF 1	α MF 15 ε MF 10 θ MF 1
	9	α MF 1 ε MF 8 θ MF 15	α MF 14 ε MF 3 θ MF 2	α MF 3 ε MF 6 θ MF 13	α MF 8 ε MF 9 θ MF 8	α MF 13 ε MF 12 θ MF 3	α MF 2 ε MF 15 θ MF 14	α MF 15 ε MF 10 θ MF 1
	10	α MF 1 ε MF 8 θ MF 15	α MF 1 ε MF 8 θ MF 15	α MF 6 ε MF 11 θ MF 10	α MF 11 ε MF 14 θ MF 5	α MF 16 ε MF 1 θ MF 16	α MF 5 ε MF 4 θ MF 11	α MF 15 ε MF 10 θ MF 1
	11	α MF 1 ε MF 8 θ MF 15	α MF 4 ε MF 13 θ MF 12	α MF 9 ε MF 16 θ MF 7	α MF 14 ε MF 3 θ MF 2	α MF 3 ε MF 6 θ MF 13	α MF 8 ε MF 9 θ MF 8	α MF 15 ε MF 10 θ MF 1
	12	α MF 1 ε MF 8 θ MF 15	α MF 7 ε MF 2 θ MF 9	α MF 12 ε MF 5 θ MF 4	α MF 1 ε MF 8 θ MF 15	α MF 6 ε MF 11 θ MF 10	α MF 11 ε MF 14 θ MF 5	α MF 15 ε MF 10 θ MF 1
	13	α MF 1 ε MF 8 θ MF 15	α MF 6 ε MF 11 θ MF 10	α MF 11 ε MF 14 θ MF 5	α MF 16 ε MF 1 θ MF 16	α MF 5 ε MF 4 θ MF 11	α MF 10 ε MF 7 θ MF 6	α MF 15 ε MF 10 θ MF 1

Like the input membership functions, the output membership functions are all triangular. The output axis azimuth variable spans the range [0 360] degrees, the output axis coelevation angle spans the range [0 180] degrees, and the output rotation angle spans the range [0 180] degrees. All three degrees of freedom of each output membership function are capable of being modified by the optimization algorithm. However, the centroids of the output membership functions are constrained to lie within the output range to ensure that the centroid of the composite output membership function lies within the acceptable output range. Additionally, the width of the output membership functions is constrained to be less than or equal to the size of the range of the output linguistic variable. The centroid is calculated over the range [-180 540] degrees for the azimuth variable, over the range [-90 270] degrees for the coelevation variable, and over the range [-90 270] degrees for the rotation angle variable. An example of output membership functions consistent with this design is shown in Fig. 4-3.

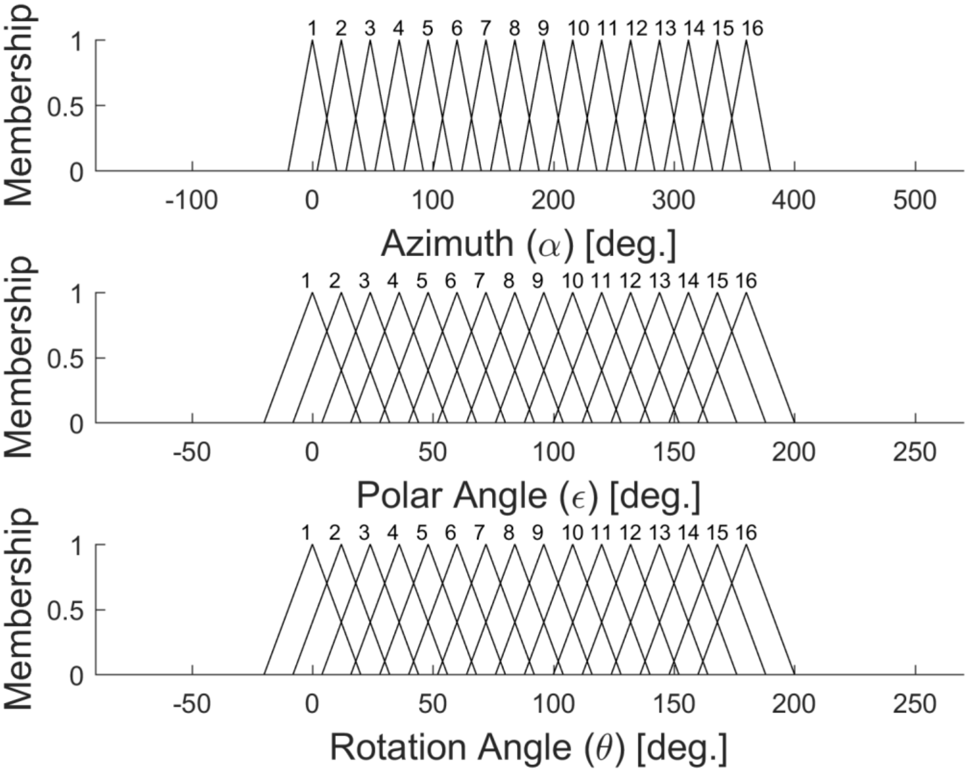

Fig. 4-3—Output membership functions for FIS consistent with constraints of optimal trajectory.

4.3 Fuzzy Output Filter

Though the FISs are theoretically in differentiability class C^0, they are implemented on a digital system, and due to program size and execution time constraints of this system, the FIS code was written such that the FIS outputs are eight-bit integers. Upon initial solution of the optimal attitude state trajectory problems, it was found that the eight-bit resolution was too coarse to prevent large jumps in attitude state, and these large jumps frequently resulted in violation of reaction wheel angular acceleration constraints. The solution was to add a filter to the output of the attitude state trajectory FIS to limit spacecraft attitude state accelerations to a range capable of being imparted by reaction wheel angular accelerations.

The filter begins by calculating the rotation, in the form of a quaternion, from the filtered orientation at the previous time step ($q_f(i-1)$) to the raw, unfiltered orientation at the next time step ($q_r(i+1)$), as shown in Eq. 4-3. This error quaternion (q_{err}) is then used in conjunction with the time difference between the previous time step and the next time step (Δt) to calculate the constant angular velocity required to get from the previous filtered orientation to the next unfiltered orientation (ω_{des}), as shown in Eq. 4-4. Note that, in order to calculate angular velocity with respect to an inertial frame, the quaternions must represent attitudes with respect to an inertial coordinate system. Also note that there are exactly two quaternions for each possible orientation (q and $-q$), and one of these quaternions corresponds to an axis-angle parameterization of the attitude with an equal or larger angle compared to the axis-angle parameterization associated with the other quaternion. In fact, the quaternion with positive real part ($q_0 > 0$) corresponds to the axis-angle parameterization with the smaller angle. Therefore, in practice, if $q_{err,0} < 0$, then the negative of the error quaternion is used in Eq.4-4.

$$q_{err} = \begin{bmatrix} q_{f,0}(i-1)q_{r,0}(i+1) + q_{f,1}(i-1) \cdot q_{r,1}(i+1) \\ q_{f,0}(i-1)q_{r,1}(i+1) - q_{r,0}(i+1)q_{f,1}(i-1) - q_{f,1}(i-1) \times q_{r,1}(i+1) \end{bmatrix} \tag{4-3}$$

$$\omega_{des} = \frac{2}{\Delta t}\cos^{-1}\left(q_{err,0}\right)\frac{q_{err,1}}{\|q_{err,1}\|} \tag{4-4}$$

The magnitude of the angular velocity calculated in Eq. 4-4 is also limited due to instabilities discovered during filter design. The instabilities were due to disturbance torques resulting from cross-coupling of the reaction wheel momentum with the spacecraft angular velocity, Eq. 4-5. It was found that the magnitudes of these disturbance torques was larger than what could be controlled by the reaction wheels.

$$-\left(\omega_b \times \left(I_w \omega_w\right)\right) \tag{4-5}$$

In order to ensure these reaction wheel disturbance torques are always smaller than what can be rejected by the reaction wheel control torque, an estimate of the worst-case magnitude is used in Eq. 4-6 to calculate an upper bound on spacecraft angular velocity. Taking $\dot{\omega}_{w,max} = 33\ RPM/s$ and $\omega_{w,max} = 7000\ RPM$ yields $\omega_{b,max} < 4.714 \times 10^{-3} rad/s$.

$$I_w \dot{\omega}_{w,max} > I_w \omega_{w,max} \omega_{b,max}$$
$$\omega_{b,max} < \frac{\dot{\omega}_{w,max}}{\omega_{w,max}} \tag{4-6}$$

After angular velocity is limited, the zero-order-hold (constant) spacecraft body angular acceleration ($\dot{\omega}_{des}$) required to change the filtered angular velocity at the previous time step (ω_f) to the desired angular velocity at the current time step (ω_{des}) is calculated using Eq. 4-7, and the corresponding reaction wheel angular acceleration is calculated using Eq. 4-8.

$$\dot{\omega}_{des} = \frac{2}{\Delta t}\left(\omega_{des} - \omega_f\right) \tag{4-7}$$

$$\dot{\omega}_w = I_w{}^{-1} I_b \dot{\omega}_{des} \tag{4-8}$$

The wheel acceleration is limited to the acceptable range and converted back to a body acceleration using the inverse of Eq. 4-8. The filtered attitude is then propagated forward in time using Eq. 3-4 and the linear change in angular velocity specified by the calculated zero-order-hold angular acceleration to the current time step, yielding a filtered attitude quaternion and angular velocity at the current time step. The time step is then incremented and the process repeated.

4.4 Genetic Algorithm

Genetic algorithms (GAs) are robust metaheuristic search methods which may be used for solving parameter optimization problems[53]. The parameters to be optimized are coded in strings of numbers, usually using binary digits but possibly using other bases[53]. A set of possible solutions is generated using the coding scheme, and the problem is evaluated using a fitness function which converts a coded string to a numerical value indicating the fitness of that particular solution. Solutions are selected to recombine with one another based on their fitness, with a small likelihood of random mutation, to produce the next generation of possible solutions. The best solutions may even be deliberately copied into the new generation, a process known as elitist selection, in order to increase likelihood of solution convergence or offset the effects of high mutation rate, which tends to lead to a longer time to find the solution[53]. The process is repeated from the solution evaluation step until the algorithm has converged on a solution.

According to Holland's Schema Theorem, or the Fundamental Theorem of Genetic Algorithms, convergence occurs because the schema, or set of stings with identical values at given positions, associated with more fit solutions and with short defining length tend to grow exponentially as a function of generation number[53]. Unfortunately, for very large problems, the number of possible schemata, including those of very large defining length, grows exponentially with string length whereas the number of usefully processed schemata per generation grows as the cube of the population size[53]. However, choosing clever groupings of string features, or genes, can effectively force the most important schemata to be of small defining length, though the best grouping of genes may not be obvious for a given problem[53]. Fortunately, genetic algorithms have been observed to be relatively robust to the choice of string parameterization[53]. Additionally, reordering operations have been developed to search for the best string ordering while simultaneously solving for the optimal set of feature values[53].

4.5 Attitude Trajectory Optimization

The attitude trajectory optimization problems were defined in section 3.2. In general, these problems contain constraints which restrict feasible solutions to a small region of the overall solution space. Constraints are not intrinsically handled by GAs, as the base algorithm just uses a fitness function to evaluate the performance of a particular solution. One method of dealing with constraints is to transform the constrained optimization problem into an unconstrained optimization problem by modifying the fitness function to penalize solutions which violate constraints[53]. Often, the penalty is incorporated into the fitness function by subtracting some positive-definite function (e.g. the square) of the amount by which the constraint is violated. This approach does not guarantee the GA will find a solution which satisfies all constraints. In fact, the constraints may be so restrictive that no point in the solution space satisfies all constraints. However, this approach does allow the GA to search for a feasible region of the solution space. Table 4-4 lists the relaxed-constraint attitude trajectory optimization problems which are modified versions of the constrained attitude trajectory optimization problems in section 3.2. The base, unconstrained objectives used in these relaxed-constraint problems are defined in Table 3-11, and the soft constraints are defined in Table 4-3. Note that the modified objective functions first seek to maximize the amount of simulated time over which the constraints are not violated, then seek the optimum of the true objective; the Kronecker delta functions, δ_{ij}, keep the contribution of the true objective equal to zero until all constraints are satisfied. This effectively forces the search into the feasible region, then to an optimum within the feasible region. Also, note that some of the modified optimization problems have been reformulated into maximization problems from the minimization problems posed in section 3.2 because GAs operate to solve for maxima of fitness or objective functions.

Table 4-3—Attitude trajectory optimization problem soft constraints..

Constraint Name	Constraint Definition
Electrical Power Storage	$\Phi_s(T) = \frac{1}{T}\int_{t=0}^{T} \phi_s(t)dt$ $\phi_s(t) = \begin{cases} 1 & C \geq 0.2C_{max} \\ 0 & C < 0.2C_{max} \end{cases}$
Communication Link Margin	$\Phi_c(T) = \begin{cases} 1 & \phi_c(t) \geq 1 \\ \phi_c(t) & \phi_c(t) < 1 \end{cases}$ $\phi_c(t) = \frac{1}{(50\%)} \frac{\int_{t=0}^{T} \psi_c(t)dt}{\int_{t=0}^{T} \psi_s(t)dt}$ $\psi_c(t) = \begin{cases} \psi_s(t) & G_{ant} \geq 5dB \\ 0 & G_{ant} < 5dB \end{cases}$ $\psi_s(t) = \begin{cases} 1 & \frac{\bar{d} \cdot R_G}{\lVert\bar{d}\rVert\lVert R_G\rVert} \geq 0.08716 \\ 0 & \frac{\bar{d} \cdot R_G}{\lVert\bar{d}\rVert\lVert R_G\rVert} < 0.08716 \end{cases}$
Reaction Wheel Speed	$\Phi_{w,\omega}(T) = \frac{1}{T}\int_{t=0}^{T} \phi_{w,\omega}(t)dt$ $\phi_{w,\omega}(t) = \begin{cases} 1 & \lVert\omega_w(t)\rVert \leq 6500\ RPM \\ 0 & \lVert\omega_w(t)\rVert > 6500\ RPM \end{cases}$
Reaction Wheel Acceleration	$\Phi_{w,\alpha}(T) = \frac{1}{T}\int_{t=0}^{T} \phi_{w,\alpha}(t)dt$ $\phi_{w,\alpha}(t) = \begin{cases} 1 & \lVert\dot{\omega}_w(t)\rVert \leq 33\ RPM/s \\ 0 & \lVert\dot{\omega}_w(t)\rVert > 33\ RPM/s \end{cases}$

Table 4-4—Attitude trajectory optimization problems with soft constraints.

Operational Mode	Optimization Problem
Emergency Power Generation	Maximize average electrical power storage, subject to reaction wheel constraints $\underset{q(t)}{\arg\max}\left(\bar{C}\Delta + \Phi_{w,\omega}(T) + \Phi_{w,\alpha}(T)\right)$ $\Delta = \delta_{(1)\left(\Phi_{w,\omega}(T)\right)}\delta_{(1)\left(\Phi_{w,\alpha}(T)\right)}$
Nominal Power Generation	Maximize average electrical power storage, subject to reaction wheel and antenna gain constraints $\underset{q(t)}{\arg\max}\left(\bar{C}\Delta + \Phi_{w,\omega}(T) + \Phi_{w,\alpha}(T) + \phi_c(T)\right)$ $\Delta = \delta_{(1)\left(\Phi_{w,\omega}(T)\right)}\delta_{(1)\left(\Phi_{w,\alpha}(T)\right)}\delta_{(1)(\Phi_c(T))}$
Power Positive Ground Station Tracking	Maximize average antenna gain, subject to reaction wheel and electrical power storage constraints $\underset{q(t)}{\arg\max}\left(\bar{G}_{ant}\Delta + \Phi_{w,\omega}(T) + \Phi_{w,\alpha}(T) + \Phi_s(T)\right)$ $\Delta = \delta_{(1)\left(\Phi_{w,\omega}(T)\right)}\delta_{(1)\left(\Phi_{w,\alpha}(T)\right)}\delta_{(1)(\Phi_s(T))}$
Nominal Ground Station Tracking	Maximize average antenna gain, subject to reaction wheel constraints $\underset{q(t)}{\arg\max}\left(\bar{G}_{ant}\Delta + \Phi_{w,\omega}(T) + \Phi_{w,\alpha}(T)\right)$ $\Delta = \delta_{(1)\left(\Phi_{w,\omega}(T)\right)}\delta_{(1)\left(\Phi_{w,\alpha}(T)\right)}$
Power Positive Science	Minimize average payload temperature, subject to reaction wheel and electrical power storage constraints $\underset{q(t)}{\arg\max}\left(\left(500K - \bar{T}_{payload}\right)\Delta + \Phi_{w,\omega}(T) + \Phi_{w,\alpha}(T) + \Phi_s(T)\right)$ $\Delta = \delta_{(1)\left(\Phi_{w,\omega}(T)\right)}\delta_{(1)\left(\Phi_{w,\alpha}(T)\right)}\delta_{(1)(\Phi_s(T))}$
Science with Ground Station Tracking	Minimize average payload temperature, subject to reaction wheel and antenna gain constraints $\underset{q(t)}{\arg\max}\left(\left(500K - \bar{T}_{payload}\right)\Delta + \Phi_{w,\omega}(T) + \Phi_{w,\alpha}(T) + \phi_c(T)\right)$ $\Delta = \delta_{(1)\left(\Phi_{w,\omega}(T)\right)}\delta_{(1)\left(\Phi_{w,\alpha}(T)\right)}\delta_{(1)(\Phi_c(T))}$
Science with Power Generation and Ground Station Tracking	Minimize average payload temperature, subject to reaction wheel, electrical power storage, and antenna gain constraints $\underset{q(t)}{\arg\max}\begin{pmatrix}\left(500K - \bar{T}_{payload}\right)\Delta + \\ \Phi_{w,\omega}(T) + \Phi_{w,\alpha}(T) + \Phi_s(T) + \phi_c(T)\end{pmatrix}$ $\Delta = \delta_{(1)\left(\Phi_{w,\omega}(T)\right)}\delta_{(1)\left(\Phi_{w,\alpha}(T)\right)}\delta_{(1)(\Phi_s(T))}\delta_{(1)(\Phi_c(T))}$
Nominal Science	Minimize average payload temperature, subject to reaction wheel constraints $\underset{q(t)}{\arg\max}\left(\left(500K - \bar{T}_{payload}\right)\Delta + \Phi_{w,\omega}(T) + \Phi_{w,\alpha}(T)\right)$ $\Delta = \delta_{(1)\left(\Phi_{w,\omega}(T)\right)}\delta_{(1)\left(\Phi_{w,\alpha}(T)\right)}$

The features encoded in the string used by the attitude trajectory optimization GAs are listed in Table 4-5 and Table 4-6. Table 4-5 is used for the optimization problems with single vector input FISs, and Table 4-6 is used for the optimization problems with dual vector input FISs.

Table 4-5—Genetic algorithm encoding of attitude trajectory FIS with only solar (or ground station) vector input.

Feature(s)	Representation	Total String Length
2 α_s Boundary Input Membership Function Locations	8 bit each	16 bit
11 α_s Input Membership Functions, 3 Locations Each	8 bit each	264 bit
2 ε_s Boundary Input Membership Function Locations	8 bit each	16 bit
5 ε_s Input Membership Functions, 3 Locations Each	8 bit each	120 bit
16 α_q Output Membership Functions, 3 Locations Each	8 bit center, 6 bit left, 6 bit right	320 bit
16 ε_q Output Membership Functions, 3 Locations Each	8 bit center, 6 bit left, 6 bit right	320 bit
16 θ_q Output Membership Functions, 3 Locations Each	8 bit center, 6 bit left, 6 bit right	320 bit
186 Rules	4 bit each	744 bit
Total	---	2,120 bit

Table 4-6—Genetic algorithm encoding of attitude trajectory FIS with solar and ground station vector inputs.

Feature(s)	Representation	Total String Length
2 α_s Boundary Input Membership Function Locations	8 bit each	16 bit
5 α_s Input Membership Functions, 3 Locations Each	8 bit each	120 bit
2 ε_s Boundary Input Membership Function Locations	8 bit each	16 bit
2 ε_s Input Membership Functions, 3 Locations Each	8 bit each	48 bit
2 α_g Boundary Input Membership Function Locations	8 bit each	16 bit

Feature(s)	Representation	Total String Length
5 α_g Input Membership Functions, 3 Locations Each	8 bit each	120 bit
2 ε_g Boundary Input Membership Function Locations	8 bit each	16 bit
2 ε_g Input Membership Functions, 3 Locations Each	8 bit each	48 bit
16 α_q Output Membership Functions, 3 Locations Each	8 bit center, 6 bit left, 6 bit right	320 bit
16 ε_q Output Membership Functions, 3 Locations Each	8 bit center, 6 bit left, 6 bit right	320 bit
16 θ_q Output Membership Functions, 3 Locations Each	8 bit center, 6 bit left, 6 bit right	320 bit
588 Rules	4 bit each	2,352 bit
Total	---	3,712 bit

The size of both solution spaces is very large: $2^{2120} \approx 1.53 \times 10^{638}$ possible solutions and $2^{3712} \approx 2.65 \times 10^{1117}$ possible solutions. However, the C^0 constraints on the input membership functions and range constraints on the output membership functions do reduce this search space slightly. The C^0 constraints on input membership functions are enforced by only allowing the portion of the string representing input membership functions for each input linguistic variable to represent a strictly increasing set of integers. The input range is further constrained so that at least one membership function and at most two membership functions are nonzero at each point in the range. The strictly increasing set of integers defining the membership functions then represent the following repeating pattern: (1) the leftmost edge (zero value) of the "next" membership function, (2) the rightmost edge (zero value) of the "previous" membership function, and (3) the center (value of one) of the "next" membership function. Output membership function constraints are defined to ensure the centroid of the composite output membership function is always within the specified output range. To ensure this, the average of the leftmost and rightmost edge locations of each output membership function is constrained to be within the output membership function range, and the centeroid of each output membership function is constrained to be within the output membership function range. Taken together, these constraints guarantee the output will always be within the specified range.

4.6 Reaction Wheel Momentum Dissipation

Reaction wheels are temporary momentum storage devices with a finite momentum capacity. They provide a means to manage excess momentum until an external torque, such as that from a thruster or a magnetorquer, can be applied to remove momentum from the system. Ideally, external torques would be used exclusively to orient the spacecraft. However, it may not be possible to generate an external control torque about the ideal rotation axis (e.g. magnetic control torques), or such control torques may be too large or uncontrollable to accomplish fine pointing (e.g. thruster torque). So reaction wheels are used to store this momentum until the external torque can feasibly be used to offload some of the stored momentum.

For the present work, a method of continuous reaction wheel momentum dissipation is used to help satisfy reaction wheel momentum storage constraints. A magnetic control torque is used to minimize reaction wheel angular velocity. The magnetic moment and reaction wheel angular acceleration are found via the optimization problem defined by Eq. 4-9, which is solved analytically here.

$$\begin{gathered}
\underset{\dot{\omega}_w(t),M}{\arg\min}\left(\omega_{w,x}^2+\omega_{w,y}^2+\omega_{w,z}^2\right)\\
\dot{\omega}_B = I_B^{-1}\left[-\omega_B\times\left(I_B\omega_B+I_{RW}\omega_{RW}\right)-I_{RW}\dot{\omega}_{RW}+\tau_{ext,dist}+M\times B\right]\\
u = -I_B^{-1}I_{RW}\dot{\omega}_{RW}+I_B^{-1}M\times B-I_B^{-1}\omega_B\times I_{RW}\omega_{RW}\\
u\ given\ by\ control\ law
\end{gathered}\tag{4-9}$$

Note that, because the reaction wheel angular velocities are all real valued numbers, this function should have one unique minimum; therefore, only the first derivative is required to find the solution. The general approach is to consider the control action over very short time scales.

Given that the magnetic field vector, B, the desired control torque, u, and the magnetic moment, M, are approximately constant over short time intervals, and the term $-I_B^{-1}\omega_B \times I_{RW}\omega_{RW} \approx 0$ is negligible, Eq. 4-10 holds over short time intervals.

$$\dot{\omega}_{RW} = -I_{RW}^{-1} I_B u + I_{RW}^{-1} M \times B \tag{4-10}$$

Integrating, over a short time interval and solving for the reaction wheel angular velocity at the end time yields Eq. 4-11.

$$\omega_{RW}(t_f) = \omega_{RW}(t_i) + I_{RW}^{-1}(M \times B - I_B u)(t_f - t_i) \tag{4-11}$$

The extrema of the cost function occur at the locations where the gradient of the cost function is zero. Solving for the gradient of the cost function at time t_f and setting equal to the zero vector yields Eq. 4-12.

$$\frac{\partial}{\partial m}\left(\omega_{w,x}^2 + \omega_{w,y}^2 + \omega_{w,z}^2\right) = 2\begin{bmatrix} \frac{\partial \omega_{RW,x}}{\partial m_1} & \frac{\partial \omega_{RW,y}}{\partial m_1} & \frac{\partial \omega_{RW,z}}{\partial m_1} \\ \frac{\partial \omega_{RW,x}}{\partial m_2} & \frac{\partial \omega_{RW,y}}{\partial m_2} & \frac{\partial \omega_{RW,z}}{\partial m_2} \\ \frac{\partial \omega_{RW,x}}{\partial m_3} & \frac{\partial \omega_{RW,y}}{\partial m_3} & \frac{\partial \omega_{RW,z}}{\partial m_3} \end{bmatrix} \begin{bmatrix} \omega_{RW,x} \\ \omega_{RW,y} \\ \omega_{RW,z} \end{bmatrix} = 2W\omega_{RW} = \begin{bmatrix} 0 \\ 0 \\ 0 \end{bmatrix} \tag{4-12}$$

From this equation, it is clear that the angular velocity vector exists in the null space of the W matrix, or, more formally, $\omega_{RW} \in \mathcal{N}(W)$. Considering time t_f, the vector quantities $\omega_{RW}(t_i)$ and $I_{RW}^{-1} I_B u(t_f - t_i)$ are known, and, in general, have components in both the null space and column space of W. Therefore, in order for the vector $\omega_{RW}(t_f)$ to exist in the null space of W, the quantity $I_{RW}^{-1}\, M \times B(t_f - t_i)$ must be in the column space of W. In fact, this quantity is $I_{RW}^{-1}\, M \times B(t_f - t_i) = WM$. Therefore, the magnetic moment vector M must exist in the column space of W unless $I_{RW}^{-1} I_B u(t_f - t_i)$ exists only in the null space of W, in which case $M = 0$. If the mass moment of inertia of each reaction wheel is identical, then I_{RW}^{-1} can be taken as a scalar value, and the null space of W is the magnetic field direction ($M \times B = 0$ when B is parallel to M). So, the minimum final reaction wheel angular velocity is given by Eq. 4-13, the optimal magnetic moment is given by Eq. 4-14, and the optimal reaction wheel acceleration can be calculated using Eq. 4-10.

$$\omega_{RW,min}(t_f) = \left(\omega_{RW}(t_i) - I_{RW}^{-1} I_B u(t_f - t_i)\right) \cdot \frac{B}{\|B\|} \tag{4-13}$$

$$M = \left(\omega_{RW}(t_i) - \omega_{RW,min}(t_f) - I_{RW}^{-1} I_B u(t_f - t_i)\right) \times \frac{B}{\|B\|^2} \frac{I_{RW}}{(t_f - t_i)} \tag{4-14}$$

5 Implementation

The spacecraft models, FISs, and GA optimization are all implemented in custom C/C++ code. This C/C++ architecture was chosen primarily because previous investigation determined that a C/C++ attitude control simulation program ran about 20 times faster than a similar MATLAB-based program, and both programs produced identical output up to rounding error. Performance similar to that of MATLAB is expected from other higher-level programming languages, such as Python. Furthermore, CryoCube-1's flight software is all written in C, so it was desirable to minimize the amount of code that needed to be rewritten between development and deployment on the flight computer. To be most compatible with the flight software while still taking advantage of the convenient object-oriented features of the C++ programming language, the optimization and spacecraft model code is primarily written in C++, and the attitude trajectory and control law code, including FISs, is written in C. This structure allows the C++-based GAs to directly optimize the C-based flight code.

The C-based FISs utilize 8-bit integer inputs, 8-bit integer outputs, and 8-bit integer representation of fuzzy membership values in order to minimize computational burden on the on-board microprocessor. However, this discretization inherently limits the resolution of the fuzzy systems as each input and output range can only evaluate to 256 unique values. Care is taken to ensure that this discretization does not prevent a feasible solution from being found for any of the optimization problems solved in this dissertation.

5.1 Flight Software Architecture

Prior to discussing how the methods presented in the previous chapter are used to find and encode optimal attitude state trajectories, it is informative to understand how this subtask of the attitude determination and control subsystem operates within the context of CryoCube-1's complete flight software package. CryoCube-1's attitude control subsystem code shares resources with its command and data handling (C&DH) subsystem as both are integrated into the main flight code which executes monolithically on a single microprocessor. Taken as a whole, the main flight code is responsible for gathering telemetry and experiment data, saving data and code execution information to data and log files, receiving ground commands from the radio, handling commands, sending data to the radio for transmission to the ground station, executing attitude determination and control algorithms, and controlling the EPS's switchable power sources. The main flight code and hardware on which it executes is best described as an embedded system which requires functionality to be built up from very low levels, controlling registers on the microprocessor to set up, enable, and perform communication with other electronic devices. Once the lower level functionality is established, the higher-level processes may be built upon it. Because those developing the software must work at many different levels of functionality, embedded systems development can be much more time-consuming than software development on other kinds of platforms.

For CryoCube-1, a Microchip Technology, Inc. (Microchip) dsPIC33FJ256GP710 microprocessor serves as the processor for the flight computer, colloquially referred to as the C&DH subsystem, which is a Pumpkin Space motherboard with pluggable processor module (PPM); the microprocessor resides on the PPM. CryoCube-1's team members at NASA KSC were primarily responsible for early work with this hardware, establishing the lowest levels of functionality and building many of the higher-level systems in CryoCube-1's code base. For the dsPIC microprocessor, the lowest levels of functionality are established by setting configuration bits, which are used to control oscillator frequency (needed to establish the correct frequency for communication), interrupts, timers, and register configurations, which control functionality of physical I/O pins on the microprocessor. Aside from simple digital or analog I/O, CryoCube-1's C&DH subsystem utilizes two Universal Asynchronous Receiver Transmitter (UART) busses and two Inter-Integrated Circuit (I^2C or I2C) busses, which are also controlled via register configuration, to communicate with the other electrical subsystems. These communication busses are set up by modifying configuration bits. One of the UART busses is used to communicate with CryoCube-1's radio to receive ground commands and send data. The other UART bus was used to send and receive information over USB, enabling debugging and other useful ground-based development and functionality testing. The I^2C busses are responsible for collecting data from and controlling all other electronic subsystems. This low-level architecture development is depicted in the "Low-Level Functionality" block in Fig. 5-1.

Once lower-level timing, interrupt, and communication bus functionality was established, higher-level functionality was developed. Each piece of higher-level functionality is built as its own software subsystem, consisting of the data structures and routines necessary to perform the tasks of the subsystem. For instance, the subsystem for receiving commands from the radio and sending data to the radio (C&DH in Fig. 5-1) is designed to interrupt normal program execution whenever the radio sends data over its UART bus; collect, process, and interpret data/commands sent by the radio; and transmit files saved on the satellite's SD card via the radio UART bus when a ground command to do so is received. The subsystem for storing and retrieving data from the SD card (Archive and Log System in Fig. 5-1) is designed to manage "archive" binary files, containing timestamped telemetry data, and "log" binary files, containing timestamped

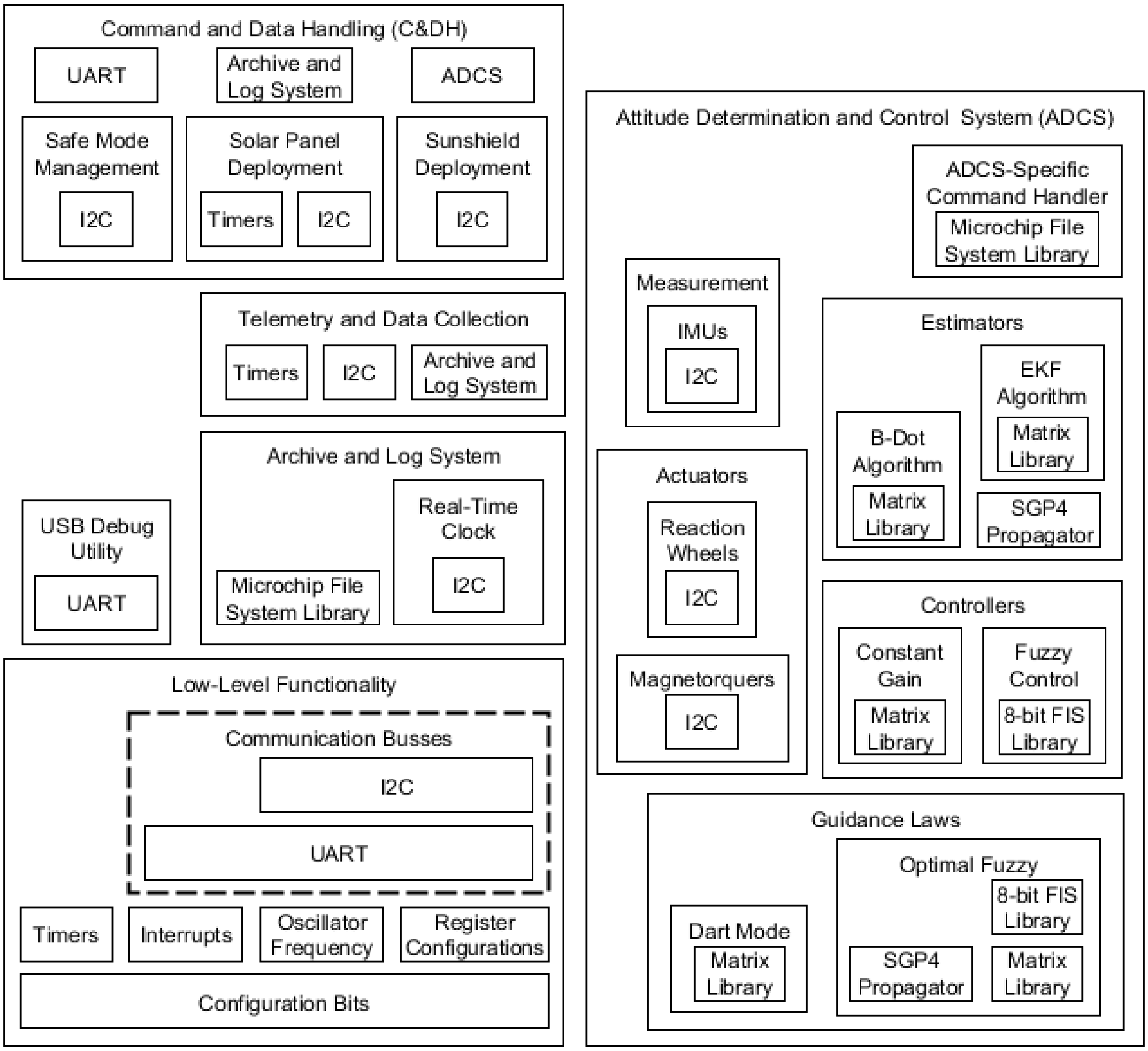

Fig. 5-1—CryoCube-1 flight software is built from low-level microprocessor functionality to high-level mission functionality.

information on major system events (e.g. reset conditions, deployments, etc.), providing a high-level functional interface used by the C&DH software subsystem and telemetry collection subsystems for writing, saving, reading, and deleting data. The subsystem for receiving debug commands and printing debug information via USB (USB Debug Utility in Fig. 5-1) is designed to interrupt normal program execution whenever data is received on its UART bus and immediately send the requested information back through the UART bus. The subsystem for collecting telemetry and experiment data from all electrical subsystems (Telemetry and Data

Collection in Fig. 5-1) is designed to automatically and periodically request a pre-defined set of information from each subsystem via the I2C busses and record this data in telemetry binary files via the functional interface of the SD card data storage subsystem. The software subsystem for managing spacecraft power usage (Safe Mode Management in Fig. 5-1) is designed to command the EPS (via an I2C bus) to turn on and off a set of switched lines which are not essential for keeping the spacecraft operating in the event the battery telemetry indicates its voltage is too low, effectively putting the spacecraft into a safe mode; safe mode is activated either automatically or via ground command and can only be deactivated via ground command. The software subsystems for deploying solar panels (Solar Panel Deployment in Fig. 5-1) and the sunshield (Sunshield Deployment in Fig. 5-1) are designed to automatically turn on and off sets of switched lines on the EPS which power the deployment circuits; solar panel deployment utilizes a timer to automatically deploy 30 minutes after flight software begins running and both solar panels and the sunshield can be deployed via ground command.

One of the more complicated software subsystems implemented in CryoCube-1's flight software is the attitude determination and control software subsystem. Like the other higher-level software subsystems, the attitude control software utilizes the lower-level I^2C busses to communicate with and control the reaction wheels, magnetorquer current drivers, and IMUs. However, unlike the other software subsystems, the attitude control subsystem utilizes a relatively large number of algorithms requiring floating point operations. Many of the algorithms utilize a compact, custom-developed matrix and vector math library, which provides common matrix and vector functions such as addition, subtraction, multiplication, and inversion. This functionality is vital for operation of CryoCube-1's EKF estimation and constant gain full state feedback control algorithms. The attitude control software also utilizes a custom-developed eight-bit integer fuzzy inference system library which is used in the fuzzy attitude modes of operation to propagate the desired attitude profile which the spacecraft can track and is used in the fuzzy full state feedback controller algorithm, which can be selected alternately with the constant gain matrix controller. The attitude control software also includes an SGP4 propagator[‡] which utilizes an on-board TLE to propagate orbit position and velocity as a function of time; both position and velocity are vital in calculating reference coordinate systems utilized in determining the desired attitude state and estimating the spacecraft's actual attitude state. A command interface also gives ground operators the ability to modify parameters used by the attitude control system, including: the state machine state, the TLE used for orbit propagation, the feedback gain matrix used for constant gain full-state feedback control, the fuzzy inference systems used for control and desired state trajectory definition, and EKF parameters (e.g. initial state estimate, covariance estimates, etc.).

On top of the estimation and control functions, CryoCube-1's attitude control software subsystem utilizes a finite state machine to define attitude control modes of operation and define the sequence of tasks to perform within each mode of operation (i.e. the control loop). Each timer-driven control loop task sequence includes measurement, estimation, mode transition criteria decision-making, and actuation, as shown in the control mode pseudocode in Fig. 5-2. Several unique states within the overall state machine do not define modes of operation but instead serve specific purposes, such as ensuring reaction wheels and magnetorquers stop actuating and the EKF is properly restarted when the ADCS runs into an issue and must reset. Fig. 5-3 shows the modes of operation and mode transitions CryoCube-1's ADCS uses during its operation. The system starts with Detumble, using the B-dot algorithm, automatically starting the EKF while still applying the B-dot control algorithm (in EKF Restart and EKF Start states) once estimated magnetic field time

---

[‡] https://www.celestrak.com/software/vallado/cpp.zip

derivative falls below a pre-set threshold value. When the magnetic field time derivative falls below another, lower threshold value, indicating the spacecraft is no longer tumbling, the ADCS enters its Dart mode, in which the spacecraft –X-axis (antenna face) points nadir and its –Z-axis is in the direction of spacecraft velocity, effectively flying "like a dart." The Dart mode is divided into "start" and nominal modes. The Start mode is effectively a slew mode, allowing for a potentially large-angle maneuver from the orientation at the end of Detumble to the final Dart orientation. Both start and nominal modes use either a constant-gain full-state feedback controller or a fuzzy full-state feedback controller (selectable via ground command) to determine control torques to be applied. A Fuzzy ADCS mode, similar to the Dart mode, is also available via ground command. This Fuzzy mode uses a FIS to define the attitude state trajectory and is the mode in which the optimal state trajectories calculated in this work may be achieved. The FIS is modifiable via ground command, so different optimal trajectories can be uploaded. The Fuzzy mode was designed to be optional as a means to reduce mission risk; the simpler Dart mode was determined to be a more conventional and therefore safer operational mode. However, once the primary mission is achieved, the Fuzzy mode may be employed. The ADCS also has a wheel desaturation mode to gradually slow, then stop reaction wheels and restart the Detumble algorithm in the event adequate full-state feedback control is lost. A Safe Mode, which stops all measurement and control, is used to conserve as much spacecraft power as possible, in the event the battery charge becomes critically low.

```
While( True )
    Stop_Actuation(); // turn of magnetorquers and keep wheels at constant velocity
    Measurements = Take_Measurements();
    State_Estimate = Estimate_State( Measurements );
    If( This_Mode.applicable )
        Desired_State = Apply_Guidance_Law();
    End If
    Next_Mode = Mode_Transition_Decision( State_Estimate );
    If( Next_Mode != This_Mode ) // if transitioning modes, skip actuation
        This_Mode = Next_Mode;
    Else // otherwise, apply feedback control
        Control = Calculate_Control( State_Estimate, Desired_State);
        Actuate( Control ); // use magnetorquers and/or reaction wheels
    End If
End While
```

Fig. 5-2—Pseudocode for generic ADCS mode.

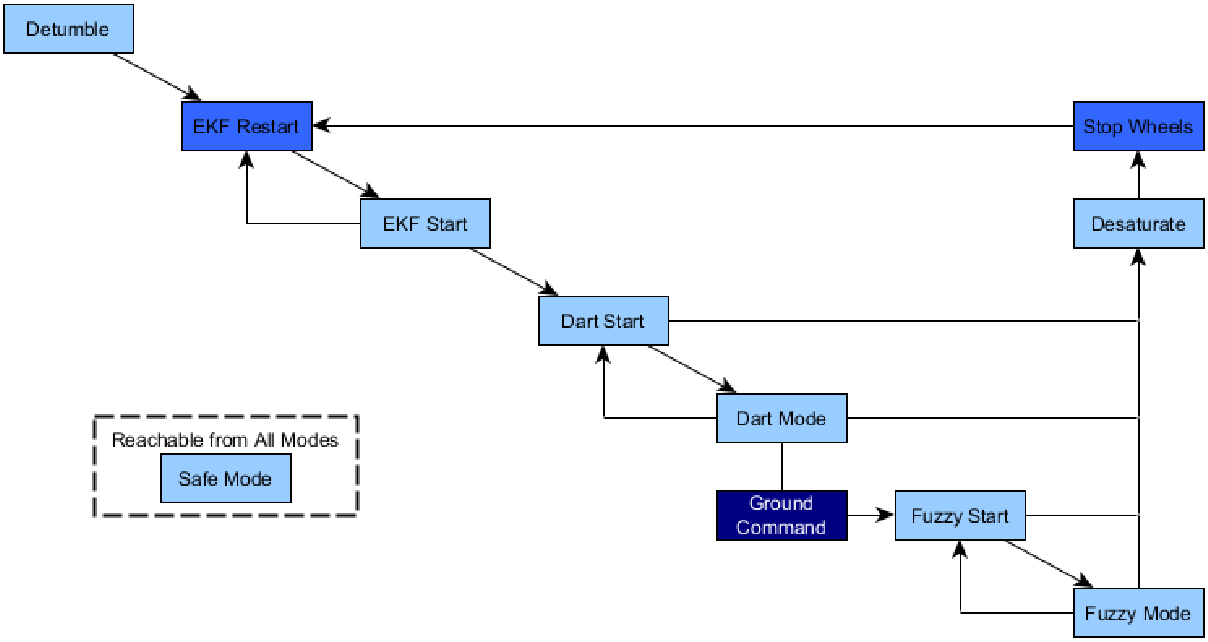

Fig. 5-3—CryoCube-1's attitude mode state transition diagram.

The main function of the flight software first initializes all software subsystems, then runs through a non-terminating loop, the main loop, containing tasks which the spacecraft flight software executes for the remainder of its mission. Every software subsystem, except for the debug utility, has one or more event handler functions which execute sequentially in the main loop. Each event handler function is designed to minimize the amount of time any one software subsystem has control over the main loop. This ensures time-critical tasks, such as transmitting data to the radio or measuring, estimating, and applying control do not get stuck waiting on other less-time-critical tasks, such as telemetry collection, or on each other. Effectively, by "freeing up the loop," each software subsystem is able to more easily execute tasks it needs to execute as close as practical to the time it needs to execute them.

```
While( True ) // Loop forever
    Process_C&DH_Transmit_Events();
    Process_C&DH_Receive_Events();
    Process_EPS_Telemetry_Events():
    Process_Battery_Telemetry_Events();
    Process_Reaction_Wheel_Telemetry_Events();
    Process_Experiment_Data_Collection_Events();
    Process_Magnetorquer_Telemetry_Events();
    Process_Deployment_Circuit_Telemetry_Events();
    Process_Attitude_Control_System_Events();
    Process_Auto_Deploy_Events();
    Process_Safe_Mode_Events();
    Process_File_System_Events();
End While
```

Fig. 5-4—Pseudocode for CryoCube-1 flight software's main loop.

5.2 Trajectory Optimization

The trajectory optimization problems are solved using genetic algorithms as discussed in section 4.5. Parameters for the GAs used to solve the trajectory optimization problems are found in Table 5-1, and the general procedure for calculating fitness of an attitude trajectory FIS is shown in Fig. 5-5. Attitude trajectory fitness evaluation starts with orbit propagation to calculate time histories of satellite position and velocity using the SGP4 algorithm discussed in section 3.1.2. Using position, velocity, and time, the magnetic field vector, sun vector, and ground station vector are calculated in terms of the local-level coordinate system shown in Fig. 5-6; this is the reference coordinate system from which the candidate optimal attitude is defined (note that it differs from

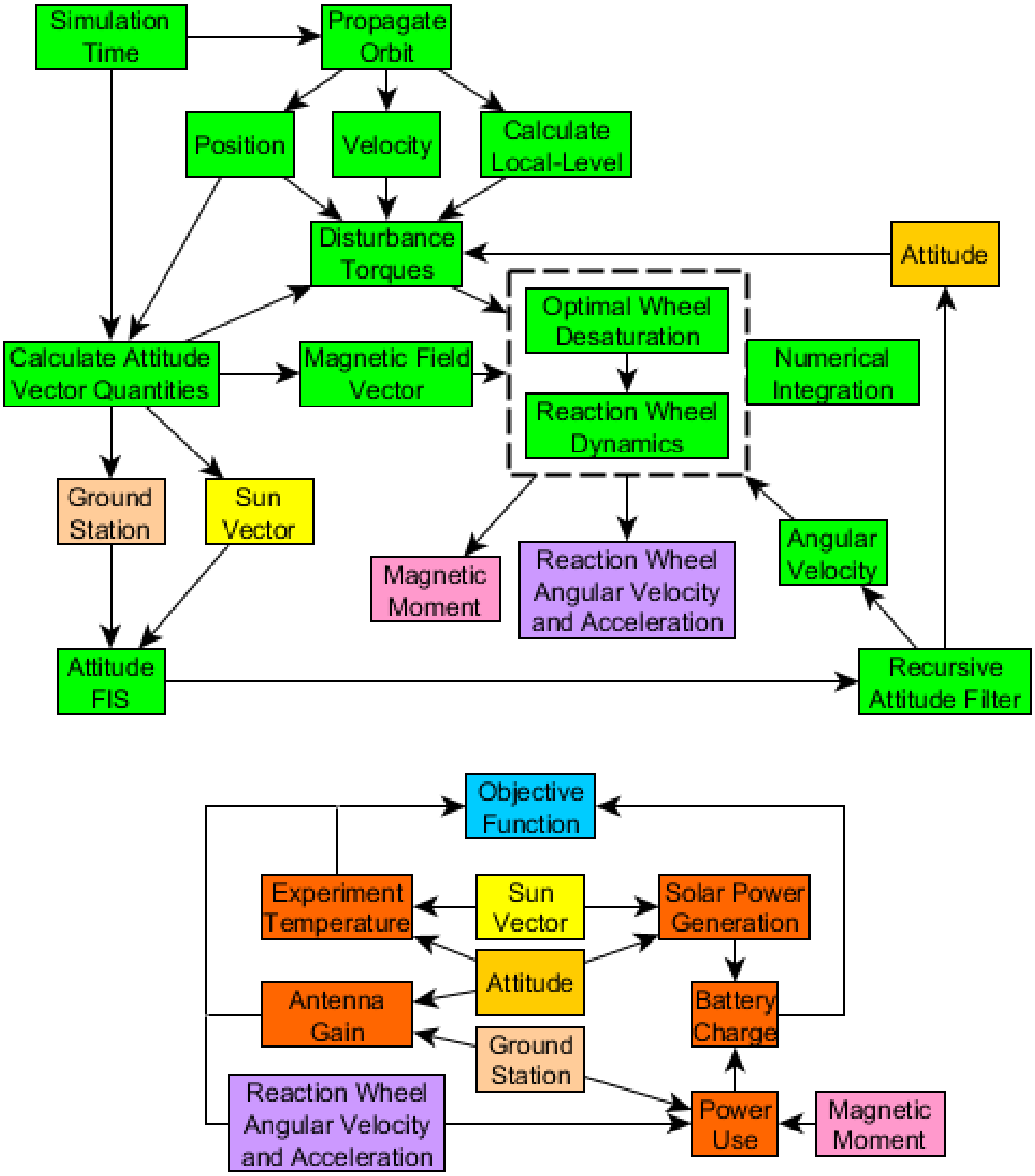

Fig. 5-5—Attitude state trajectory optimization objective function evaluation block diagram.

the LVLH coordinate system described in section 3.1.1). The sun vector and/or ground station vector are then used as inputs to the attitude trajectory FIS to calculate an attitude with respect to the local-level coordinate system. This attitude is then used as input to the recursive filter described in section 4.3, which outputs an attitude quaternion and angular velocity state trajectory which is capable of being realized with the given reaction wheel angular acceleration constraints.

Table 5-1—Optimization problem GA parameters.

GA Parameter	Value
Population Size	30
String size	2,120 (2 inputs) or 3,712 (4 inputs)
Selection Type	Tournament
Tournament Size	5
Crossover Probability	0.7
Mutation Probability	0.0005
Convergence	25 generations w/ unchanged optimum
Maximum Generations	1,000

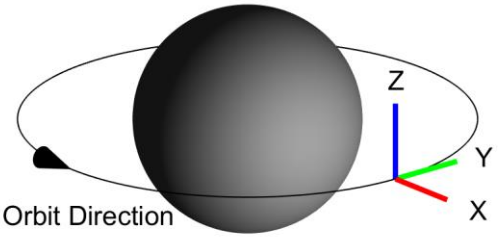

Fig. 5-6—This local-level coordinate system is used as the reference coordinate system in which sun and ground station vectors input to optimal state trajectory FISs are defined. Attitude quaternions output from the FISs are also defined with respect to this reference coordinate system.

Once the filtered candidate optimal attitude state trajectory is computed, the velocity vector, magnetic field vector, and spacecraft position vector, all expressed in the candidate optimal attitude coordinate system, are used with the geometry and mass properties of the spacecraft to calculate disturbance torques the spacecraft would experience in this orientation using the models in section 3.1.3.1. This information is then used in the algorithm discussed in section 4.6 to calculate the magnetic moment which optimally desaturates reaction wheels. External torques, the magnetic control torque, and candidate attitude angular velocities are then used to solve for reaction wheel angular accelerations, which are in turn used in a numerical integration algorithm to solve for reaction wheel angular velocities. Once time histories of spacecraft attitude, reaction wheel angular velocities, reaction wheel angular accelerations, magnetorquer actuation, sun vector, and ground station vector are calculated, the models in sections 3.1.5, 3.1.6, and 3.1.7 are evaluated to determine spacecraft battery charge, antenna gain, and experiment temperature time histories. With this information, one of the fitness functions in Table 4-4 is evaluated.

In order to ensure the optimal FISs found by the genetic algorithm will be valid for the range of the inputs the spacecraft will experience in its operational lifetime while maintaining a reasonable solution time, the sun vector and ground station vectors were analyzed over an extended period of time. First, the sun vector was considered in the local-level coordinate system. In low earth orbit, a spacecraft takes about 92 minutes to revolve one time about the earth; therefore, the local-level coordinate system in Fig. 5-6 takes about 92 minutes to spin one time about its Z-axis, which means the full range of azimuth angles of the sun vector, which remains relatively constant over this time interval, is experienced in this 92-minute period. The sun vector elevation angle in the local-level coordinate system remains nearly constant over this same time period. However, taking an orbit about the earth with fixed orientation in inertial space and moving its center about the sun, as the orbit moves with the earth, it is clear the sun elevation angle in the local-level coordinate system, whose X-Y-plane is the orbit plane, does change very slowly over time, similar to the way the sun elevation as viewed from the surface of earth varies seasonally. Therefore, it should be expected that the sun vector elevation angle should reach a maximum value equal to the sum of earth's obliquity (axial tilt, about 23.4°) and the orbit inclination (about 51.6°), or vary over the range ±74.0°. Fig. 5-7 shows how the sun elevation angle in the local-level coordinate system varies over the course of a year. Note that there are short-period oscillations, on the order of about two months, due to precession of the orbit plane, which cause the variation in elevation to occur more quickly. Clearly, the simulation used to find optimal attitude trajectories should use a good sampling of this sun elevation range to find optimal trajectories.

Instead of simulating a full year worth of orbit and attitude for each evaluation of the fitness function, a sampling approach was used to save computation time. Evaluation of a simulated year using the custom C/C++ optimization program developed for this work is estimated to take one to two days per GA generation, or as much as 5.5 years to solve one optimization problem (if the limit of 1000 generations were reached)[§]. Instead, twenty periods, each 100 minutes long and uniquely identified by their start epoch, were selected to be evaluated as part of the objective function. The initial spacecraft conditions at each start epoch are identical, and objective functions are evaluated by clipping the time between start epochs, effectively concatenating time histories of state variables used to calculate objective functions. Evaluation of the sampled time periods takes five to fifteen minutes per GA generation, or as long as about a week to solve one optimization problem.

[§] The program does not take advantage of multi-threading and was primarily run using the Windows 10 OS on a Dell Inspiron 15 7000 series laptop with an Intel® Core™ i7-7500 CPU (at 2.70 GHz) and 16.0 GB RAM.

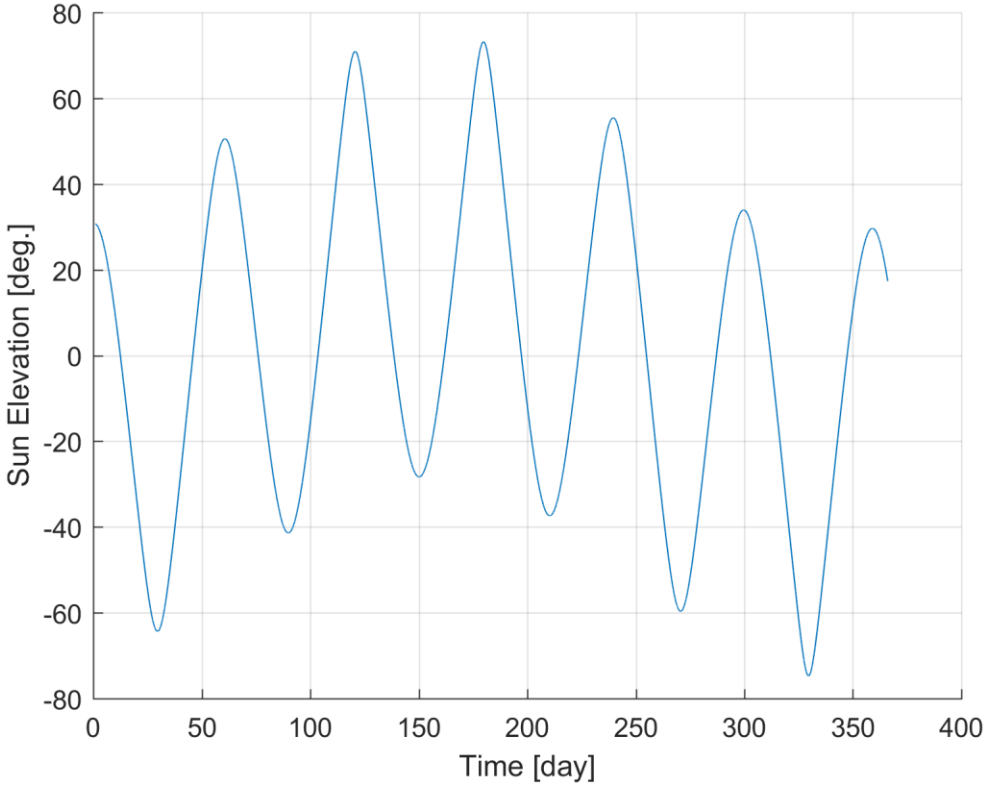

Fig. 5-7—The sun elevation angle, as viewed in the local-level coordinate system, varies both annually and as a function of shorter-term precession of the orbit plane.

The epochs were selected from the period of time about 30 days after TLE epoch to about 60 days after TLE epoch; the sun elevation angle during this time period is shown in Fig. 5-8. Though not all of the possible sun elevation angles attained through the year are attained in this time period, this time period does contain a representative sample of the elevations the sun vector will attain over the majority of the mission, and only about 15-20° are omitted from either extreme of the chosen range of elevations.

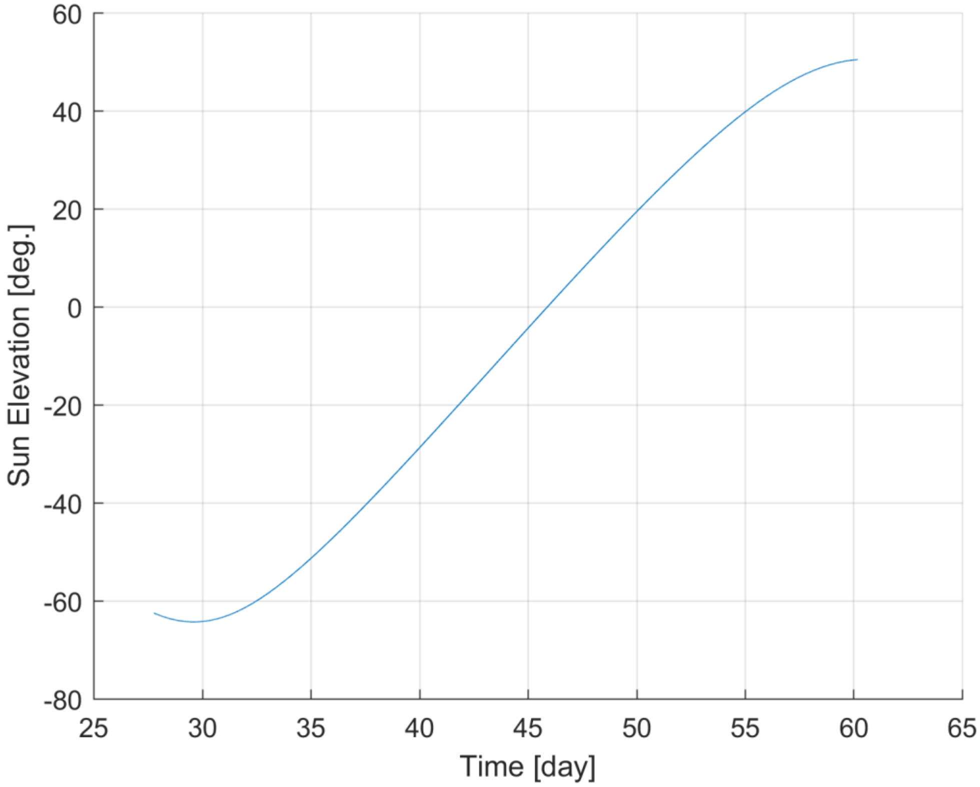

Fig. 5-8—The sun elevation angle, as viewed in the local-level coordinate system, over the time period used to select simulation start epochs.

In addition to the sun vector azimuth and elevation parameters, ground station vector azimuth and elevation parameters are also critical in selecting appropriate start epochs for the simulations used to find optimal attitude state trajectories. With just one ground station, the number of orbits which include a ground station pass is limited to about three per day with many of these being very low-elevation, short-duration passes with little practical communication use. Fig. 5-9 shows the co-elevation of the spacecraft with respect to the ground station, demonstrating the scarcity of relatively high-elevation ground station passes over the approximately 30-day period from which start epochs are chosen. Fig. 5-9 also shows that higher-elevation ground station passes tend to occur in clusters, rather than being equally spaced through time. The twenty lowest co-elevations simulated over this time interval are circled in magenta. For simulations used in optimizing attitude profile FISs with ground station parameter inputs, start epochs were chosen such that these minimum co-elevation values occurred halfway through the simulation period.

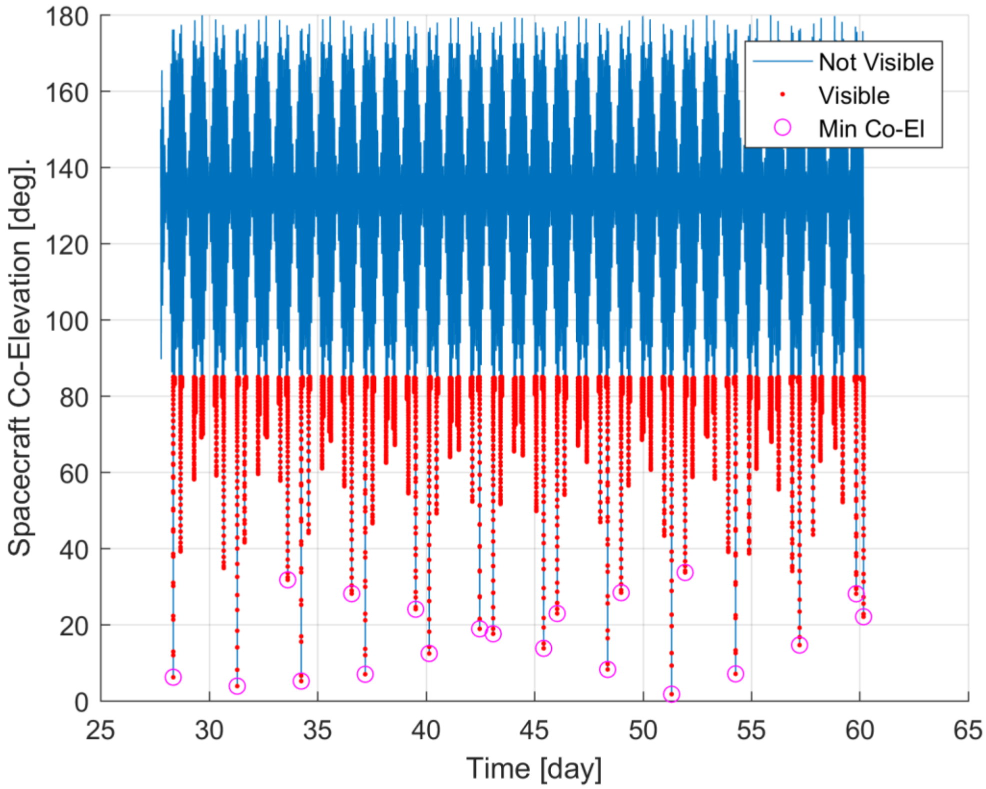

Fig. 5-9—The co-elevation of the spacecraft with respect to the ground station (angle between ground station zenith and ground-station-to-spacecraft vector) is rarely below 85 degrees, leaving few orbit periods over which the ground station is visible.

For simulations used in optimizing attitude profile FISs without ground station parameter inputs, start epochs were chosen to be equally spaced over the 30-day time interval in order to maximize the number of unique sun elevations evaluated. Orbit parameters, taken from a RaInCube CubeSat TLE published in early 2019, are shown in Table 5-2. As mentioned previously, this is the TLE used to simulate CryoCube-1's orbit. The second column of Table 5-3 lists the start epochs (in terms of seconds after spacecraft TLE epoch) used for optimizing FISs with only sun vector parameter inputs, and the third column of Table 5-3 lists start epochs used for optimizing FISs with ground station vector parameter inputs.

Table 5-2—Simulation orbit parameters are taken from the RaInCube TLE published on January 17, 2019.

Parameter	**Value**
Epoch	January 17, 2019, 05:24:15.032736 UTC
Right Ascension	29.0526 deg.
Inclination	51.6391 deg.
Argument of Perigee	289.1017 deg.
Eccentricity	0. 0005133
Mean Anomaly	70.9419 deg.
Mean Motion	15.57816634 revolutions per day

Table 5-3—Simulation start epochs occur within a window approximately 30–60 days after the TLE epoch

Pass #	**Start Epochs — Problems with Sun Vector Parameters Only (seconds since TLE epoch)**	**Start Epochs — Problems with Ground Station Vector Parameters (seconds since TLE epoch)**
1	2,592,000	2,446,970
2	2,721,600	2,701,830
3	2,851,200	2,902,920
4	2,980,800	2,956,690
5	3,110,400	3,157,770
6	3,240,000	3,211,530
7	3,369,600	3,412,600
8	3,499,200	3,466,360
9	3,628,800	3,667,430
10	3,758,400	3,721,190
11	3,888,000	3,922,250
12	4,017,600	3,976,000
13	4,147,200	4,177,050
14	4,276,800	4,230,810
15	4,406,400	4,431,850
16	4,536,000	4,485,600
17	4,665,600	4,686,640
18	4,795,200	4,941,420
19	4,924,800	5,166,930
20	5,054,400	5,196,190

6 Results & Discussion

The eight attitude state trajectory optimization problems presented in section 4.5 were solved using the approach presented in section 5.2. The performance of these optimal state trajectories is then compared to the performance of the nominal operation "Dart" mode introduced in section 5.1. While it is shown that Dart mode is suitable for achieving the goals of the CryoCube-1 mission, it is also shown that each optimized state trajectory clearly outperforms Dart mode with respect to the objective of optimization. The results of individual optimal trajectories are briefly discussed and compared. The performance of all optimal attitude profile FISs is demonstrated by plotting spacecraft state information over a representative orbit period. For FISs with only sun vector parameter inputs, this orbit period is taken to be Pass #6 as defined in Table 5-3, and for FISs with ground station parameter inputs, this orbit period is taken to be Pass #17 as defined in Table 5-3.

6.1 Objective 1: Emergency Power Generation

The optimal attitude profile FIS for the "Emergency Power Generation" objective was found by the GA in 273 generations, taking 22 hours 45 minutes, or an average of five minutes per generation to solve. The optimal FIS has an objective function value of 1126.8[**]. Examining Fig. 6-1 and Fig. 6-2 clearly shows that battery charge decreases during periods of eclipse (the period of time when no solar power is generated) and when the transceiver turns on for a ground station pass, as the total power use exceeds total power generated during both of these periods. Fig. 6-3 shows that the solar panels, especially the +X and –Y panels, point mainly toward the sun as one

---

[**] Not accounting for the lack of power generation during eclipse, this objective has a maximum theoretical value of 1202.0 as maximum battery charge is 1200 mA·h and there are two reaction wheel constraints, each with a maximum value of 1.0.

would expect at least one solar panel to point toward the sun to maximize power generation. Fig. 6-4 shows that the filter presented in section 4.3 successfully keeps reaction wheel angular acceleration within the 33 RPM/s limits, and Fig. 6-5 shows that the wheel angular velocity stays within about 10% of the maximum rated reaction wheel angular velocity of 7500 RPM. The wheels do tend to relatively frequently reverse spin direction, crossing through zero angular velocity, which can be an issue for some applications, because reaction wheels can have a large static friction which results in abrupt stopping around zero angular velocity which can, in turn, induce structural vibrations which can induce jitter in optical systems. However, CryoCube-1 has no optical systems, so frequent zero crossings are not an issue. For applications in which pointing of optical systems is critical, zero crossings could be reduced by biasing the reaction wheel momentum away from zero angular velocity. Fig. 6-6, Fig. 6-7, Fig. 6-8, Fig. 6-9, and Fig. 6-10 show the input and output membership functions of the optimal attitude profile FIS. Almost all of these membership functions are used in at least one of the passes defined in Table 5-3 with the notable exception of input sun vector elevation, which is limited to the range ±74.0° as discussed in section 5.2.

Fig. 6-11 shows the time-dependent spacecraft attitude with respect to the reference local-level coordinate system and the local-level-referenced celestial sphere with projected images of the earth, sun, and ground station location. During eclipse, the spacecraft appears to align its body-fixed axes with the reference coordinate system, making a move at about 2000 s simulation time in preparation for the sunrise. While in sunlight, the solar panels appear to roughly track the sun position, confirming observations with respect to Fig. 6-3, with some dramatic reorientation which effectively minimizes reaction wheel angular velocity, according to Fig. 6-5, at about 5000 s simulation time.

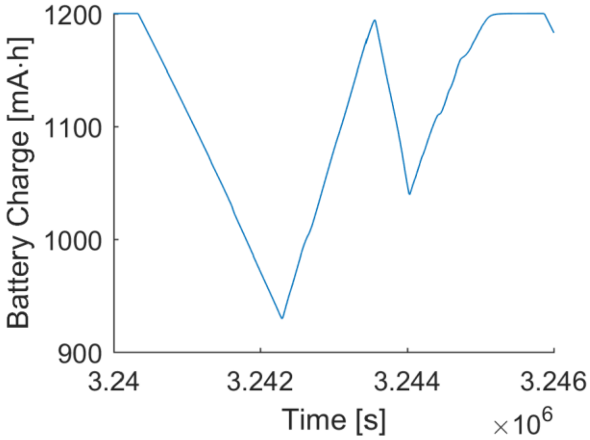

Fig. 6-1—Battery charge time history for Objective 1, Pass 6 optimal attitude profile. Battery charge decreases during eclipse and ground station transmission.

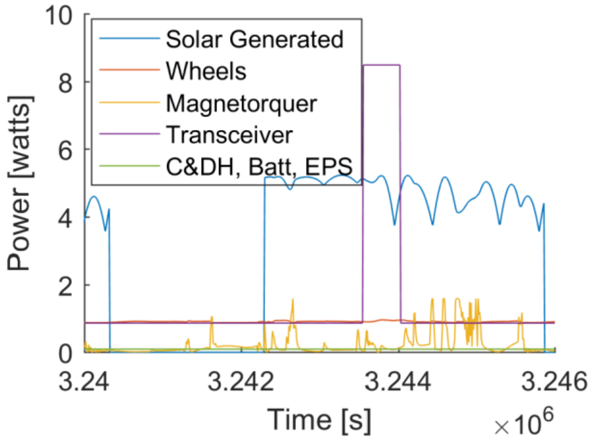

Fig. 6-2—Power use and generation for Objective 1, Pass 6 optimal attitude profile. Solar power generation drops to zero during eclipse and transceiver power demand spikes during ground station pass.

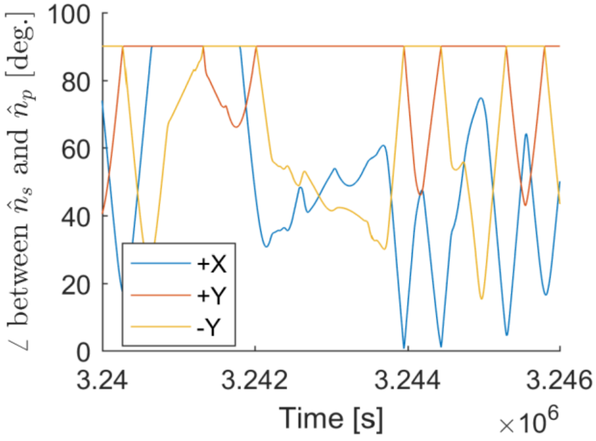

Fig. 6-3—Solar panel normal to sun vector angles for Objective 1, Pass 6 optimal attitude profile. The +X and –Y solar panels track the sun when not in eclipse.

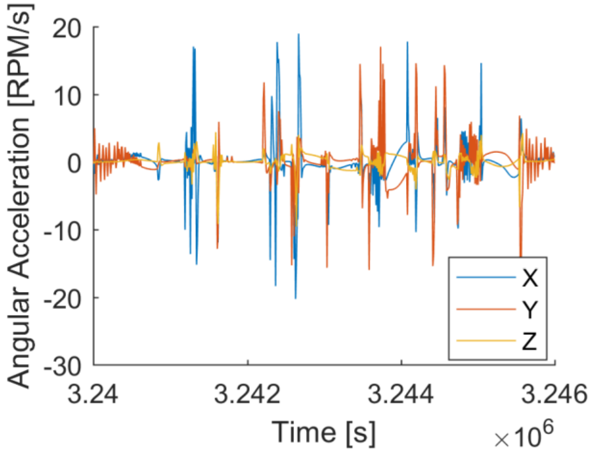

Fig. 6-4—Reaction wheel angular acceleration for Objective 1, Pass 6 optimal attitude profile.

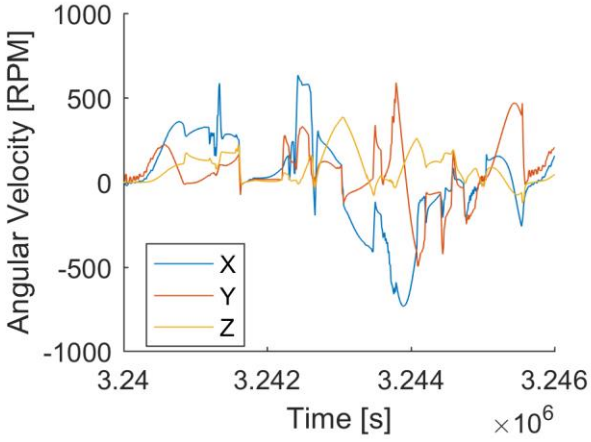

Fig. 6-5—Reaction wheel angular velocity for Objective 1, Pass 6 optimal attitude profile.

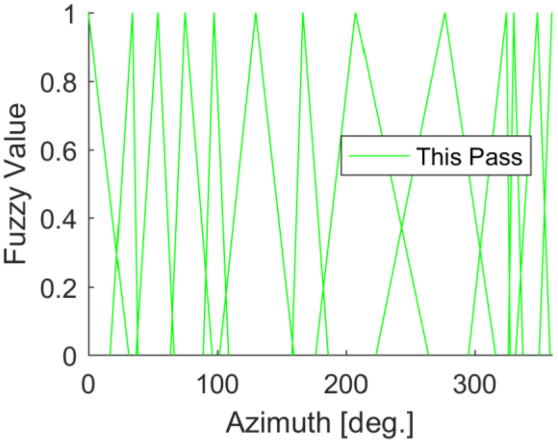

Fig. 6-6—Sun vector azimuth input membership functions for Objective 1 optimal attitude profile FIS. The FIS uses all sun vector azimuth input MFs during Pass 6.

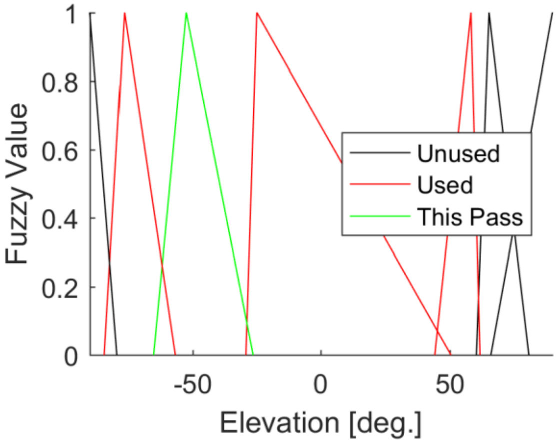

Fig. 6-7—Sun vector elevation input membership functions for Objective 1 optimal attitude profile FIS. The FIS only uses four of these MFs, and only one for Pass 6.

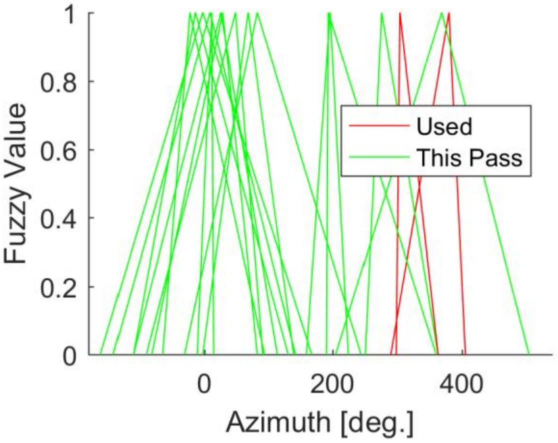

Fig. 6-8—Axis-angle axis azimuth output membership functions for Objective 1 optimal attitude profile FIS. All output MFs are used by the FIS, but two are not used for Pass 6.

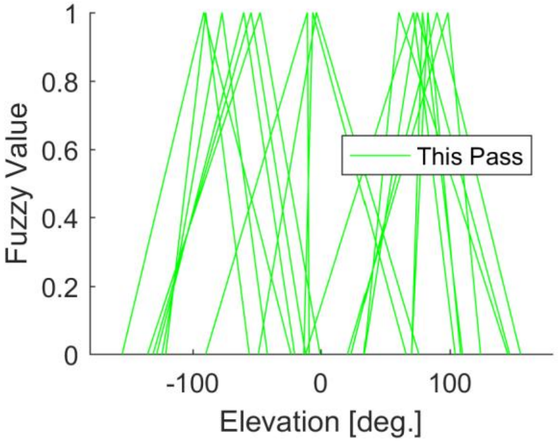

Fig. 6-9—Axis-angle axis elevation output membership functions for Objective 1 optimal attitude profile FIS. All output MFs are used by the FIS for all passes.

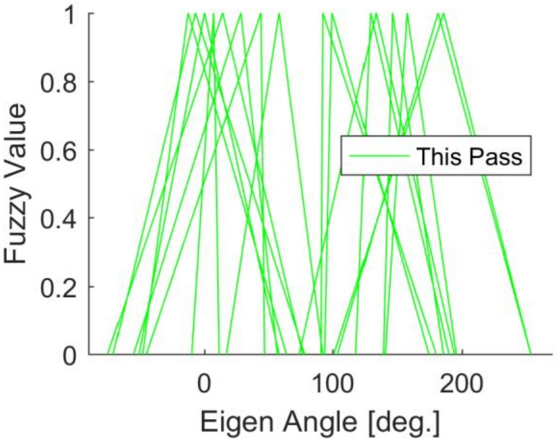

Fig. 6-10—Axis-angle angle output membership functions for Objective 1 optimal attitude profile FIS.

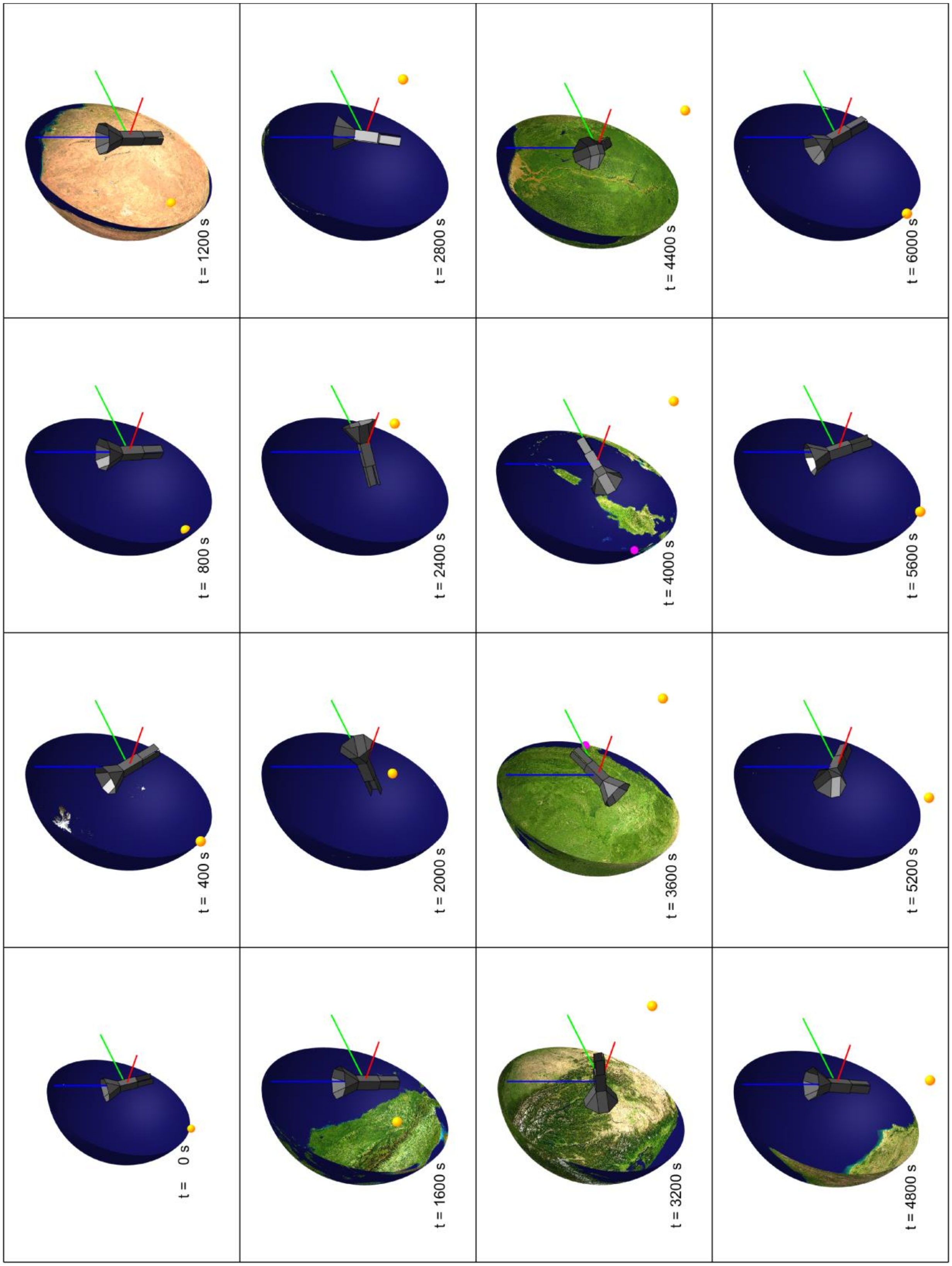

Fig. 6-11—The spacecraft Objective 1, Pass 6 orientation with respect to the reference coordinate system (red X, green Y, blue Z) is shown with the earth, sun (yellow sphere), and ground station (magenta sphere) projected on the celestial sphere.

6.2 Objective 2: Nominal Power Generation

The optimal attitude profile FIS for the "Nominal Power Generation" objective was found by the GA in 278 generations, taking 68 hours 59 minutes, or an average of 14 minutes 53 seconds per generation to solve. The optimal FIS has an objective function value of 939.7[††], indicating this solution is significantly worse at keeping the battery charged than optimal solution found for Objective 1. Fig. 6-12 shows that, for nearly the entire simulated duration of Pass #17, the battery charge decreases, and, at times, decreases dramatically. Fig. 6-13 shows why: much of the decrease is due to the fact that no power is generated during eclipse, and almost immediately after eclipse, the transceiver turns on for a ground station pass, draining the battery further. Furthermore, after the ground station pass, Fig. 6-14 shows that the spacecraft still does not orient its solar panels in a way that maximizes power generation, instead allowing two separate instances where power generation drops close to zero. During the ground station pass, Fig. 6-15 indicates that the spacecraft is generally able to point its antennas toward the ground, yielding a large antenna gain for the second half of the pass. Fig. 6-16 indicates that this orientation is able to maintain positive link margin through the duration of the pass. Fig. 6-17 shows that the filter presented in section 4.3 successfully keeps reaction wheel angular acceleration within the 33 RPM/s limits, and Fig. 6-18 shows that the wheel angular velocity stays within about 25% of the maximum rated reaction wheel angular velocity of 7500 RPM. As was discussed with Objective 1, the wheels do exhibit frequent zero crossing behavior. Fig. 6-19, Fig. 6-20, Fig. 6-21, Fig. 6-22, Fig. 6-23, Fig. 6-24, and Fig. 6-25 show the input and output membership functions of the optimal attitude profile FIS. Almost all of these membership functions are used in at least one of the passes defined in Table

---

[††] Not accounting for the lack of power generation during eclipse, this objective has a maximum theoretical value of 1204.0 as maximum battery charge is 1200 mA·h and there are three constraints (two reaction wheel constraints with a maximum value of 1.0 and one antenna gain constraint with a maximum value of 2.0).

5-3 with the notable exceptions of input sun vector elevation, which was discussed during Objective 1 results, and input ground station vector elevation, whose elevation in the reference local-level coordinate system remains close to zero for all ground station passes simulated in this work due to the fact that higher-elevation (with respect to the ground station) ground station passes were selected.

Fig. 6-26 shows the time-dependent spacecraft attitude with respect to the reference local-level coordinate system and the local-level-referenced celestial sphere with projected images of the earth, sun, and ground station location. This visualization gives some clues as to why power generation in this mode is not as effective as it was in the “Emergency Power Generation” mode. Between 2800 s and 3200 s simulation time, the spacecraft is tracking the ground station by rotating about its Z-axis. Initially, the sun and ground station are in nearly the same location on the celestial sphere, and because the spacecraft points its antenna face (this face has no solar panels) toward the ground station, it misses out on generating extra power at this instant. After the ground station pass, it briefly performs a maneuver which points the open end of the sun shield toward the sun, again missing out on generating power. Finally, it aligns its Z-axis with the reference local-level coordinate system Z-axis and rotates about this axis, which does not generate as much power as it could, due to the relatively high elevation of the sun, and actually produces close to no power as the antenna face of the satellite points toward the sun near the end of the pass.

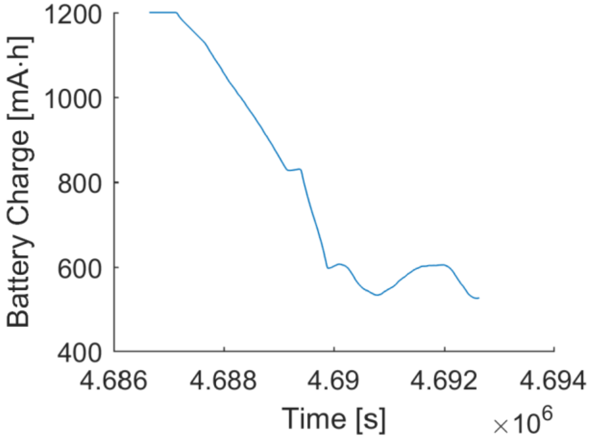

Fig. 6-12—Battery charge time history for Objective 2, Pass 17 optimal attitude profile. Battery charge decreases over the majority of this pass.

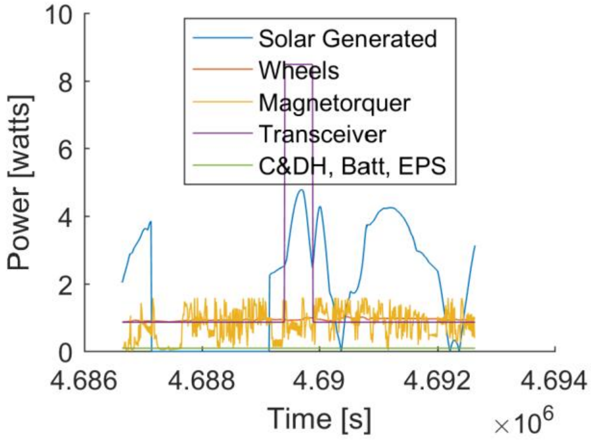

Fig. 6-13—Power use and generation for Objective 2, Pass 17 optimal attitude profile. Solar power generation drops to zero during eclipse and transceiver power demand spikes during ground station pass.

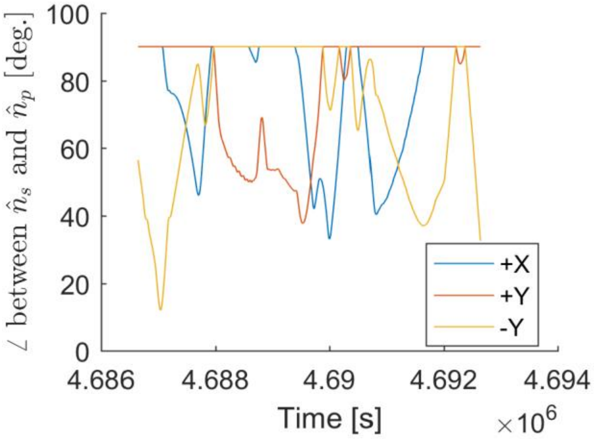

Fig. 6-14—Solar panel normal to sun vector angles for Objective 2, Pass 17 optimal attitude profile. Large angles when not in eclipse indicate poor power generation.

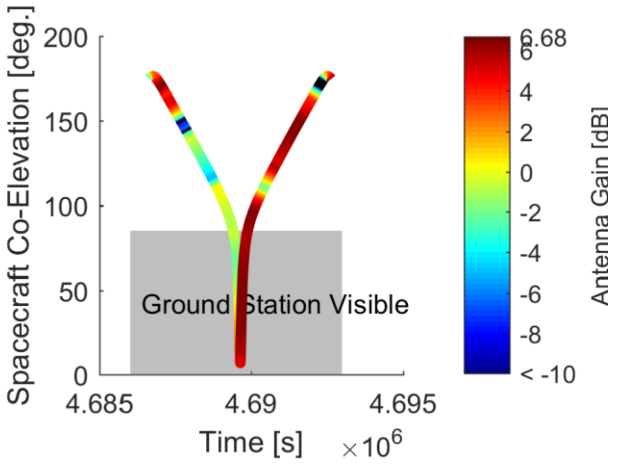

Fig. 6-15—Antenna gain for Objective 2, Pass 17 optimal attitude profile. Only about half of pass has gain above 0 dB.

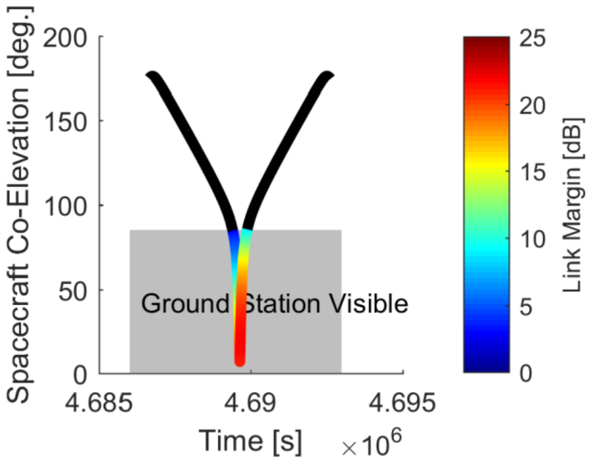

Fig. 6-16—Link Margin for Objective 2, Pass 17 optimal attitude profile. All of pass has link margin above 0 dB.

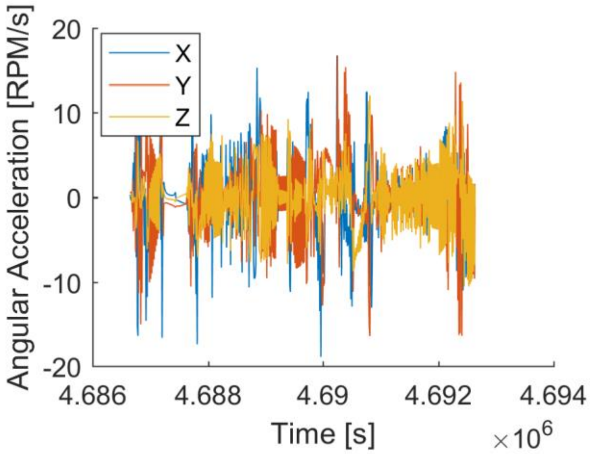

Fig. 6-17—Reaction wheel angular acceleration for Objective 2, Pass 17 optimal attitude profile.

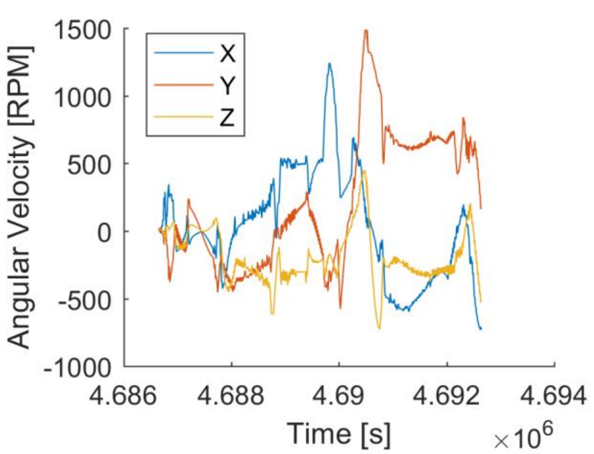

Fig. 6-18—Reaction wheel angular velocity for Objective 2, Pass 17 optimal attitude profile.

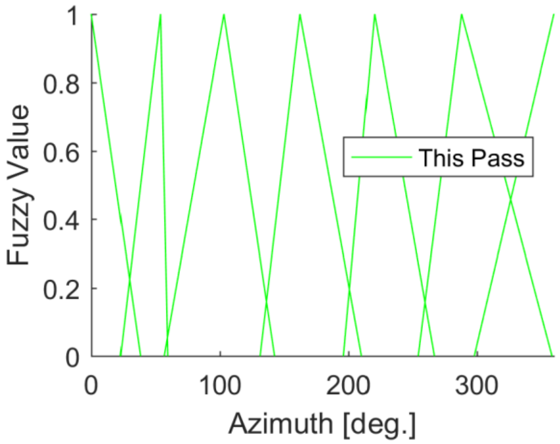

Fig. 6-19—Sun vector azimuth input membership functions for Objective 2, Pass 17. The FIS uses all sun vector azimuth input MFs during Pass 17.

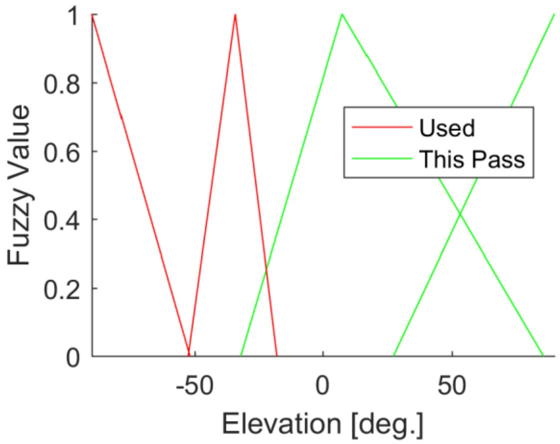

Fig. 6-20—Sun vector elevation input membership functions for Objective 2, Pass 17. The FIS uses all sun vector elevation input MFs, two of which during Pass 17.

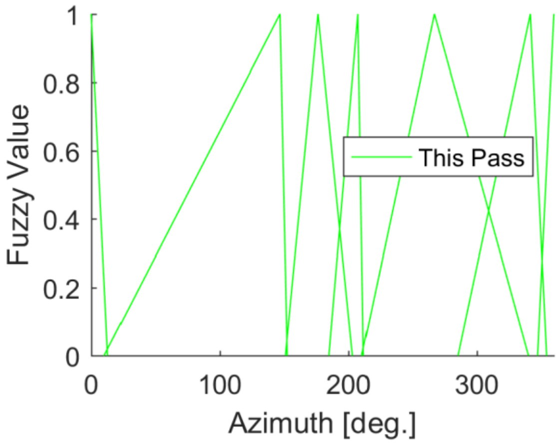

Fig. 6-21—Ground station vector azimuth input membership functions for Objective 2, Pass 17. The FIS uses all ground station vector input MFs during Pass 17.

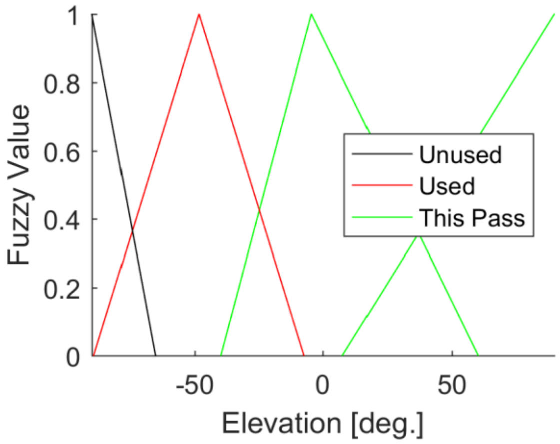

Fig. 6-22—Ground station vector elevation input membership functions for Objective 2, Pass 17. The FIS uses 3/4 of all input MFs, two of which during Pass 17.

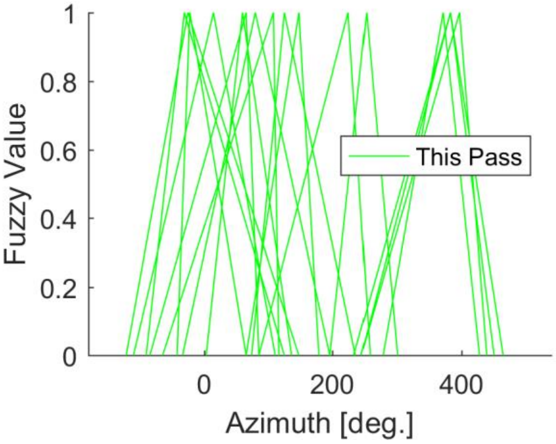

Fig. 6-23—Axis-angle axis azimuth output membership functions for Objective 2 optimal attitude profile FIS. All output MFs are used by the FIS for all passes.

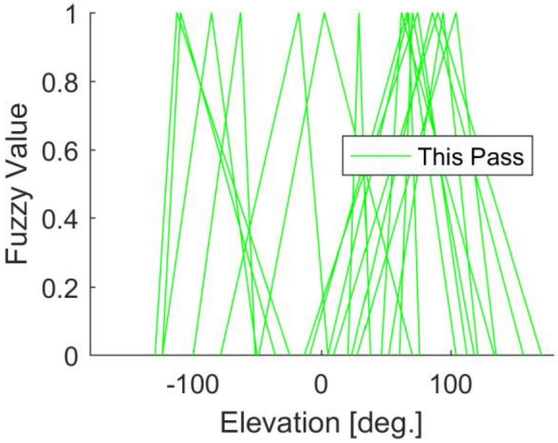

Fig. 6-24—Axis-angle axis elevation output membership functions for Objective 2 optimal attitude profile FIS. All output MFs are used by the FIS for this pass.

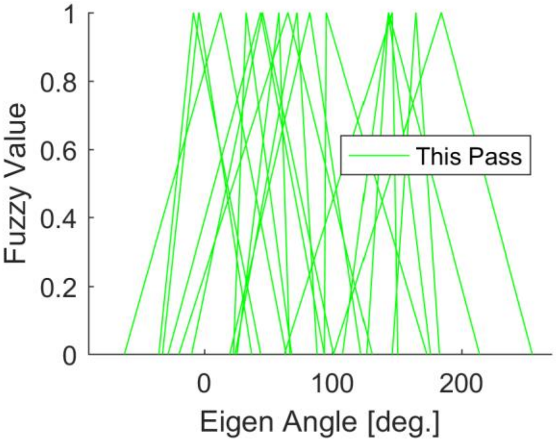

Fig. 6-25—Axis-angle angle output membership functions for Objective 2 optimal attitude profile FIS. All output MFs are used by the FIS for this pass.

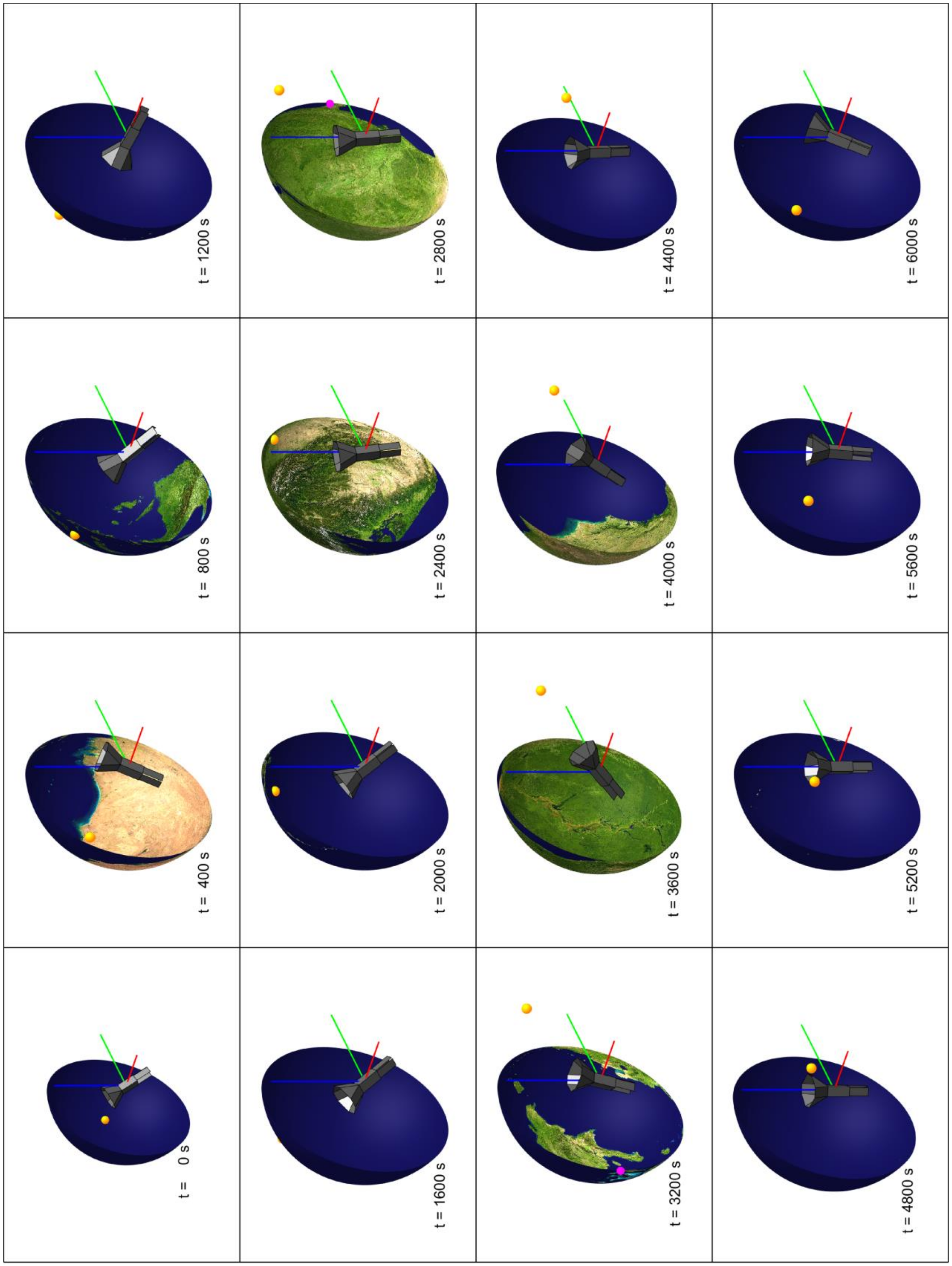

Fig. 6-26—The spacecraft Objective 2, Pass 17 orientation with respect to the reference coordinate system (red X, green Y, blue Z) is shown with the earth, sun (yellow sphere), and ground station (magenta sphere) projected on the celestial sphere.

6.3 Objective 3: Power Positive Ground Station Tracking

The optimal attitude profile FIS for the “Power Positive Ground Station Tracking” objective was found by the GA in 859 generations, taking 230 hours 58 minutes, or an average of 16 minutes 8 seconds per generation to solve. The optimal FIS has an objective function value of 443.77[‡‡]. Unlike the sample performance of the optimal solution found for Objective 2, Fig. 6-27 shows that the optimal Objective 3 attitude profile for Pass #17 allows the battery to recharge after the ground station pass. Fig. 6-28 indicates a more consistent solar power generation of 3–4 W after the ground station pass, and Fig. 6-29 shows that this is due to the fact that the +X and –Y solar panels do a better job at tracking the sun when the ground station is not visible. Fig. 6-30 shows that the optimal attitude FIS does a better job at tracking the ground station, as well, as the antenna gain never falls below 2.9 dB during Pass #17. Similarly, Fig. 6-31 shows that the link margin never falls below 8.25 dB for the duration of Pass #17. The reaction wheel angular acceleration and angular velocity, respectively shown in Fig. 6-32 and Fig. 6-33, also exhibit behavior similar to that in Objectives 1 and 2, never accelerating faster than 33 RPM/s and remaining within about 10% of their maximum angular velocity. Fig. 6-34, Fig. 6-35, Fig. 6-36, Fig. 6-37, Fig. 6-38, Fig. 6-39, and Fig. 6-40 show the input and output membership functions of the optimal attitude profile FIS. Almost all of these membership functions are used in at least one of the passes defined in Table 5-3 with the notable exceptions of input sun vector elevation and input ground station vector elevation, which were discussed during Objective 1 and 2 results.

Fig. 6-41 shows the time-dependent spacecraft attitude with respect to the reference local-level coordinate system and the local-level-referenced celestial sphere with projected images of the

---

[‡‡] This objective has a maximum theoretical value of 468.586 ($100\times10^{0.668} + 3.0$) as the maximum antenna gain is 6.68 dB and there are three constraints (two reaction wheel constraints and one power constraint), each with a maximum value of 1.0.

earth, sun, and ground station location. For the duration of the pas, the spacecraft Z-axis remains approximately aligned with the Z-axis of the reference local-level coordinate system. When a ground station pass occurs, the antenna (–X) side of the spacecraft tracks the ground station azimuth as best as possible. The spacecraft does not track the ground station exactly as is evident in the slightly lower antenna gain at the beginning and end of the ground station pass in Fig. 6-30; however, the Objective 3 optimal solution does a much better job than the Objective 2 optimal solution at tracking the ground station. When a ground station pass is not occurring, the spacecraft spins about its Z-axis to orient one of its solar panels, the –Y panel for Pass #17, toward the sun, tracking the sun vector azimuth. However, this optimal attitude profile does not track the sun vector elevation, which could further increase power generation. Note that search for a more optimal solution to Objective 3 is unlikely to result in a FIS that tracks sun elevation, because solar power generation is only a constraint in this objective, and it is already satisfied in the attitude profile presented.

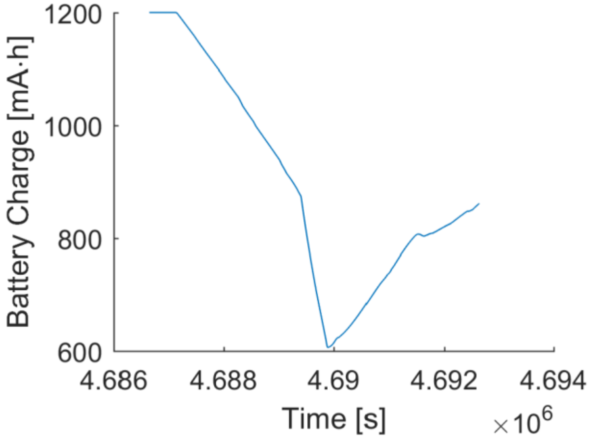

Fig. 6-27—Battery charge time history for Objective 3, Pass 17 optimal attitude profile. Battery charge decreases during eclipse and ground station transmission.

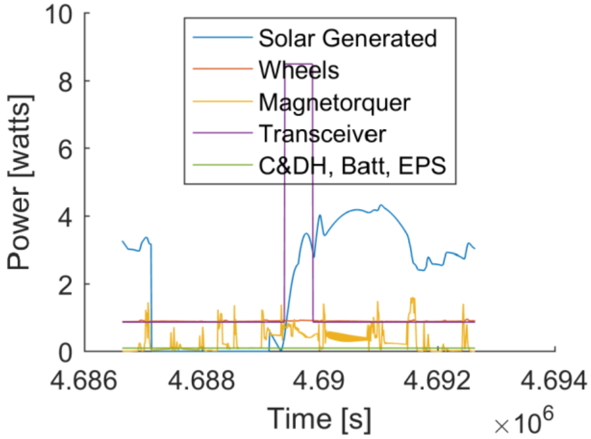

Fig. 6-28—Power use and generation for Objective 3, Pass 17 optimal attitude profile. Solar power generation drops to zero during eclipse and transceiver power demand spikes during ground station pass.

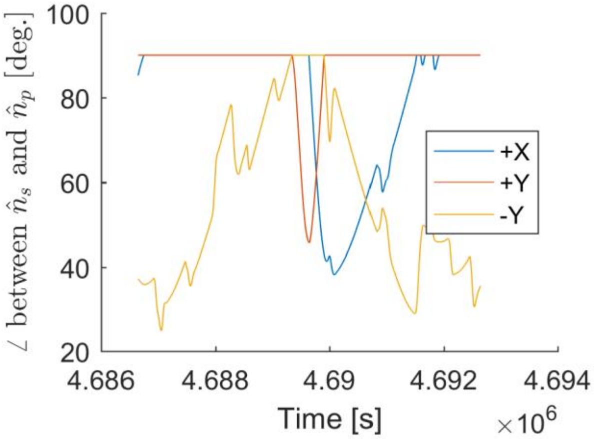

Fig. 6-29—Solar panel normal to sun vector angles for Objective 3, Pass 17 optimal attitude profile. The +X and –Y solar panels track the sun when not in eclipse.

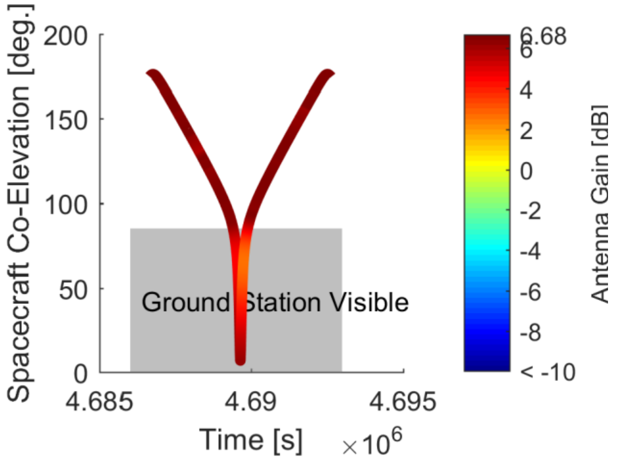

Fig. 6-30—Antenna gain for Objective 3, Pass 17 optimal attitude profile. High antenna gain indicates antennas are always pointed toward ground station (even when occluded).

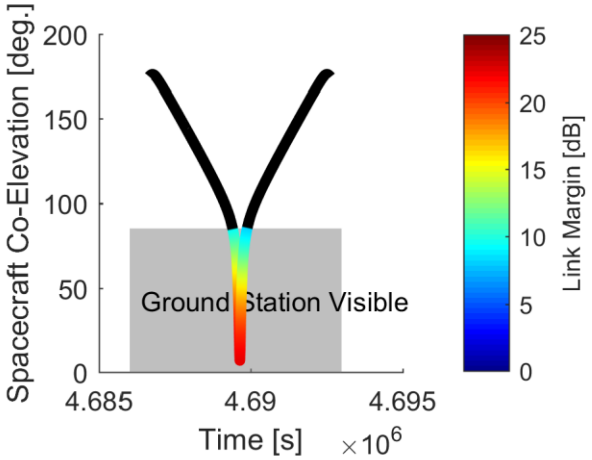

Fig. 6-31—Link Margin for Objective 3, Pass 17 optimal attitude profile. All of pass has link margin above 8 dB.

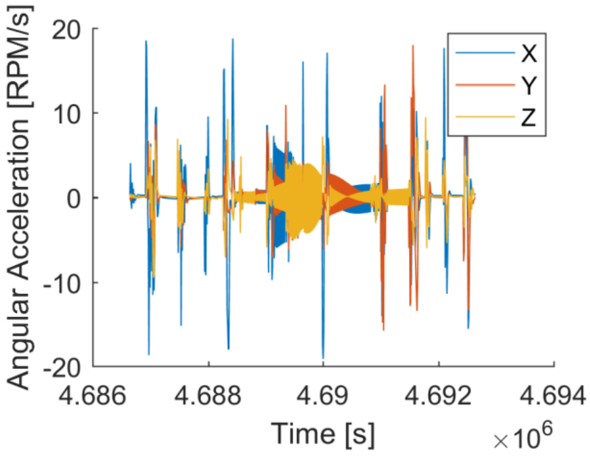

Fig. 6-32—Reaction wheel angular acceleration for Objective 3, Pass 17 optimal attitude profile.

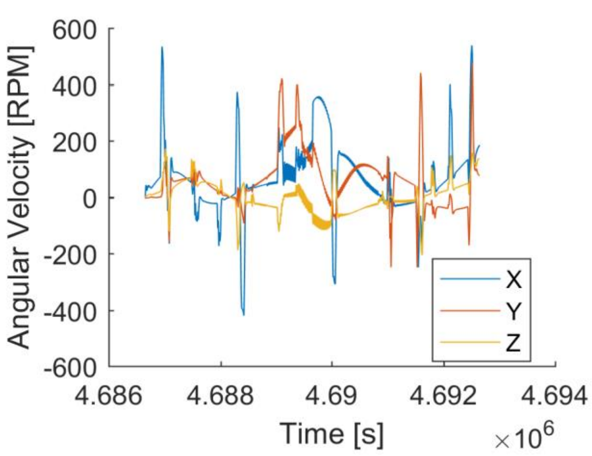

Fig. 6-33—Reaction wheel angular velocity for Objective 3, Pass 17 optimal attitude profile.

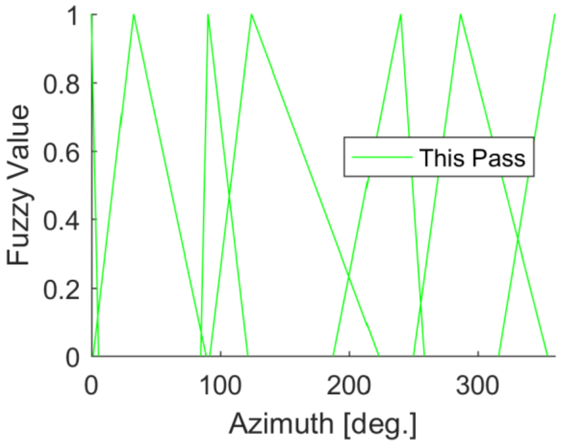

Fig. 6-34—Sun vector azimuth input membership functions for Objective 3 optimal attitude profile FIS. The FIS uses all sun vector azimuth input MFs for all passes..

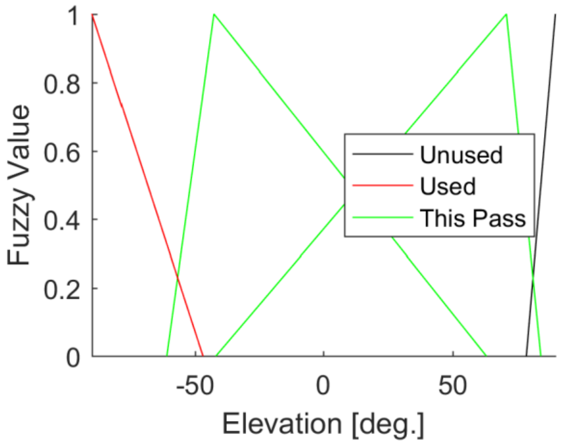

Fig. 6-35—Sun vector elevation input membership functions for Objective 3 optimal attitude profile FIS. The FIS only uses three of these MFs, and only two for Pass 17.

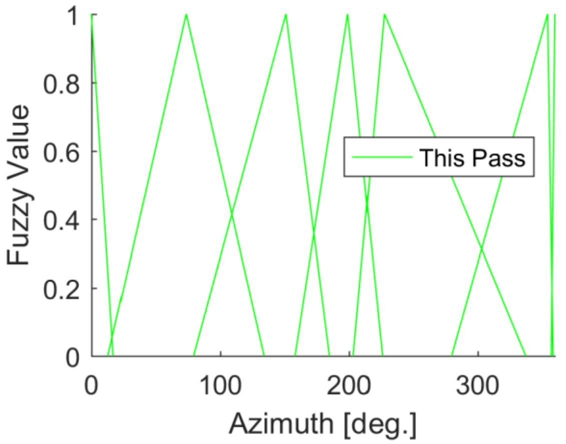

Fig. 6-36—Ground station vector azimuth input membership functions for Objective 3, Pass 17. The FIS uses all ground station vector input MFs for all passes.

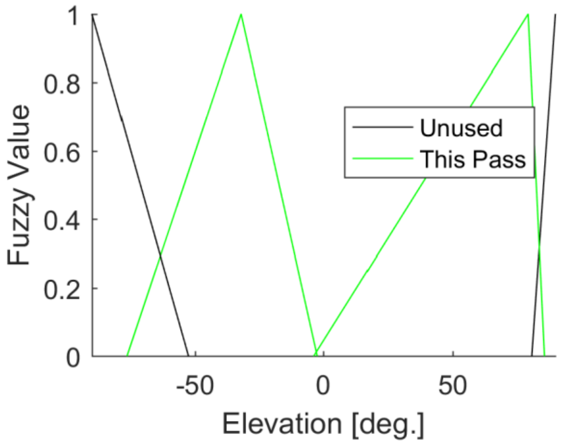

Fig. 6-37—Ground station vector elevation input membership functions for Objective 3, Pass 17. The FIS uses half of all input MFs for all passes.

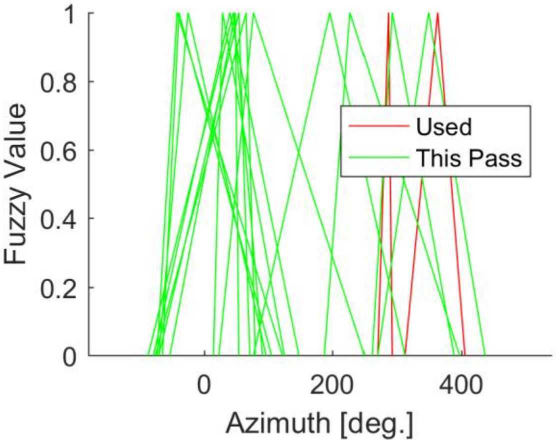

Fig. 6-38—Axis-angle axis azimuth output membership functions for Objective 3 optimal attitude profile FIS. All output MFs are used by the FIS, but two are not used for Pass 17.

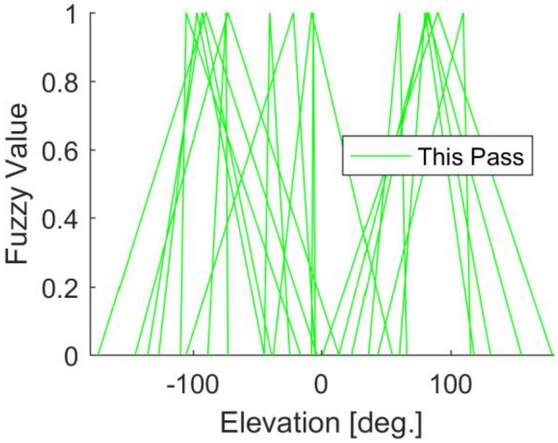

Fig. 6-39—Axis-angle axis elevation output membership functions for Objective 3 optimal attitude profile FIS. Not all output MFs are used by the FIS for all passes.

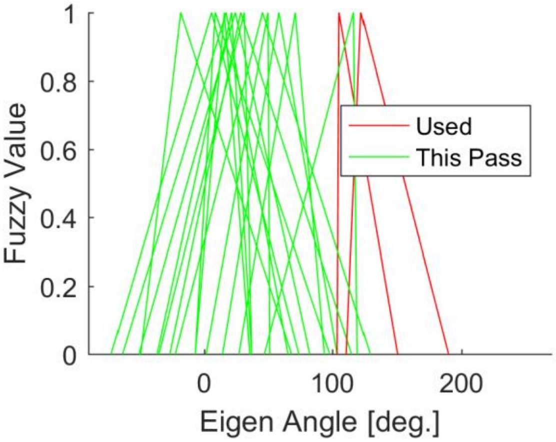

Fig. 6-40—Axis-angle angle output membership functions for Objective 3 optimal attitude profile FIS. All output MFs are used by the FIS, but two are not used for Pass 17.

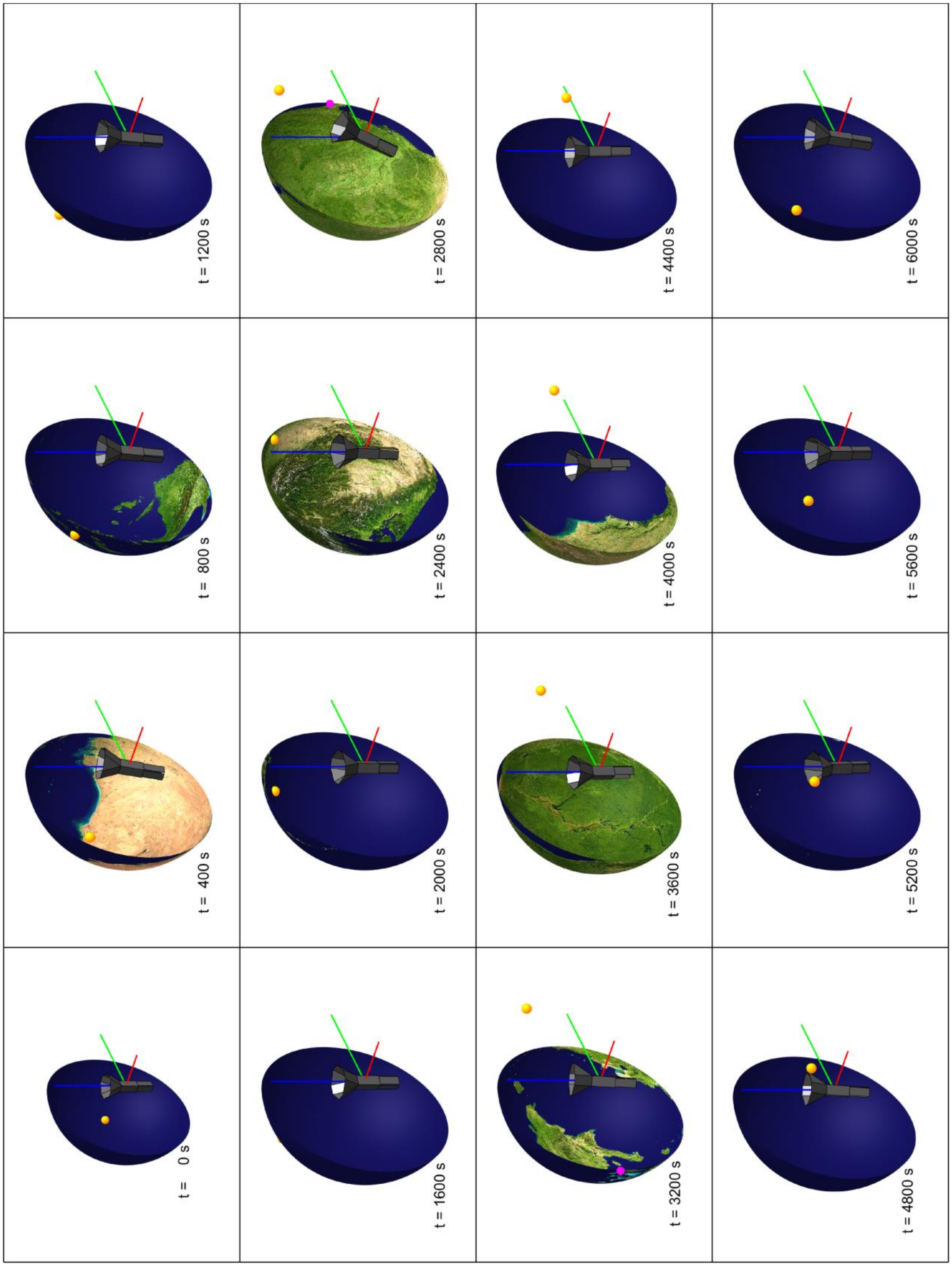

Fig. 6-41—The spacecraft Objective 3, Pass 17 orientation with respect to the reference coordinate system (red X, green Y, blue Z) is shown with the earth, sun (yellow sphere), and ground station (magenta sphere) projected on the celestial sphere.

6.4 Objective 4: Nominal Ground Station Tracking

The optimal attitude profile FIS for the "Nominal Ground Station Tracking" objective was found by the GA in 220 generations, taking 18 hours 47 minutes, or an average of 5 minutes 7 seconds per generation to solve. The optimal FIS has an objective function value of 418.04[§§]. Comparing this value to that of the Objective 3 objective function value clearly indicates this attitude profile FIS is suboptimal. During solution, the GA most likely got stuck on a local optimum and terminated before it could find other, better solutions, which clearly exist. Many differences between the formulations of the Objective 3 problem and the Objective 4 problem, including the number of inputs and number of input membership functions for corresponding inputs, caused the GA to take two separate paths when finding these two vastly different solutions. Fig. 6-42 indicates that antenna direction lags ground station direction as the antenna gain becomes slightly negative at the end of the pass, compared to Fig. 6-30 where the antenna gain is more symmetrical about the highest elevation of the pass. However, Fig. 6-43 still indicates positive link margin for the duration of the ground station pass. Like previous optimal solutions, Fig. 6-44 and Fig. 6-45 indicate the reaction wheel accelerations stay within 33 RPM/s and reaction wheel angular velocities stay within about 10% of their maximum allowable value. Fig. 6-46, Fig. 6-47, Fig. 6-48, Fig. 6-49, and Fig. 6-50 show the input and output membership functions of the optimal attitude profile FIS. Notably, Fig. 6-47 shows just how narrow of a range of ground station elevations (in the reference local-level coordinate system) are considered in these high-spacecraft-elevation ground station passes ass only one narrow input membership function about zero degrees elevation is used for all simulated passes.

[§§] This objective has a maximum theoretical value of 467.586 ($100\times10^{0.668} + 2.0$) as the maximum antenna gain is 6.68 dB and there are two reaction wheel constraints, each with a maximum value of 1.0.

Lastly, Fig. 6-51 shows behavior of this attitude trajectory FIS is similar to that of the optimal Objective 3 attitude FIS, but without sun tracking and degraded ground station tracking performance. An improved solution to this objective may be found either by restarting the GA from the final population used in this first optimization attempt or by starting the GA from an initial population different from the initial population used in this first optimization attempt. The former strategy would give the GA an opportunity to combine the best aspects of current population members in the search for a more optimal solution. The latter strategy would give the GA an opportunity to take a different path in its optimization, which could avoid the local optimum it found in the first solution attempt and lead the GA to discover better solutions.

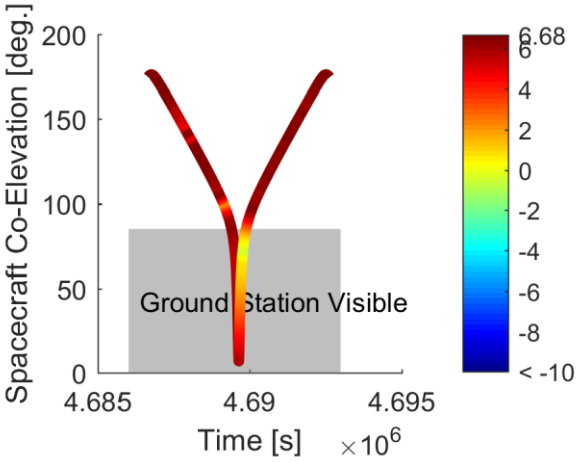

Fig. 6-42—Antenna gain for Objective 4, Pass 17 optimal attitude profile. Most of pass has gain above 0 dB.

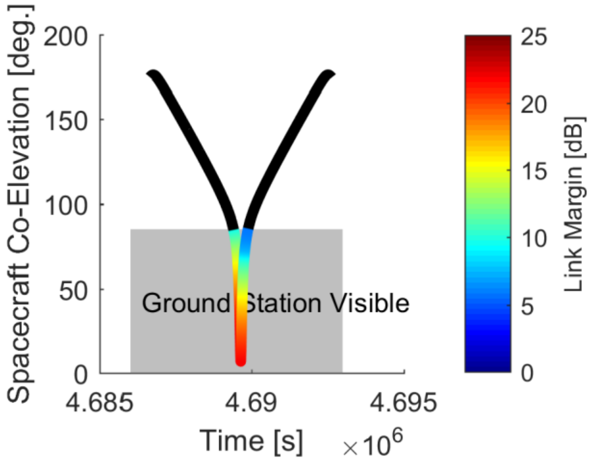

Fig. 6-43—Link Margin for Objective 4, Pass 17 optimal attitude profile. All of pass has link margin above 0 dB.

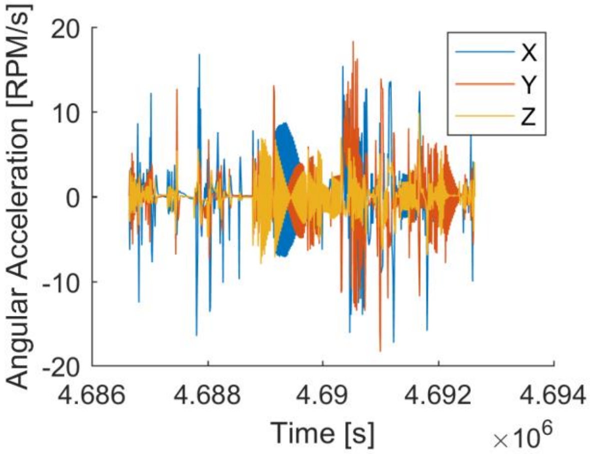

Fig. 6-44—Reaction wheel angular acceleration for Objective 4, Pass 17 optimal attitude profile.

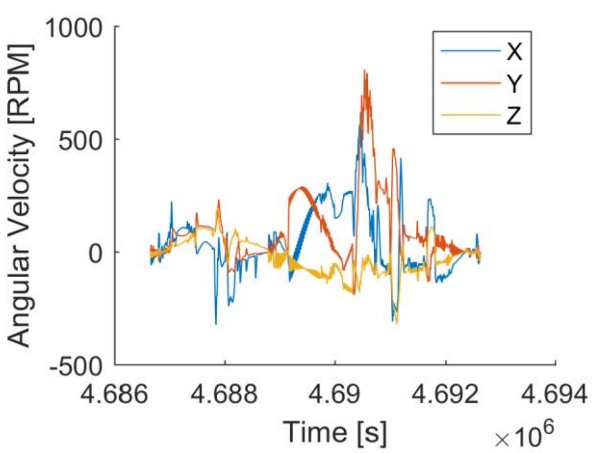

Fig. 6-45—Reaction wheel angular velocity for Objective 4, Pass 17 optimal attitude profile.

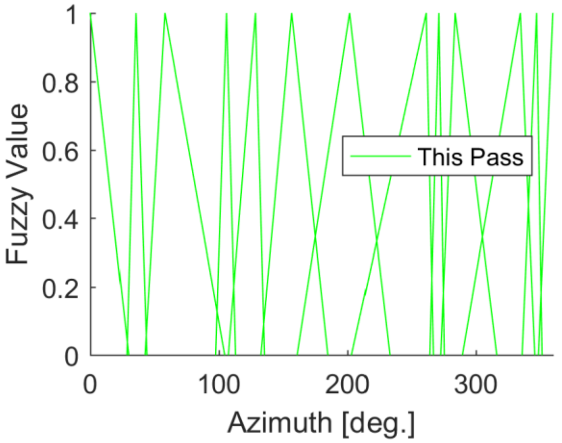

Fig. 6-46—Ground station vector azimuth input membership functions for Objective 4, Pass 17. The FIS uses all ground station vector input MFs for all passes.

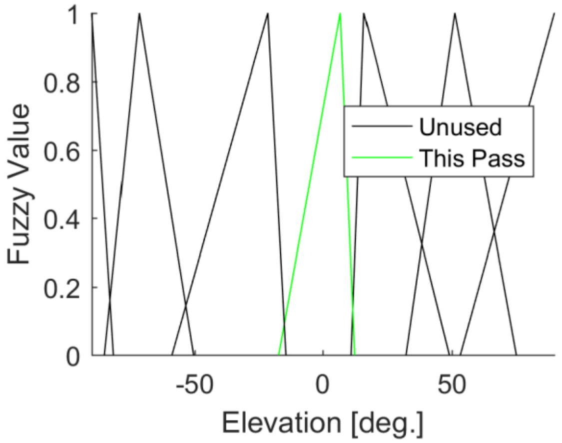

Fig. 6-47—Ground station vector elevation input membership functions for Objective 4, Pass 17. The FIS uses only one input MF for all passes as all simulated ground station passes have very low elevation in the reference coordinate system.

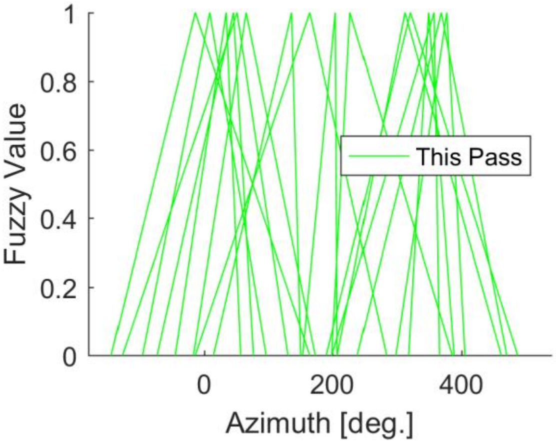

Fig. 6-48—Axis-angle axis azimuth output membership functions for Objective 4 optimal attitude profile FIS. All output MFs are used by the FIS for all passes.

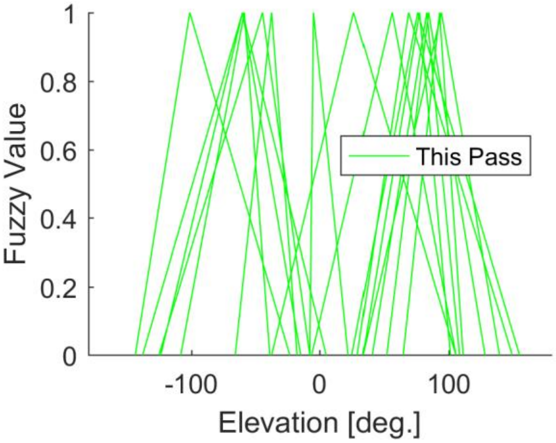

Fig. 6-49—Axis-angle axis elevation output membership functions for Objective 4 optimal attitude profile FIS. All output MFs are used by the FIS for all passes.

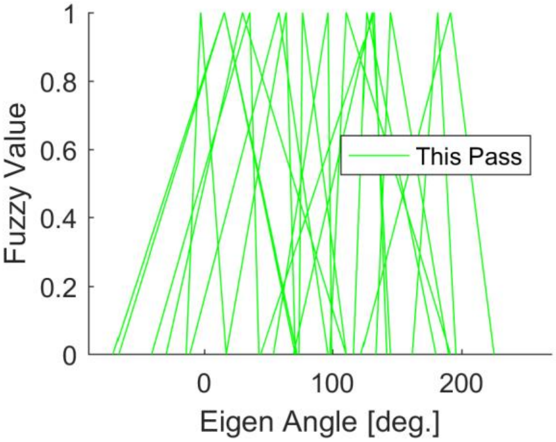

Fig. 6-50—Axis-angle angle output membership functions for Objective 4 optimal attitude profile FIS. All output MFs are used by the FIS for all passes.

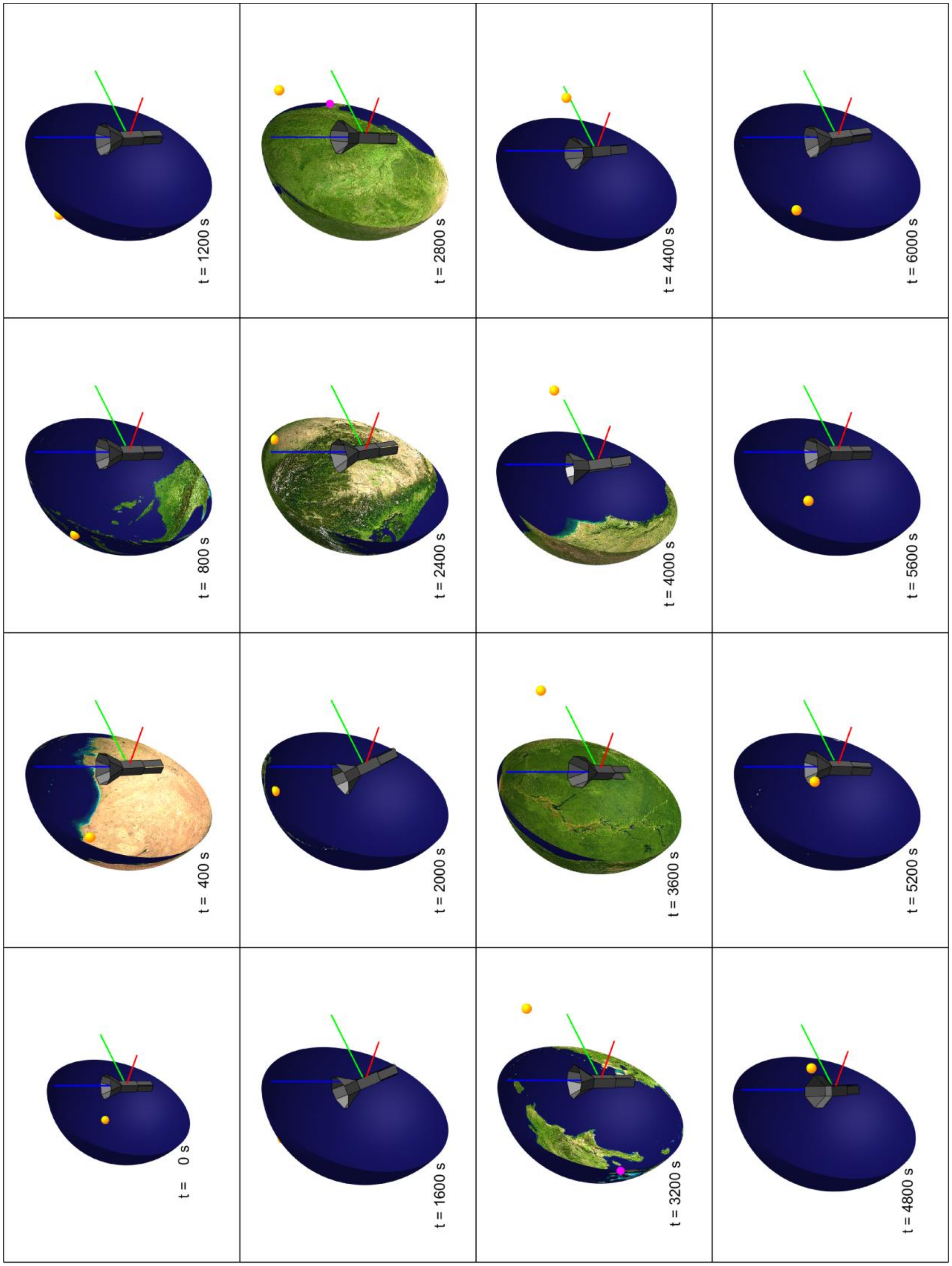

Fig. 6-51—The spacecraft Objective 4, Pass 17 orientation with respect to the reference coordinate system (red X, green Y, blue Z) is shown with the earth, sun (yellow sphere), and ground station (magenta sphere) projected on the celestial sphere.

6.5 Objective 5: Power Positive Science

The optimal attitude profile FIS for the "Power Positive Science" objective was found by the GA in 314 generations, taking 30 hours 4 minutes, or an average of 5 minutes 45 seconds per generation to solve. The optimal FIS has an objective function value of 336.04[***]. Like previous attitude profile optimization results, Fig. 6-52 shows that the battery charge generally decreases over the course of the simulated pass, especially during eclipse and radio transmission. Fig. 6-53 and Fig. 6-54 show that power is generated at varying rates as all three solar panels take turns facing toward the sun. Fig. 6-55 shows that the experiment temperature drops to about 120 K in eclipse and rises to about 200 K in the sun. Again, it should be noted that these are not true temperatures but are interpolated temperatures calculated using a steady-state heat transfer model which is only a function of earth-sun geometry and vehicle attitude; the true temperatures are time-dependent with dynamics that depend on temperature state(s) at previous times in addition to the sun-earth geometry and vehicle attitude. Fig. 6-56 shows that these steady-state temperature minima are achieved by keeping the earth nadir and sun vectors an average of about 120 degrees and no less than 90 degrees from the spacecraft +Z-axis, effectively shading the experiment from direct views of both the sun and the earth at all times. Like all other optimal attitude profile solutions, Fig. 6-57 and Fig. 6-58 indicate the reaction wheel accelerations stay within 33 RPM/s and reaction wheel angular velocities stay within about 10% of their maximum allowable value. Fig. 6-59, Fig. 6-60, Fig. 6-61, Fig. 6-62, and Fig. 6-63 show the input and output membership functions of the optimal attitude profile FIS.

[***] An estimate for the maximum theoretical value of this objective is 394.37 as the minimum achievable temperature is 108.63 (at only one particular earth-sun geometry and spacecraft orientation) and there are three constraints (two reaction wheel and one power), each with a maximum value of 1.0.

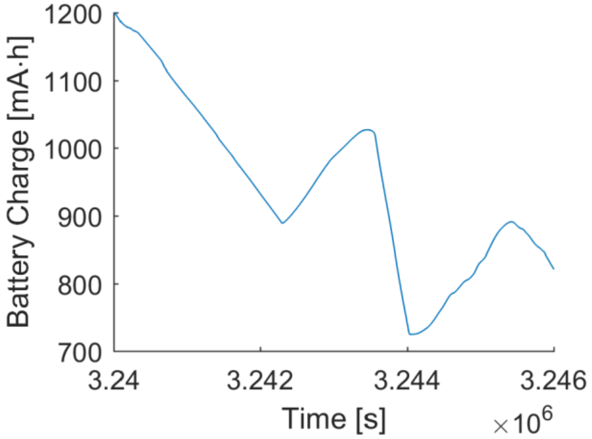

Fig. 6-52—Battery charge time history for Objective 5, Pass 6 optimal attitude profile. Battery charge decreases during eclipse and ground station transmission.

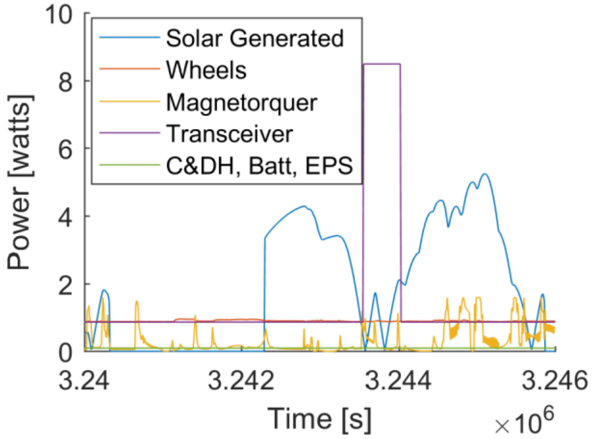

Fig. 6-53—Power use and generation for Objective 5, Pass 6 optimal attitude profile. Solar power generation drops to zero during eclipse and transceiver power demand spikes during ground station pass.

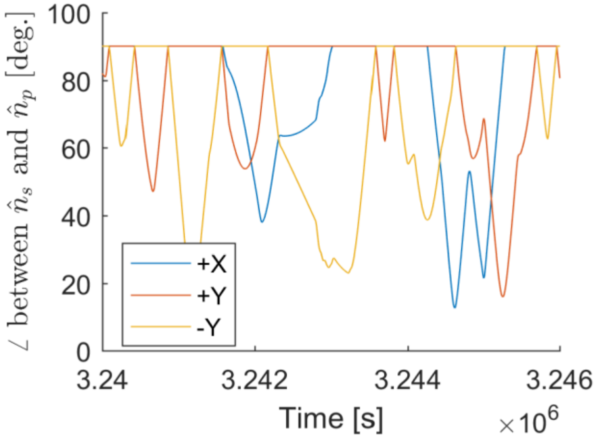

Fig. 6-54—Solar panel normal to sun vector angles for Objective 5, Pass 6 optimal attitude profile.

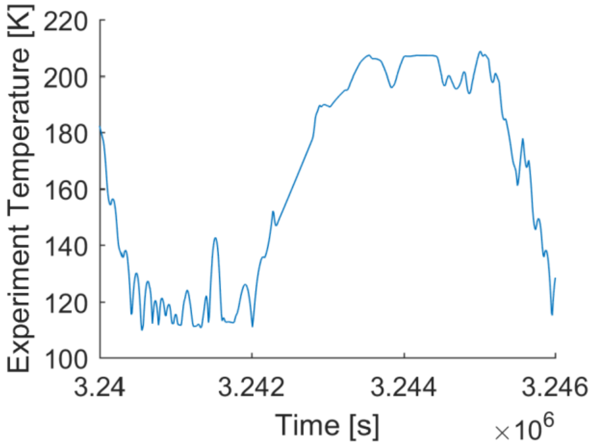

Fig. 6-55—Experiment temperature for Objective 5, Pass 6 optimal attitude profile. Eclipse has lower temperatures.

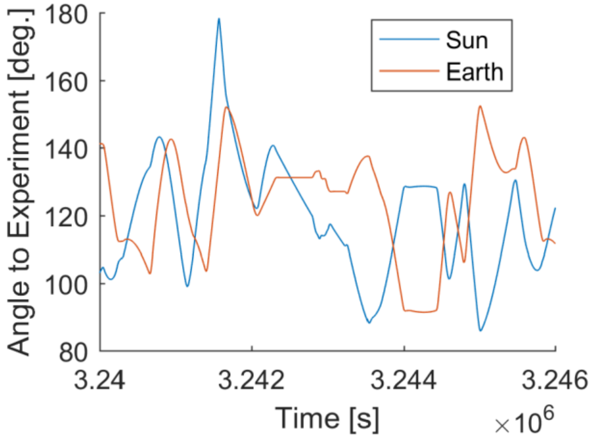

Fig. 6-56—Sun and earth to experiment angles for Objective 5, Pass 6 optimal attitude profile. The smaller the angle (especially sun angle), the larger the temperature.

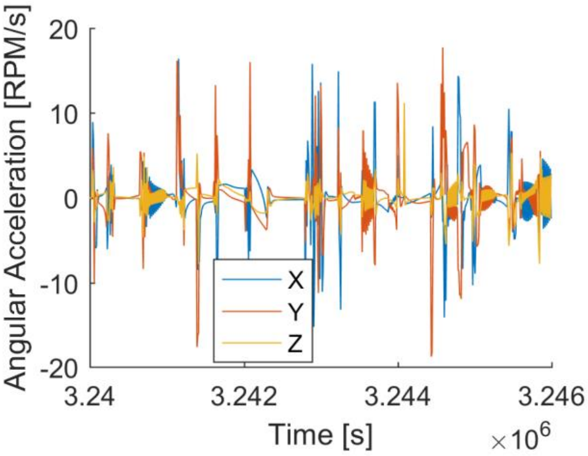

Fig. 6-57—Reaction wheel angular acceleration for Objective 5, Pass 6 optimal attitude profile.

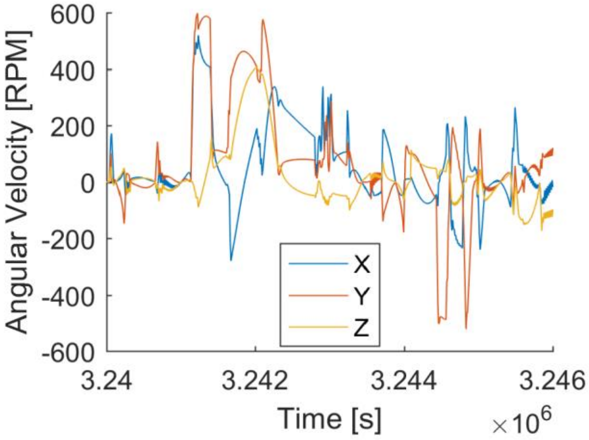

Fig. 6-58—Reaction wheel angular velocity for Objective 5, Pass 6 optimal attitude profile.

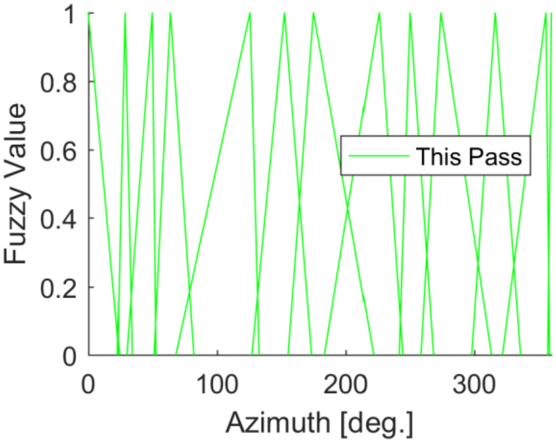

Fig. 6-59—Sun vector azimuth input membership functions for Objective 5 optimal attitude profile FIS. The FIS uses all sun vector azimuth input MFs for all passes.

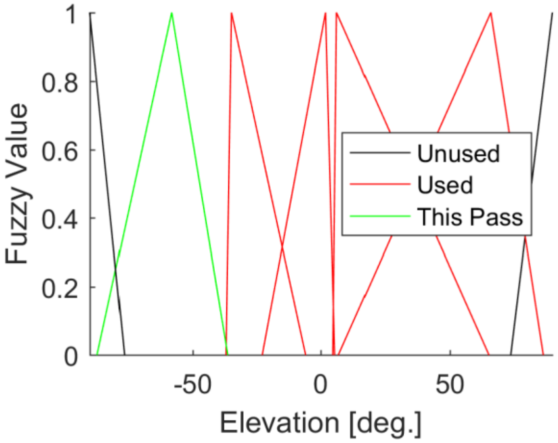

Fig. 6-60—Sun vector elevation input membership functions for Objective 5 optimal attitude profile FIS. The FIS only uses five of these MFs, and only one for Pass 6.

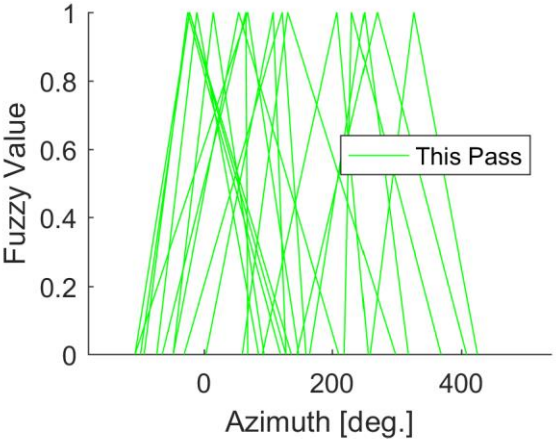

Fig. 6-61—Axis-angle axis azimuth output membership functions for Objective 5 optimal attitude profile FIS. All output MFs are used by the FIS for all passes.

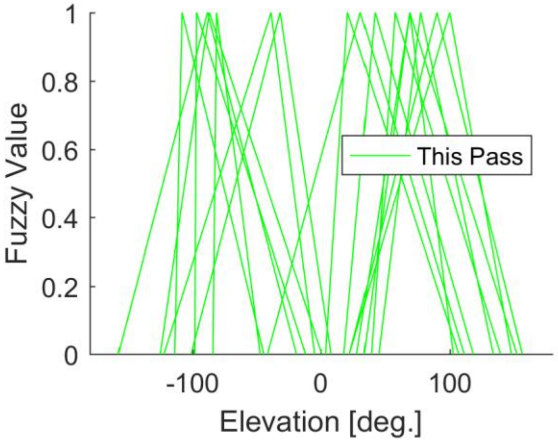

Fig. 6-62—Axis-angle axis elevation output membership functions for Objective 5 optimal attitude profile FIS. Not all output MFs are used by the FIS for all passes.

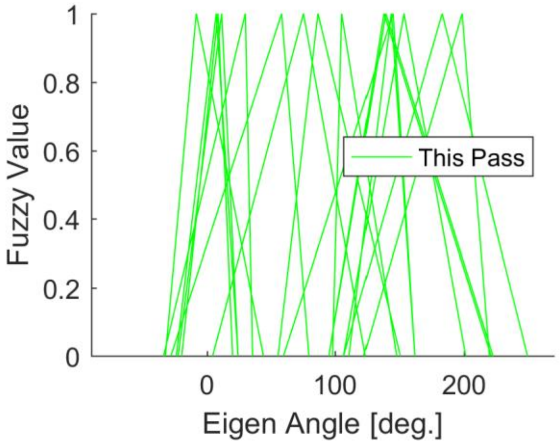

Fig. 6-63—Axis-angle angle output membership functions for Objective 5 optimal attitude profile FIS. All output MFs are used by the FIS for all passes.

Fig. 6-64 shows the time-dependent spacecraft attitude with respect to the reference local-level coordinate system and the local-level-referenced celestial sphere with projected images of the earth, sun, and ground station location. It confirms the observation that the open end of the sunshield is always pointed generally away from both the sun and earth and that the solar panels generally face toward the sun but do not necessarily track the sun. Often, the open end of the sunshield (spacecraft-body-fixed +Z) is pointed toward the +X-direction of the reference local-level coordinate system.

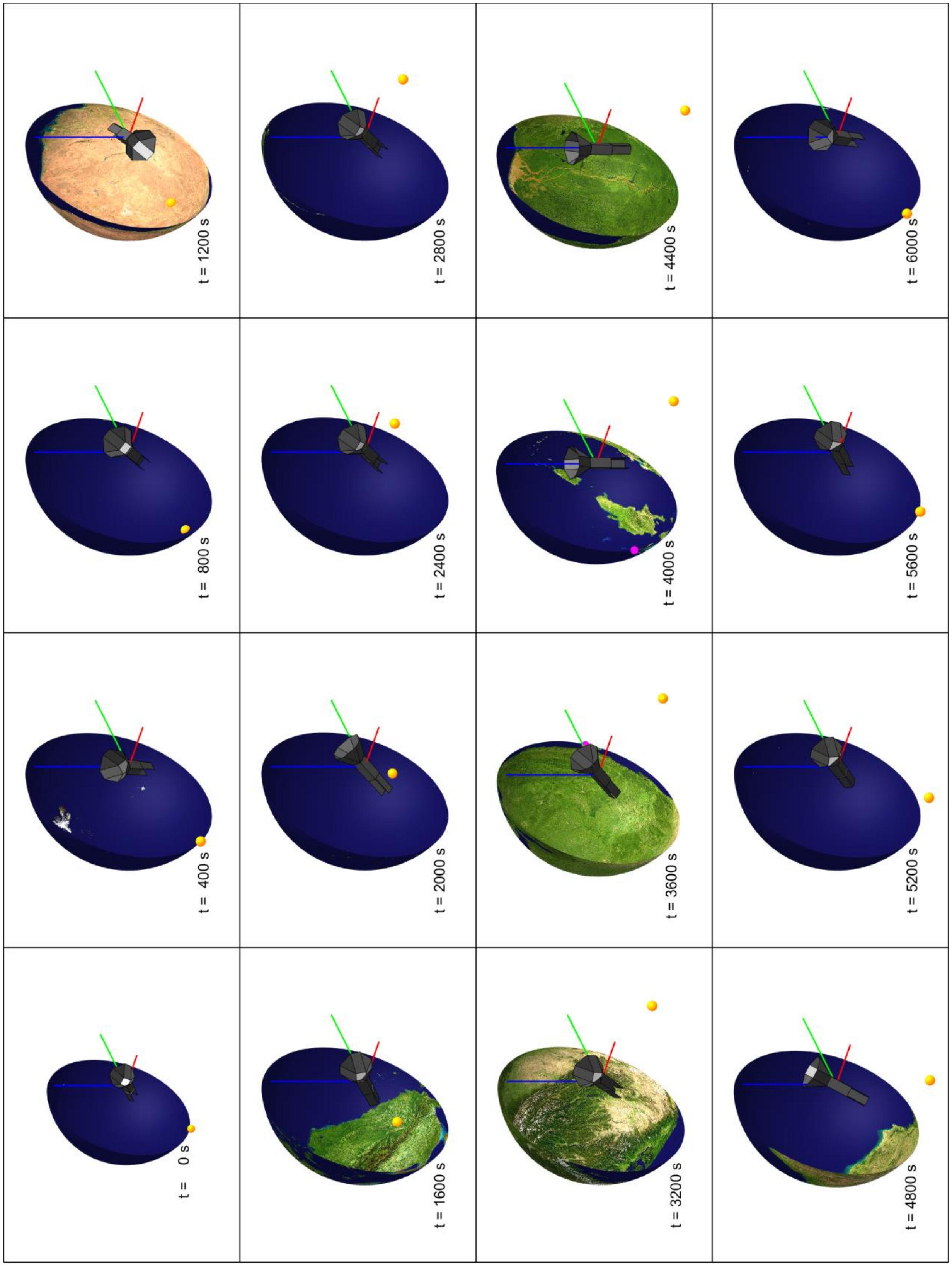

Fig. 6-64—The spacecraft Objective 5, Pass 6 orientation with respect to the reference coordinate system (red X, green Y, blue Z) is shown with the earth, sun (yellow sphere), and ground station (magenta sphere) projected on the celestial sphere.

6.6 Objective 6: Science with Ground Station Tracking

The optimal attitude profile FIS found for Objective 6 is identical to that found for the more-constrained Objective 7. The only additional constraint Objective 7 includes that Objective 6 does not is the relatively easily attainable battery charge constraint which, when met, only adds 1.0 to the fitness function value, which was not significant enough of a difference to change the path the GA took to find the optimal solutions. Because Objective 7 is more restrictive, there are more variables of interest to show for the results of Objective 7 than for the results of Objective 6, and rather than repeating the same information, all results for Objective 7 and Objective 6 are presented in the next section.

6.7 Objective 7: Science with Power Generation and Ground Station Tracking

The optimal attitude profile FIS for the "Science with Power Generation and Ground Station Tracking" objective was found by the GA in 257 generations, taking 81 hours 25 minutes, or an average of 19 minutes per generation to solve. The optimal FIS has an objective function value of 299.91[†††]. The performance of the optimal Objective 7 attitude profile is very similar, but not identical to the performance of the optimal Objective 2 attitude profile. Fig. 6-65 shows the same general pattern of battery charge decrease as was observed in Fig. 6-12. Fig. 6-66 and Fig. 6-67 show that the solar panels are not pointed toward the sun as well as they could be and therefore generate relatively small amounts of solar power to recharge the spacecraft batteries. Fig. 6-68 shows that the antennas point toward the ground during the second half of the ground station pass in Pass #17, and Fig. 6-69 indicates there is positive link margin for the duration of the ground station pass. Fig. 6-70 and Fig. 6-71 show that this optimal attitude profile does not do a

---

[†††] An estimate for the maximum theoretical value of this objective is 396.37 as the minimum achievable temperature is 108.63 (at only one particular earth-sun geometry and spacecraft orientation) and there are four constraints (two reaction wheel and one power, each with a maximum value of 1.0, and one antenna gain with a maximum value of 2.0).

particularly good job minimizing the spacecraft experiment temperature, which is the main objective of the profile. For much of the pass, the experiment temperature is in the slightly cold to ambient (250 K – 300 K) range with brief dips into the 200 K – 250 K range and even more brief dips into the 150 K – 200 K range. For a significant portion of the time in Pass #17, the open end of the sunshield is pointed in the general direction of the sun, with only about 40–50 degrees between the sun vector and the spacecraft +Z-axis, keeping the spacecraft experiment relatively warm. Like all previous optimal state trajectories, Fig. 6-72 and Fig. 6-73 show that the reaction wheel angular accelerations remain within 33 RPM/s and reaction wheel angular velocities remain within about 25% of the maximum allowable reaction wheel angular velocity. Fig. 6-74, Fig. 6-75, Fig. 6-76, Fig. 6-77, Fig. 6-78, Fig. 6-79, and Fig. 6-80 show the input and output membership functions of the optimal attitude profile FIS. Almost all of these membership functions are used in at least one of the passes defined in Table 5-3 with the notable exceptions discussed previously in section 6.2.

Fig. 6-81 shows the time-dependent spacecraft attitude with respect to the reference local-level coordinate system and the local-level-referenced celestial sphere with projected images of the earth, sun, and ground station location. It is substantially similar to the optimal Objective 2 attitude profile, which was not optimized for minimum experiment temperature but instead optimized for maximum power generation. This attitude profile does all the things the optimal Objective 5 attitude profile did not do which allowed it to minimize experiment temperature. Mainly, the optimal Objective 7 attitude profile frequently points the open end of its sunshield along the reference local-level coordinate system –X-axis (toward the earth) and does not point it away from the sun. Though it is able to meet reaction wheel, battery charge, and antenna gain constraints, this optimal attitude profile appears to be too constrained to find a good minimum temperature solution.

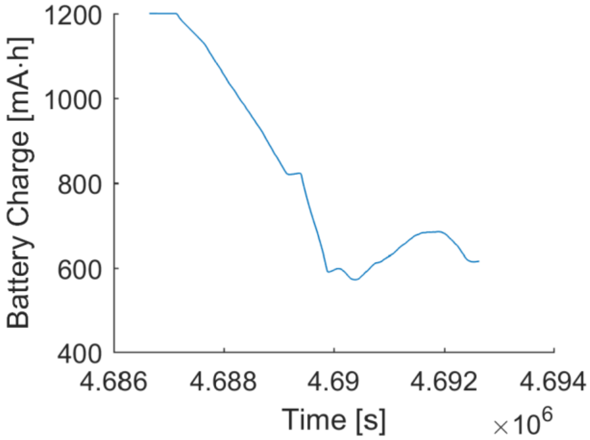

Fig. 6-65—Battery charge time history for Objective 7, Pass 17 optimal attitude profile. Battery charge decreases during eclipse and ground station transmission.

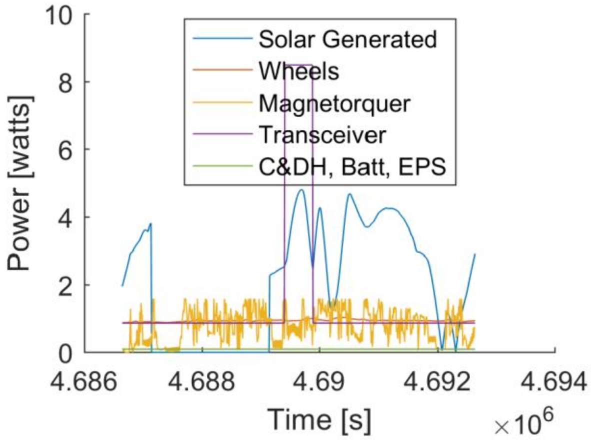

Fig. 6-66—Power use and generation for Objective 7, Pass 17 optimal attitude profile. Solar power generation drops to zero during eclipse and transceiver power demand spikes during ground station pass.

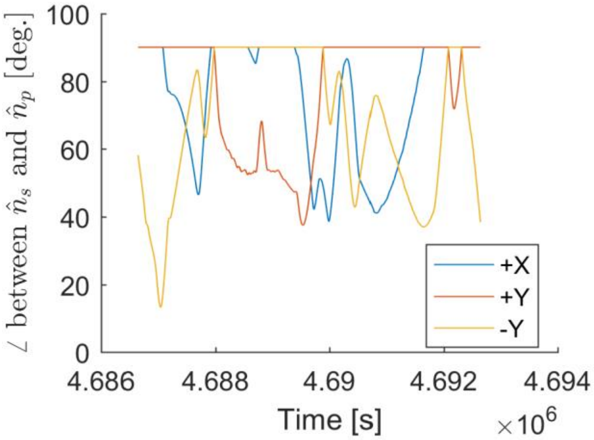

Fig. 6-67—Solar panel normal to sun vector angles for Objective 7, Pass 17 optimal attitude profile. The +X and –Y solar panels track the sun when not in eclipse.

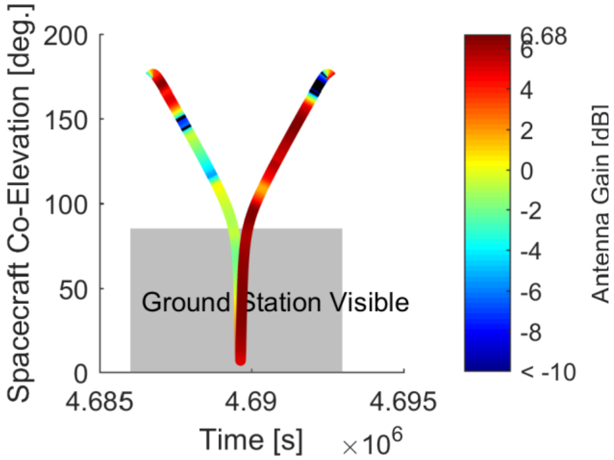

Fig. 6-68—Antenna gain for Objective 7, Pass 17 optimal attitude profile. More than half of pass has gain above 0 dB.

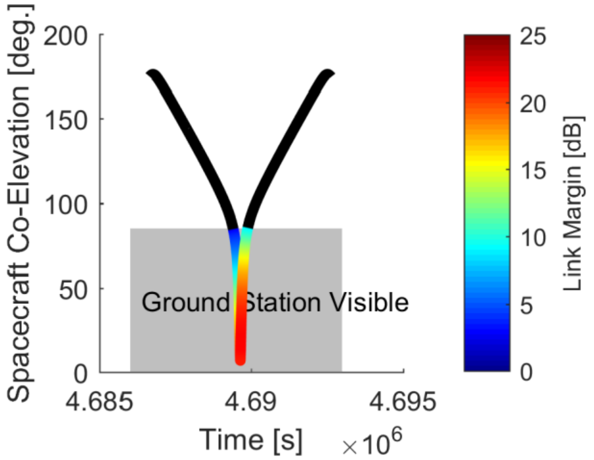

Fig. 6-69—Link Margin for Objective 7, Pass 17 optimal attitude profile. All of pass has link margin above 0 dB.

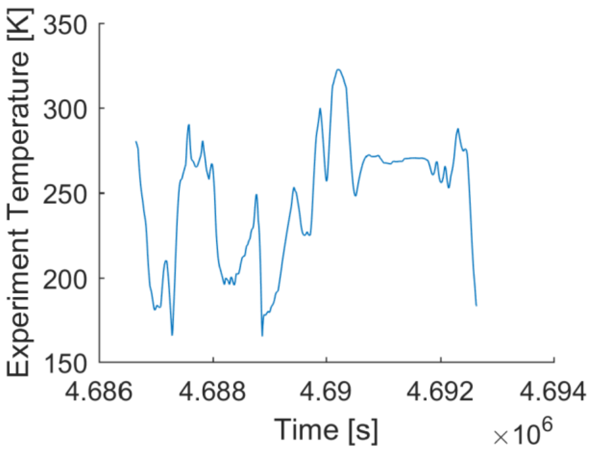

Fig. 6-70—Experiment temperature for Objective 7, Pass 17 optimal attitude profile. Constraints prevent temperatures from entering into cryogenic range.

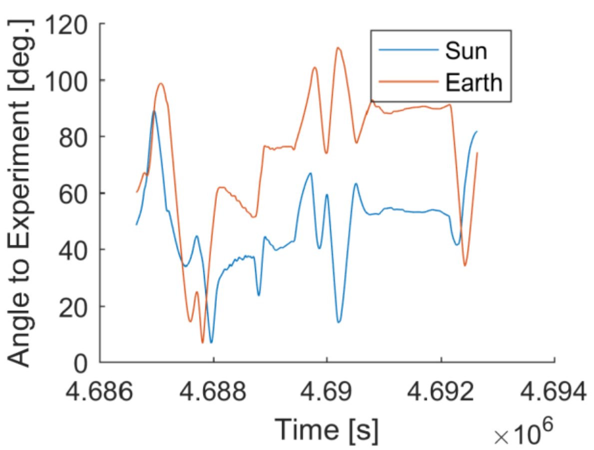

Fig. 6-71—Sun and earth to experiment angles for Objective 7, Pass 17 optimal attitude profile. Small angles (especially sun angle) result in large experiment temperature.

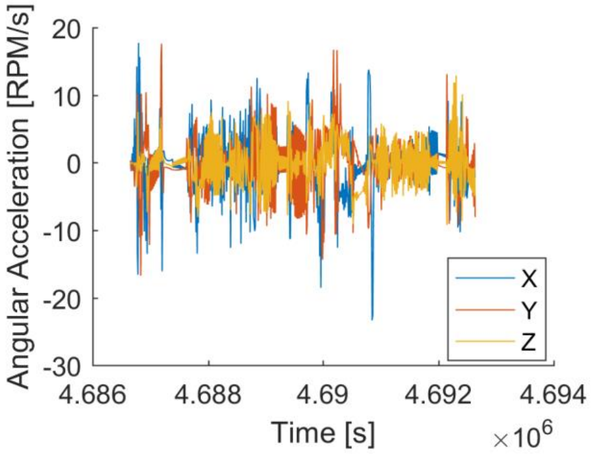

Fig. 6-72—Reaction wheel angular acceleration for Objective 7, Pass 17 optimal attitude profile.

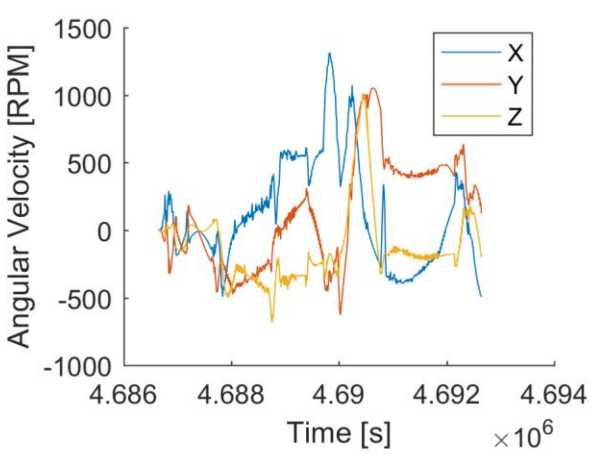

Fig. 6-73—Reaction wheel angular velocity for Objective 7, Pass 17 optimal attitude profile.

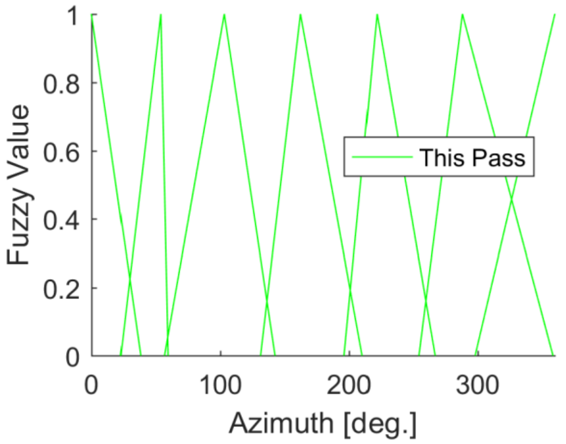

Fig. 6-74—Sun vector azimuth input membership functions for Objective 7 optimal attitude profile FIS. The FIS uses all sun vector azimuth input MFs for all passes.

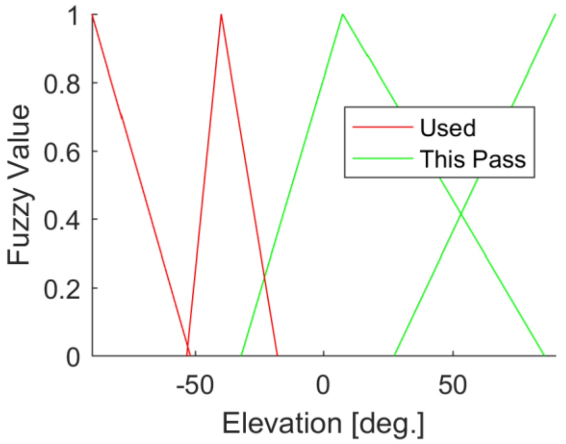

Fig. 6-75—Sun vector elevation input membership functions for Objective 7 optimal attitude profile FIS. The FIS all of these MFs but only one for Pass 17.

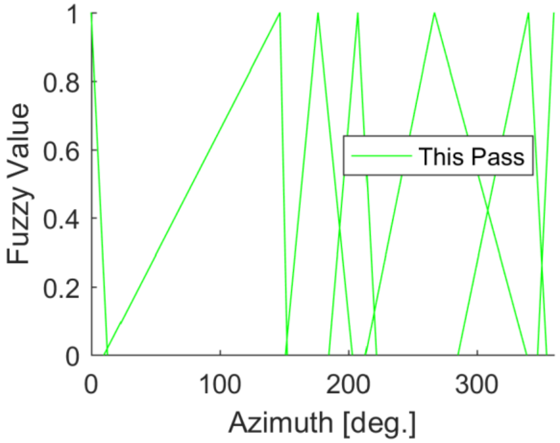

Fig. 6-76—Ground station vector azimuth input membership functions for Objective 7, Pass 17. The FIS uses all ground station vector input MFs for all passes.

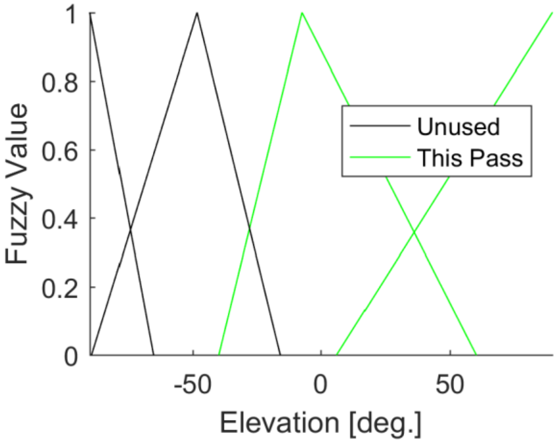

Fig. 6-77—Ground station vector elevation input membership functions for Objective 7, Pass 17. The FIS uses half of all input MFs for all passes.

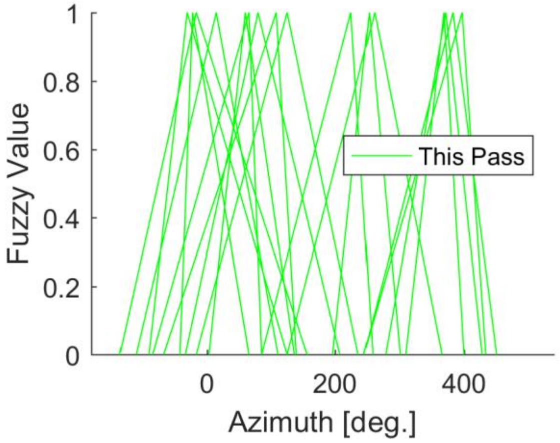

Fig. 6-78—Axis-angle axis azimuth output membership functions for Objective 7 optimal attitude profile FIS. Not all output MFs are used by the FIS for all passes.

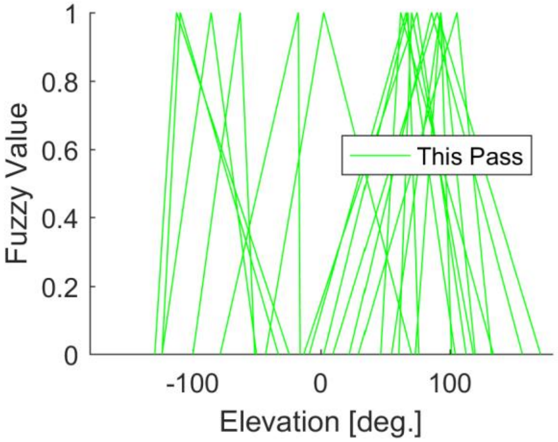

Fig. 6-79—Axis-angle axis elevation output membership functions for Objective 7 optimal attitude profile FIS. Not all output MFs are used by the FIS for all passes.

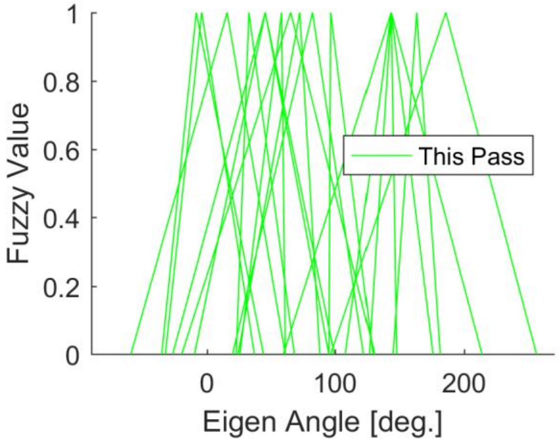

Fig. 6-80—Axis-angle angle output membership functions for Objective 7 optimal attitude profile FIS. Not all output MFs are used by the FIS for all passes.

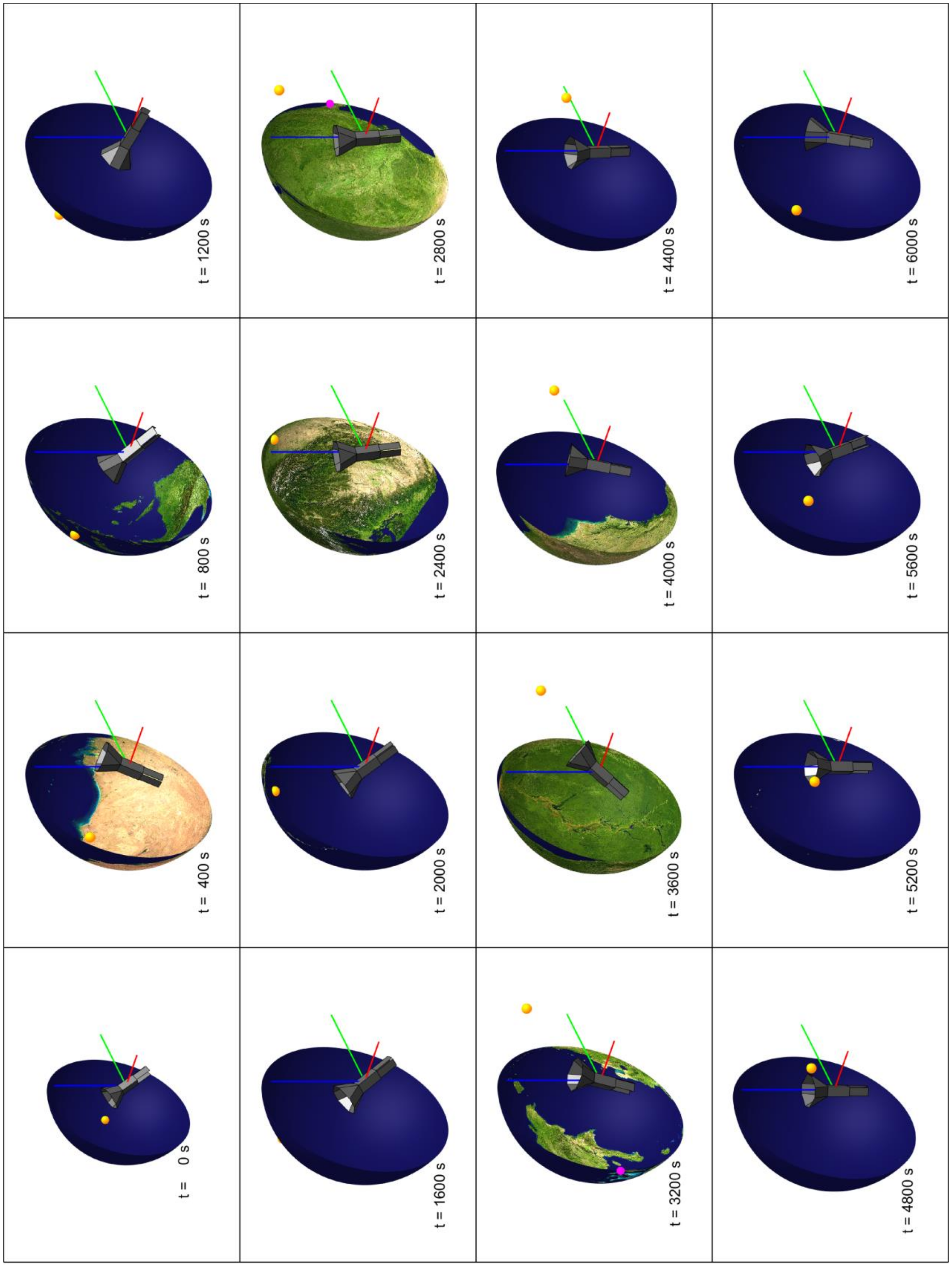

Fig. 6-81—The spacecraft Objective 7, Pass 17 orientation with respect to the reference coordinate system (red X, green Y, blue Z) is shown with the earth, sun (yellow sphere), and ground station (magenta sphere) projected on the celestial sphere.

6.8 Objective 8: Nominal Science

Like the optimal attitudes for Objectives 6 and 7, the optimal attitude profile FIS found for Objective 8 is identical to that found for the more-constrained Objective 5. The only additional constraint Objective 5 includes that Objective 8 does not is the relatively easily attainable battery charge constraint which, when met, only adds 1.0 to the fitness function value, which was not significant enough of a difference to change the path the GA took to find the optimal solutions. Because Objective 5 is more restrictive, there are more variables of interest to show for the results of Objective 5 than for the results of Objective 8, and rather than repeating the same information, all results for Objective 5 and Objective 8 are presented in the section 6.5.

6.9 Dart Mode

The Dart Mode was conceived as an operational mode which would minimize the drag disturbance torque and therefore control torque required to maintain an orientation in which the satellite can generate adequate solar power and maintain adequate link margin at the expense of attaining the lowest possible experiment temperatures. Fig. 6-82 shows that Dart Mode is able to generate significantly more power than all the optimal state trajectories, except the optimal Objective 1 state trajectory, which maximized power generation. Fig. 6-83 and Fig. 6-84 show that the way it does this is by keeping one solar panel, in the case the +Y solar panel, at a constant angle with respect to the sun at all times, while another solar panel, in this case the +X solar panel, is periodically exposed to the sun. In the worst case, when sun elevation is zero, neither the +Y or –Y solar panel has a view of the sun at any point in the orbit, but the +X solar panel is still periodically exposed to the sun. In addition to maintaining good power generation, Dart Mode also maintains very good antenna gain and therefore link margin, as shown in Fig. 6-85 and Fig. 6-86. Antenna gain stays above -2 dB for the duration of the Pass #17 ground station pass, with an antenna gain greater than 0 dB for most of the ground station pass. This antenna gain is able to keep link margin greater than 0 dB for the duration of the ground station pass. Though both power generation and link margin are good in Dart Mode, the experiment temperature climbs to ambient temperatures (near 300 K) once per orbit, as can be seen in Fig. 6-87. While the minimum experiment temperature in Dart Mode appears to be less than 150 K, note that the plotted temperatures are from a steady-state model, which serves as a proxy for the true time-dependent temperature, so actual experiment temperatures will likely be higher. Fig. 6-88 shows that the primary reason the experiment temperature reaches ambient temperatures is because the sun angle drops below 40 degrees. In fact, the minimum sun angle with respect to the experiment is the elevation of the sun in the reference local-level coordinate system, so in Dart Mode, the spacecraft experiment temperature will reach its minimum value approximately once a month corresponding with the maximum sun elevation; however, this temperature is likely not the minimum value the experiment could attain if it were in another orientation, because the minimum experiment-to-sun angle is still less than 90 degrees. Fig. 6-89 and Fig. 6-90 show that the active control required to maintain Dart Mode is not very demanding, compared with the actuation required to follow the optimal attitude state trajectories presented in the previous sections. The reaction wheel angular accelerations are all within 1.0 RPM/s, and the reaction wheel angular velocities stay within 5% of the maximum allowable reaction wheel angular velocities.

Fig. 6-91 shows the Dart Mode orientation, which is constant with respect to the reference local-level coordinate system. Also shown is the local-level-referenced celestial sphere with projected images of the earth, sun, and ground station location.

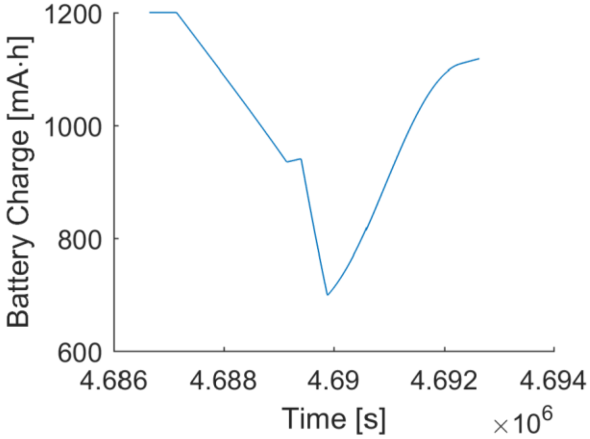

Fig. 6-82—Battery charge time history for Dart Mode Pass 17 (ground station). Battery charge increases significantly after eclipse and ground station transmission.

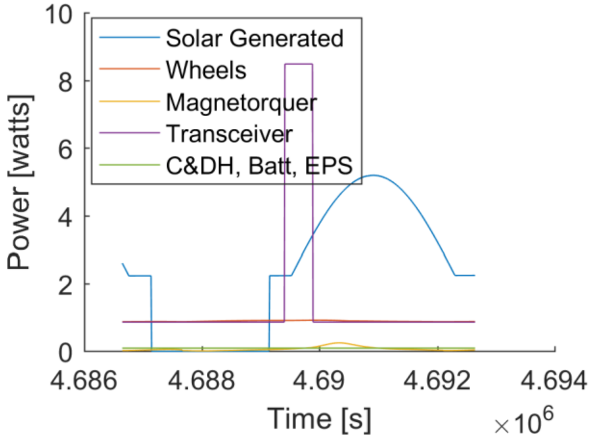

Fig. 6-83—Power use and generation for Dart Mode Pass 17 (ground station). Solar power generation drops to zero during eclipse but increases significantly in sun.

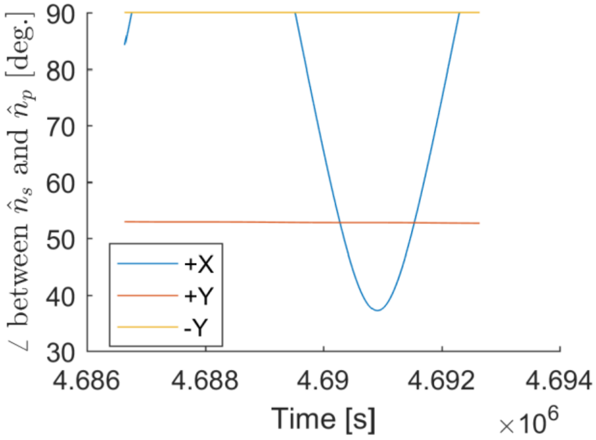

Fig. 6-84—Solar panel normal to sun vector angles for Dart Mode Pass 17 (ground station). The –Y panel maintains a constant angle while the +X panel angle decreases in sun .

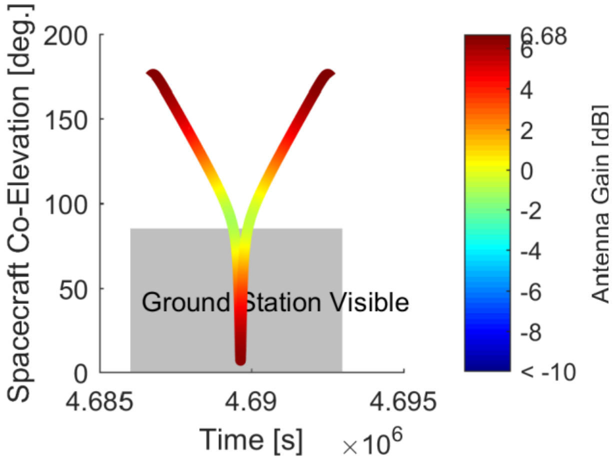

Fig. 6-85—Antenna gain for Dart Mode Pass 17 (ground station). Gain near horizons is negative but is positive for most of pass.

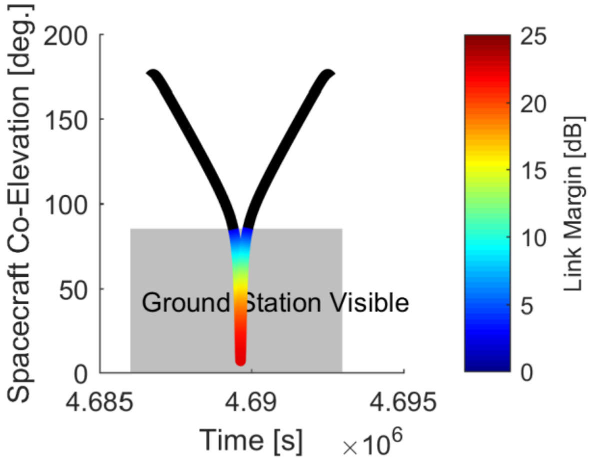

Fig. 6-86—Link Margin for Dart Mode Pass 17 (ground station). All of pass has link margin above 0 dB.

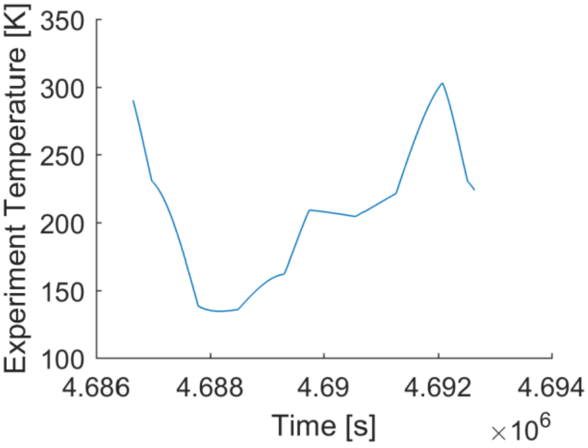

Fig. 6-87—Experiment temperature for Dart Mode Pass 17 (ground station). Eclipse temperatures fall to cryogenic range (<150 K) but temperature peaks near ambient 300K.

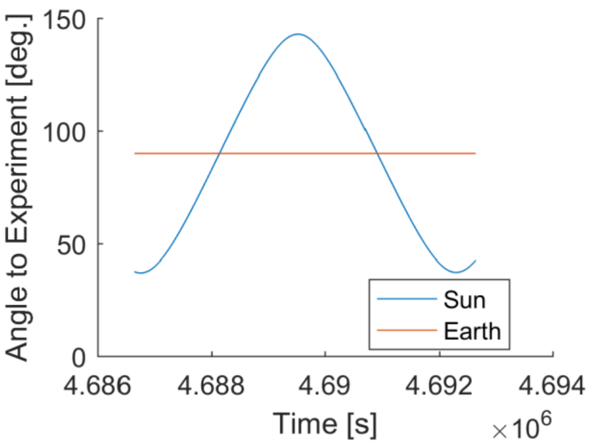

Fig. 6-88—Sun and earth to experiment angles for Dart Mode Pass 17 (ground station). Small sun angles once per orbit result in ambient spikes in temperature.

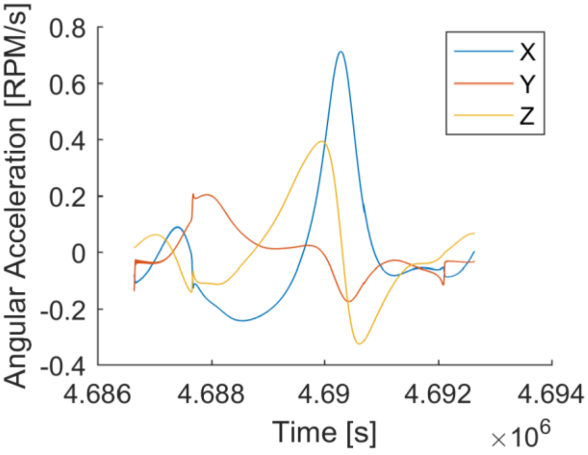

Fig. 6-89—Reaction wheel angular acceleration for Dart Mode Pass 17 (ground station). Relatively small control torques are needed to maintain Dart Mode.

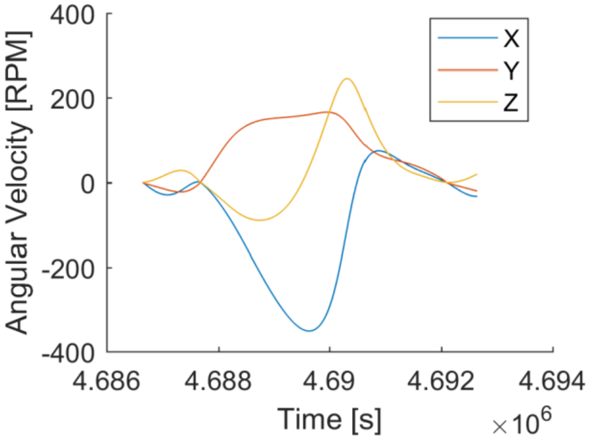

Fig. 6-90—Reaction wheel angular velocity for Dart Mode Pass 17 (ground station)..

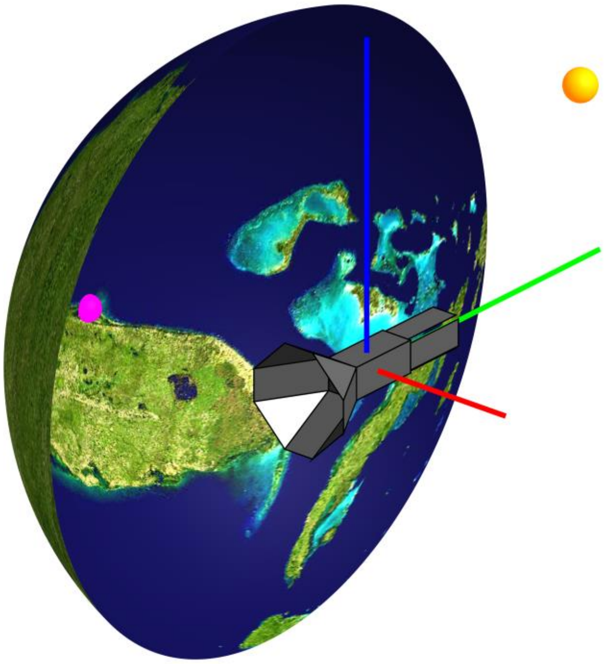

Fig. 6-91—The spacecraft Dart Mode orientation with respect to the reference coordinate system (red X, green Y, blue Z) is shown with the earth, sun (yellow sphere), and ground station (magenta sphere) projected on the celestial sphere. Dart Mode maintains this constant orientation with respect to the reference coordinate system for all time.

6.10 Attitude Mode Comparison

The optimal attitude profiles, or attitude modes, found for each of the eight optimization objectives each have their own strengths and weaknesses. Examining the objective function values of each of these solutions reveals exactly what makes each solution better than the others with respect to the objective function of the optimization problem which generated it. Table 6-1 presents the values of the eight objective functions for each of the nine attitude modes discussed above using the start epochs used to optimize FISs with only sun vector input parameters, and Table 6-2 breaks down the components of these objective functions for each of the nine attitude modes. Similarly, Table 6-3 presents the values of the eight objective functions for each of the nine attitude modes discussed above using the start epochs used to optimize FISs with ground station vector input parameters, and Table 6-4 breaks down the components of these objective functions for each of the nine attitude modes.

From Table 6-2 and Table 6-4, it is clear that all nine attitude profiles always satisfy the reaction wheel angular acceleration and angular velocity constraints as well as the battery charge constraint. However, antenna gain constraints are only met for the optimal attitude profiles whose objectives require them (i.e. objective 2, 6, and 7) and only one of the objectives whose goal is to maximize antenna gain. Furthermore, the optimal attitude profiles which do satisfy the antenna gain constraint only satisfy it for the set of ground station pass epochs. These ground station passes are much higher-elevation and represent a much larger portion of the overall simulation time in comparison with the ground station passes in the sun-vector-parameter-only epochs. Of the five ground station passes in the sun-vector-only epoch data set, three have maximum spacecraft elevations of about 10 degrees above the horizon and two have maximum elevations of about 45 degrees above the horizon, whereas all twenty ground station passes in the ground-station-vector epoch data set have maximum spacecraft elevations of at least 55 degrees above the horizon. Of all constraints included in this work, the antenna gain constraint may be the most stringent. The antenna gain constraint is an inequality constraint: the constraint is satisfied when the value of the constraint term in the optimization problem is at least 1.0, and this term has a maximum value of 2.0. Table 6-4 shows that this term is equal to 1.0 for the optimal solutions to the problems with this constraint, indicating that this is an active constraint, and without it, the value of the unconstrained objective could increase[‡‡‡]. Viewing the need to communicate with the ground station from another perspective, the optimization problems which seek to maximize antenna gain do not necessarily satisfy the antenna gain constraint. In fact, the solution to Objective 3, which was found to maximize average antenna gain for both sun-vector-parameter epochs and ground-station-parameter epochs does not satisfy the antenna gain constraint, because antenna gain drops

---

[‡‡‡] This term is 1.05 for the optimal Objective 4 solution. Objective 4 does not use this constraint in its objective function, but the objective of Objective 4 is to maximize antenna gain.

Table 6-1—Objective function values of each optimal attitude profile for each optimization problem, using the set of sun vector start epochs. The optimal objective solutions should maximize their respective objective function.

	Objective 1	**Objective 2**	**Objective 3**	**Objective 4**	**Objective 5**	**Objective 6**	**Objective 7**	**Objective 8**
Opt. Obj. 1 Sol.	1126.82	2.00	183.99	182.99	298.21	2.00	3.00	297.21
Opt. Obj. 2 Sol.	1049.35	2.44	149.82	148.82	296.59	2.44	3.44	295.59
Opt. Obj. 3 Sol.	1057.24	2.12	310.76	309.76	304.17	2.12	3.12	303.17
Opt. Obj. 4 Sol.	1037.30	2.23	141.99	140.99	294.72	2.23	3.23	293.72
Opt. Obj. 5 Sol.	1050.58	2.00	99.58	98.58	336.04	2.00	3.00	335.04
Opt. Obj. 6 Sol.	1051.70	2.20	168.01	167.01	298.15	2.20	3.20	297.15
Opt. Obj. 7 Sol.	1051.70	2.20	168.01	167.01	298.15	2.20	3.20	297.15
Opt. Obj. 8 Sol.	1050.58	2.00	99.58	98.58	336.04	2.00	3.00	335.04
Dart	1093.46	2.00	244.45	243.45	299.40	2.00	3.00	298.40

Table 6-2—Components of objective function values for each optimization problem, using the set of sun vector start epochs.

	$\|\|\boldsymbol{\omega}_w\|\|$ Constraint	**$\|\|\dot{\boldsymbol{\omega}}_w\|\|$ Constraint**	**Battery C Constraint**	**G_{ant} Constraint**	**G_{margin} >0 dB**	**G_{margin} >10 dB**	**G_{margin} >20 dB**	**Battery C Objective**	**G_{ant} Objective**	**$T_{payload}$ Objective**
Opt. Obj. 1 Sol.	1.00	1.00	1.00	0.00	0.84	0.18	0.00	1124.82	180.99	295.21
Opt. Obj. 2 Sol.	1.00	1.00	1.00	0.44	0.76	0.24	0.00	1047.35	146.82	293.59
Opt. Obj. 3 Sol.	1.00	1.00	1.00	0.12	0.88	0.16	0.00	1055.24	307.76	301.17
Opt. Obj. 4 Sol.	1.00	1.00	1.00	0.23	0.75	0.31	0.00	1035.30	138.99	291.72
Opt. Obj. 5 Sol.	1.00	1.00	1.00	0.00	0.49	0.08	0.00	1048.58	96.58	333.04
Opt. Obj. 6 Sol.	1.00	1.00	1.00	0.20	0.77	0.25	0.00	1049.70	165.01	295.15
Opt. Obj. 7 Sol.	1.00	1.00	1.00	0.20	0.77	0.25	0.00	1049.70	165.01	295.15
Opt. Obj. 8 Sol.	1.00	1.00	1.00	0.00	0.49	0.08	0.00	1048.58	96.58	333.04
Dart	1.00	1.00	1.00	0.00	1.00	0.20	0.00	1091.46	241.45	296.40

Table 6-3—Objective function values of each optimal attitude profile for each optimization problem, using the set of ground station vector start epochs. The optimal objective solutions should maximize their respective objective function.

	Objective 1	Objective 2	Objective 3	Objective 4	Objective 5	Objective 6	Objective 7	Objective 8
Opt. Obj. 1 Sol.	1047.09	2.11	191.90	190.90	295.71	2.11	3.11	294.71
Opt. Obj. 2 Sol.	938.73	939.73	215.69	214.69	295.03	295.03	296.03	294.03
Opt. Obj. 3 Sol.	919.96	2.92	443.77	442.77	305.28	2.92	3.92	304.28
Opt. Obj. 4 Sol.	905.85	906.90	419.04	418.04	300.68	300.73	301.73	299.68
Opt. Obj. 5 Sol.	935.51	2.15	104.44	103.44	335.23	2.15	3.15	334.23
Opt. Obj. 6 Sol.	919.64	920.64	193.78	192.78	298.91	298.91	299.91	297.91
Opt. Obj. 7 Sol.	919.64	920.64	193.78	192.78	298.91	298.91	299.91	297.91
Opt. Obj. 8 Sol.	935.51	2.15	104.44	103.44	335.23	2.15	3.15	334.23
Dart	993.29	2.24	268.52	267.52	297.96	2.24	3.24	296.96

Table 6-4—Components of objective function values for each optimization problem, using ground station vector start epochs.

	$\|\|\omega_w\|\|$ Constraint	$\|\|\dot{\omega}_w\|\|$ Constraint	Battery C Constraint	G_{ant} Constraint	G_{margin} >0 dB	G_{margin} >10 dB	G_{margin} >20 dB	Battery C Objective	G_{ant} Objective	$T_{payload}$ Objective
Opt. Obj. 1 Sol.	1.00	1.00	1.00	0.11	0.65	0.27	0.03	1045.09	188.90	292.71
Opt. Obj. 2 Sol.	1.00	1.00	1.00	1.00	0.85	0.59	0.09	936.73	212.69	292.03
Opt. Obj. 3 Sol.	1.00	1.00	1.00	0.92	1.00	0.72	0.12	917.96	440.77	302.28
Opt. Obj. 4 Sol.	1.00	1.00	1.00	1.05	1.00	0.67	0.11	903.85	416.04	297.68
Opt. Obj. 5 Sol.	1.00	1.00	1.00	0.15	0.52	0.22	0.01	933.51	101.44	332.23
Opt. Obj. 6 Sol.	1.00	1.00	1.00	1.00	0.85	0.59	0.09	917.64	190.78	295.91
Opt. Obj. 7 Sol.	1.00	1.00	1.00	1.00	0.85	0.59	0.09	917.64	190.78	295.91
Opt. Obj. 8 Sol.	1.00	1.00	1.00	0.15	0.52	0.22	0.01	933.51	101.44	332.23
Dart	1.00	1.00	1.00	0.24	1.00	0.45	0.10	991.29	265.52	294.96

to as low as 1.26 dB during Pass #7. This provides more evidence that the 5 dB constraint may, in fact, be too stringent. Because the reaction wheels constrain both the angular acceleration and angular velocity of the spacecraft so much, it cannot slew fast enough to track the ground station with the boresight of its antennas. Therefore, it may make sense to relax this to a 1 dB antenna gain constraint or switch to a link margin constraint, requiring positive link margin for the duration of the pass, though such a constraint could de-emphasize the desirable quality of attaining a large link margin for high-elevation ground station passes.

Comparing the objective function values of all optimal solutions, it is clear that, for the majority of the optimal solutions found, each optimal solution maximizes the objective function for which it was optimized. The most notable exception is Objective 4, which is optimized by the solution found for Objective 3. With respect to Objective 4, the optimal Objective 4 attitude profile has an objective function value of 418.04 whereas the optimal Objective 3 attitude profile has an objective function value of 442.77, which corresponds to an average antenna gain for the optimal Objective 3 attitude profile which is about 0.25 dB greater than the average antenna gain for the optimal Objective 4 attitude profile. The optimal Objective 3 attitude profile FIS likely outperforms the optimal Objective 4 attitude profile FIS due to relatively early termination of the Objective 4 solution and the difference in the number of inputs to each FIS, discussed above in section 6.4.

A less obvious exception is that Objectives 6 and 7 are optimized by Objective 4. Here, the optimal Objective 4 attitude profile outperforms the optimal Objectives 6 and 7 attitude profile (note that solutions to 6 & 7 are identical), in terms of Objective 6 and Objective 7, by an objective function value of about 1.82. This corresponds to the optimal Objective 4 attitude profile's average experiment temperature being about 1.77 K lower and its antenna gain constraint being satisfied slightly more than the optimal Objectives 6 and 7 attitude profile. Like the Objective 3 / Objective

4 optimization exception discussed in section 6.4, this outperformance of the optimal Objectives 6 and 7 attitude profile FIS by the optimal Objective 4 attitude profile FIS could be the result of differences in the FIS structure. The optimal Objectives 6 and 7 FIS has both sun vector parameter and ground station parameter inputs, whereas the optimal Objective 4 FIS has only ground station parameter inputs, so not only is the number of inputs different, the number of input membership functions for the common input variables (i.e. ground station vector parameters) is different. The solution to Objectives 6 and 7 could also be suboptimal due to the path the GA took when solving the problems. Both Objectives 6 and 7 have an antenna gain constraint, which was previously surmised to be overly restrictive. Because the GA is forced to satisfy this constraint before moving on to maximizing the objective, the GA population on the generation that first satisfies the constraint is significantly narrowed. The schemata necessary to maximize the temperature objective may have been removed from the population in the process of satisfying the constraints. Alternatively, because the population size is relatively small and string size relatively large, these schemata may not have existed in the population. If the useful schemata were removed or never existed, the GA would have to rely on mutation operations to generate the schemata which are most useful for maximizing the temperature objective, a random process which could take a significant number of generations. Missing or relatively inefficiently processing useful schemata in the population likely caused the GA to converge on a local optimum solution for the Objective 6 and 7 attitude profile FIS.

Comparing the temperature objective of the optimal Objectives 6 and 7 attitude profile to the temperature objectives of the other attitude profiles reveals that these communication-constrained temperature minimization problems were unable to find attitude profiles with temperature performance significantly different from that of the non-temperature-optimization solutions. The optimal solution for the lesser-constrained temperature optimization problems, Objective 5 and Objective 8, has an average experiment temperature of about 165 K (again, the solutions to these two problems were found to be identical), whereas all other optimal attitude profiles have average experiment temperatures of about 200 K. This suggests that the antenna gain constraint makes it more difficult to reach lower temperatures, which is somewhat intuitive, because, in order for CryoCube-1 to point its antennas at the ground station, in many cases, the interior of the sunshield has a view of at least part of the earth. Specifically, for high-elevation ground station passes, the ground station passes very close to spacecraft nadir, and due to the geometry of the spacecraft, there is no way to point the spacecraft antennas nadir without the interior of the sunshield viewing at least part of the earth. A brief look back at Fig. 6-64 shows that the minimum temperature attitude profile nearly exclusively points the open end of its sun shield more than 90 degrees away from earth nadir with a very brief period of pointing 90 degrees away from nadir corresponding to the warmest part of the pass. There is a tradeoff between closing the communication link and achieving minimum experiment temperature.

Dart Mode, the human-conceived operational mode nominally used for the CryoCube-1 mission, has similar performance to the other non-temperature-optimal modes and represents a good tradeoff between power generation and communication link margin. Though Dart Mode does not satisfy the antenna gain constraint, it does provide positive link margin for the duration of all the passes simulated. Dart Mode’s average antenna gain is second only to the optimal Objective 3 attitude profile’s average antenna gain for sun-vector-parameter epochs and third to the optimal Objective 3 and optimal Objective 4 attitude profiles’ average antenna gains for ground-station-vector-parameter epochs. Additionally, Dart Mode also offers a large average battery charge, second only to the optimal Objective 1 battery charge performance. Dart Mode’s average experiment temperature is on par with the average experiment temperature of the optimal solutions found for the optimization problems without any temperature component in their objective functions. Though Dart Mode is a good compromise among the three performance parameters (i.e. average battery charge, average link margin or antenna gain, and average experiment temperature), individual optimal modes found using the genetic-fuzzy optimization process could provide better performance with respect to each parameter, especially so with respect to minimizing average experiment temperature.

7 System Flight Acceptance

In early 2018, the CryoCube-1 design was relatively mature, and all major electrical subsystems had been purchased. Most of the hardware was at SLI's Milan, Ohio facility, but the radio, antennas, and a spare C&DH subsystem were at NASA KSC, where the C&DH software subsystem had been under development. The sunshield was still in a prototype phase and primarily consisted of an additively manufactured plastic mechanism with some rubber bands to provide the deployment spring force. This prototype sunshield had undergone several deployment tests, but a method was still under development for folding or otherwise stowing the thin shield material so that it could attach to the deployable mechanism, fit within the stowed shield volume, and deploy to the correct dimensions along with the mechanism. The satellite had not been manifested on a flight and so its operational orbit was not yet determined[§§§].

A significant amount of work was still required to finish CryoCube-1 and deliver it for flight. The team had to finish assembly of the electronics stack, finish development of the flight software, finish design and assembly of the experiment section, integrate the experiment section with the electronics bus section, and perform a number of verification activities to be accepted for flight. A number of last-minute modifications resulting from selection of the flight (i.e. the addition of several safety/integration requirements), continued sunshield prototyping and testing, and electrical hardware failures and replacements complicated the process of finishing and delivering CryoCube-1. This chapter describes the nearly-two-year effort required to complete design, assemble, test, and deliver CryoCube-1 to orbit.

[§§§] CryoCube-1 had had the opportunity to be manifested on several previous flights which could have put it in circular orbits at various altitudes and inclinations or one which would have placed it into a very elliptical orbit.

7.1 Management Approach

A discussion of the work done to get CryoCube-1 accepted for flight is not complete without an overview of the processes, tools, and techniques used to manage the project. As mentioned in section 1.1, the final push to assemble, integrate, and test the satellite was divided into two periods of relatively fast-paced work. The first period started in January 2018 and ended at the end of April 2018. The goal of this first period of work was to assemble the flight hardware that had been purchased into a CubeSat system for the first time, which would facilitate software development prior to delivery. The second period started in April 2019 and ended at the end of September 2019. The goals of this second period of work were to finalize assembly of the CubeSat, verify system functionality, receive approval for launch integration, and deliver the satellite for integration. Because these two periods of work each had very ambitious goals with a fairly aggressive schedule, project status was tracked and managed very closely.

A detailed Microsoft Project schedule was developed and updated daily to track the hundreds of tasks that needed to be completed over the course of a few months by a team dedicating, at most, 2–3 full-time equivalent (FTE) to the project. Individual tasks tracked at the project level often included details such as fastener specifications (e.g. screw size and material) and were often as small a task as plugging one connector of a wiring harness into a connector on a circuit board (a task which should only take seconds) to ensure tasks were assigned and completed in an appropriate, chronological order and that any necessary materials were purchased and available for use at the time they were needed. Breaking down tasks to this level of detail also helped provide sufficient slack in the schedule, in case, for example, a wiring harness was found to be too short and needed to be re-built. The project team assembled for brief (15–30 minutes) daily meetings to review the schedule for upcoming deadlines, report the status and/or completion of their assigned tasks (e.g. assembly, test, etc.), update the team on the status of procurements, and discuss their time-sensitive need(s) for the work products of other team members (i.e. what one individual was waiting on another to finish). Because SLI's CryoCube-1 team was divided into two groups, one focusing on completing the electronics bus half of the spacecraft and the other focusing on completing the gas storage and experiment half of the spacecraft, these daily meetings became vital to help plan and perform integration of the electronics and the experiment sections together into the complete spacecraft.

Ultimately, the detailed project schedule concluded with delivery of the spacecraft. However, the release of the satellite to the ISS program for launch integration was performed only after a series of acceptance criteria were reviewed and verified. Many of these acceptance criteria were internally generated by the CryoCube-1 team and were intended to verify spacecraft functionality. Functional tests were developed and conducted to verify solar panel deployment, sun shield deployment, and appropriate radio frequency response to commands. Sunshield thermal performance data was also collected in a series of thermal tests in order to validate thermal models and compare on-orbit performance to predicted performance. ADCS system performance, including B-dot performance, LQR performance, EKF performance, and the fuzzy attitude profile performance, was validated via simulation. ADCS system functionality was verified during flight software and communication functional testing. In addition to the internally-generated acceptance criteria, the International Space Station, from which CryoCube-1 was deployed, required a Payload Safety Review Panel (PSRP) to review and accept hardware documentation and test data in order for the spacecraft to be allowed on ISS. Once all acceptance criteria were met to the satisfaction of the CryoCube-1 team and the ISS program, CryoCube-1 was delivered to the ISS program.

7.2 Design and Assembly

Up to 2018, the satellite system design had primarily followed a waterfall approach, starting with a concept definition phase and maturing through preliminary and detailed design phases. As the project approached assembly and test, a more iterative approach was adopted. The custom-designed spacecraft components used in CryoCube-1 underwent several build and test cycles in parallel with flight software development for the primarily COTS electronics components. The pressure system, for instance, was assembled and disassembled several times to determine the best techniques and components to use to minimize leak rates. Similarly, the Telemetry and Data Collection software subsystem was developed by iteratively writing and debugging code to determine how best to communicate with each of the electronics subsystems via the I^2C busses. This iterative development approach ultimately resulted in some design changes as portions of the baseline critical design proved to be infeasible. Due to the cost to purchase and/or manufacture some of the spacecraft components, flight and protoflight hardware was used in this iterative development approach, so extreme care was taken to ensure these components were not irreparably damaged in the process of making design modifications.

Prior to assembly, a detailed system-level solid model had been developed in Creo. This solid model served several purposes, including mechanical design development, checking the fit and spacing of electronics stack components, and serving as the basis for other spacecraft models. The CryoCube-1 electronics stack contains five stackable printed circuit boards with the 104-pin CubeSat Kit (CSK) header, allowing the cards to plug directly into one another. The solid model was used with detailed vendor-supplied models of these circuit boards to select the appropriate spacing, ensuring that components on the boards would not interfere with one another and that wiring harnesses needing to plug into the boards would have enough clearance when plugged in. Detailed subsystem solid models of the experiment section, sunshield deployment mechanism, and gas storage subsystem were also developed in the process of mechanical design of these subsystems. Additionally, the COTS electronics bus structure, a Pumpkin 1.5 U chassis, was modified to be able to accommodate the electrical connectors on the Clyde Space solar panels, mount the antennas with threaded fasteners, accommodate a rail-mounted separation switch, and accommodate the wiring harness for experiment section instrumentation. Modifications to the structure were planned and modification drawings were generated using the system solid model. Aside from mechanical design, a copy of the solid model was de-featured and used to develop the detailed system thermal model, shown in Fig. 3-12, and mass properties of the solid model (i.e. center of mass and mass moments of inertia) were calculated and used to develop the attitude control software subsystem.

Fig. 7-1—A detailed solid model of the CryoCube-1 system was used to help design and package all subsystems within the CubeSat.

Machinist drawings, assembly drawings, and even G-code for additive manufacturing were all exported from system and subsystem-level solid models of CryoCube-1 and used in the manufacture and assembly of many of the custom components on the spacecraft. The modification drawings for the COTS chassis were used by a skilled SLI machinist using a CNC machine to cut the required relief holes for solar panel electrical connectors, the rail-mounted separation switch, and the experiment section instrumentation wiring harness. The experiment tank, storage tank components, and manifold tying them together were all additively manufactured with Inconel using solid models of these pressure system components. An SLI welder welded the storage tank components together to form four separate storage tanks, which were X-ray inspected to check for imperfections. The additively manufactured tanks and manifold were further machined with threaded holes, and very small tubes and fittings were used to connect the pressure system components together along with other custom-machined structural elements of the spacecraft, including anodized aluminum rail sections, additively manufactured plastic beams, and G-10 plates, to form the fully-assembled pressure system. The fully-assembled pressure system was proof-pressure tested, then filled with helium and checked for leaks using a helium mass spectrometer. Leaks were fixed by disassembling and reassembling the pressure system with different, more-leak-tight fittings, which was a very tedious task due to the highly-integrated nature of the pressure vessels and structure. In parallel with the pressure system machining and assembly, parts for an anodized aluminum version of the plastic prototype sunshield were ordered and assembled, first with custom-made rubber bands, then with custom-made springs, when it was found the rubber bands would not sufficiently deploy the sunshield.

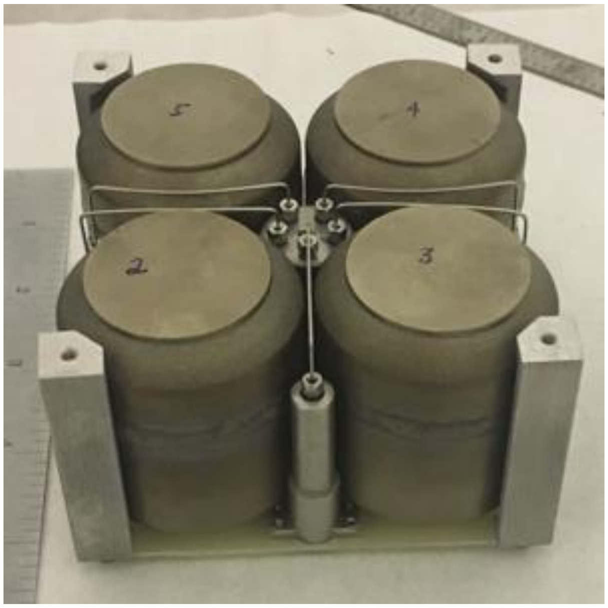

Fig. 7-2—CryoCube-1's pressure system gas storage section contains the manifold (center), used to tie all tanks together, and the fill port (front), used to pressurize the system with gaseous Xenon.

During the first period of fast-paced development in 2018, the electronics bus was fully assembled for the first time. This assembly occurred in parallel with mechanical assembly of the pressure system. Assembly of electronics components primarily consists of stacking the C&DH, Battery, EPS, Reaction Wheel, and custom-designed Experiment Interface printed circuit boards (PCBs), plugging each board's 104-pin CSK stack header in to the header of the board below it and standing the boards off from one another using spacers in each of the four corners of the circuit board stack. Four threaded rods, rigidly attached to a chassis baseplate, are slid through four through-holes in each of the corners of the circuit boards in order to align the boards and give the electronics stack some structural stiffness; the hollow cylindrical spacers also slide over these rods. In addition to the 104-pin CSK stack header, separate wiring harnesses were assembled and used to connect other electrical connectors on some of the boards to one another. These wiring harnesses provide many important connections, including: connecting the solar panels to the EPS and connecting the Radio, experiment instrumentation, and IMUs to the Experiment Interface PCB. When stacking the electronics components for the first time, basic I^2C interface software was developed to allow the C&DH subsystem to communicate with all other electronics subsystems. This software provided the basis for the Telemetry and Data Collection software subsystem as well as the Solar Panel Deployment and Sunshield Deployment functionality of the C&DH software subsystem and the IMU, Reaction Wheel, and Magnetorquer communication needed for the ADCS software subsystem. On top of the Experiment Interface PCB, the radio sits in its additively manufactured plastic mounting structure with through-holes which slide over the four threaded rods, and on top of the radio sits a bracket to which the IMUs mount. Nuts screwed on to the top of the threaded rods hold the entire electronics stack in compression. Around the outside of the electronics stack is the electronics bus structure, consisting of the bottom plate to which the threaded rods of the stack were rigidly attached, a top plate, and four-walled structure made of sheet metal which attaches to the top and bottom plate using threaded fasteners. Clips attached to the base and top plates of the structure hold the solar panels in place against the walls of the electronics bus structure.

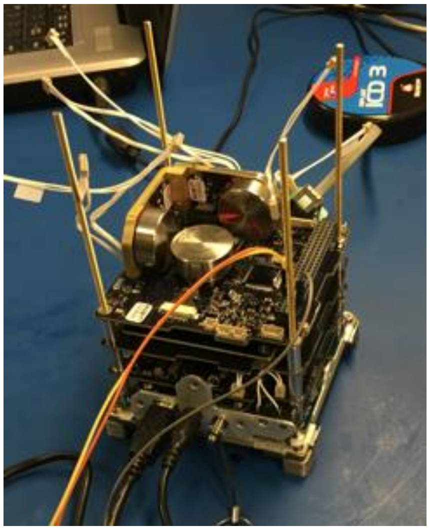

Fig. 7-3—During initial assembly, the electronics stack was built up one board at a time to facilitate software development.

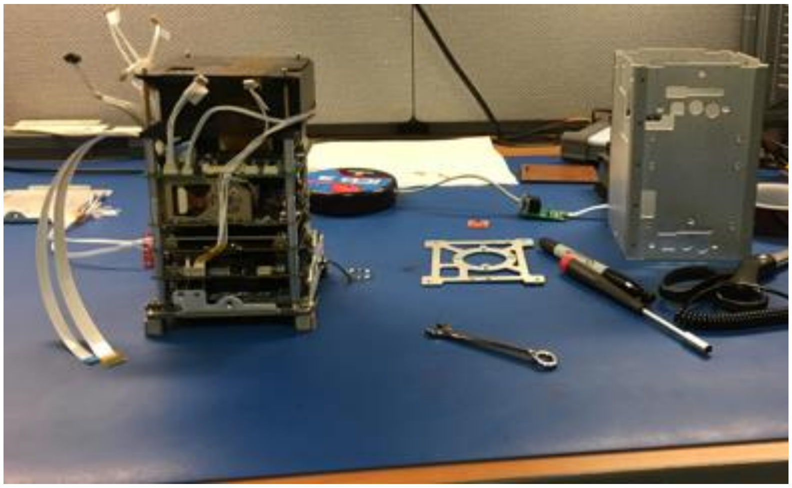

Fig. 7-4—Once the electronics stack was fully assembled, the four-walled sheet metal chassis was slid over the exterior of the stack and fastened to the top and bottom chassis structure plates.

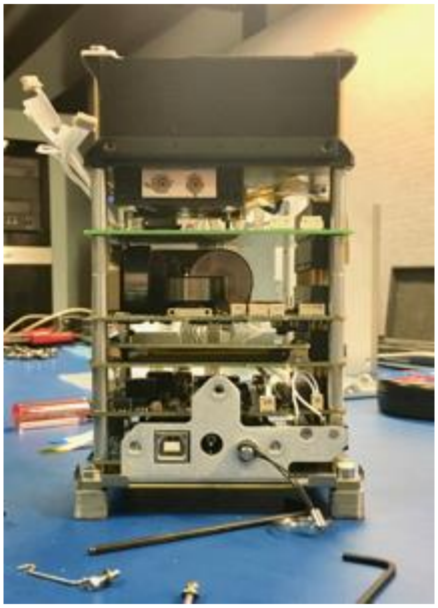

Fig. 7-5—Spacers along the four threaded rods at the corners of the electronics stack prevent the stack components from touching one another.

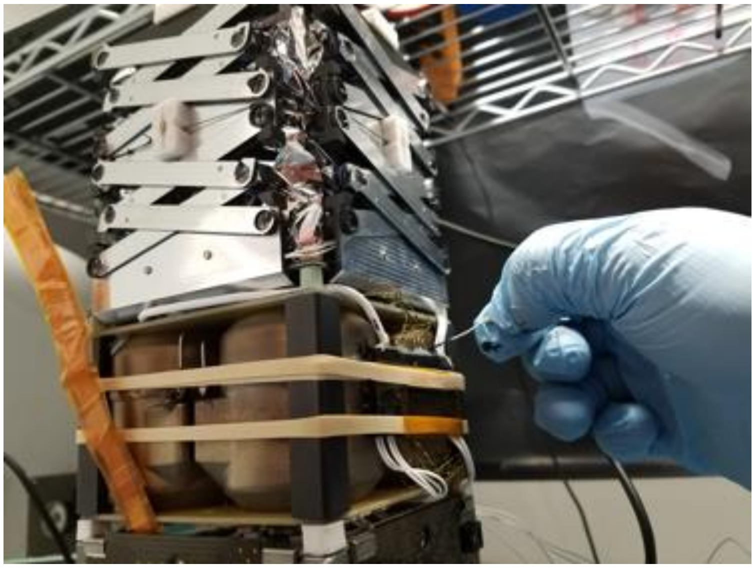

Fig. 7-6—Once the two halves of the spacecraft were mechanically mated together, final electrical connections were made between the experiment and electronics bus. Epoxy was used to rigidly attach the electrical connectors to the spacecraft.

Once the experiment and pressure subsystem and the electronics bus are assembled, these two halves of the spacecraft are integrated relatively easily into the complete CubeSat system. However, requirements changes, design changes, and electronics hardware failures in 2019 required the electronics bus to be disassembled and reassembled four separate times. During this time, the pressure system was also disassembled and reassembled with its new fittings to stop leaks that had been measured the previous year. In 2019, when the plan to manifest CryoCube-1 on a flight to ISS started to develop, the team was given an updated set of requirements it had to meet to be accepted to fly as part of a manned mission. The new flight acceptance requirements included using three separation switches instead of the two that CryoCube-1 had initially planned to use and testing the spacecraft's lithium ion battery cells to verify they met safety requirements for storage on the ISS. To meet separation switch requirements, last-minute design changes were made to include a roller switch along one of CryoCube-1's rails. In the process of preparing to perform the required battery tests, it was discovered that the COTS battery had stopped holding a charge, so it was replaced with a spare. Later, during communication testing, it was discovered that the EPS had stopped functioning normally as it would not charge the spare battery to a voltage corresponding to a full charge, but instead would only charge the battery to about 5% capacity. Therefore, new battery and EPS subsystems were ordered, and the old subsystems were swapped out within weeks of delivery of the system.

7.3 Acceptance for Flight

As discussed in the previous section, part of the criteria determining whether or not CryoCube-1 was approved for flight was defined by the ISS safety requirements. The remainder of the acceptance criteria was generated by the CryoCube-1 team and served to define the spacecraft functionality the team believed would ensure mission success. In contrast, the ISS safety requirements are intended to ensure that, in the event of failure, the CubeSat does no harm to the primary mission, ISS. The CryoCube-1 team worked with NanoRacks to collect and generate documentation providing evidence the CubeSat met the ISS safety requirements. NanoRacks, in turn, presented this information to the Payload Safety Review Panel (PSRP) on behalf of the CryoCube-1 team. The process of collecting, generating, and presenting this information took several months and required NanoRacks to relay questions or concerns of the PSRP to the CryoCube-1 team and relay the CryoCube-1 team's responses back to the PSRP.

The amount of information presented to the PSRP for its acceptance was extensive, encompassing all aspects of the system. A detailed bill of materials (BOM), including masses, composition, and exposed surface areas of all spacecraft components, was submitted to ensure the final spacecraft mass was acceptable, no restricted or forbidden materials were used in construction, and any off-gassing of acceptable materials would be within acceptable limits. The solid model and measured as-built exterior dimensions were submitted to ensure the satellite met interface requirements for the NanoRacks CubeSat Deployer (NRCSD). Deployable information, including methods used to restrain the deployables in their stowed state and theoretical maximum forces of unrestrained deployables on the interior walls of the NRCSD, was submitted to instill confidence that the deployable would remain restrained for deployment and that, in the event of premature deployment, the NRCSD would still be able to deploy the spacecraft. Very detailed pressure subsystem information was submitted, as this subsystem was viewed as a potentially high-risk item which could cause harm to the primary mission in the event of an anomaly. The pressure system documentation package included reports indicating temperatures and machine status of the additive manufacturing machines used to build the pressure system tanks; the weld request form, Weld Procedure Specification (WPS), Procedure Qualification Record (PQR), and Qualification Test Record (QTR) for the welds and welder used on the pressure system tanks; test records for pressure system proof pressure test; test records for pressure system tank cold shocks; non-destructive X-Ray inspection reports of the welded tanks; test records for pressure system helium leak check; and an identification of the pressure system's final fill pressure. Information on the spacecraft inhibit architecture, including detailed information on the number, type, make, model, actuation distance, and physical location of the inhibit switches, was submitted. Following the do-no-harm philosophy of CubeSats on the ISS, the inhibit architecture was required to be two-fault tolerant; if two of the three inhibit switches were to fail, the third switch would still inhibit the spacecraft from powering on. CryoCube was originally designed and built following less restrictive inhibit switch requirements and needed to be modified before it could be accepted for flight on ISS. The hazards of flying batteries, especially rechargeable lithium-ion batteries, are serious enough that the NanoRacks and the PSRP limit the cell chemistries to those which have previously successfully been demonstrated safe to fly and require flight qualification tests to be conducted on all lithium-ion batteries. Flight qualification tests include: measuring physical exterior dimensions of the cells; measuring open-circuit voltage (OCV) of fully-charged cells; measuring OCV of fully-discharged cells for a two-week period to ensure OCV meets stability requirements; estimating nominal cell capacity using a series of charge/discharge cycles; subjecting the cells to a specified vibration profile and measuring physical dimensions, OCV, and cell capacity afterward to ensure stability requirements are met; subjecting the cells to a specified vacuum environment and measuring physical dimensions, OCV, and cell capacity afterward to ensure stability requirements are met; and measuring the short-circuit protection response time of a cell from the same lot as the flight qualified cells. Radio communication information, including operating frequencies, antenna type and location, modulation scheme, and licensing information, were submitted to ensure the spacecraft was properly licensed to communicate and that no electromagnetic interference (EMI) or compatibility (EMC) issues existed. Just prior to delivery of the satellite to NanoRacks for integration into the NRCSD, CryoCube-1 underwent vibration testing, successful completion of which was necessary to be accepted for flight to the ISS.

Fig. 7-7—Flight battery cells were charged and discharged using a custom-made test setup.

Fig. 7-8—Flight battery cells were exposed to vibration in all three axes.

Fig. 7-9—Flight battery cells were exposed to vacuum conditions under a small bell jar.

Functional acceptance criteria conceived and verified by the CryoCube-1 team was used in addition to the safety-driven acceptance criteria required by the PSRP to indicate to the team that the system was functioning as intended and was ready for flight. These acceptance criteria were mainly verified using a series of functional tests. The thermal performance of the sunshield subsystem, in terms of temperature and heat flux, was measured during a thermal-vacuum test in which the open end of the sun shield, mounted in a bell jar at vacuum pressure, was exposed to a liquid-nitrogen-temperature cold plate, and the exterior surface of the sunshield was exposed to a solar simulator light source. Sunshield subsystem deployment functionality was extensively tested under a variety of conditions to ensure the mechanism would successfully deploy the shield with a high degree of confidence. Several deployment tests were successfully conducted in both air and in vacuum at room temperature. However, when cold (-15–-40°F) deployment tests were initially conducted, the mechanism was found to stick shut, most likely due to trapped moisture which froze at reduced temperatures. Several design modifications, including the use of stiffer springs, and continued testing were able to yield a design which was consistently able to deploy the shield at room temperature, at cold temperatures, at atmospheric pressure, and in vacuum. Similar testing for the solar panels was able to demonstrate that, when integrated with the spacecraft, the solar panels could be consistently deployed using at least one of the two deployment circuits available on each of the COTS panels. Of all the functional testing performed, flight software functionality and radio frequency (RF) communication testing constituted the majority of functional testing. The purpose of this testing was to verify all RF commands could be successfully executed and the flight software responded to RF commands as intended. However, due to the compressed nature of the project schedule, much of the software development work on the Telemetry and Data Collection, Safe Mode Management, Solar Panel Deployment, Sunshield Deployment, and ADCS software subsystems was performed concurrently with RF communication testing, slowing this testing to develop and debug the incomplete software. Appropriate response of the satellite to each of the commands, the ability of the satellite to downlink requested data files, and extended periods of flight software execution without faults or resets demonstrated acceptability of flight software and

RF communication systems to SLI and KSC. Taken together, successful functional testing demonstrated to the CryoCube-1 team that the satellite had been built to satisfy operational requirements, so the team approved the spacecraft to move forward with delivery for launch and operations.

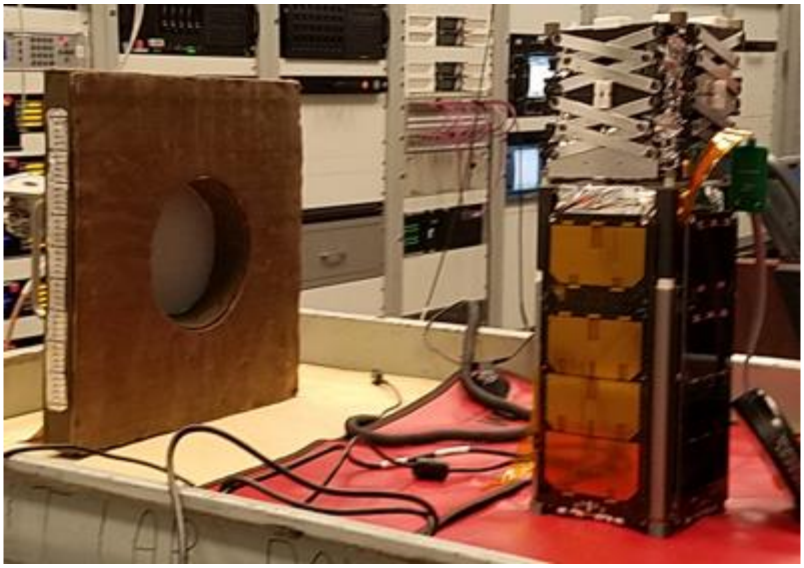

Fig. 7-10—During RF communication tests, a small antenna (left) was pointed directly at CryoCube-1's antennas.

Fig. 7-11—Prior to deployment, the sunshield fits within a 1U volume.

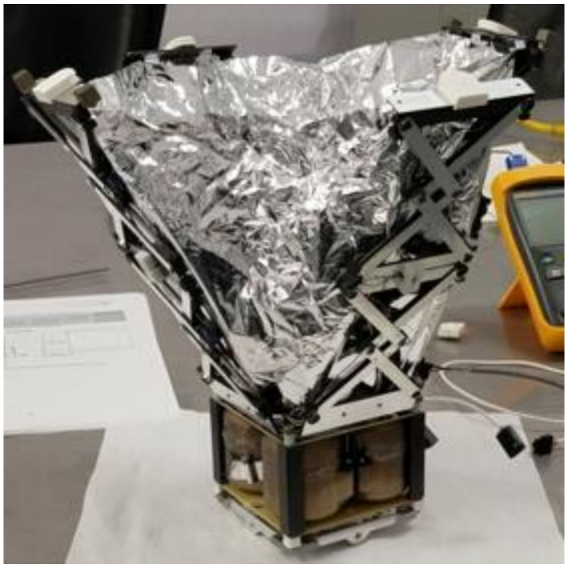

Fig. 7-12—After deployment, the sunshield provides a shade that allows the experiment tank to reach cryogenic temperatures.

Though the PSRP and the CryoCube-1 team approved the satellite to move forward with launch and operations, the CryoCube-1 team had identified and accepted some operational risks affecting

CryoCube-1's mission success. One of these risks is that the satellite's on-board orbit estimation may be significantly different from its actual orbit position and velocity, resulting in attitude estimation errors and an inability to attain the Dart Mode attitude, pointing antennas nadir to ensure initial acquisition and communication with the ground station. This orbit estimation error results from the use of an on-board TLE, which becomes outdated in the months between delivery of the satellite and its deployment. With large position and velocity vector errors, the predicted measurement vector calculated in the EKF will have a large error, and in turn, a posteriori state and state covariance estimates will have large errors. This will result in the spacecraft either slowly tumbling as it keeps applying the B-Dot algorithm, never successfully exiting its EKF Start attitude mode, or, if it does enter Dart Mode, slowly tumbling as it tries to follow an incorrect state estimate. Because the S-band antennas are directional, a slowly tumbling spacecraft makes communication difficult. It may take several attempts at communication over several ground station passes to catch the spacecraft in a favorable orientation for communication. For instance, if there is a 50% chance the spacecraft is in a favorable orientation during any given ground station pass, it would take seven ground station passes to have greater than a 99% chance of communicating with the spacecraft at least once. Another risk carried into operation is that the EPS appears to charge the battery at a slower rate than expected. During RF communication testing after the battery and EPS had been replaced, it was observed that the EPS would not charge the battery at a rate faster than what was used by the system, including the power-hungry transmitting radio, even when a USB cable was plugged in to the EPS to provide power to charge the battery. With the USB plugged in, the battery would provide about an hour of intermittent downlink time before discharging to the level at which the EPS turns off power to the rest of the spacecraft. This behavior made communication testing on the ground somewhat challenging as tests could only be completed for relatively small time durations. However, for on-orbit operations, each ground station pass is, at most, about seven minutes, leaving ample time for the solar panels to recharge batteries in the nominal Dart Mode and while slowly rotating, such as during detumble.

7.4 Delivery, Launch, Deployment, and Early Operations

On September 27, 2019, the CryoCube-1 team finalized its approval process for the satellite and delivered CryoCube-1 to NanoRacks in Houston, Texas. On September 30, 2019, NanoRacks integrated CryoCube-1 into its NRCSD along with another CubeSat, AzTechSat (the first satellite built by students in México). The NRCSD assembly was delivered to the ISS program and received final approval signatures from the ISS program PSRP on October 4, 2019. On December 5, 2019, the SpaceX CRS-19 (commercial resupply) mission to the ISS launched CryoCube-1 from Cape Canaveral Air Force Station. On February 19, 2020, CryoCube-1 was deployed from the ISS.

Fig. 7-13—CryoCube-1 launched to the ISS onboard the SpaceX CRS-19 mission's Falcon 9 launch vehicle.

A number of extenuating circumstances complicated early operations, including attempted ground communications. As CryoCube-1 deployed from the NRCSD, its solar panels were observed deploying, an event which was scheduled to occur 30 minutes after deployment from the NRCSD. An analysis of potential faults indicated that the most likely cause of premature solar panel deployment was that the spacecraft had turned on for a period spanning at least 30 minutes while it was in the NRCSD. This could have happened during integration as inhibits were actuated and de-actuated and the CubeSat was charged via USB for two separate periods estimated to be about 20 minutes each. However, without telemetry data, it is unclear what exactly caused CryoCube-1 to turn on or how long CryoCube-1 may have been on within the NRCSD.

Fig. 7-14—CryoCube-1 deployed from the International Space Station along with the 1U AzTechSat. (Image courtesy of NASA.)

Shortly after deployment, the ISS program supplied the CryoCube-1 team with estimated state vector and orbital elements of the CubeSat at time of deployment. This information was used to initiate several unsuccessful communication attempts over the course of a few days after deployment. By February 22, NORAD had catalogued CryoCube-1 in its database and published TLEs for the spacecraft. The NORAD orbit estimate, actually estimated by the 18th Space Control Squadron of the United States Air Force (USAF), was found to be significantly different from the initial state vector and orbital element estimate provided by the ISS program. The two orbits were different enough that, due to a relatively narrow beam width, the ground station antenna would not have been able to establish communication with the satellite if it had been pointed at the ISS-program-estimated orbit and the satellite were in the USAF-estimated orbit. Several attempts at communicating with the satellite in the USAF-estimate orbit were also unsuccessful, however. After further investigation, including contacting an online community tracking the nine CubeSats deployed on February 19, 2020[****], the CryoCube-1 team determined that the majority of these satellites had been misidentified. The TLEs appeared to describe the orbits of the nine CubeSats deployed on that day, but mapping of satellites to TLEs was incorrect. The online community had identified a mapping of TLEs to satellites which was consistent with successful radio communications they had established with a number of the satellites. Using the information gained from the online community, in early March 2020, the CryoCube-1 team developed a two-prong approach to attempt to establish communication with its satellite. The CryoCube-1 team would work through the list of candidate TLEs, starting with those which were most likely to correspond with CryoCube-1, in order to attempt to communicate with the satellite; due to the uncertainty in orientation, several attempts to communicate would be made for each candidate satellite. In parallel, the CryoCube-1 team would work with a different group within the USAF in an attempt to positively identify each of the nine satellites deployed the same day as CryoCube-1. By mid-March 2020, the team had started implementing the plan. A few additional unsuccessful communication attempts had been made, and the USAF had started searching for, but had not found, CryoCube-1. Unfortunately, starting in mid-March, operation of the ground station used to communicate with CryoCube-1 and the USAF's search for CryoCube-1 were both suspended due to the effects of COVID-19, and, as of this writing in early May 2020, have not been resumed.

[****] https://community.libre.space/t/iss-cubesat-deployment-2020-02-17-phoenix-qarman-radsat-u-argus-2-aztechsat-1/5459/69

7.5 Lessons Learned

Throughout the CryoCube-1 project, a number of issues have arisen whose solutions have provided the team insight which may be generally useful to other future CubeSat projects. A brief list of lessons learned and the issues that helped teach these lessons follows below.

Lesson 1: Even though a datasheet provides a value for a given attribute, the value may not be correct, so always test to verify the accuracy of critical values reported in datasheets.

Setting the oscillator frequency for the dsPIC microcontroller did not work exactly as described in the user manuals. The user manuals provided a mathematical formula to use to determine an integer value which would set the oscillator frequency. The formula yielded an integer value which did not correctly set the oscillator frequency, so trial and error was required to set the frequency, allowing communication at the correct baud rates and forcing timers to count in real-time values, so for example, a one-second timer lasts for one second.

The power usage reported on some of the datasheets of the electrical subsystems was significantly different from the power usage measured during testing. Normal quiescent power usage was much higher than expected, resulting in a decrease in battery charge much faster than anticipated.

Lesson 2: Documentation detailing functionality of embedded systems or embedded systems components may be sparse or difficult to interpret, so provide ample time in the project schedule to develop and debug embedded systems software.

During debugging, some programming errors, most notably attempted out-of-bounds access of arrays, were caught by built-in interrupt service routines running on the dsPIC microcontroller. These error-handling interrupts would cause the microprocessor to reset and thus were first detected by seemingly random software resets. During step-by-step debugging, it was found the reset occurred at different locations in the code, especially if lines of code were temporarily removed, or the reset did not occur at all if the step-by-step debugger was made to step into all functions. Eventually, the interrupts handling the software-related errors were located and used to help track down the source of the errors. However, the non-intuitive, seemingly non-deterministic behavior of the software resets was difficult to diagnose and correct, especially for a team relatively inexperienced with developing embedded systems.

Though I^2C is a standardized communication protocol used by many electronic devices, the functions available for use in the Microchip programming libraries were low-level, relatively sparsely documented pieces of the protocol which had to be built up into more-functional routines. During software development, it was found that some functional sequences which were used to successfully communicate with some subsystems did not work at all with other subsystems, making the process of developing generically useful I^2C functions capable of communicating with all subsystems somewhat challenging.

The exact series of commands required to control the angular velocity and angular acceleration of the reaction wheels was somewhat difficult to interpret from the reaction wheel subsystem user manual. Many attempts to control speed and acceleration resulted in no actions. Other times, one of the wheels would seemingly randomly turn on and reach its maximum speed. The correct command sequences were eventually discovered, and the seemingly random spinning up to maximum speed was resolved.

Lesson 3: Buy and use flight spares and dedicated development hardware: they are invaluable.

The datasheet for the dsPIC microprocessor used on CryoCube-1 only guaranteed 100 writes to program memory before parts of program memory could fail. The program memory of the spare C&DH microprocessor used for development was written thousands of times during software development. While no program memory failures were detected on the development microprocessor, the CryoCube-1 team took precautions to keep the number of software writes on the flight microprocessor below 100.

Both the original flight battery subsystem and the original flight EPS stopped functioning and required replacement. The battery stopped holding a charge, and the EPS was not able to fully charge a new battery. Troubleshooting the issue with the vendor did not provide any clues as to why these subsystems may have failed, but analysis of the boards indicated some components on the EPS may have overheated and failed.

Lesson 4: When assembling the satellite electronics, verify functionality frequently and especially before assembly steps which are more difficult to reverse to ensure no faults have been introduced.

One of the times the electronics bus was being assembled, a wire harness was pinched between a spacer and the Experiment Interface PCB, shorting one or more of these wires to ground, which tripped the EPS's overcurrent protection, shutting off power to the busses and/or switches which were shorted. Functionality of these busses was checked only after assembly of the electronics bus was completed. Disassembly of the electronics bus to correct the issue involved reversing the most complex tasks of assembly, including: attaching solar panels to the bus exterior, attaching antennas to the bus exterior, fastening the structure together, and integrating the radio into the electronics stack. The issue could have been detected shortly after the radio was integrated into the electronics stack as the weight of the radio was found to have caused the wires to be pinched.

Lesson 5: Avoid designing "deadly logical traps" into the electronics hardware configuration.

The Innoflight S-band transceiver used by CryoCube-1 offers a “firecode” pin which can be used to hold a line low to trigger an interrupt or some other event on another microprocessor. The behavior of this pin can be configured in the radio’s settings, but when the radio is off, the pin is low. In its original designed configuration, this firecode pin was attached directly to the RESET pin of the dsPIC microcontroller. When the dsPIC’s RESET pin is held low, the microprocessor effectively turns off. The radio is powered by a 12 V switched line on the EPS. If this line were to be switched off, the radio would effectively be turned off and the CubeSat would be unable to respond to commands. Furthermore, in the original designed configuration, the firecode pin would trigger the C&DH microprocessor RESET line, effectively stopping the flight software from executing, leaving no possibility of ever turning the 12 V switch or the main flight microcontroller back on. Therefore, the line connecting the firecode pin to the RESET line was cut and periodic tasks to turn on the switched 12 V line powering the radio were added to ensure this line stays powered and communication with the ground remains possible.

Lesson 6: Verify the compatibility of sensors with materials to which they are exposed prior to exposing them.

The pressure transducer in the pressure system is a vacuum-referenced transducer with a diaphragm and seal between the pressure-side being measured and the reference vacuum side. Calibration of the transducer before and after leak checking the pressure system was found to be significantly different. After discussing the issue with the manufacturer, it was discovered that small molecules, such as hydrogen or helium, may leak past the seal into the reference volume, changing the calibration. Original discussion with the manufacturer in selecting this transducer only mentioned the working fluid, not the fact that the pressure system would be leak checked using helium and a helium mass spectrometer.

Lesson 7: Use a robust communication architecture that (1) provides a position/velocity beacon, (2) provides or allows at least some telemetry, command, and control independent of orientation, or (3) both.

The baseline initial acquisition plan is somewhat paradoxical in that an updated TLE is required to determine how to point the spacecraft's antennas to the ground in order to communicate, but the spacecraft must first communicate with the ground to receive an updated TLE. An orientation-independent means of communication is preferable as this allows ground operators to send and receive information without having to wait for the ADCS to stabilize the spacecraft. Furthermore, a beacon, not only indicating whether or not the spacecraft is alive, but also indicating the spacecraft's position and velocity is ideal for determining where to point ground-based antennas to communicate with the satellite.

Lesson 8: Use a robust means of orbit determination for attitude control (e.g. GPS).

Early operational issues resulted from relying on TLE-based orbit determination. Without an accurate orbit estimate, the EKF estimating spacecraft attitude state will produce a very erroneous state estimate. Using this erroneous state estimate for attitude control could cause the spacecraft to tumble. A GPS receiver could be used to provide a very accurate estimate of spacecraft position and velocity.

8 Conclusions & Future Work

Solutions for eight optimal attitude state trajectory problems were found using a novel genetic-fuzzy approach. State trajectories were encoded in fuzzy inference systems as a function of state vectors rather being expressed as a function of time. This encoding scheme allows these FISs to be used generically for many different time periods rather than having to periodically compute optimal state trajectories and upload them to the spacecraft. Due to program memory constraints of the hardware on which they were designed to operate, these FISs use eight-bit integers to represent vector input parameters and angle-axis attitude output parameters. A filter was designed to smooth the relatively rough eight-bit attitude output, limiting both angular acceleration and angular velocity of the raw FIS output attitude profile to values capable of being controlled by the satellite's reaction wheels. Given these smoothed spacecraft attitude profiles, reaction wheel angular velocity and angular acceleration were calculated using the dynamic equations of spacecraft and reaction wheel motion. An optimal reaction wheel desaturation algorithm was designed to minimize reaction wheel angular velocity using the magnetic control torque. Models of spacecraft power use and generation, antenna gain and link margin, and experiment temperature were used to calculate objective function values for the eight optimal attitude state trajectory problems. Power use and antenna gain models were based on data measured from CryoCube-1 flight hardware, power generation models were based on datasheet values for CryoCube-1 flight hardware, and link margin and experiment temperature models were based on detailed link budget and detailed thermal models developed to analyze CryoCube-1 performance.

The eight optimal attitude profiles found by the genetic algorithm demonstrated CryoCube-1's performance limits and highlighted key tradeoffs in selection of its attitude modes of operation. The optimization problems with maximum power generation objectives indicate the satellite is able to maintain an average charge of about 1100 mA·h with a full charge being 1200 mA·h. The optimization problems with maximum antenna gain objectives indicate the satellite is able to maintain an average antenna gain of about 6.44 dB with an ideal antenna boresight tracking of the ground station corresponding to 6.68 dB. The optimization problems with minimum experiment temperature objectives indicate the satellite is able to maintain an average experiment temperature of about 165 K, near the cryogenic range (< 150 K). The attitude rate filter and optimal magnetic desaturation algorithms developed for this work successfully forced all optimal attitude profile solutions to satisfy reaction wheel angular velocity and angular acceleration constraints. Non-reaction-wheel constraints used in the optimization problems clearly showed a tradeoff between maintaining a high antenna gain and achieving a minimum experiment temperature. The average experiment temperature of the attitude profile solutions found for the temperature minimization problems with antenna gain constraints were not significantly different from the average experiment temperature of the attitude profile solutions found for the other non-temperature-minimization problems. However, inconsistencies between the optimal attitude profiles satisfying antenna gain constraints and the attitude profile with maximum antenna gain indicate the antenna gain constraint used in these problems may be too restrictive. For higher-elevation ground station passes, the maximum antenna gain attitude profile maintains a larger link margin than the attitude profile satisfying antenna gain constraints. The Dart Mode attitude selected for CryoCube-1's nominal operations provides a good tradeoff between power generation and link margin. However, Dart Mode is not able to achieve near-cryogenic average experiment tank temperature. Minimum experiment tank temperature can be achieved using the optimal attitude profile FIS found for the experiment temperature minimization problem. Similarly, maximum average battery charge and maximum antenna gain attitude profile FISs do achieve better performance than Dart Mode with respect to these performance parameters.

During nominal operations, CryoCube-1's attitude determination and control system is designed to detumble the spacecraft, then enter Dart Mode, the low-risk constant local-level referenced attitude profile mode of operation. From Dart Mode, the spacecraft can then be commanded to enter a fuzzy attitude profile mode. Dart Mode provides adequate power and link margin, satisfying the lower-level needs of the spacecraft and mission, but it provides poor experiment thermal performance. In order to achieve lower, near-cryogenic experiment temperatures, the minimum experiment temperature attitude profile FIS will be uploaded to the spacecraft, and the spacecraft's ADCS will be commanded to enter its fuzzy attitude profile mode of operation. If CryoCube-1 successfully completes its primary mission to demonstrate thermal performance of the sunshield and CFM of the Xenon in the experiment tank, other optimal attitude profile FISs may be uploaded to the spacecraft and tested to verify actual performance against predicted performance.

Though CryoCube-1 was successfully built, delivered, launched, and deployed from ISS, its mission is still ongoing, complicated by a list of extenuating circumstances. The systems engineering effort to design, build, prototype, test, and get CryoCube-1 accepted for launch to the ISS followed an aggressive schedule through its own challenges, including: testing and troubleshooting sunshield deployment issues, tracking down and fixing experiment pressure system leaks, debugging flight software with seemingly nondeterministic behavior, modifying and testing the inhibit switch architecture and lithium-ion battery cells due to unforeseen ISS safety requirements, and replacing the battery and EPS PCBs due to sudden hardware failures. The team was able to keep up with this fast-paced iterative design-prototype-build approach, however, and successfully demonstrated to themselves and the ISS program PSRP that CryoCube-1 was ready to fly. The CryoCube-1 team remains optimistic that communication will be established with the satellite as ground station and satellite tracking operations return to normal functionality following the March–May stay-at-home orders issued to slow the spread of COVID-19.

In addition to the continued search and attempted communication with CryoCube-1, work will continue on genetic-fuzzy attitude state trajectory optimization. A Monte Carlo analysis will be run to evaluate the performance of the optimal attitude profile FISs to general expected orbit conditions, not just the conditions dictated by the time periods over which the optimization objective function simulations were run. The robustness of the genetic-fuzzy attitude state trajectory solutions could also be evaluated through use of a sensitivity analysis. Though it is not currently planned to conduct a sensitivity analysis, one could provide significant insight into the strengths and weaknesses of the optimal solutions, quantify the robustness of the optimal solutions, and highlight areas in which it is critical to minimize modeling uncertainty. For instance, CryoCube-1's mass moment of inertia tensor was never measured and was only estimated by constructing a detailed solid model. The uncertainty in this estimate was not quantified, yet mass moment of inertia is one of the primary components of the dynamic attitude model. Slight variations in principal moments of inertia or the orientation of principal axes of inertia with respect to the body axes could subtly or drastically affect performance of a spacecraft following the optimal trajectory. Other factors introducing uncertainty into the dynamic model include aerodynamic modeling parameters (i.e. atmospheric density, drag coefficient, and center of pressure) and orbit modeling uncertainties. Similarly, an analysis of the sensitivity of spacecraft performance with respect to variations in parameters used in the power generation, storage, and consumption models could highlight risks or demonstrate adequacy of the optimal trajectories to meet power constraints. Uncertainties in power system model parameters, such as solar flux, solar cell efficiencies (which degrade with age), and load-dependent electrical power conversion efficiencies could all compound to demonstrate there is a chance that battery charge constraints may be violated. Like the power models, variations in the communication link models could affect the ability of the spacecraft to meet communication constraints.

To conduct an effective sensitivity analysis, all sources of modeling uncertainty should first be quantified. These uncertainties should then be used in a design of experiments to determine how the variation of these uncertain model parameters about the nominal values used to calculate the optimal attitude state trajectories affect the components of the objective functions, specifically the constraint/penalty terms and the unconstrained objective terms, as was presented in Table 6-2 and Table 6-4 in section 6.10. The components of the objective functions provide direct measures of effectiveness which can be used to quantify performance of the spacecraft following the optimal genetic-fuzzy attitude state trajectory. Though this method may be used to directly evaluate the genetic-fuzzy system performance, it may be informative to vary uncertain model parameters and re-solve the optimization problems to compare optimal solutions, again using the same objective function components. Variation of the re-solved optimal attitude trajectory performance as a function of uncertain model parameters may help contextualize the variation of the originally-solved optimal attitude trajectory performance to determine whether performance variation can be primarily attributed to qualities of the original solution or to qualities of the underlying optimization problem.

Lastly, the optimization problems presented will be solved using more mathematically-rigorous trajectory optimization techniques, such as collocation or pseudospectral methods, and these optimal trajectories will be compared to those of the optimal attitude profile FISs. Work is already underway on applying both fuzzy and more-mathematically rigorous techniques to determine temperature-optimal attitude state trajectories for Sierra Lobo's next CubeSat, the Bichromatic Littoral Temperature Observatory (BLTO) (pronounced Balto). BLTO's mission, funded by the Office of Naval Research (ONR) through a National Oceanographic Partnership Program (NOPP) award, is to use an infrared detector to measure ocean surface temperature at the Amazon River delta. Similar to CryoCube-1, BLTO will use a deployable sunshield to passively cool a thermal radiator attached to the heat rejection side of a cryocooler. The BLTO team is currently wrapping up Phase A mission definition development and anticipates continuing the program through detailed design and build in Phase B.

References

[1] Sutton, G. P., and Biblarz, O., Rocket Propulsion Elements, 8th ed, Wiley, Hoboken, NJ, 2010.

[2] McLean, C., Mustafi, S., Walls, L., Pitchford, B., Wollen, M. and Schmidt, J., "Simple, Robust Cryogenic Propellant Depot for Near Term Applications," IEEE Aerospace Conference, IEEE, Big Sky, MT, 2011.

[3] Smitherman, D. and Woodcock, G., "Space Transportation Infrastructure Supported by Propellant Depots," AIAA Space Conference and Exposition, AIAA, Long Beach, CA, 2011.

[4] Ho, K., Gerhard, K., Nicholas, A. K., Buck, A. J., and Hoffman, J., "On-Orbit Architectures Using Contingency Propellant," Acta Astronautica, Vol. 96, 2014, pp. 217–226.

[5] Terrier, D. et al. "TX13.1.4 Propellant Production, Transfer, and Storage," 2020 NASA Technology Taxonomy, NASA, 2020, pp. 161.

[6] Sherman, A., "Cryogenic Cooling for Spacecraft Sensors, Instruments, and Experiments," Journal of Astronautics and Aeronautics, Vol. 16, No. 11, 1978, pp. 39–47.

[7] Prejean, T., et al. NanoRacks CubeSat Deployer (NRCSD) Interface Definition Doument (IDD), NR-NRCSD-S0003, Initial Release, 2018.

[8] Walker, A., Putman, P., and Cohen, K., "Solely Magnetic Genetic/Fuzzy-Attitude-Control Algorithm for a CubeSat," Journal of Spacecraft and Rockets, Vol. 52, No. 6, 2015, pp. 1627–1639.

[9] Starin, S. R. and Eterno, J., "Spacecraft Subsystems II—Control Systems," Space Mission Engineering: The New SMAD, 2nd ed., Microcosm Press, 2015, pp. 565–600.

[10] Shrivastava, S. K., and Modi, V. J., "Satellite Attitude Dynamics and Control in the Presence of Environmental Torques–A Brief Survey," Journal of Guidance, Vol. 6, No. 6, 1983, pp. 461–471.

[11] Wertz, J. R., Spacecraft Attitude Determination and Control, Reidel, Dordrecht, Holland, 1978.

[12] Luo, J, Chen, L., and Tang, G., "Attitude Optimization of Optical Space Surveillance Satellite to Observe Specific Geostationary Orbit Object," Optik, Vol. 127, 2016, pp. 11706–11716.

[13] Olsen, C. D., Echols, R. T., Woods, W. K., Onken, J. F., Horvath, T. J., and Stewart, R. L., "Orbiter Attitude Design for the Astro-1 Spacelab Mission," AIAA-92-1466, AIAA Space Programs and Technologies Conference, Huntsville, AL, 1992.

[14] Horvath, T. J., Grimaldi, R. S., Onken, J. F., Lochmaier, G. D., "Orbiter Attitude Design for the Astro-2 Spacelab Mission," AIAA-95-3613, AIAA 1995 Space Programs and Technologies Conference, Huntsville, AL, 1995.

[15] Arif, H., "Spacecraft Attitude Impacts on COLD-SAT Non-Vacuum Jacketed LH2 Supply Tank Thermal Performance," AIAA-90-1672, AIAA/ASME 5th Joint Thermophysics and Heat Transfer Conference, Seattle, WA, 1990.

[16] Hwang, J. T., Lee, D. Y., Cutler, J. W., and Martins, J. R. R. A., "Large-Scale Multidisciplinary Optimization of a Small Satellite's Design and Operation," Journal of Spacecraft and Rockets, Vol. 51, No. 5, 2014, pp. 1648–1663.

[17] Wu, W., Huang, H., Chen, S., Wu, B., "Satellite Multidisciplinary Design Optimization with a High-Fidelity Model," Journal of Spacecraft and Rockets, Vol. 50, No. 2, 2013, pp. 463–467.

[18] Shi, R., Liu, L., Long, T., Liu, J., Yuan, B., "Surrogate Assisted Multidisciplinary Design Optimization for an All-Electric GEO Satellite," Acta Astronautica, Vol. 138, 2017, pp. 301-317.

[19] Candini, G. P., Piergentili, F., Santoni, F., "Miniaturized Attitude Control System for Nanosatellites," Acta Astronautica, Vol. 81, 2012, pp. 325–334.

[20] Choueiri, M. N., Bell, M. R., and Peck, M., "Cost-Effective and Readily Manufactured Attitude Determination and Control System for Nanosatellites," 2018 AIAA/ASCE/AHS/ASC Structures, Structural Dynamics, and Materials Conference, AIAA SciTech Forum, 2018.

[21] Skullestad, A., and Gilbert, J. M., "H_∞ Control of a Gravity Gradient Stabilised Satellite," Control Engineering Practice, Vol. 8, 2000, pp. 975–983.

[22] Alkhodari, S. B., and Varatharajoo, R., "H_2 and H_∞ Control Options for the Combined Attitude and Thermal Control System (CATCS)," Advances in Space Research, Vol. 43, 2009, pp. 1897–1903.

[23] Liu, C., Sun, Z., Shi, K., and Wang, F., "Mixed H_2/H_∞ Control Approach and Its Application in Satellite Attitude Control System," International Journal of Engineering Research in Africa, Vol. 25, 2016, pp. 89–97.

[24] Han, C. Guo, J., and Pechev, A., "Nonlinear H_∞ Based Underactuated Attitude Control for Small Satellites with Two Reaction Wheels," Acta Astronautica, Vol. 104, 2014, pp. 159–172.

[25] Tayebi, J., Nikkhah, A. A., and Roshanian, J., "LQR/LQG Attitude Stabilization of an Agile Microsatellite with CMG," Aircraft Engineering and Aerospace Technology: An International Journal, Vol. 89, No. 2, 2017, pp. 290–296.

[26] Guarnaccia, L., Bevilacqua, R., and Pastorelli, S. P., “Suboptimal LQR-Based Spacecraft Full Motion Control: Theory and Experimentation,” Acta Astronautica, Vol. 122, 2016, pp. 114-136.

[27] Wu, S., Zhang, K., Peng, H., Wu, Z., and Radice, G., “Robust Optimal Sun-Pointing Control of a Large Solar Power Satellite,” Acta Astronautica, Vol. 127, 2016, pp. 226-234.

[28] Horri, N. M., Palmer, P., and Roberts, M., “Gain-Scheduled Inverse Optimal Satellite Attitude Control,” IEEE Transactions on Aerospace and Electronic Systems, Vol. 48, No. 3, 2012, pp. 2437–2457.

[29] Kristiansen, R., Nicklasson, P. J., and Gravdahl, J. T., “Satellite Attitude Control by Quaternion-Based Backstepping,” IEEE Transactions on Control Systems Technology, Vol. 17, No. 1, 2009, pp. 227–232.

[30] Li, Y., Ye, D., and Sun, Z., “Robust Finite Time Control Algorithm for Satellite Attitude Control,” Aerospace Science and Technology,” Vol. 68, 2017, pp. 46–57.

[31] Lo, S., Chen, Y., “Smooth Sliding-Mode Control for Spacecraft Attitude Tracking Maneuvers,” Journal of Guidance, Control, and Dynamics, Vol. 18, No. 6, 1995, pp. 1345–1349.

[32] Bingqiang, J., Dong, Y., and Zhaowei, S., “Trajectory Optimization for Satellite Fast Attitude Maneuver Based on Collocation Method,” 2014 International Conference on Mechatronics and Controm (ICMC), Jinzhou, China, 2014.

[33] Sathyan, A., Cohen, K., “Development of a Genetic Fuzzy Controller and its Application to a Noisy Inverted Double Pendulum,” *Fuzzy Logic Based in Optimization Methods and Control Systems and its Applications*, IntechOpen, 2018, pp. 27–40.

[34] Ernest, N., Cohen, K., Kivelevitch, E., Schumacher, C., Casbeer, D., “Genetic Fuzzy Trees and their Application Towards Autonomous Training and Control of a Squadron of Unmanned Combat Aerial Vehicles,” Unmanned Systems, Vol. 3, No. 3, 2015, pp. 185–204.

[35] Ernest, N., Carroll, D., Schumacher, C., Clark, M., Cohen, K., Lee, G., “Genetic Fuzzy Based Artificial Intelligence for Unmanned Combat Aerial Vehicles Control in Simulated Air Combat Missions,” Journal of Defense Management, Vol. 6, No. 1, 2016.

[36] Cook, B., Cohen, K., Kivelevitch, E., “A Fuzzy Logic Approach for Low Altitude UAS Traffic Management (UTM),” AIAA SciTech, AIAA Infotech @ Aerospace, San Diego, CA, 2016.

[37] Cook, B., Arnett, T., Cohen, K., “A Fuzzy Logic Approach for Separation Assurance and Collision Avoidance for Unmanned Aerial Systems,” *Modern Fuzzy Control Systems and its Applications*, Intech, 2017, pp. 225–256.

[38] Cook, B., Cohen, K., “Multi-Source Sensor Fusion for Small Unmanned Aircraft Systems Using Fuzzy Logic,” FUZZ-IEEE, Naples, Italy, 2017.

[39] Calvo, D., Avilés, T., Lapuerta, V., Laverón-Simavilla, A., “Fuzzy Attitude Control for a Nanosatellite in Low Earth Orbit,” Expert Systems with Applications, Vol. 58, 2016, pp. 102–118.

[40] Sathyan, A., Ma, O., Cohen, K., “Intelligent Approach for Collaborative Space Robot Systems,” 2018 AIAA SPACE and Astronautics Forum and Exposition, September 2018.

[41] Arnett, T., Cook, B., Clark, M., Rattan, K., “Fuzzy Logic Controller Stability Analysis Using a Satisfiability Modulo Theories Approach,” AIAA SciTech Forum, 19th AIAA Non-Deterministic Approaches Conference, Grapevine, Texas, 9–13 January, 2017.

[42] Sorgenfrei, M., and Fusco, J., “Testbed Validation of Spacecraft Safe Mode for a Deep Space CubeSat,” 2018 AIAA Aerospace Sciences Meeting, AIAA SciTech Forum, Kissimmee, Florida, 2018.

[43] Quadrino, M. K., “Testing the Attitude Determination and Control of a CubeSat with Hardware-in-the-Loop,” Master’s Thesis, MIT, 2014.

[44] Meissner, D. M., “A Three Degrees of Freedom Test Bed for Nanosatellite and Cubesat Attitude Dynamics, Determination, and Control,” Master’s Thesis, Naval Postgraduate School, Monterey, CA, 2009.

[45] Thomas, D., Wolosik, A., and Black, J., “CubeSat Attitude Control Simulator Design,” 2018 AIAA Modeling and Simulation Technologies Conference, AIAA SciTech Forum, 2018.

[46] Shuster, M. D., "A Survey of Attitude Representations," The Journal of the Astronautical Sciences, Vol. 41, No. 4, 1993, pp. 439-517.

[47] Vallado, David A., Paul Crawford, Richard Hujsak, and T.S. Kelso, "Revisiting Spacetrack Report #3," presented at the AIAA/AAS Astrodynamics Specialist Conference, Keystone, CO, 2006 August 21–24.

[48] Thébault et al. “International Geomagnetic Reference Field: The 12th Generation,” Earth, Planets and Space, 67:79, 2015.

[49] Bhat, S. P., “Controllability of Nonlinear Time-Varying Systems: Applications to Spacecraft Attitude Control Using Magnetic Actuation,” IEEE Transactions on Automatic Control, Vol. 50, No. 11, November 2005.

[50] Mantelli, M. B. H., and Yovanovich, M. M., “Thermal Contact Resistance,” *Spacecraft Thermal Control Handbook*, 2nd ed., Vol. 1: Fundamental Technologies, The Aerospace Press, El Segundo, CA, 2002, pp.599–638.

[51] Noton, M. “Appendix A.4,” *Spacecraft Navigation and Guidance*, Springer, London, 1998, pp. 172–173.

[52] Ross, T. J., Fuzzy Logic with Engineering Applications, 3rd Ed., John Wiley and Sons, Inc., West Sussex, UK, 2010.

[53] Goldberg, D. E., *Genetic Algorithms in Search, Optimization, and Machine Learning*, Addison Wesley Longman, Inc., Crawfordsville, IN, 1989.